Early-type stellar systems in nearby galaxy clusters: from dwarf galaxies to star clusters

Ingo Misgeld

München 2011

für Guadalupe

Early-type stellar systems
in nearby galaxy clusters:
from dwarf galaxies to star clusters

Ingo Misgeld

Dissertation
an der Fakultät für Physik
der Ludwig–Maximilians–Universität
München

vorgelegt von
Ingo Misgeld
aus Essen

München, den 19.04.2011

Contents

List of Figures

List of Tables

Zusammenfassung

Die vorliegende Dissertation beschäftigt sich mit den Eigenschaften von Frühtyp-Sternensystemen in den nahen Galaxienhaufen Hydra I und Centaurus. Zu diesen Sternensystemen zählen sowohl elliptische Galaxien (Riesen- und Zwerggalaxien), als auch Kugelsternhaufen und die sogenannten ultrakompakten Zwerggalaxien (ultra-compact dwarf galaxies, UCDs). Der Fokus der Arbeit liegt dabei insbesondere auf der Untersuchung von Zwerggalaxien und UCDs.

In Kapitel 2 und 4 werden Zwerggalaxien (Zwergellipsen, dwarf ellipticals (dEs) und Zwergsphäroiden, dwarf spheroidals (dSphs)) in Hydra I und Centaurus anhand morphologischer Selektionskriterien und mit Hilfe von gegenseitigen Relationen ihrer Grundparameter Helligkeit, Farbe und Flächenhelligkeit identifiziert. Aus ihrer auf Vollständigkeit korrigierten Anzahl wird die Galaxienleuchtkraftfunktion (galaxy luminosity function, GLF) abgeleitet. Es stellt sich heraus, dass die Steigung der GLF im leuchtschwachen Bereich wesentlich geringer ist, als die von kosmologischen Modellen vorhergesagte Steigung der Massenfunktion für dunkle Materie Halos. Mögliche Erklärungen für die gefundene Diskrepanz werden diskutiert.

Kapitel 3 präsentiert die Entdeckung einer großen Anzahl von UCDs/hellen Kugelsterhaufen im Hydra I Galaxienhaufen. Die UCDs wurden mittels einer großangelegten spektroskopischen Durchmusterung potenzieller UCD Kandidaten gefunden. Die Grundparameter Helligkeit, Farbe und Grösse der identifizierten UCDs werden erfasst und mit UCDs aus anderen Galaxienhaufen verglichen. Die hellste UCD in Hydra I gehört dabei zu den massereichsten UCDs, die jemals entdeckt wurden. Die aufgenommenen Spektren ermöglichen es zudem, anhand von Geschwindigkeitsmessungen die Dynamik des UCD/Kugelsterhaufensystems zu untersuchen. Es stellt sich heraus, dass die hellsten UCDs im Vergleich zu einer Auswahl an leuchtschwächeren Objekten eine signifikant geringere Geschwindigkeitsdispersion aufweisen. Dieses Ergebnis wird im Kontext verschiedener UCD Entstehungsszenarien diskutiert.

In Kapitel 5 werden Leuchtkraft, Grösse, Masse und projizierte Flächendichte der Zwerggalaxien aus Hydra I und Centaurus mit denen anderer Frühtyp-Sternensysteme, wie z.B. massereiche elliptische Galaxien, sehr schwache Zwergsphäroiden der Lokalen Gruppe, UCDs und Kugelsternhaufen, verglichen. Dabei wird der Parameterraum über 25 Grössenordnungen in der Leuchtkraft, 10 Grössenordnungen in der Masse und 5 Grössenordnungen in der Grösse abgedeckt. Dies eröffnet ein bisher nicht dagewesenes Gesamtbild von Frühtyp-Sternensystemen im lokalen Universum.

Chapter 1

Introduction

Besides giant elliptical galaxies, many low-mass, early-type stellar systems populate the cores of galaxy clusters, such as dwarf elliptical/spheroidal galaxies (dEs/dSphs), ultra-compact dwarf galaxies (UCDs) and globular clusters (GCs). The nomenclature already implies that one usually discriminates between galaxies and star clusters, but this distinction is not unambiguous, especially if taking the simplest definition of a galaxy as a gravitationally bound system of stars (e.g. Sparke & Gallagher 2000).

Traditionally, star clusters (in particular globular clusters) have been distinguished from galaxies by their morphological appearance, i.e. they are less luminous, small and roughly spherical stellar systems, containing several 10^4–10^6 stars. However, the discovery of unusual objects, such as the so-called 'ultra-compact dwarf galaxies' (Phillipps et al. 2001) or 'dwarf-globular transition objects' (DGTOs, Haşegan et al. 2005), other 'compact objects' (e.g. Chilingarian & Mamon 2008), and 'ultra-faint (Local Group) dwarf galaxies' (e.g. Gilmore et al. 2007), has challenged the conventional classification scheme, as these objects are intermediate in size and luminosity between traditional globular clusters and (dwarf) galaxies. In many cases, these objects have properties that do not allow to un-ambiguously assign them to one or the other category of stellar systems (for an extensive discussion on this topic see also Forbes & Kroupa 2011).

Also the definition of a 'dwarf galaxy' is not standardised in the literature. Dwarf galaxies are usually distinguished from giant elliptical and spiral galaxies by their low luminosities and low surface brightnesses and, just as for giant galaxies, one refers to early-type and late-type dwarf galaxies (dwarf irregulars). In Grebel (2001), dwarf elliptical galaxies are defined as objects with low luminosities ($M_V \gtrsim -17$ mag) and typical central surface brightnesses of $\mu_V \lesssim 21$ mag arcsec^{-2}. Dwarf spheroidal galaxies have even lower luminosities ($M_V \gtrsim -14$ mag) and central surface brightnesses ($\mu_V \gtrsim 22$ mag arcsec^{-2}).

Unless stated otherwise, the term early-type dwarf galaxy is used throughout this work for both types (dEs and dSphs), and the classical morphological distinction between galaxies and star clusters is adopted.

1.1   A Universe of dwarf galaxies

This study focuses on the characteristics of *early-type* dwarf galaxies and UCDs in nearby galaxy clusters. While giant elliptical (and spiral) galaxies dominate the light in the Universe, dwarf galaxies are the most abundant type of galaxy (e.g. Ferguson & Sandage 1991; Ferguson & Binggeli 1994; Secker & Harris 1996). They have mostly been studied in nearby galaxy clusters, such as Virgo, Coma, Fornax and Antlia (e.g. Sandage & Binggeli 1984; Binggeli et al. 1985; Ferguson & Sandage 1988; Binggeli & Cameron 1991; Ulmer et al. 1996; Secker et al. 1997; Trentham & Hodgkin 2002; Graham & Guzmán 2003; Hilker et al. 2003; Sabatini et al. 2003; Adami et al. 2006; Mieske et al. 2007a; Lisker et al. 2008; Smith Castelli et al. 2008a). Also in the Local Group (LG) a number of dwarf galaxies has been identified (e.g. Mateo 1998; van den Bergh 1999, 2000; Grebel et al. 2003, and references therein). For a list of LG dwarf galaxies, including the ultra-faint Milky Way dwarf spheroidals and the Andromeda satellites, see Table 5.1.

However, large samples of dwarf galaxies, as faint as the classical LG dwarf galaxies ($-15 \lesssim M_V \lesssim -10$ mag) are still missing for many environments. Based on deep VLT/FORS1 imaging, the early-type dwarf galaxy population of the Hydra I and Centaurus galaxy clusters is investigated in Chapter 2 and Chapter 4, for the first time reaching faint magnitude limits comparable with the regime of LG dwarf galaxies. In Chapter 5, the structural properties of the Hydra I and Centaurus dwarf galaxies are compared to other early-type stellar systems, including giant elliptical galaxies, compact elliptical galaxies, LG ultra-faint dwarf spheroidal galaxies, globular clusters and ultra-compact dwarf galaxies, resulting in a coverage of 25 orders of magnitude in luminosity and 5 orders of magnitude in size.

1.1.1   The faint end of the galaxy luminosity function

Probing the faint end of the galaxy luminosity function (GLF) in clusters and groups has in many cases exposed a discrepancy between the number of observed dwarf galaxies and the number of dark matter (DM) sub-haloes predicted by current hierarchical cold dark matter models – the so-called missing satellites problem (e.g. Kauffmann et al. 1993; Klypin et al. 1999; Moore et al. 1999; Diemand et al. 2008; Springel et al. 2008, for a comprehensive review see also Bullock 2010). Its origin is still a matter of debate: either there are many faint satellites not yet discovered, the predictions of the hierarchical models are not reliable, or the large majority of low-mass DM haloes have not formed any stars. If every small DM sub-halo contained luminous matter, hundreds of dwarf galaxies are expected to be observed in the LG, but already there the number of observed satellite galaxies is too low by about one order of magnitude. Although the Sloan Digital Sky Survey (SDSS) led to the discovery of several extremely faint ($M_V \gtrsim -8$ mag) LG dwarf galaxies (for references see Table 5.1), they are still not abundant enough to explain the expected DM sub-structure.
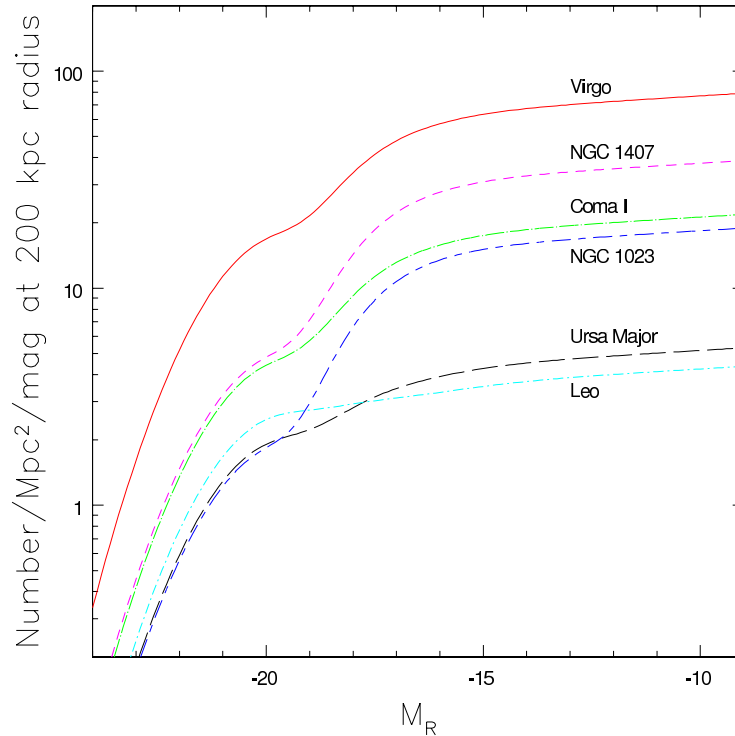
Fig. 1.1. Luminosity functions of six different environments, i.e. the Virgo Cluster, the NGC 1407 Group, the Coma I Group, the NGC 1023 Group, the Ursa Major Cluster and the Leo Group. Figure taken from Trentham & Tully (2002).

To quantify the discrepancy between the number of observed and the number of predicted dwarf galaxies, the GLF can be parametrised by the Schechter (1976) function

$$\phi(L)dL = \phi^* \left(\frac{L}{L^*} \right)^\alpha e^{-(L/L^*)} d\left(\frac{L}{L^*} \right). \tag{1.1}$$

Figure 1.1 shows the shape of the luminosity function in six different environments. The logarithmic faint-end slope α can be contrasted with the predicted slope of about -1.8 for the mass spectrum of cosmological dark-matter haloes (e.g. Press & Schechter 1974; Moore et al. 1999; Jenkins et al. 2001). Inconsistent with the predictions, rather flat slopes of $-1.0 \lesssim \alpha \lesssim -1.5$ have been derived for low density environments like the LG, as well as for massive galaxy clusters (e.g. van den Bergh 1992; Pritchet & van den Bergh 1999; Trentham & Tully 2002; Christlein & Zabludoff 2003; Hilker et al. 2003; Mobasher et al. 2003; Trentham et al. 2005; Chiboucas & Mateo 2006; Mieske et al. 2007a; Adami et al. 2009). Other authors, however, reported on steeper slopes (e.g. Sabatini et al. 2003; Milne et al. 2007, and references therein). The GLF of the Hydra I cluster has previously been determined by Yamanoi et al. (2007), who found $\alpha \sim -1.6$ in the magnitude range $-20 < M_{B,R} < -10$ mag. This is a steeper slope than reported by Yagi et al. (2002), who gave $\alpha = -1.31$ for the faint end slope of the composite GLF of 10 nearby clusters (including Hydra I) at $-23 < M_R < -16$ mag. Christlein & Zabludoff (2003) found $\alpha = -1.21$

for the composite GLFs of six clusters (also including Hydra I) at $-22 < M_R < -14$ mag, derived from deep spectroscopic samples. For the Centaurus cluster, Chiboucas & Mateo (2006) found $\alpha \sim -1.4$. Besides cluster-to-cluster variations, α also varies with cluster-centric radius and is galaxy type-specific (e.g. Kashikawa et al. 1995; Jerjen & Murdin 2000; De Filippis et al. 2011).

For the galaxy clusters Fornax, Perseus, Virgo and Coma, the faint-end slope of the GLF has been determined by direct cluster membership assignment via spectroscopic redshift measurements (e.g. Hilker et al. 1999; Drinkwater et al. 2001; Penny & Conselice 2008; Rines & Geller 2008; Adami et al. 2009). For other galaxy clusters, however, only photometric data are available at magnitudes where α dominates the shape of the GLF, i.e. $M_V \gtrsim -14$ mag. In this case, cluster galaxies have to be separated from background galaxies either by means of statistical background subtraction, or by their morphology and correlations between global photometric and structural parameters. For the latter case, the colour–magnitude relation – also known as the 'red sequence' – can be used, which is observed not only for giant elliptical galaxies (e.g. Visvanathan & Sandage 1977; Kodama & Arimoto 1997; Gallazzi et al. 2006), but also for early-type *dwarf* galaxies (e.g. Secker et al. 1997; Hilker et al. 2003; Adami et al. 2006; Mieske et al. 2007a; Lisker et al. 2008).

1.1.2   Photometric scaling relations of early-type galaxies

Correlations among global parameters of early-type galaxies can provide insight into the physical processes that have impact on the formation mechanisms and the evolution of these galaxies. For example, luminosity, colour, surface brightness, central velocity dispersion and the Mg_2 absorption line index are related to each other (the Fundamental Plane (FP) scaling relations, e.g. Faber & Jackson 1976; Kormendy 1977, 1985; Djorgovski & Davis 1987; Ferguson & Sandage 1988; Bender et al. 1992, 1993; Burstein et al. 1997; Bernardi et al. 2003a,b,c). In particular, the colour–magnitude relation and the magnitude–surface brightness relation connect the physical properties of the underlying stellar population and the structural properties with the galaxy masses. Investigating those scaling relations in multiple environments sets constraints on galaxy formation and evolutionary models of early-type galaxies.

A tight colour–magnitude relation (CMR) for early-type cluster galaxies has been known for a long time (Visvanathan & Sandage 1977). It is most commonly explained by an increase of the mean stellar metallicity with increasing galaxy mass, leading to redder colours of the more luminous galaxies (e.g. Kodama & Arimoto 1997; Ferreras et al. 1999). With a large sample from the SDSS, Gallazzi et al. (2006) confirmed this perception. The metallicity of a galaxy strongly depends on the fraction of gas that has been turned into stars. Due to their deeper potential well, massive galaxies are able to retain their interstellar gas and stellar ejecta longer and more effectively than low-mass galaxies since the escape velocity of stellar yields depends on the galaxy mass. Hence, subsequent generations of stars will be formed out of already enriched gas. Because giant elliptical galaxies with their high star formation rate (SFR) consume their gas very fast, the mean

stellar metallicity can reach high values in a short time. That accounts for the reddest colours of the most luminous galaxies.

Köppen et al. (2007) demonstrated that a variable integrated galactic initial mass function (IGIMF) that depends on the SFR can also explain the observed mass–metallicity relation. For a low SFR the IGIMF differs from the standard IMF in the sense that fewer high mass stars are expected to form. It has been found that galaxies with a low current SFR contain star clusters with a lower maximum mass (Weidner et al. 2004), and less massive star clusters less likely contain very massive stars (Kroupa & Weidner 2003). Since less massive galaxies are expected to have lower star formation rates, the effective upper mass limit for stars in such galaxies is lower. This reduces the number of type II supernovae as the main source of α-elements. Hence, the dependence of the IGIMF on the SFR implies a dependence of the metal abundance on the mass of the galaxy.

As an alternative to the aforementioned scenarios, Worthey (1994) and Poggianti et al. (2001) suggested that a change in the mean age of a stellar population could at least in part explain the CMR. A stellar population will gradually redden as stars with increasing age evolve off the main sequence towards the red giant branch. In this picture, redder colours of more massive galaxies imply systematically older ages. Observational evidence for this was given by Rakos & Schombert (2004), who reported on younger ages of dwarf elliptical galaxies in the Coma and Fornax clusters. Hence, an increase of age at fixed metallicity has the same effect on galaxy colours as an increase of metallicity at fixed age. This ambiguous interpretation of the CMR is based on the well-known *age-metallicity degeneracy* of integrated optical colours.

1.1.3 Surface brightness profiles of early-type galaxies

The surface brightness profiles of most dwarf galaxies can reasonably well be described by an exponential law:

$$I(R) = I_0 \exp\left(-\frac{R}{h_R}\right), \tag{1.2}$$

where I_0 is the central surface intensity and h_R denotes the scale length. The light profiles of giant elliptical galaxies and bulges of spiral galaxies, however, closely follow the de Vaucouleurs (1948) law:

$$I(R) = I_e \exp\left\{-7.67\left[\left(\frac{R}{R_e}\right)^{1/4} - 1\right]\right\}, \tag{1.3}$$

where I_e is the effective surface intensity, and R_e is the effective radius. The continuous transition between exponential and de Vaucouleurs profiles can be described by the Sérsic (1968) law:

$$I(R) = I_e \exp\left\{-b_n\left[\left(\frac{R}{R_e}\right)^{1/n} - 1\right]\right\}, \tag{1.4}$$
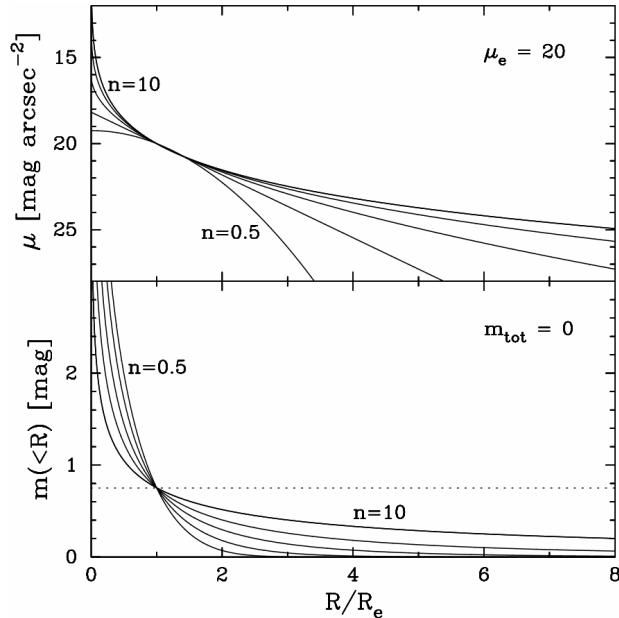
Fig. 1.2. Sérsic surface brightness profiles (*top panel*) and Sérsic aperture magnitude profiles (*bottom panel*) for $n = 0.5$, 1, 2, 4, and 10. The profiles are normalised at $\mu_e = 20$ mag arcsec^{-2}, and such that the total magnitude equals zero. The dotted line is offset by 0.75 mag (a factor of 2 in flux) from the total magnitude. Figure taken from Graham & Driver (2005).

where I_e is the intensity at the half-light radius R_e, and n is the profile shape parameter. The parameter b_n is chosen so that a circle of radius R_e encloses half the total light from the model. b_n is defined such that

$$\Gamma(2n) = 2\gamma(2n, b_n), \tag{1.5}$$

where γ is the incomplete gamma function, and Γ is the complete gamma function. For a reference of analytical approximations of b_n and related quantities see Graham & Driver (2005). Clearly, the exponential model and the de Vaucouleurs model result from $n = 1$ and $n = 4$, respectively.

Figure 1.2 illustrates Sérsic surface brightness and aperture magnitude profiles for different values of n. The surface brightness profile is given by

$$\mu(R) = \mu_e + \frac{2.5b_n}{\ln(10)} \left[(R/R_e)^{1/n} - 1 \right], \tag{1.6}$$

and the total apparent magnitude results from the aperture magnitude profile (also known as the 'curve of growth')

$$m(< R) = \mu_e - 5 \log R_e - 2.5 \log \left[2\pi n \frac{e^{b_n}}{(b_n)^{2n}} \gamma(2n, x) \right], \tag{1.7}$$

as R tends to infinity and $\gamma(2n, x) \to \Gamma(2n)$.

Previous studies showed that for dwarf galaxies the surface brightness increases with luminosity, whereas the opposite trend is seen for giants. Moreover, a weaker dependence of size on luminosity was observed for dwarf galaxies than for giant elliptical galaxies (e.g. Kormendy 1977, 1985; Binggeli & Cameron 1991; Bender et al. 1992, 1993). Kormendy et al. (2009) reaffirmed those results in their study of a large sample of Virgo cluster early-type galaxies. They concluded that dwarf galaxies are structurally distinct from giant elliptical galaxies and that different mechanisms are responsible for their formation (see also Boselli et al. 2008; Janz & Lisker 2008).

However, the apparent change in the scaling relations can also be explained by the gradual variation of the light profile shape with luminosity. If the light profile is described by the Sérsic law, the different behaviour of dwarf and giant early-type galaxies in the surface brightness vs. magnitude relation is a consequence of the linear relation between Sérsic index n and galaxy magnitude (e.g. Jerjen & Binggeli 1997; Graham & Guzmán 2003; Gavazzi et al. 2005; Ferrarese et al. 2006; Côté et al. 2007, 2008).

1.2 Ultra-compact dwarf galaxies (UCDs)

Within the last decade, a new class of stellar systems, called 'ultra-compact dwarf galaxies' (UCDs), has been discovered in the nearby galaxy clusters Fornax, Virgo, Centaurus and Coma (e.g. Hilker et al. 1999; Drinkwater et al. 2000a, 2003; Phillipps et al. 2001; Mieske et al. 2004, 2007b, 2009; Haşegan et al. 2005; Jones et al. 2006; Firth et al. 2007; Gregg et al. 2009; Price et al. 2009; Chiboucas et al. 2010; Madrid et al. 2010). Recently, UCDs have also been identified in several group environments (e.g. Evstigneeva et al. 2007a; Rejkuba et al. 2007; Blakeslee & Barber DeGraaff 2008; Hau et al. 2009; Da Rocha et al. 2011; Norris & Kannappan 2011). Example images of UCDs in comparison with normal dwarf galaxies and giant elliptical galaxies are shown in Fig. 1.3.

It is important to note that the term 'ultra-compact dwarf galaxy' might suggest that these objects are galaxies rather than star clusters, with all the implications the use of these categories gives rise to. However, this origin of UCDs is not yet clear, and possible formation scenarios will be discussed in more detail below. Before the term UCD became widely accepted as the generic term for this type of object, other circumscriptions have been proposed, such as compact stellar system, compact object, super-massive star cluster, extremely large star cluster, etc. The term 'ultra-diffuse star cluster' was suggested by Kissler-Patig (2004) to point to the possible link of massive star cluster formation. Trying to find a neutral description, Haşegan et al. (2005) named these objects 'dwarf-globular trasition objects' (DGTOs). However, to simplify matters the term UCD will be used throughout this study for objects with properties described in the next paragraph.

UCDs are characterised by evolved stellar populations (e.g. Mieske et al. 2006; Evstigneeva et al. 2007b), typical luminosities of $-13.5 < M_V < -11.0$ mag, masses of $2 \times 10^6 < m < 10^8$ M$_\odot$ (e.g. Mieske et al. 2008), and half-light radii of $10 < r_{\rm h} < 100$ pc. Unlike globular clusters (GCs), UCDs follow a luminosity-size relation, in the sense that more luminous UCDs have larger half-light radii (e.g. Haşegan et al. 2005; Evstigneeva et al.
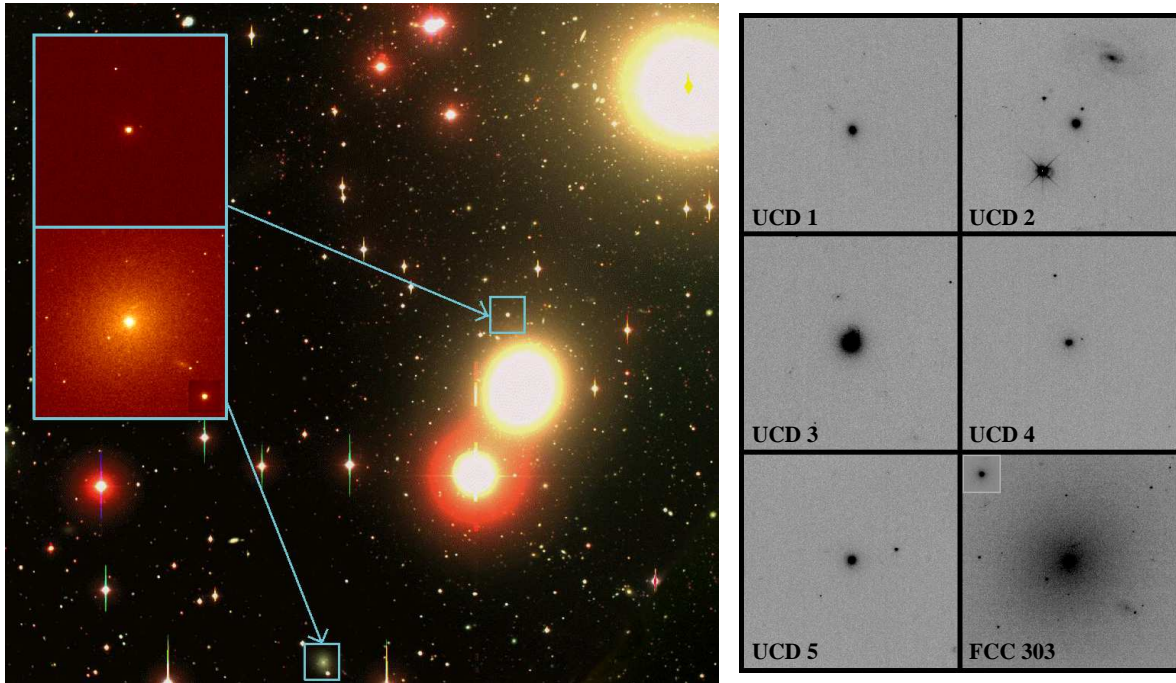
Fig. 1.3. *Left panel:* The central region of the Fornax galaxy cluster with the central cD galaxy NGC 1399 in the upper right corner. The insets on the left show HST images of one of the UCDs (top) and a normal nucleated dwarf galaxy (bottom). Credit: image taken by M. Hilker with the 2.5-meter du Pont Telescope (Las Campanas Observatory); insets: Hubble Space Telescope. *Right panel:* HST images of five Fornax UCDs and the nucleated dwarf galaxy from the left panel. Figure taken from Drinkwater et al. (2003).

2008). Moreover, UCDs show enhanced dynamical mass-to-light (M/L) ratios in comparison to Galactic globular clusters of similar metallicity (e.g. Haşegan et al. 2005; Hilker et al. 2007; Rejkuba et al. 2007; Dabringhausen et al. 2008, 2009; Mieske et al. 2008; Taylor et al. 2010).

UCDs are hence of intermediate nature between dwarf elliptical galaxies and GCs, however, they are not a homogeneous class of objects. For example, Virgo UCDs are on average more metal-poor, have larger α abundances, and extend to higher M/L ratios than UCDs in Fornax (Haşegan et al. 2005; Mieske et al. 2006, 2007b; Evstigneeva et al. 2007b; Hilker et al. 2007), although this might not be true if one could examine complete samples in either cluster. The colours of UCDs cover the full range of colours observed for regular GCs (e.g. Evstigneeva et al. 2008; Hilker 2009), but the brightest UCDs tend to have red colours. Apparently, they represent the extension of the red (metal-rich) GC population to higher luminosities. Blue (metal-poor) UCDs, on the other hand, share the location of nuclei of early-type dwarf galaxies in a colour–magnitude diagram and follow a mass-colour relation (the 'blue tilt', e.g. Mieske et al. 2010; Norris & Kannappan 2011, and references therein). These properties may indicate that more than one formation channel for UCDs exists.

As one possible formation scenario, it was proposed that UCDs formed from the amalgamation of many young, massive star clusters during the interaction of gas-rich galaxies (e.g. Kroupa 1998; Fellhauer & Kroupa 2002). Indeed, hundreds of young, massive star clusters have been discovered in the merging Antennae galaxies NGC 4038/4039 (e.g. Whitmore et al. 1999). They are themselves clustered into groups, and will likely merge on time scales of a few tens to a hundred Myr. An example of such a merged star cluster complex could be the massive cluster W3 in NGC 7252, which has, apart from its young age of 500 Myr, properties very similar to those of UCDs (Maraston et al. 2004; Fellhauer & Kroupa 2005; Kissler-Patig et al. 2006). Thus, UCDs might be regarded as the brightest and most massive (metal-rich) globular clusters, representing the bright tail of the globular cluster luminosity function (GCLF) (e.g. Mieske et al. 2002, 2004). This scenario is supported by the smooth appearance of the GCLF of several giant elliptical galaxies, which extends continuously to very bright objects which fall into the luminosity range of UCDs (e.g. Mieske et al. 2005a; Wehner et al. 2008; Harris 2009). In this context, the high M/L ratios of the most massive UCDs can be interpreted as either the consequence of a non-canonical IMF, top-heavy (Dabringhausen et al. 2009) or bottom-heavy (Mieske & Kroupa 2008), or as the consequence of GC/UCD formation in dark matter haloes (e.g. Baumgardt & Mieske 2008). In a recent study by Gieles et al. (2010), it was shown that also the size-luminosity relation of UCDs can be explained by assuming that low-mass GCs have formed with the same relation as the more massive UCDs, and have moved away from this relation due to dynamical evolution.

An alternative suggestion is that UCDs are genuine compact dwarf galaxies, originating from primordial small scale dark matter peaks and having survived the galaxy cluster formation and evolution until the present time (Phillipps et al. 2001; Drinkwater et al. 2004).

Another possible formation scenario is that UCDs are the remnant nuclei of dwarf galaxies which lost their outer envelopes during the interaction with the tidal field of the parent galaxy or galaxy cluster (e.g. Bassino et al. 1994; Bekki et al. 2001a, 2003; Goerdt et al. 2008). Observations show that the structural parameters of the brightest, metal-poor UCDs resemble present-day nuclei of dwarf galaxies. However, the high metallicities of many Fornax UCDs seem to be contradictory to this formation scenario (Mieske et al. 2006, 2007b).

Because of the apparent heterogeneity of UCDs, it is essential to broaden the environmental baseline of UCD investigations beyond the well studied Fornax and Virgo clusters. Chapter 3 presents the basic properties of a large number of UCDs discovered in the more distant Hydra I galaxy cluster.

Chapter 2

The early-type dwarf galaxy population of the Hydra I cluster

Except for Sect. 2.4, this chapter is based on the publication
Misgeld, I., Mieske, S., & Hilker, M. 2008, A&A, 486, 697

In the following, a study of the early-type dwarf galaxy population in the Hydra I cluster is presented. The study is based on a spectroscopic and a photometric survey. The spectroscopic survey was performed with LDSS2 at Magellan I, aiming at the cluster membership confirmation of early-type dwarf galaxy candidates by means of redshift measurements. The photometric survey, based on deep VLT/FORS1 images, was used to identify further cluster dE/dSph candidates. This chapter is organised as follows: in Sect. 2.1 the observations, the candidate selection and the data reduction for the spectroscopic survey are described. In Sect. 2.2 the photometric analysis of the candidate cluster dEs/dSphs, as selected from the VLT/FORS1 images, is addressed. The results of the spectroscopic and the photometric survey are presented in Sect. 2.3. Additionally, first results of an extended follow-up spectroscopic survey are given in Sect. 2.4. The findings are discussed and summarized in Sect. 2.5.

Hydra I (Abell 1060) is a relatively poor cluster [richness class $R = 1$ (Abell 1958), BM classification III (Bautz & Morgan 1970)]. A pair of bright galaxies is located near the cluster centre. NGC 3309 is a regular giant elliptical galaxy (E3). The brighter and larger galaxy NGC 3311 possesses an extended cD halo and an extraordinarily rich globular cluster system (van den Bergh 1977; McLaughlin et al. 1995; Mieske et al. 2005a; Wehner et al. 2008). The cluster is the prototype of an evolved and dynamically relaxed cluster, being dominated by early-type galaxies and having a regular core shape. From X-ray measurements, Tamura et al. (2000) derived an isothermal distribution of the intracluster medium within $\sim 160\ h^{-1}$ kpc. They give $2.1 \times 10^{14}\ h^{-1}\ \mathrm{M_\odot}$ as the cluster virial mass. From optical studies, Girardi et al. (1995) found a core radius of $r_\mathrm{c} = 170\ h^{-1}$ kpc. Applying the virial theorem to the member galaxies, Girardi et al. (1998) calculated a virial mass of $1.9 \times 10^{14}\ h^{-1}\ \mathrm{M_\odot}$.

The Hydra I cluster is close enough for current 8-m class telescopes like the VLT to re-solve faint dwarf galaxies under good seeing conditions. Only a few images of about 7×7 ar-cmin (the typical field-of-view size for most CCD cameras) are needed to observe the cluster centre as well as areas out to about one core radius (see Fig. 2.1). Mieske et al. (2005a) estimated the distance to Hydra I from I-band surface brightness fluctuations (SBF). They found the distance to be 41.2 ± 1.4 Mpc (distance modulus $(m - M) = 33.07 \pm 0.07$ mag). This is at the low end of distance estimates by other authors whose mean is $\sim 15\%$ higher (see discussion in Mieske et al. 2005a). From a deep spectroscopic sample of clus-ter galaxies, extending to $M_R = -14$ mag, Christlein & Zabludoff (2003), hereafter CZ03, derived $\overline{cz} = 3683 \pm 46$ km s^{-1} as the mean cluster redshift with a velocity dispersion of $\sigma = 724 \pm 31$ km s^{-1}. This corresponds to a distance of 51.2 ± 5.7 Mpc, assuming $H_0 = 72 \pm 8$ km s^{-1} Mpc^{-1} (Freedman et al. 2001). Already earlier, it was discovered that the cluster is clearly isolated in redshift space, having no foreground galaxies and no back-ground galaxies up to $cz \sim 8000$ km s^{-1} (Richter et al. 1982; Richter 1987). This implies huge empty regions of space of about 50 Mpc path length in front and behind the cluster. Throughout this chapter, a Hydra I distance modulus of $(m - M) = 33.07$ mag is adopted (Mieske et al. 2005a). This corresponds to a physical scale of 200 pc/arcsec.

2.1 Spectroscopy

2.1.1 Observations and selection of candidates

For the spectroscopic survey, seven fields in the central region of the Hydra I cluster were observed with Magellan I at Las Campanas Observatory together with the Low Dispersion Survey Spectrograph (LDSS2) in April/May 2001 (see Fig. 2.1). The goal of the LDSS2-survey was to identify cluster dwarf galaxies by radial velocity measurements.

On Magellan I, LDSS2 images a 7.5$'$ diameter field onto the LCO SITe#1 detector of 2048×2048 pixel with a scale of 0.378$''$/pixel. The high dispersion grism with a central wavelength of 4200 Å and a dispersion of 2.4 Å/pixel was used. With a slit width of 1.25$''$ (≈ 3 pixel), the effective resolution was about 7 Å, corresponding to 525 km s^{-1} at 4000 Å. Except for fields 4, 6 and 7 (see Fig. 2.1), two slit masks were observed in each field. For each mask two exposures were taken, each with an integration time of 1200 s.

The objects observed with LDSS2 were selected from VLT/FORS1 images (see Sect. 2.2.1). The sample contains both the bright giant elliptical galaxies and a number of possible dwarf elliptical galaxies (dE, dE,N, dS0) or dwarf spheroidal galaxies (dSph), selected by their morphology. Compact, unresolved objects, being candidates for glob-ular clusters (GCs), isolated nuclei from dissolved dEs, or ultra-compact dwarf galaxies (UCDs), complement the sample. Figure 2.2 shows a colour–magnitude diagram of all observed objects.
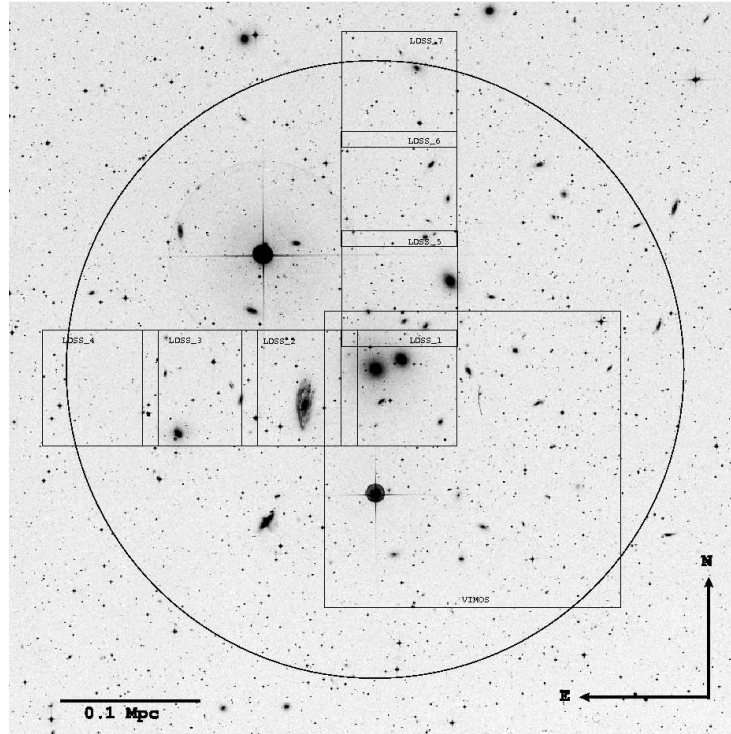
Fig. 2.1. $45' \times 45'$ (540×540 kpc at the cluster distance) image of the Hydra I cluster centred on NGC 3311, extracted from the Digital Sky Survey (DSS). The small squares are the fields observed with LDSS2 (see Sect. 2.1). The large square marks represents a VLT/VIMOS-pointing (see also Chapter 3). The circle indicates the cluster core radius $r_c = 170 \ h^{-1}$ kpc (Girardi et al. 1995), adopting $h = 0.75$.

2.1.2   Data reduction and radial velocity measurements

The standard process of data reduction, comprising bias subtraction, cosmic ray removal by means of the `lacosmic` routine (van Dokkum 2001), correction for spatial distortion, flatfield normalization and wavelength calibration, was performed with the IRAF-packages `onedspec` and `twodspec`. After these reduction steps, the one-dimensional object spectra were extracted with simultaneous sky subtraction.

Radial velocities were measured by performing Fourier cross-correlations between object and template spectra, using the IRAF-task `fxcor` in the `rv` package. The object spectra were initially cross-correlated against six template spectra. One template is a galaxy spectrum of NGC 1396 (Dirsch et al. 2004), a second one is HD 1461, an old metal-rich star in the solar neighbourhood (Chen et al. 2003). The remaining four template spectra were taken from Quintana et al. (1996). Three of them are spectra from early-type galaxies (NGC 1407, NGC 1426, NGC 1700) and one is a synthetic template. The wavelength range of the three galaxy spectra, [3800:6500] Å, is similar to that of the object spectra. Only the wavelength range of the synthetic spectrum extends to about 7400 Å.

The four template spectra from Quintana et al. (1996) were found to give the best cross-correlation results. The peak of the cross-correlation function (CCF) was most pro-
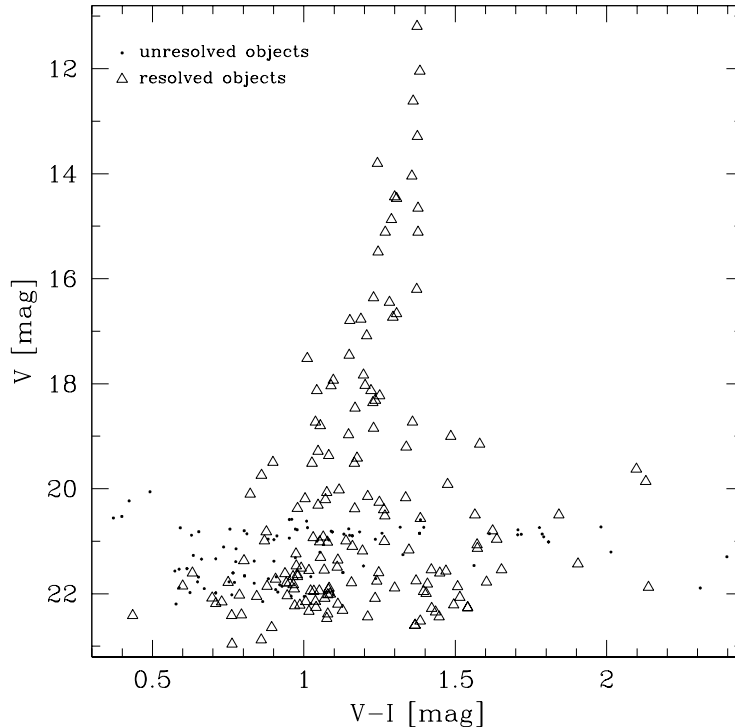
Fig. 2.2. Colour–magnitude diagram of all observed objects in the seven LDSS2 fields. Dots (open triangles) mark unresolved (resolved) sources, according to SExtractor star-galaxy classifier (Bertin & Arnouts 1996). The photometry is taken from VLT/FORS1 images (see Sect. 2.2.1).

nounced and the coefficient R, which gives the significance of the cross-correlation match (Tonry & Davis 1979), was similar for all four templates. Also the four obtained radial velocities were consistent within the errors. The R-values of the correlations with the other two templates were clearly lower (by about 20–50%).

The R coefficient was used as an indicator for the reliability of the measurement. Only values of $R \geq 4$ (averaged over the four templates) were considered reliable. This was the limit where the peak of the CCF could easily be distinguished from the noise. Several correlations still showed a clear peak in the CCF, despite having a relatively low S/N ratio ($R < 4$). If in those cases the CCF-peak was visible within the errors at the same radial velocity for all four cross-correlations, the measurement was accepted. Heliocentric velocity corrections were applied to all measurements.

2.2 Photometry of early-type dwarf galaxies

2.2.1 Observations and selection of dE/dSph candidates

The imaging data for Hydra I were obtained in a VLT/FORS1 service mode run in April 2000 at ESO/Paranal (ESO observing programme 65.N-0459, PI: M. Hilker). Seven $7' \times 7'$ fields were observed in Johnson V and I filters. All images were taken during dark time
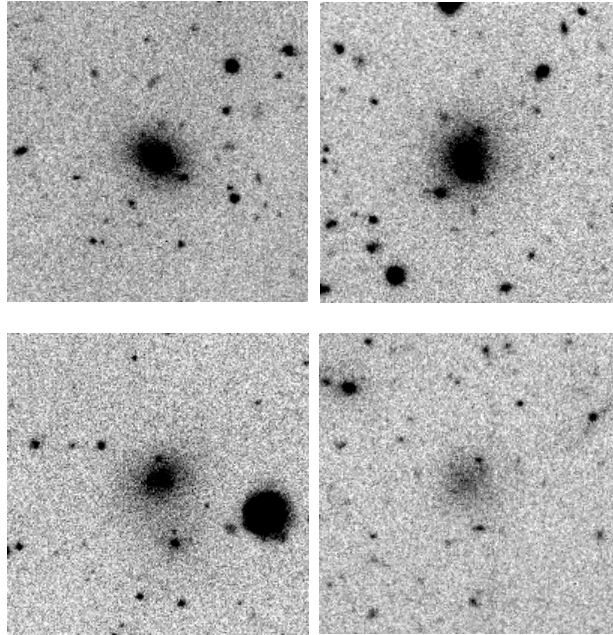
Fig. 2.3. Thumbnails of four cluster dwarf galaxy candidates that fulfilled the selection criteria. The thumbnail sizes are $40'' \times 40''$ (8×8 kpc at the cluster distance).

with a seeing between $0.5''$ and $0.7''$. The integration time was 3×8 min for the V images and 9×5.5 min for the I images. Since most of the bright cluster galaxies were saturated on the long exposures, their photometric parameters were determined from unsaturated short integration time images (30 s in V and I).

In analogy to investigations in the Fornax cluster (Hilker et al. 2003; Mieske et al. 2007a), the strategy for identifying dwarf galaxy candidates was a combination of visual inspection of the images and the use of SExtractor (Bertin & Arnouts 1996) detection routines. In a first step, several LG dEs and dSphs (projected to the cluster distance) were simulated and added to the images. The photometric parameters for these simulated galaxies were taken from Grebel et al. (2003). After that, the images were inspected by eye and candidate cluster dwarf galaxies were selected by means of their morphological resemblance to the simulated LG dwarfs. The main criterion was that they showed an extended low surface brightness envelope and no substructure or clear features such as spiral arms. The search resulted in the selection of 73 previously uncatalogued dE/dSph candidates. Fig. 2.3 shows V-band images of four cluster dwarf galaxy candidates.

In a second step, SExtractor detection routines were used with the aim of quantifying the detection completeness in the data, and in order to find more dwarf galaxy candidates, especially at the faint magnitude and surface brightness limits. The detection-sensitive parameters of SExtractor were optimised such that most of the objects of the by-eye-catalogue were detected by the programme. Only three of the obvious by-eye detections were not found by SExtractor, due to the proximity of a bright foreground star. The search for new dwarf galaxy candidates was focused on those sources in the SEXtractor output
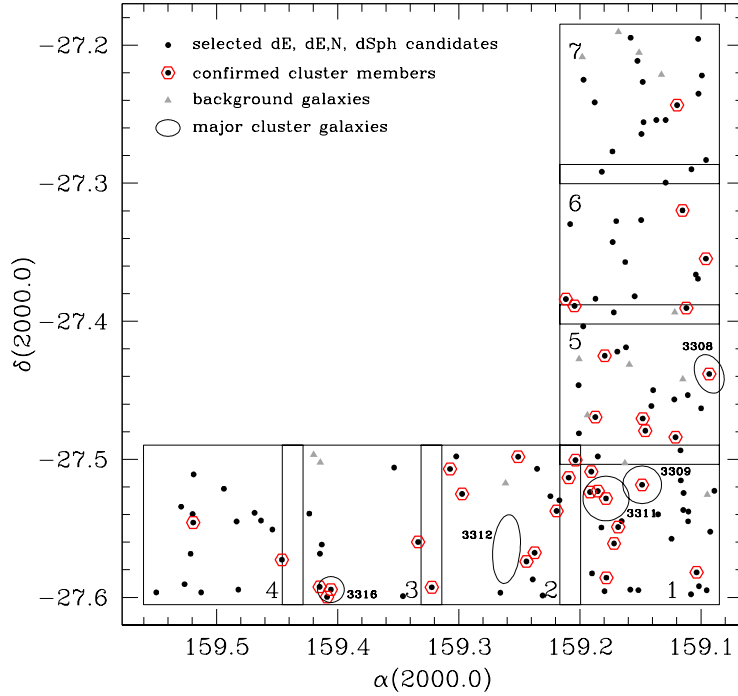
Fig. 2.4. Coordinate map of the cluster dwarf galaxy candidates, confirmed cluster members, background galaxies and major cluster galaxies with their corresponding NGC number. The seven observed VLT/FORS1 fields are marked by large open squares, the field number is indicated.

catalogue whose photometric parameters matched the parameter range of the simulated dE galaxies. The cuts in `magbest`, `mupeak`, `fwhm` and `area` that were applied to constrain the output parameter space to the one found for the simulated dEs are discussed in detail in Sect. 2.3.4. A total of 9 additional SExtractor detections, covering a magnitude range $-11.7 < M_V < -9.7$ mag, were found and added to the by-eye catalogue.

Finally, 36 spectroscopically confirmed cluster early-type galaxies from this study and from CZ03 were added to the photometric sample. The CZ03 catalogue has a full spatial coverage over the observed fields and a limiting magnitude of $M_R = -14$ mag. For comparison, also 14 identified background galaxies from the LDSS2 survey were added to the sample. A map of the observed fields and the 132 objects chosen for the photometric analysis is presented in Fig. 2.4.

2.2.2   Data analysis

The surface brightness profile for each selected object was derived by fitting elliptical isophotes to the galaxy images, using the IRAF-task `ellipse` in the `stsdas`[1] package. Sky subtraction and isophote fitting for each object were performed on cut out thumbnail images that extended well into the sky region (see Fig. 2.3). Isophotes with fixed centre

---

[1]Space Telescope Science Data Analysis System, STSDAS is a product of the Space Telescope Science Institute, which is operated by AURA for NASA.
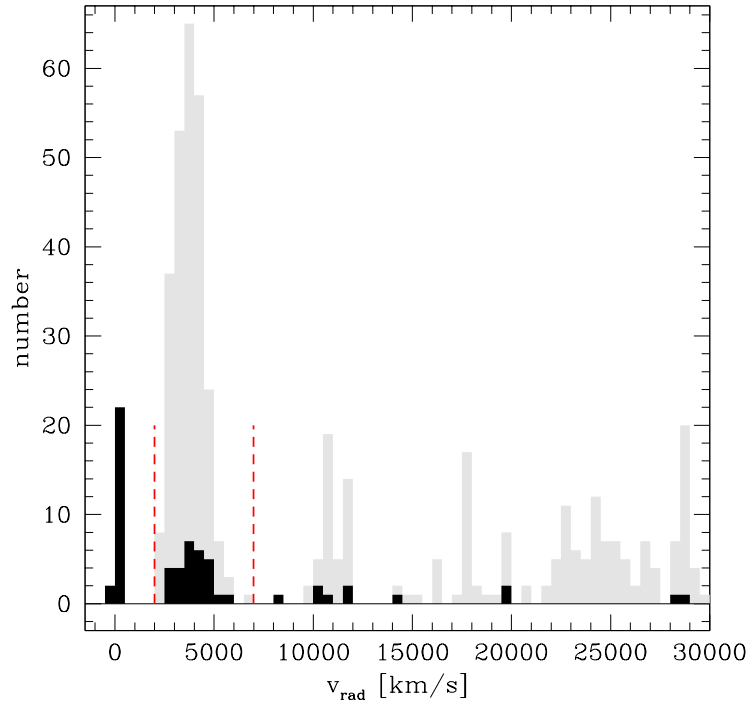
Fig. 2.5. Radial velocity distribution of all successfully measured objects with $v_{\mathrm{rad}} < 30\,000$ km s^{-1} (black histogram). The grey histogram shows the data from CZ03. Vertical dashed lines mark the velocity range assumed for cluster membership. Note also the overdensity at $v_{\mathrm{rad}} \sim 11\,000$ km s^{-1} from which five members are identified.

coordinates, ellipticity and position angle were fitted to the galaxy images. However, in particular for the brightest cluster galaxies ($V \lesssim 16$ mag), the ellipticity considerably changed from the inner to the outer isophotes. In those cases the ellipticity was not fixed during the fitting procedure.

The photometric parameters of the objects were derived from the analysis of their surface brightness profiles: the total magnitude from a curve of growth analysis and the central surface brightness from both an exponential and a Sérsic fit to the profile. For the fit the inner $1''$ (about 1.5 seeing disks) and the outermost part of the profile was excluded, where the measured surface brightness was below the estimated error of the sky background. Photometric zero points were taken from Mieske et al. (2005a). In order to correct for interstellar absorption and reddening the values from Schlegel et al. (1998) were used. They give $A_V = 0.263$ mag and $E(V - I) = 0.110$ mag for the coordinates of the Hydra I cluster. Table A.1 in the appendix lists the photometric calibration coefficients for the observed fields.

The obtained photometric parameters along with the available radial velocities for all early-type galaxies in the sample (111 objects) are presented as the Hydra I Cluster Catalogue (HCC) – see Table A.2 in the appendix.
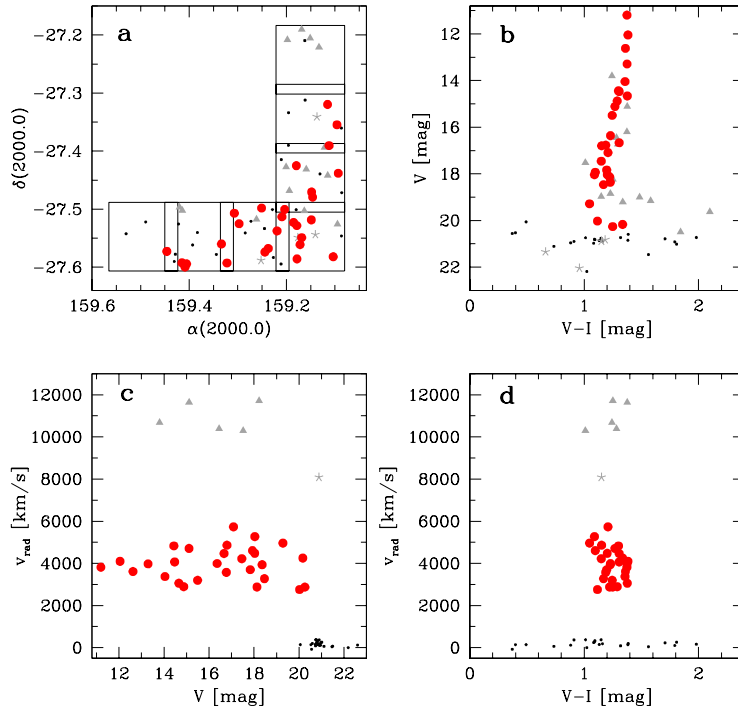
Fig. 2.6. Properties of all successfully observed objects. Filled red circles are confirmed cluster members, grey triangles (asterisks) represent resolved (unresolved) background objects, small black dots are foreground stars. **a)** Coordinate map of all foreground stars, background sources and cluster members. The observed fields are indicated by large open squares. **b)** Colour–magnitude diagram of all objects. **c)** Magnitude velocity diagram of all objects, except for background objects with $v_{rad} > 13\,000$ km s^{-1}. **d)** Colour velocity diagram of all objects, except for background objects with $v_{rad} > 13\,000$ km s^{-1}.

2.3   Results

In this section a detailed analysis of the spectroscopic and photometric data is presented. The results of the spectroscopic survey are given in Sect. 2.3.1. In Sects. 2.3.2 and 2.3.3 the colour–magnitude and the magnitude–surface brightness relation of the Hydra I dwarf galaxies are presented. Section 2.3.4 addresses the galaxy luminosity function for early-type dwarf galaxies in Hydra I.

2.3.1   Properties of confirmed cluster galaxies

A total of 279 objects were observed with LDSS2. Reliable radial velocities could be derived for 70 of them. 24 foreground stars, 18 background objects and 28 cluster galaxies were identified. The criterion for cluster membership was adopted to be $2000 < v_{rad} < 7000$ km s^{-1} (see Fig. 2.5). Radial velocity uncertainties were of the order of 20–100 km s^{-1}. Figure 2.6 gives a coordinate map, a colour–magnitude diagram, a magnitude-velocity and a colour-velocity diagram of the successfully observed objects.

In Table A.2 the radial velocities of the 28 cluster galaxies are given. The mean value is $\bar{v}_{rad} = 3982 \pm 148$ km s^{-1} with a standard deviation of $\sigma = 784$ km s^{-1}. This deviates

by 2σ from the result of CZ03. However, there is no systematic velocity shift in the LDSS2 data. For the 24 previously known galaxies, differences of $-110 < \Delta v_{\rm rad} < 140$ km s^{-1} to the radial velocities from CZ03 are measured. Taking into account the relatively large velocity error of ± 80 km s^{-1} in the literature values, 75% of all LDSS2 velocities are still consistent with them. Furthermore, the mean radial velocity of the 24 galaxies from the CZ03 catalogue, which are also in the LDSS2 sample, is 3998 ± 150 km s^{-1}, in agreement with the mean velocity of the entire LDSS2 sample. The large discrepancy between the mean radial velocity of the LDSS2 sample and the whole CZ03 sample can thus be explained by selection effects.

Note that there is no significant difference in velocity dispersion between brighter (thus more massive) cluster galaxies ($V < 16$ mag) and fainter ones, which would be an indication of mass segregation. A velocity dispersion of $\sigma = 634^{+376}_{-165}$ km s^{-1} for the brighter galaxies and $\sigma = 862^{+268}_{-190}$ km s^{-1} for the fainter ones (90% confidence level) is found. The number counts are too low to judge on a possible larger velocity dispersion for dwarf galaxies as found in the Fornax cluster (Drinkwater et al. 2001).

The colour–magnitude diagram in Fig. 2.6b clearly shows the CMR of confirmed cluster galaxies, in the sense that fainter galaxies are on average bluer. The cluster galaxies have colours of $1.02 < V - I < 1.38$. Five objects ($V < 18.3$ mag) scattering around the CMR belong to a background group at $v_{\rm rad} \sim 11\,000$ km s^{-1} (see also Fig. 2.5). The cluster CMR is analysed in more detail in the next section.

2.3.2   The colour–magnitude relation of early-type galaxies

A well-defined CMR for cluster galaxies brighter than $V \sim 20$ mag was already visible in the analysis of the spectroscopic data (Sect. 2.3.1). Fig. 2.7 shows the colour–magnitude diagram (CMD) of all early-type galaxies in the photometric sample (E and S0 as well as dE/dSph galaxies), as listed in Table A.2. Clearly, the CMR stretches across the entire magnitude range of $11 < V_0 < 23$ mag, from the brightest giant elliptical galaxies all the way down to the regime of dwarf galaxies. The more luminous galaxies are on average redder than galaxies of lower luminosity. Adopting a distance modulus of $(m - M) = 33.07$ mag (Mieske et al. 2005a), a linear fit to *all* data points leads to $(V - I)_0 = -0.040 \cdot M_{V,0} + 0.44$ with a rms of 0.12. The larger scatter at the faint magnitudes is consistent with the larger error in $(V - I)$. The magnitude limit at which faint dwarf galaxies could still be identified is $M_V \sim -10$ mag, comparable to the Local Group dSph Sculptor (Grebel et al. 2003). Due to the detection and resolution limit of the data, the existence of even fainter galaxies in Hydra I cannot be tested.

Colour–magnitude relations for dwarf galaxies have been observed in a number of other nearby galaxy clusters, such as Coma, Virgo, Perseus and Fornax (e.g. Secker et al. 1997; Conselice et al. 2003; Hilker et al. 2003; van Zee et al. 2004; Adami et al. 2006; Mieske et al. 2007a; Lisker et al. 2008). The CMR for early-type dwarf galaxies in Fornax is given by $(V - I)_{\rm Fornax} = -0.033 \cdot M_{V,0} + 0.52$ in the magnitude range $-17 < M_V < -9$ mag
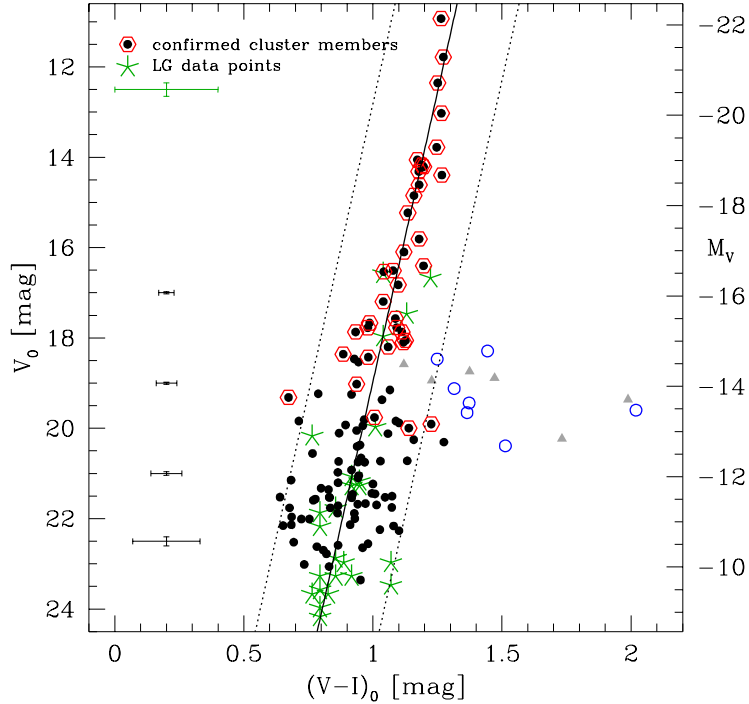
Fig. 2.7. Colour–magnitude diagram of early-type galaxies in the Hydra I cluster in comparison with Local Group dEs and dSphs. Black filled circles are probable cluster galaxies, selected by their morphology. Red open hexagons mark cluster members, confirmed by radial velocity measurements. Blue open circles are presumable background galaxies (see text for futher explanations). Grey triangles are confirmed background elliptical galaxies with $R^{1/4}$ surface brightness profiles. Typical errorbars are indicated. The solid line is a linear fit to dwarf galaxies with $M_V > -17$ mag (Eq. (2.1)). Dotted lines are the 2σ deviations from the fit. Green asterisks represent the Local Group dEs and dSphs (data from Grebel et al. 2003) projected to the Hydra I distance. Mean errors for the LG dwarfs are indicated in the upper left corner.

(Mieske et al. 2007a). Restricting the fit for the Hydra I sample to $M_V > -17$ mag leads to:

$$(V - I)_0 = -0.039 \cdot M_{V,0} + 0.45 \tag{2.1}$$

with a rms of 0.12, as indicated by the solid line in Fig. 2.7. This is in good agreement with the relation found in Fornax. Moreover, it is almost indistinguishable from the CMR defined by the whole Hydra I sample. Note that the adopted distance modulus of $(m-M) = 33.07$ mag is a comparatively low value. Other recent publications give a larger distance to Hydra I with a mean distance modulus of $(m - M) = 33.37$ mag (see also discussion in Mieske et al. 2005a), but using the higher value shifts the CMR only marginally (by 0.01 mag) towards the blue.

In addition, Eq. (2.1) is compared with the CMR of LG dwarf ellipticals and dwarf spheroidals. Homogeneous $(V - I)$ colours for LG dwarfs do not exist (see Mateo 1998), but they can be calculated from their average iron abundances. Assuming single stellar populations, Hilker et al. (2003) transform the average iron abundances from Grebel et al. (2003) to $(V - I)$ colours using Eq. (4) given in Kissler-Patig et al. (1998). It turns out
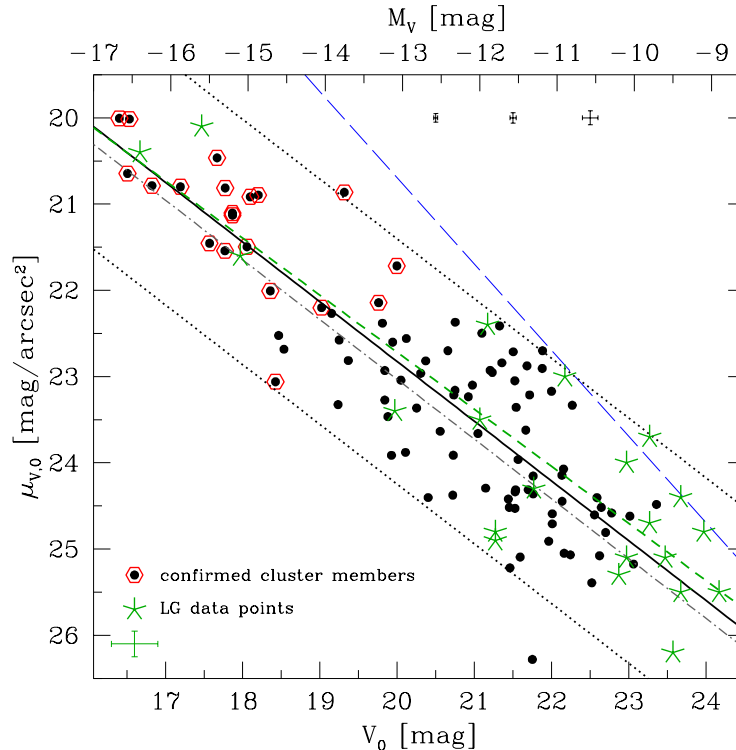
Fig. 2.8. Magnitude–surface brightness diagram of all early-type dwarf galaxies ($M_V > -17$ mag) in comparison with Local Group dEs and dSphs. The symbols are as in Fig. 2.7. Typical errorbars are indicated. The solid line is a linear fit to the data (Eq. (2.2)). Dotted lines are the 2σ deviations from the fit. The dash-dotted line is a fit to the same data, but using a higher distance modulus (see text for details). Green asterisks represent Local Group dEs and dSphs (data from Grebel et al. 2003) projected to the Hydra I distance. The green dashed line is the LG magnitude–surface brightness relation. Mean errors for the LG dwarfs are indicated in the lower left corner. The blue long-dashed line indicates a scale length of $0.7''$ for an exponential profile, representing the resolution limit of the images.

that the colours, estimated in this way, match remarkably well the CMR found for the Hydra I dwarf galaxies. A linear fit to the LG data gives $(V - I)_{LG} = -0.038 \cdot M_V + 0.48$ with a rms of 0.09, matching very well the Hydra I CMR.

However, one has to be aware of the uncertainties in this analysis. Equation (4) in Kissler-Patig et al. (1998) describes a linear relation between the average iron abundances and colours of globular clusters. The direct application to *other* stellar systems like dwarf galaxies is, at first, not evident. But the assumption of a single stellar population seems to be a good approximation in most cases, since nearby dwarf galaxies are mostly dominated by an old stellar population. Integrated $(V - I)$ colours are tabulated for eight LG dwarfs (Mateo 1998). The comparison of the transformed colours with the measured colours from Mateo (1998) shows only small discrepancies of about 0.1 mag. The errors for the transformed colours, as indicated in Fig. 2.7, are of the order of $\Delta(V - I) = 0.2$ mag.

A few remarks about the sample selection have to be made at this point. Object se-lection solely based on morphological classification can lead to the contamination of the sample with background galaxies that only resemble cluster dwarf elliptical galaxies. Bright

background galaxies ($M_V \lesssim -15$ mag) could be excluded from the sample on the basis of radial velocity measurements. Towards the faintest magnitudes ($M_V \gtrsim -12$ mag), dwarf galaxies tend to be extended objects with very low surface brightnesses and less concentrated light profiles (typical of dSphs). Apparently small objects of the same apparent magnitude with a high central concentration of light or barely resolved objects, both being likely background galaxies, were therefore excluded (see Sect. 2.3.4 for more details). In the intermediate magnitude range, the distinction between cluster dEs and background elliptical galaxies was more difficult. As indicated in Fig. 2.7 by blue open circles, seven objects with $-14.8 < M_V < -12.7$ mag were found, appearing very similar to confirmed cluster dEs in terms of their morphology. A first indication that they likely do not belong to the cluster is that they have significantly redder colours than other objects in the same magnitude range. Some of them are even too red to be a galaxy at $z \sim 0$. Moreover, they have surface brightness profiles that follow the de Vaucouleurs law ($R^{1/4}$ law), which is typical of giant elliptical galaxies. The comparison with spectroscopically confirmed background galaxies in the same magnitude range, which also exhibit $R^{1/4}$ surface brightness profiles, shows that they are the same group (see Fig. 2.7). Hence, it is reasonable to assume that the seven arguable objects only *resemble* cluster dwarf galaxies, but they are in fact background giant elliptical galaxies. The success rate of the morphological classification will be quantified in Sect. 2.4 by means of spectroscopic follow-up observations.

2.3.3   The magnitude–surface brightness relation

In Fig. 2.8, the central surface brightness $\mu_{V,0}$, as estimated from an exponential law, is plotted vs. M_V for all early-type galaxies fainter than $M_V = -17$ mag. A magnitude–surface brightness relation is visible in the sense that the central surface brightness increases with luminosity. A linear fit to the data yields

$$\mu_{V,0} = 0.69 \cdot M_{V,0} + 31.88 \tag{2.2}$$

with a rms of 0.71. The relation is well-defined down to very low luminosities and surface brightnesses. The trend of the relation is similar to those found in other galaxy groups and clusters (e.g. Ferguson & Sandage 1988; Ulmer et al. 1996; Binggeli & Jerjen 1998; Jerjen et al. 2000; Hilker et al. 2003; Adami et al. 2006; Mieske et al. 2007a). Local Group dEs and dSphs follow almost the same magnitude–surface brightness relation (data from Grebel et al. 2003). Using the larger distance modulus of $(m - M) = 33.37$ mag changes the y-intercept of Eq. (2.2) by $+0.2$ mag (indicated by the dash-dotted line in Fig. 2.8).

In order to also include the brighter ($M_V < -17$ mag) cluster early-type galaxies in the analysis, Sérsic (1968) models were fitted to the galaxy surface brightness profiles. The effective surface brightness μ_{e} against M_V is shown in the upper panel of Fig. 2.9. An increase of effective surface brightness with magnitude is visible between $-18 \lesssim M_V \lesssim -10$ mag. In this interval, the effective radius stays virtually constant, as the dashed line illustrates, which represents a constant radius of $4''$ (0.8 kpc at the cluster distance). This phenomenon has also been observed for dwarf galaxies in Coma, Virgo and in the Antlia cluster (Smith Castelli et al. 2008a, and references therein).
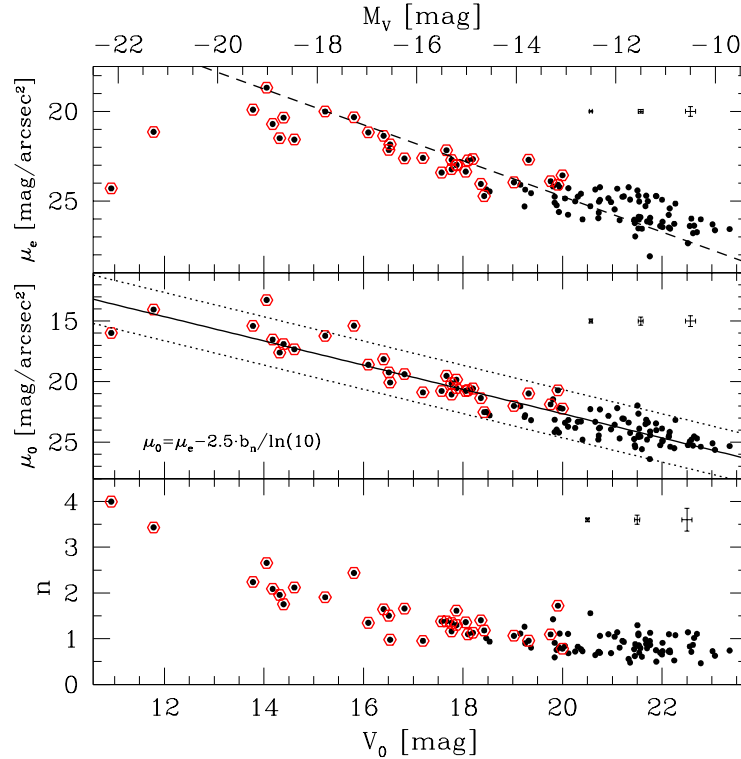
Fig. 2.9. Results of the Sérsic fits: effective surface brightness μ_e (*top panel*), central surface brightness μ_0 (*middle panel*) and profile shape index n (*bottom panel*) plotted vs. magnitude for all early-type galaxies. The dashed line in the upper panel indicates an effective radius of $4''$ (0.8 kpc at the cluster distance). The solid line in the middle panel is a linear fit to the data (Eq. (2.3)) with its 2σ deviations (dotted lines). Red open hexagons mark spectroscopically confirmed cluster members. Typical errorbars are indicated.

A different behaviour is observed at magnitudes brighter than $M_V \sim -18$ mag, in the sense that μ_e levels off, with the exception of the brightest cluster galaxy. This has been reported by many authors in the past (e.g. Kormendy 1985; Ferguson & Sandage 1988; Bender et al. 1992; Kormendy et al. 2009). However, according to Graham & Guzmán (2003, see their Fig. 12) there is no discontinuity in the relation when plotting the central surface brightness μ_0 of a Sérsic model vs. the galaxy magnitude instead of μ_e or $\langle\mu\rangle_e$. μ_0 is given by $\mu_0 = \mu_e - 2.5 b_n/\ln(10)$, in which b_n is approximated by $b_n = 1.9992n - 0.3271$ for $0.5 < n < 10$ (Graham & Driver 2005). For the Hydra I sample, μ_0 vs. M_V is shown in the middle panel of Fig. 2.9. A continuous relation is visible for the low mass dwarf galaxies and the high mass Es and S0s ($M_V < -17$ mag). This continuity was also observed in the ACS Virgo and Fornax Cluster Surveys (Ferrarese et al. 2006; Côté et al. 2006, 2007, 2008). A linear fit to the data reveals a direct correlation between μ_0 and M_V:

$$\mu_0 = 1.00 \cdot M_{V,0} + 35.73 \tag{2.3}$$

with an rms of 1.00. Four of the brightest cluster galaxies (HCC-003, HCC-004, HCC-008, HCC-012) are excluded from the analysis, since their surface brightness profiles could not reasonably be fitted by a single Sérsic profile, but rather showed two components (bulge
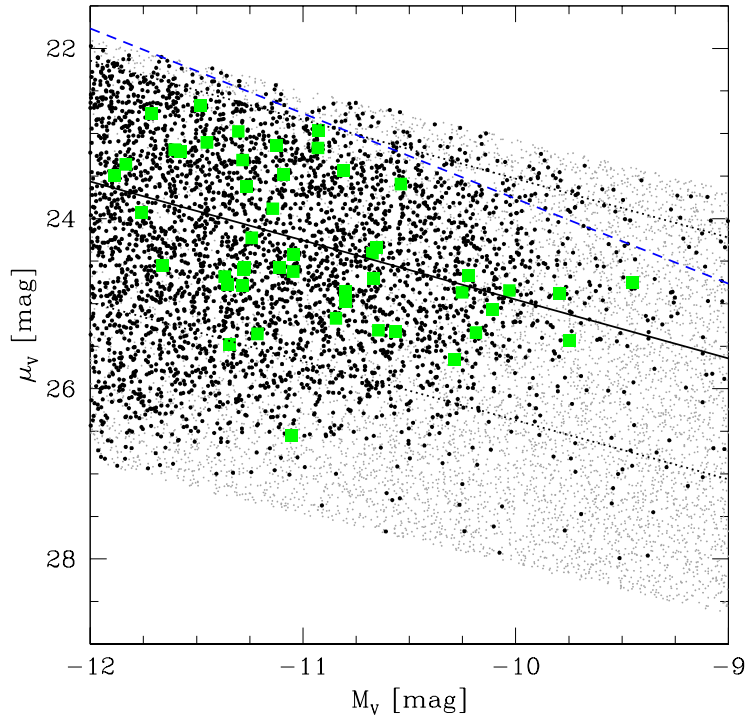
Fig. 2.10. Plot of the input-parameter range of the artificial dwarf galaxies (small grey dots). Black dots are the simulated galaxies recovered by SExtractor after applying several cuts (see text for further explanation). The objects from Fig. 2.8 are plotted as green squares. Equation (2.2) with its 2σ deviations is plotted as in Fig. 2.8. The blue dashed line indicates a scale length of $0.7''$ for an exponential profile, representing the resolution limit of the images.

+ disk). These galaxies are morphologically classified as SAB(s)0, SB(rs)0, SB(s)0, and S(rs)0 respectively. However, they closely follow the cluster CMR (cf. Table A.2 and Fig. 2.7).

The lower panel of Fig. 2.9 shows how the Sérsic profile shape index n varies with magnitude. An increase of n with increasing magnitude is visible for the magnitude range $-22 \lesssim M_V \lesssim -14$ mag, whereas the data points scatters around a mean of $n = 0.9$ for $M_V \gtrsim -14$ mag. A similar result was obtained for early-type galaxies in the Fornax cluster (Infante et al. 2003).

2.3.4 The faint end of the galaxy luminosity function

For the study of the faint end of the galaxy luminosity function, the number counts of dE/dSph candidates have to be completeness corrected. For this, 10 000 simulated dwarf galaxies were randomly distributed (in 500 runs) in each of the seven CCD fields, using a C++ code. The magnitudes and central surface brightnesses of the simulated galaxies were chosen such that they extended well beyond the observed parameter space at the faint limits. Exemplary for one field, Fig. 2.10 shows the input-parameter range of the simulated galaxies. SExtractor was then used to recover the artificial galaxies, and the SExtractor
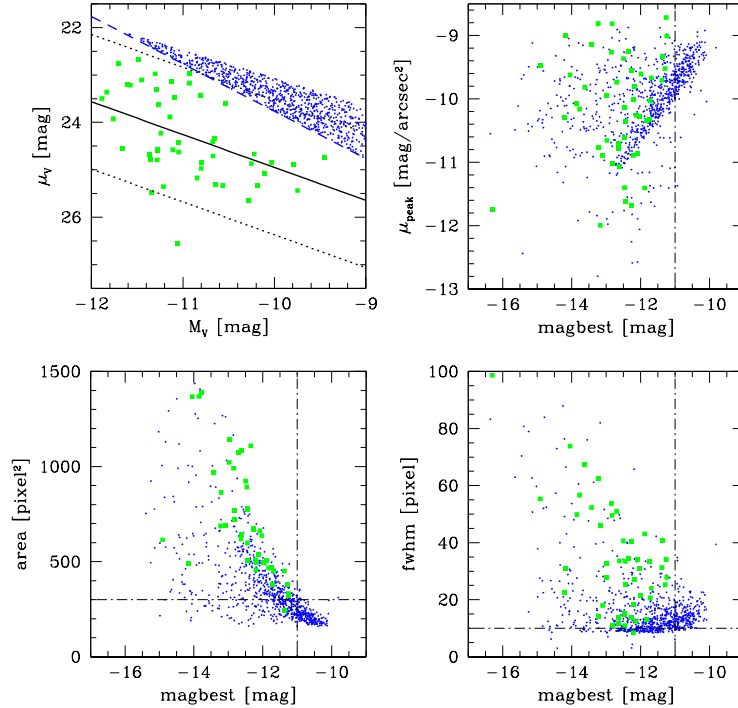
Fig. 2.11. SExtractor output-parameters of the artificial galaxies below the resolution limit (blue dots). The *upper left panel* shows the input-parameters M_V and μ_V. The SExtractor output-parameter `magbest` is plotted against `mupeak` (*upper right*), `area` (*lower left*) and `fwhm` (*lower right*). Green squares are the objects from Fig. 2.8. Dash-dotted lines indicate the global cuts on `magbest`, `fwhm` and `area`.

output-parameters, i.e. `magbest`, `mupeak`, `fwhm`, `area`, were compared with the parameters derived for the sample of actual cluster dwarf galaxies, as described in Sects. 2.3.3 and 2.3.2.

As already mentioned in Sect. 2.2.1, several cuts to the SExtractor output-parameters were applied, with the aim of rejecting high surface brightness and barely resolved background objects. These objects were defined to be located above the (blue) dashed line in Fig. 2.10, which represents the resolution limit of the images. Figure 2.11 shows the SExtractor output-parameters of the artificial galaxies below this resolution limit. They define well localised areas in plots of `magbest` versus `mupeak`, `area` and `fwhm`. However, also some of the previously selected dwarf galaxy candidates scatter into the same areas. Hence, only those objects were rejected that *simultaneously* occupied the locus of unresolved galaxies in all three parameters `mupeak`, `area` and `fwhm`.

In this way, only one of the previously selected galaxies was missed, but the majority of objects below the resolution limit was rejected. Additionally, global cuts at the lower limits of `magbest`, `fwhm` and `area` were applied, in order to reject very faint, almost unresolved background objects (see Fig. 2.11). All artificial galaxies that were recovered after the application of the cuts are highlighted in Fig. 2.10.

Without applying any cuts, SExtractor recovers 85–95% of the artificial galaxies at $M_V \leq -12$ mag, except for field 2 where the completeness is only 70%, due to the large
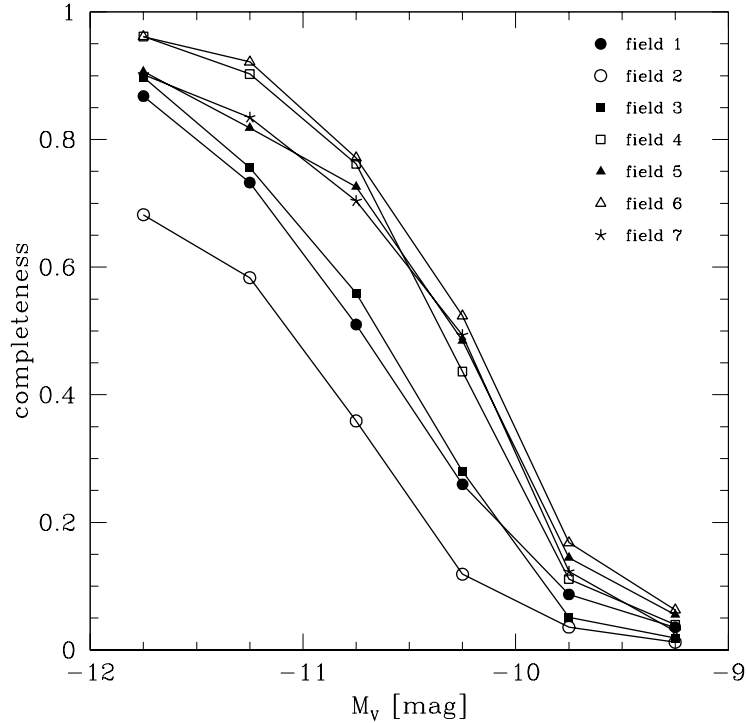
Fig. 2.12. Completeness as a function of magnitude for the seven observed fields. The low completeness in field 2 is due to the high geometrical incompleteness.

spiral galaxy in the field (cf. Figs. 2.1 and 2.4). This reflects the geometrical incompleteness caused by blending. By applying the cuts in `magbest`, `mupeak`, `area` and `fwhm`, about 15% of the artificial galaxies at $M_V = -12$ mag are additionally rejected. The fraction of visually classified galaxies with $M_V > -12$ mag that are excluded by applying the same cuts is 6 out of 43. This fraction is consistent with the fraction of excluded artificial galaxies. Since all visually selected galaxies are included into the GLF, the completeness values for $M_V > -12$ mag are scaled up by 15%, so that they are consistent with the geometrical completeness at $M_V = -12$ mag. Figure 2.12 shows the corrected completeness values in 0.5 mag bins. The galaxy number counts are completeness corrected individually for each CCD field using these curves.

In Fig. 2.13, the resulting luminosity function of the Hydra I dwarfs in the magnitude range $-17.0 < M_V < -9.5$ mag is shown. By fitting a single Schechter (1976) function to the number counts with a completeness larger than 50%, a faint-end slope of $\alpha = -1.13 \pm 0.04$ is derived. The slope does not change if including only data points with a completeness larger than 80%. Alternatively, a power-law model is fitted to the faint end of the GLF. This results in $\alpha = -1.37 \pm 0.08$ for $-16.0 < M_V < -10.6$ mag and $\alpha = -1.40 \pm 0.18$ for $-14.0 < M_V < -10.6$ mag (indicated by the dashed line in Fig. 2.13). Interestingly, the small dip in the GLF at about $M_V = -14$ mag (although maybe the result of low number counts) appears near the luminosity where the separation of dEs and
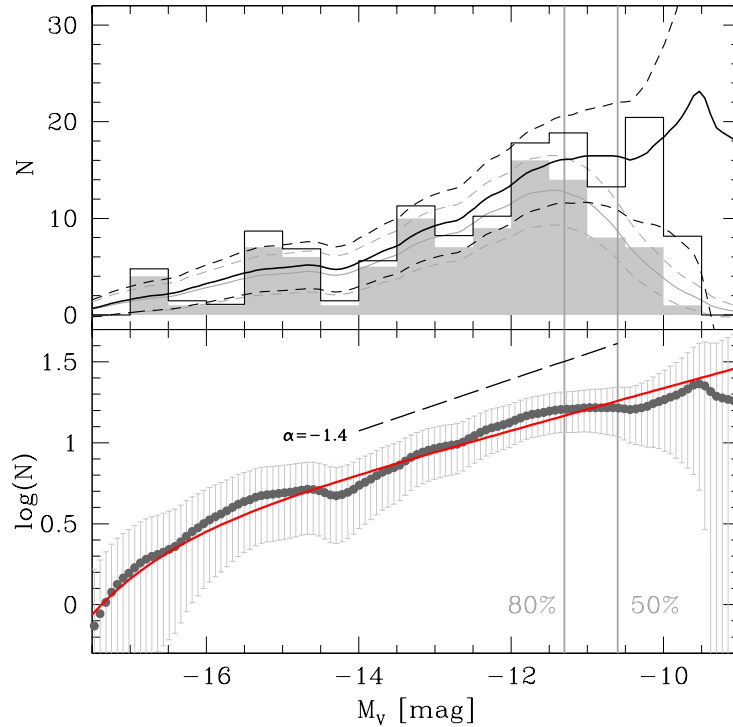
Fig. 2.13. Luminosity function of the Hydra I dwarf galaxies. The vertical lines mark the 80% and 50% completeness limits. *Upper panel*: the uncorrected galaxy number counts are displayed by the shaded histogram. The thin grey curve gives a binning independent representation for the counts (Epanechnikov kernel with 0.5 mag width). The completeness corrected number counts are given by the open histogram. The thick black curve represents the completeness corrected number counts with the 1σ uncertainties (dashed lines). *Lower panel*: completeness corrected number counts in logarithmic representation. The best fitting single Schechter function (solid red curve) is overlaid. A power-law slope of $\alpha = -1.4$ is indicated by the dashed line.

dSphs is defined (e.g. Grebel 2001). Hilker et al. (2003) reported on the same phenomenon in the Fornax cluster (see their figure 3).

2.4   Follow-up spectroscopy

Since the previous analyses are mainly based on the morphological identification of cluster dEs by correlations between global photometric and structural parameters, it is essential to also have *direct* cluster membership assignment by redshift measurements down to magnitudes of $M_V \gtrsim -14$ mag. In this regime the slope α starts to dominate the shape of the galaxy luminosity function (see Figs. 2.13 and 4.8). Beyond the Local Group, this has up to now only been achieved in studies of the rather nearby galaxy clusters Fornax, Perseus and Virgo (e.g. Hilker et al. 1999; Drinkwater et al. 2001; Penny & Conselice 2008; Rines & Geller 2008).

   The next step should therefore be the extension of those surveys to other galaxy clusters like Hydra I or Centaurus, in order to thoroughly verify the results of the photometric
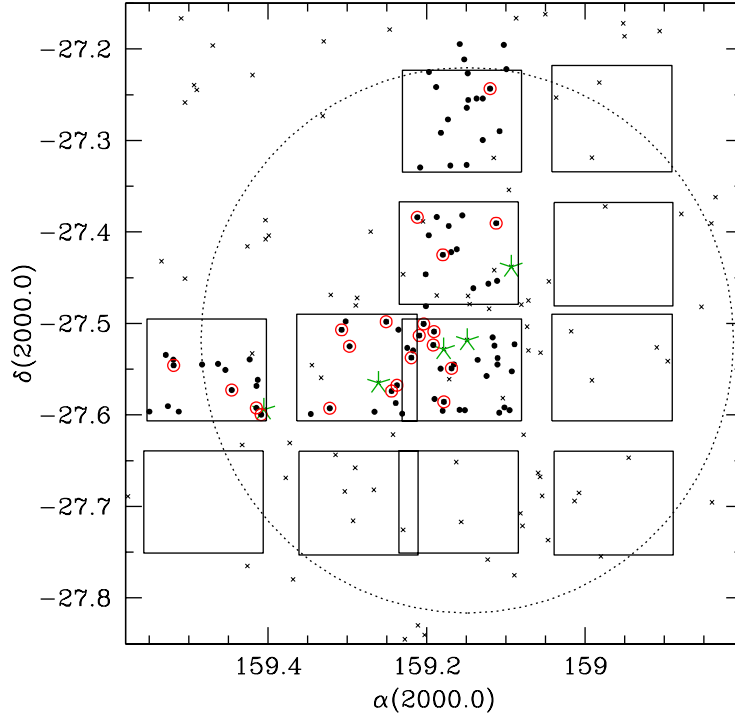
Fig. 2.14. Arrangement of the VIMOS pointings for the spectroscopic follow-up survey in Hydra I, with the dwarf galaxy candidates ($16.5 < V < 22.5$ mag and $\mu_V < 25$ mag/arcsec^2) from Fig. 2.8. Black filled circles are probable cluster galaxies, selected by their morphology. Red open circles mark cluster members, confirmed by radial velocity measurements. The pointings are arranged such that they cover a maximum number of those objects and a large fraction of the inner cluster region at the same time. The large dotted circle indicates the cluster core-radius as in Fig. 2.1. Green asterisks mark the location of the major NGC cluster galaxies. Small crosses are known Hydra I members from Christlein & Zabludoff (2003), with luminosities at least 3–4 mag brighter than those of the targets.

studies. With a reasonable amount of observing time (~ 2 hours integration time) the spectroscopic confirmation of low surface brightness objects is technically feasible for objects with $\mu_V \lesssim 25$ mag/arcsec^2, using low-resolution spectrographs like FORS or VIMOS at the VLT[2]. This surface brightness limit corresponds to an absolute magnitude limit of $M_V \sim -11$ mag at the distance of Hydra I or Centaurus (cf. Figs. 2.8 and 4.5). Naturally, at a given magnitude the surface brightness limit introduces a bias towards more successfully measuring the redshifts of smaller objects with higher surface brightnesses. However, the cluster membership assignment via morphological classification for exactly those rather compact objects turns out to be more difficult than for extended low surface brightness galaxies (see Sects. 2.3 and 4.2). This means that the observational bias in spectroscopic surveys primarily excludes objects for which the morphological membership assignment in photometric studies is more accurate.

In order to broaden the environmental baseline of previous studies, deep spectroscopic surveys of the dE population ($-17 < M_V < -11$ mag and $20 < \mu_V < 25$ mag/arcsec^2)

---

[2]see http://www.eso.org/observing/etc/ for exposure time calculators
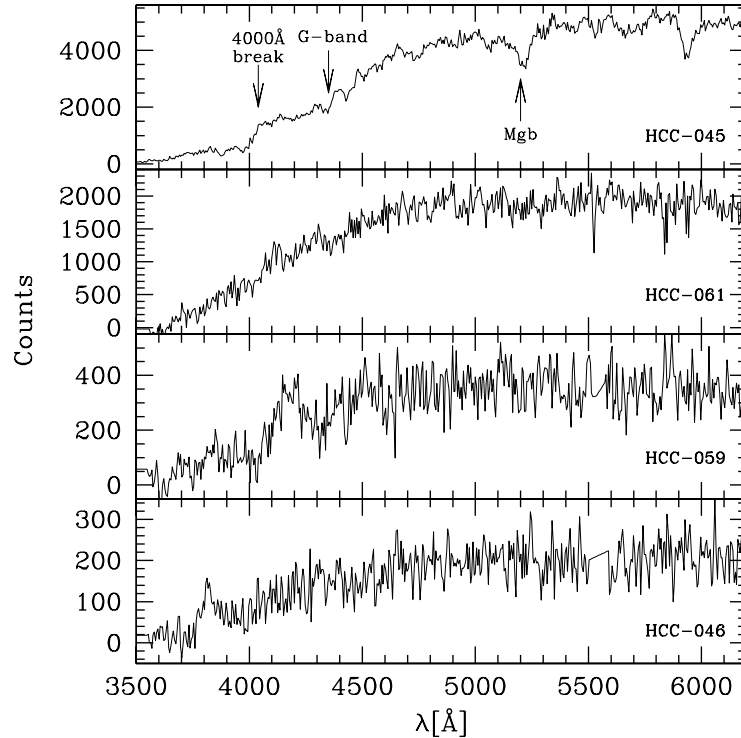
Fig. 2.15. The high S/N spectrum of HCC-045 (upper panel) in comparison to three spectra for which the TDR value, which gives the significance of the cross-correlation result, was ≤ 3 (cf. Table 2.1).

in the core regions of Hydra I and Centaurus were performed (see also Sect. 4.3). This section and Sect. 4.3 focus on the spectroscopic follow-up observations of cluster dwarf galaxy candidates (and a few potential background objects) that were previously identified in the FORS1 images (see Sects. 2.3 and 4.2). Other dwarf galaxy candidates, located in the surveyed areas but not in the FORS1 images, are not considered here.

2.4.1   Observations and data reduction

The observations were carried out in a service mode run in April/May 2009 with the VIsible Multi Object Spectrograph VIMOS (LeFevre et al. 2003) mounted on UT3 at the VLT (ESO observing programme 083.B-0640, PI: I. Misgeld). VIMOS allows the simultaneous observation of 4 quadrants in one telescope pointing. Each quadrant is of dimension $7' \times 8'$, with a gap of about $2'$ between the quadrants. Figure 2.14 shows a map of the observed region in the core of the Hydra I cluster. Three multi-object spectroscopy (MOS) pointings were observed, arranged such that they covered a maximum number of previously selected dwarf galaxy candidates (Sect. 2.2) and a large fraction of the inner cluster region at the same time.

The spectra were obtained using the low resolution LR-blue grism and the OS-blue order sorting filter. The grism gives a wavelength coverage of [3700:6700] Å at a dispersion of 5.3 Å/pixel. The pixel scale is $0.205''$/pixel, so that with the used slit width of $1.5''$ the
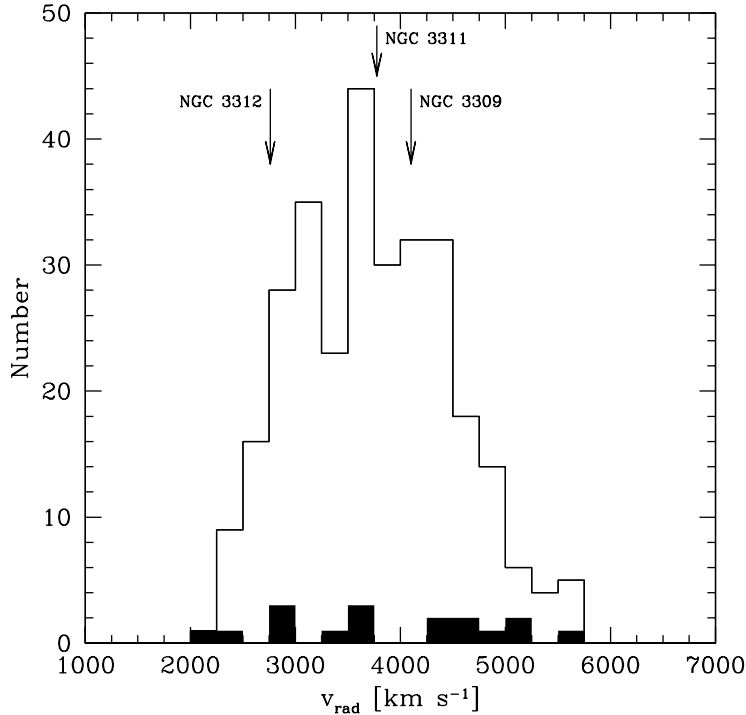
Fig. 2.16. Radial velocity distribution of all identified Hydra I cluster galaxies from CZ03 and this study. The filled histogram represents the 17 newly discovered faint dwarf galaxies. Arrows mark the individual radial velocities of NGC 3312, NGC 3311 and NGC 3309.

instrumental resolution of the spectra in terms of Gaussian σ corresponds to $\simeq 1000$ km s^{-1}. The total on-source integration time was 7960 s, subdivided into four single exposures.

The VIPGI (VIMOS Interactive Pipeline and Graphical Interface) data reduction pipeline (Scodeggio et al. 2005) was used for reducing the 2D raw spectra to 1D wavelength calibrated spectra. Redshifts were measured by means of Fourier-cross correlation (IRAF task `fxcor`) with a synthetic template spectrum (Quintana et al. 1996), or by identification of the [OII], Hγ, Hβ, [OIII] and Hα lines for emission line objects (IRAF task `rvidlines`).

2.4.2   Results

Spectra were obtained for 30 dwarf galaxy candidates from the HCC catalogue (Table A.2), and for 3 background galaxy candidates. A radial velocity could be determined for 30 of these. Table 2.1 lists the photometric parameters and the redshifts of the 33 measured objects. Figure 2.15 shows the high S/N spectrum of HCC-045 in comparison to three spectra for which the TDR value, which gives the significance of the cross-correlation result, was ≤ 3 (cf. Table 2.1). Despite the low TDR value, these spectra still show typical features of an early-type galaxy spectrum, such as the 4000 Å break, the G-band or the Mgb absorption line. Therefore, the cross-correlation match is regarded significant.

25 of the 30 cluster galaxy candidates are confirmed cluster members, only 2 objects (HCC-058 and HCC-076) turn out to be background objects. Three presumable background galaxies are probed and spectroscopically confirmed as such. Hence, the success rate of the morphological membership assignment (Sect. 2.2.1) is 90%.

Radial velocities have already been measured for 8 objects before (cf. Tables 2.1 and A.2). Most of the new radial velocities agree with the previously determined values within their measurement errors. The larger deviations for some objects can be explained by the instrument instabilities of VIMOS, which may result in differences of up to ~ 200 km s^{-1} (see also Sect. 3.2.1). Figure 2.16 shows the radial velocity distribution all known Hydra I galaxies from CZ03 and this study, with the 17 newly confirmed dwarf galaxies highlighted. The new dwarf galaxies have velocities in the full range of the other Hydra I galaxies found by CZ03. The combined sample (CZ03 + this study) shows an indication for 3 velocity subcomponents, approximately at the radial velocities of NGC 3312 (a giant late-type galaxy), NGC 3311 and NGC 3309. However, the CZ03 sample covers a much wider cluster area than investigated here, and which of the dwarf galaxies might dynamically be associated with one of the major cluster galaxies can only be investigated, once radial velocities are available for a larger sample of dwarf galaxies.

Updated versions of Fig. 2.7 and Fig. 2.8 are shown in Fig. 2.17, with the newly confirmed cluster/background galaxies highlighted. Cluster dwarf galaxies with absolute magnitudes down to $M_V = -12$ mag could be confirmed, extending the magnitude range of secure cluster members by 2–3 magnitudes. At the same time, these dwarf galaxies have surface brightnesses of $\mu_{V,0} \lesssim 24.5$ mag/arcsec^2, much lower than the previously known cluster members ($\mu_{V,0} \lesssim 22.0$ mag/arcsec^2).

2.5 Summary and discussion

In this chapter a spectroscopic and photometric study of the early-type dwarf galaxy population in the Hydra I cluster was presented. Two spectroscopic surveys were analysed, one executed with Magellan I/LDSS2 at Las Campanas Observatory (Sect. 2.1), the other with VLT/VIMOS at ESO/Paranal (Sect. 2.4). The imaging data were obtained with VLT/FORS1 (Sect. 2.2).

By radial velocity measurements the cluster membership of 45 galaxies was confirmed, of which 17 are previously uncatalogued dwarf galaxies (Sect. 2.4.2). The confirmed cluster galaxies define a tight colour–magnitude relation (see Figs. 2.6b, 2.7 and 2.17). In combination with the visual inspection of the images, 111 cluster early-type dwarf galaxies were identified. Dwarf galaxies fainter than $M_V = -17$ mag follow a colour–magnitude relation being the extension of the CMR of the brighter cluster galaxies. This is consistent with earlier studies, where early-type dwarf galaxies are reported to follow the CMR of giant early-type galaxies (e.g. Secker et al. 1997; Conselice et al. 2003; Hilker et al. 2003; López-Cruz et al. 2004; Adami et al. 2006).

The sample of early-type dwarf galaxies defines a magnitude–surface brightness relation in the sense that the central surface brightness (as estimated from an exponential law)
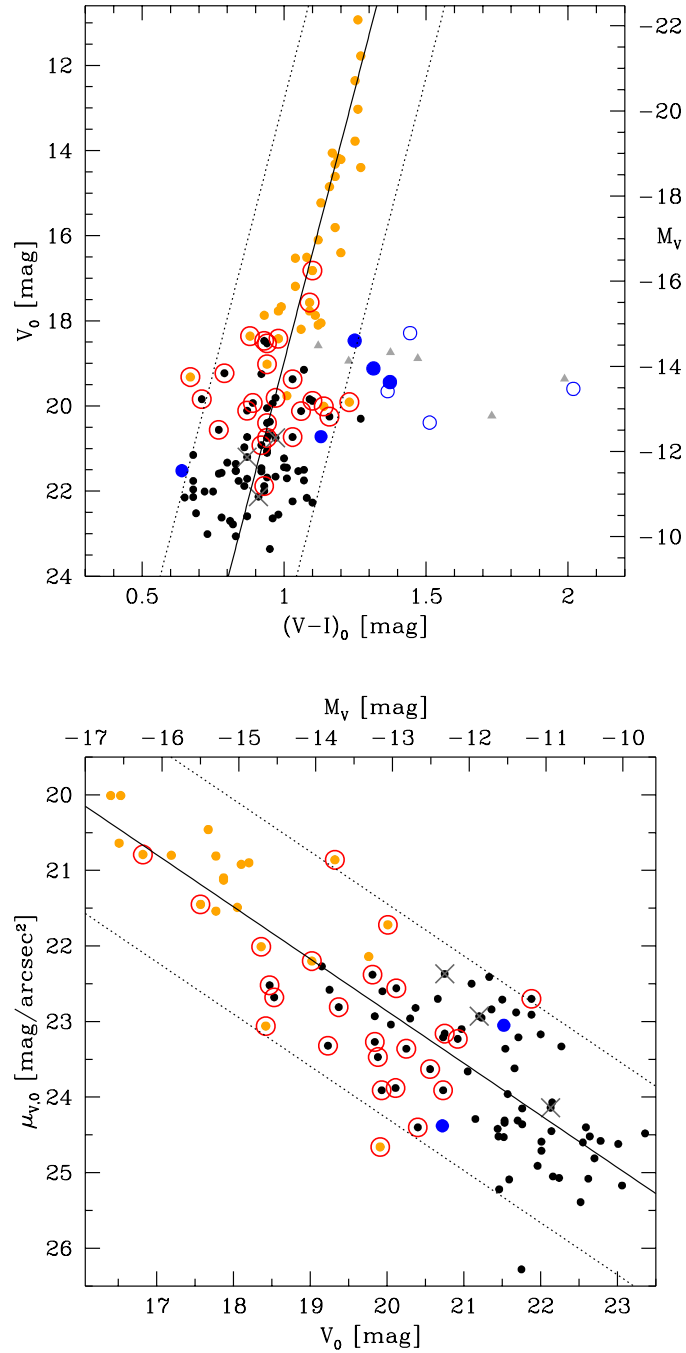
Fig. 2.17. Photometric properties of the newly confirmed Hydra I dwarf galaxies. The *top panel* shows an updated version of Fig. 2.7. The previously known cluster galaxies are represented by orange dots. The newly identified dwarf galaxies are marked by red open circles. Blue filled circles are confirmed background galaxies, and grey crosses mark objects for which no redshift could be determined (cf. Table 2.1). The other symbols are as in Fig. 2.7. The *bottom panel* shows an updated version of Fig. 2.8, with the same symbols as in the upper panel.

increases with luminosity (Fig. 2.8). Local Group dEs and dSphs follow reasonably well the same relation. By fitting Sérsic models to the galaxies surface brightness profiles, a common relation for dwarf galaxies and E/S0 galaxies in a $\mu_0 - M_V$ diagram is found, consistent with the results of Graham & Guzmán (2003), Ferrarese et al. (2006) and Côté et al. (2006, 2007, 2008). The slope of the relation is equal to one. Moreover, in a $\mu_e - M_V$ diagram, galaxies fainter than $M_V = -18$ mag define to a good approximation a relation of constant effective radius $R_e \sim 0.8$ kpc (see Fig. 2.9).

The Hydra I CMR is found to be similar to both the Fornax and the LG relation. Since the environments in Hydra I and Fornax are different from the Local Group in terms of mean density and strength of the gravitational potential (Girardi et al. 1993, 1998; Karachentsev & Kashibadze 2006), this could imply that internal evolution is more important for the global photometric properties of dwarf galaxies than external influences due to different environments. The almost identical magnitude–surface brightness relations of the Hydra I and the LG dwarfs may support this hypothesis. Smith Castelli et al. (2008a) argue in the same manner based on the results of their photometric study of the galaxy population in the Antlia cluster. Further deep photometric studies in various clusters of different mass and dynamical state have to be performed in order to investigate the influence of different environments on the photometric and structural properties of dwarf galaxies.

2.5.1 The Hydra I galaxy luminosity function

A very flat galaxy luminosity function ($\alpha \sim -1.1$, as derived from a Schechter fit) is deduced for the Hydra I cluster. Using Subaru Cuprime-Cam imaging, Yamanoi et al. (2007) found $\alpha \sim -1.6$ for the cluster GLF. Their central observed region overlaps with the fields observed in this study. A similar limiting magnitude is reached in both studies, however, the seeing of the FORS1 images is slightly better. Yamanoi et al. (2007) do not fit Schechter functions to their data but use a power-law model to determine the parameter α at the faint end of the GLF. In an analogous manner a slope of $\alpha \sim -1.4$ is derived from the FORS1 data, being more consistent with the results of Yamanoi et al. Qualitatively, the same behaviour is found for the Fornax GLF (Hilker et al. 2003; Mieske et al. 2007a). When fitting a power-law to the faint end, a slope of $\alpha \sim -1.3$ for $-14.0 < M_V < -9.8$ mag is measured, as opposed to $\alpha \sim -1.1$ when fitting a Schechter function. These findings can be interpreted in the way that the description by a power-law model seems to result in steeper slopes than the description by Schechter functions. The slope of the power-law model might be considered as an upper limit in this context.

It has to be stressed that the differences in α could also arise from the different methods used to construct the GLF. The dwarf galaxy candidates in Yamanoi et al. (2007) were selected only by setting lower limits in FWHM to the SExtractor detections. Contaminating background galaxies were statistically subtracted. No curve-of-growth analysis or surface brightness profile fitting was performed to cross-check the SExtractor results. By means of the surface brightness profile and the colour a number of objects could be excluded from the FORS1 sample (see Sect. 2.3.2 and Fig. 2.7). The follow-up spectroscopy of some of the

presumable background galaxies, which still sit relatively close to the colour–magnitude relation of the cluster galaxies, confirmed their nature as background galaxies. Given that the membership assignment success rate, as investigated in Sect. 2.4, is 90% for the given sample, the entire sample should not be contaminated by many background galaxies that only resemble cluster dwarf galaxies.

Being consistent with the results obtained here, Trentham & Tully (2002) measured the GLF in different local environments (including the Virgo cluster) and found shallow logarithmic slopes of $\alpha \sim -1.2$. They applied selection criteria similar to this study (based on surface brightness and morphology). Trentham & Tully (2002) stated that it is unlikely that they have missed a large number of dwarfs, since they were sensitive to very low surface brightness galaxies and the seeing was good enough to distinguish high surface brightness dwarfs from background galaxies. The same is true for the Hydra I data. Potentially, very compact cluster members that resemble objects like M32 could have been missed, but these objects are rare (Drinkwater et al. 2000b; Mieske et al. 2005b; Chilingarian et al. 2007; Chilingarian & Mamon 2008) and do not significantly contribute to the GLF.

Clearly, for the determination of the faint-end of the GLF it is crucial which method is used to identify contaminating background galaxies. Different methods in constructing the GLF can lead to different results. One example for this is the Fornax cluster. Applying morphological selection criteria, Hilker et al. (2003) found a flat GLF, whereas Kambas et al. (2000) reported on a very steep GLF ($\alpha \simeq -2$) for the same cluster. However, by comparing the data sets Hilker et al. (2003) could show that most of Kambas' dwarf galaxy candidates were non-members of the Fornax cluster.

At least for nearby galaxy clusters which are close enough for large telescopes like the VLT to resolve even faint dwarf spheroidal galaxies under good seeing conditions, the membership assignment by means of morphology and surface brightness seems to be an appropriate way to construct the galaxy luminosity function and constrain photometric scaling relations.

Table 2.1. Photometry and redshifts of the dwarf galaxy and background galaxy candidates. The TDR value gives the significance of the cross-correlation result. $v_{\rm rad,HCC}$ are the values from Table A.2. [a] Radial velocity determined from emission lines.

ID	V_0	$(V-I)_0$	$\mu_{V,0}$	$v_{\rm rad}$	$\Delta v_{\rm rad}$	TDR	$v_{\rm rad,HCC}$
	[mag]	[mag]	[mag/arcsec^2]	[km s^{-1}]	[km s^{-1}]		[km s^{-1}]
HCC-019	16.82	1.10	20.79	5513	142	10.0	5735 ± 55
HCC-021	17.57	1.09	21.45	4023	139	9.0	3700 ± 41
HCC-030	18.36	0.88	22.01	4419	187	8.2	4306 ± 134
HCC-031	18.42	0.98	23.06	2054	284	5.9	2418 ± 256
HCC-032	18.47	0.93	22.52	3519	237	6.3	
HCC-033	18.53	0.94	22.68	2924	172	8.8	
HCC-034	19.02	0.94	22.20	4869	219	6.3	4962 ± 79
HCC-036	19.23	0.79	23.32	4975	217	6.4	
HCC-038	19.32	0.67	20.86	3658^a	122	...	3989 ± 80
HCC-039	19.37	1.03	22.81	5127	220	6.5	
HCC-041	19.81	0.97	22.38	2378	261	6.6	
HCC-042	19.84	0.71	23.27	4694	378	2.6	
HCC-044	19.88	1.10	23.47	4390	290	3.9	
HCC-045	19.91	1.23	24.66	4001	196	7.8	4252 ± 60
HCC-046	19.93	0.89	23.91	3714	278	2.5	
HCC-048	20.01	1.14	21.72	3352	152	8.0	2876 ± 38
HCC-050	20.11	0.87	23.88	2971	327	4.6	
HCC-051	20.12	1.06	22.56	2764	180	7.6	
HCC-052	20.25	1.16	23.36	5233	354	3.6	
HCC-055	20.40	0.94	24.40	3740	249	5.6	
HCC-056	20.56	0.77	23.63	4609^a	68	...	
HCC-058	20.72	1.13	24.38	81708	140	7.8	
HCC-059	20.73	1.03	23.91	2135	311	3.0	
HCC-061	20.75	0.94	23.16	5541	399	2.8	
HCC-062	20.75	0.97	22.37	...	...	...	
HCC-063	20.92	0.92	23.23	3398	447	3.4	
HCC-068	21.20	0.87	22.93	...	...	...	
HCC-076	21.52	0.64	23.05	28193^a	137	...	
HCC-091	21.88	0.93	22.70	4325	295	3.5	
HCC-096	22.13	0.91	24.14	...	...	...	
4-21	18.47	1.25	...	32088	302	4.1	
4-145	19.12	1.32	...	57627	91	13.3	
4-924	19.44	1.37	...	73368	145	7.7	

Chapter 3

A search for UCDs in the Hydra I galaxy cluster

Because of the apparent heterogeneity of UCDs (see Sect. 1.2), it is essential to broaden the environmental baseline of UCD studies beyond the well studied clusters Fornax and Virgo. In this chapter, a spectroscopic census of compact objects in the core region of the Hydra I galaxy cluster (Abell 1060) is presented. Hydra I is well suited for a search for UCDs, since the cluster centre is dominated by the prominent cD galaxy NGC 3311, which exhibits a very pronounced diffuse light component and an extremely rich globular cluster system (van den Bergh 1977; McLaughlin et al. 1995; Mieske et al. 2005a; Wehner et al. 2008). The aim of this chapter is to investigate the globular cluster system of the two central cluster galaxies NGC 3311 and NGC 3309, including the very bright end of the globular cluster luminosity function, where UCDs are expected to be found. For this, two spectroscopic surveys are analysed, which were carried out with the VIsible Multi-Object Spectrograph (VIMOS, LeFevre et al. 2003) mounted on UT3 at the VLT. One survey explicitly targets at UCD candidates (ESO observing programme 082.B-0680, PI: I. Misgeld), the other one targets at fainter sources, mainly GC candidates (ESO observing programme 076.B-0154, PI: T. Richtler). Throughout this chapter a Hydra I distance modulus of $(m - M) = 33.37$ mag is adopted, which is the mean value from different studies (see Mieske et al. 2005a, and references therein). This corresponds to a physical scale of 229 pc/arcsec at 47.2 Mpc.

The observations and the candidate selection are described in Sect. 3.1. The data reduction of the raw 2D spectra and the radial velocity measurements from the calibrated 1D spectra are presented in Sect. 3.2. The photometric and kinematic properties of the GC/UCD candidates are given in Sect. 3.3, and the results are discussed in Sect. 3.4.

Table 3.1. Observing Log.

Pointing/ Mask	$\alpha(2000.0)$ [h:m:s]	$\delta(2000.0)$ [°:′:″]	Date	T_{exp} [sec]
P1M1	10:36:15.7	-27:37:12.0	2007/11/11	2×2100
P1M2	10:36:15.7	-27:37:12.0	2008/12/26	2×2555
P2M1	10:36:58.6	-27:27:40.4	2008/12/27	2×2555
P2M2	10:36:58.6	-27:27:40.4	2009/01/31	2×2555
P3M1	10:36:07.1	-27:24:29.9	2009/02/18	2×2555
P3M2	10:36:07.1	-27:24:29.9	2009/02/01	2×2555
P4M1	10:37:09.8	-27:41:11.3	2009/02/28	2×2555
P4M2	10:37:09.8	-27:41:11.3	2009/02/24	2×2555
P5M1	10:36:18.0	-27:28:39.6	2006/02/28	4×2185
P5M2	10:36:18.0	-27:28:39.6	2007/01/27	4×2185
P5M3	10:36:18.0	-27:28:39.6	2007/02/22	4×2185
P6M1	10:36:28.9	-27:30:58.7	2007/01/21	4×2185
P6M2	10:36:28.9	-27:30:58.7	2007/01/24	4×2185

3.1   Observations and candidate selection

VIMOS allows the simultaneous observation of 4 quadrants in one telescope pointing. Each quadrant is of dimension $7' \times 8'$, with a gap of about $2'$ between the quadrants. For the UCD survey, four multi-object spectroscopy (MOS) pointings were placed around NGC 3311, the central cD galaxy of the Hydra I cluster (pointings Nr. 1–4 in Fig. 3.1). Each MOS pointing was observed with two different slit masks which were created with the VIMOS mask creation software VMMPS. Pointing Nr. 1 was already observed with one slit mask in 2007 as part of a previous observing programme 076.B-0293 (see Misgeld et al. (2008) for details). For reasons of consistency, the results from this run are included into the following analyses. For the new UCD survey, this pointing was re-observed with one additional slit mask. Table 3.1 lists all observations analysed in this chapter. The first column of the table indicates the pointing and the mask number, columns 2 and 3 give the central coordinates of the pointing (cf. Fig. 3.1), column 4 lists the date of observation, and column 5 the exposure time.

3.1.1   The UCD survey

The candidates for pointings Nr. 1 and Nr. 2 were selected as being unresolved in the VIMOS V- and R-band pre-images, and restricted in apparent magnitude and colour to $19.2 < V < 22.7$ mag and $0.48 < V - R < 0.93$ mag.

The UCD candidates for the new MOS pointings Nr. 3 and Nr. 4 were again selected from VIMOS pre-imaging in V and R, however in a slightly different manner. Figure 3.2
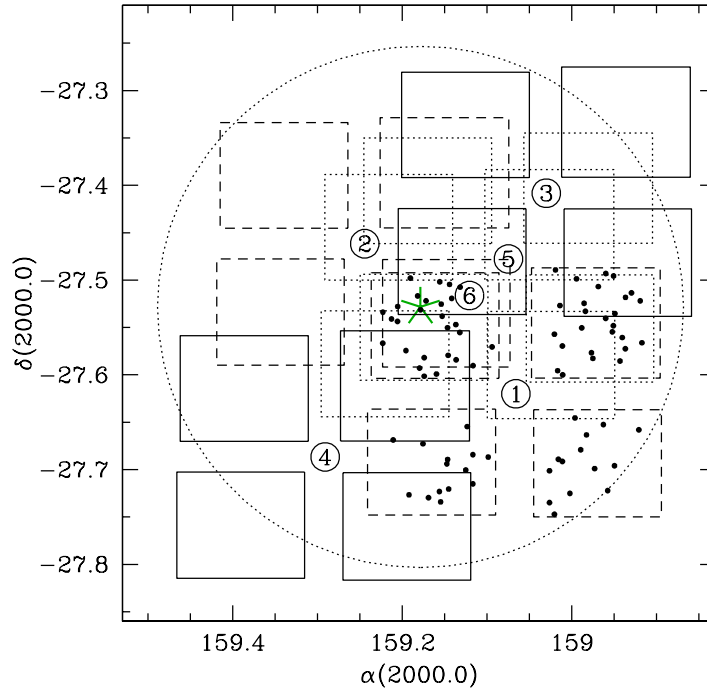
Fig. 3.1. Map of the surveyed area in the Hydra I cluster. The dashed squares mark the two pointings, which had been approved for observations in 2007 (Nr. 1 and Nr. 2), but from which only pointing Nr. 1 was observed with one slit mask. Black dots are all compact sources observed in this particular programme (see Misgeld et al. 2008). The solid squares mark the two additional pointings for the new UCD survey in 2009 (Nr. 3 and Nr. 4). The two pointings of the GC survey (see Sect. 3.1.2) are represented by the dotted squares (Nr. 5 and Nr. 6). The large dotted circle indicates the projected cluster core-radius of $r_c \sim 170 \ h^{-1}$ kpc (Girardi et al. 1995), adopting $h = 0.75$. The large green asterisk marks the location of the central cluster galaxy NGC 3311.

shows exemplarily for pointing Nr. 4 all SExtractor (Bertin & Arnouts 1996) detections in the four quadrants and the UCD candidates that were selected by the following requirements:

1. Being unresolved, as judged by the SExtractor star-galaxy separator (CLASS_STAR > 0.5, with 1 for an unresolved source ("star") and 0 for a resolved source ("galaxy")). In order to minimize false detections, additional limits were set on the FWHM, so that the selected candidates were clearly located on the stellar sequence in the magnitude vs. FWHM plot (see right panel of Fig. 3.2).

2. Having apparent magnitudes of $19.4 < V < 22.4$ mag, corresponding to absolute magnitudes of $-14.2 < M_V < -11.2$ mag, adopting an interstellar absorption coefficient of $A_V = 0.26$ mag (Schlegel et al. 1998). This encompasses the luminosity range of all known UCDs, although the distinction between UCDs and GCs at the faint magnitude limit is arbitrary to some extent.
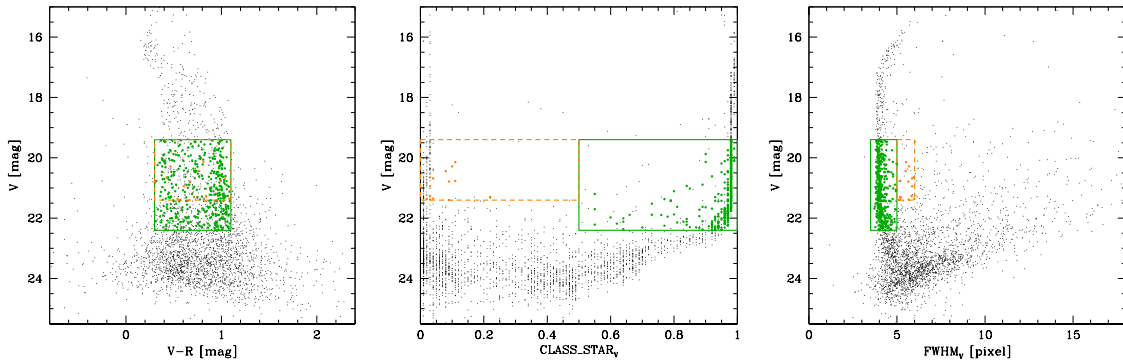
Fig. 3.2. Selection of the UCD candidates. The apparent V magnitude of all detected objects in pointing Nr. 4 (black dots) is plotted vs. their $V - R$ colour (*left panel*), the SExtractor star-classifier value (*middle panel*), and their FWHM (*right panel*). Green solid boxes represent the selection criteria for the main UCD sample, orange dashed boxes are the cuts set for the additional sub-sample of slightly resolved UCD candidates (see text for details). Green and orange points are those objects which fulfil the selection criteria.

3. Having colours of $0.3 < V - R < 1.1$ mag. This extends the colour range of previous studies (e.g. Mieske et al. 2007b, 2009) to both the blue and the red side, and thus prevents a possible bias caused by a too narrow colour window.

As shown in Mieske et al. (2009) for UCD candidates in the Centaurus cluster, the SExtractor star-classifier value flips from ~ 1 to ~ 0 at a certain physical size (i.e. r_{eff}) of the object. At the Centaurus cluster distance of ~ 45 Mpc (Mieske et al. 2005a) and a seeing of $\sim 0.8''$ this happens at $r_{\mathrm{eff}} \gtrsim 70$ pc (cf. Fig. 1 in Mieske et al. 2009). Since the Hydra I cluster lies at about the same distance (Mieske et al. 2005a), and the pre-imaging was done under similar seeing conditions, the limitation to objects with CLASS_STAR > 0.5 would not select the largest known UCDs with effective radii $r_{\mathrm{eff}} \simeq 100$ pc (e.g. Evstigneeva et al. 2008).

Therefore, an additional sub-sample of slightly resolved UCD candidates was defined, having brighter magnitudes ($19.4 < V < 21.4$ mag), lower star-classifier values (CLASS_STAR ≤ 0.5), and a slightly larger FWHM than the primary UCD candidates (see Fig. 3.2).

Wehner & Harris (2007) and Wehner et al. (2008), W7W8 hereafter, performed a photometric study of the globular cluster system around NGC 3311 and NGC 3309 and identified several UCD candidates. 48 objects with magnitudes $i' < 22.2$ mag from their list of candidates were included to this spectroscopic survey (see also Fig. 3.6).

All spectra were obtained with VIMOS, using the medium resolution MR grism and the order sorting filter GG475. The grism gives a wavelength coverage of [4800:10 000] Å at a dispersion of 2.5 Å/pixel. The pixel scale is $0.205''$/pixel, so that with a slit width of $1''$ the instrumental resolution corresponds to a FWHM ≈ 5 pixel, or 12 Å. This equates to a velocity resolution of 600 km s^{-1} at 6000 Å. The average seeing for this set of spectroscopic

observations was $\sim 0.8''$. The total on-source integration time was 1.4 hours, subdivided into two exposures.

3.1.2 The GC survey

Two MOS pointings were observed for the GC survey. Pointing Nr. 5 was observed with three different slit masks, pointing Nr. 6 with two (cf. Table 3.1 and Fig. 3.1). From the pre-images in V- and R-band, all unresolved sources (CLASS_STAR > 0.7) with colours $0.45 < V - R < 0.80$ mag and magnitudes $18.5 < V < 24.0$ mag were selected as GC candidates.

The spectra of the GC candidates were obtained with the same instrument setup as for the UCD candidates, but given the fainter magnitudes of most of the targets, the total on-source integration time was 2.4 hours. The seeing ranged between $0.6''$ and $1.2''$.

3.2 Data reduction and radial velocity measurements

For the data reduction from a 2D raw spectrum to a wavelength calibrated 1D spectrum, the VIPGI (VIMOS Interactive Pipeline and Graphical Interface) data reduction pipeline (Scodeggio et al. 2005) was used. This pipeline is based on the core reduction routines which are also used by the ESO VIMOS pipeline[1]. VIPGI is particularly suited for reducing and combining sequences of exposures, and allows amongst others the interactive control of the wavelength calibration of each spectrum.

Since the individual science exposures were taken in at least two different nights, the bias subtraction, flat field division, sky subtraction and wavelength calibration were performed separately for each exposure. Afterwards, the pipeline combined these exposures into a single sky subtracted and wavelength calibrated 2D science frame, and extracted the 1D spectra using the Horne extraction algorithm (Horne 1986).

Radial velocities were then measured by performing a Fourier cross-correlation between the calibrated 1D object spectra and a template spectrum (IRAF-task `fxcor` in the `rv` package). A synthetic template spectrum was used, which resembles a typical early-type galaxy (Quintana et al. 1996). This template has proven to give the best and most reliable cross-correlation results for this type of survey (e.g. Mieske et al. 2004; Misgeld et al. 2008; Mieske et al. 2009).

For a radial velocity measurement to be regarded as reliable, a cross-correlation confidence value of $R \geq 5.0$ (Tonry & Davis 1979) was required. All spectra for which a lower R-value was achieved, were re-measured independently by Ingo Misgeld, Steffen Mieske and Michael Hilker, and the $v_{\rm rad}$ measurement was only accepted if the three independent measurements were in agreement. Redshifts for objects showing emission lines were determined with the IRAF-task `rvidlines`. In most of these cases the [OII], Hγ, Hβ, [OIII] and Hα emission lines were used for measuring the redshift. Heliocentric velocity corrections

---

[1]`http://www.eso.org/sci/software/pipelines/`
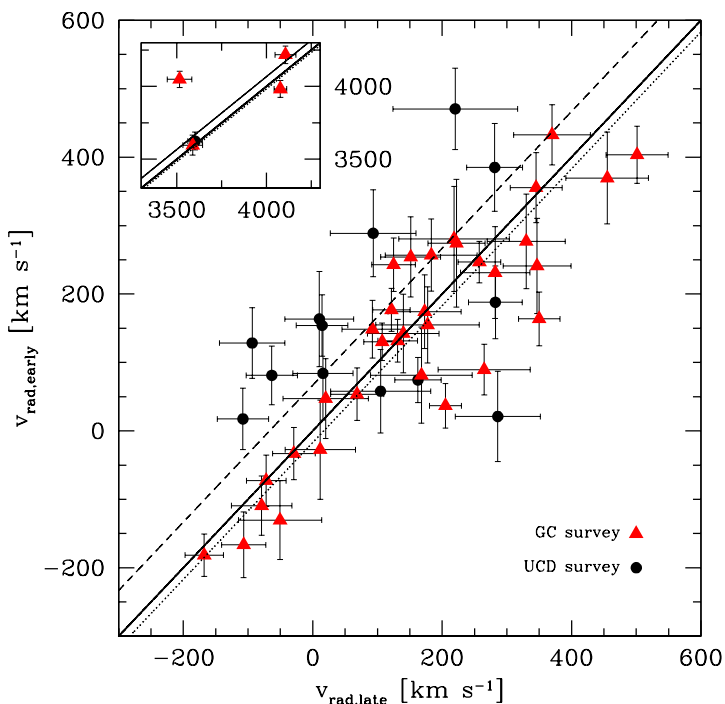
Fig. 3.3. Comparison of radial velocities for objects which were observed twice, in either the GC survey (red triangles) or the UCD survey (black dots). Plotted is the radial velocity derived from the earlier observation ($v_{\mathrm{rad,early}}$) versus the one derived from the later observation ($v_{\mathrm{rad,late}}$). The inset in the upper left corner shows the comparison for cluster GCs/UCDs. The solid line is the one-to-one relation, the dotted (dashed) line is the fitted relation with slope one for the GC (UCD) data points.

were applied to all measurements. The individual measurement uncertainties were of the order of 25–160 km s^{-1}, with a median of 54 km s^{-1}.

3.2.1   Systematic radial velocity shifts

The VIPGI pipeline allows to compute for each slit the offset of a particular sky line in the spectrum from its expected position. With this data it is possible to correct for systematic wavelength shifts which correspond to radial velocity shifts.

Since the wavelength range [5000:7000] Å was used for the radial velocity measurements, the 5577.4 Å [OI] and the 6299.7 Å [OI] sky lines were chosen to estimate the systematic wavelength shifts. Given that the shifts were found to be largely independent of the position of the slit on the mask, the median offset and the according rms of each of the two sky lines were recorded for each quadrant and mask. The final radial velocity shift Δv_{rad} was then computed by

$$\Delta v_{\mathrm{rad}} = \frac{\delta \lambda}{\lambda_m} \cdot c, \tag{3.1}$$
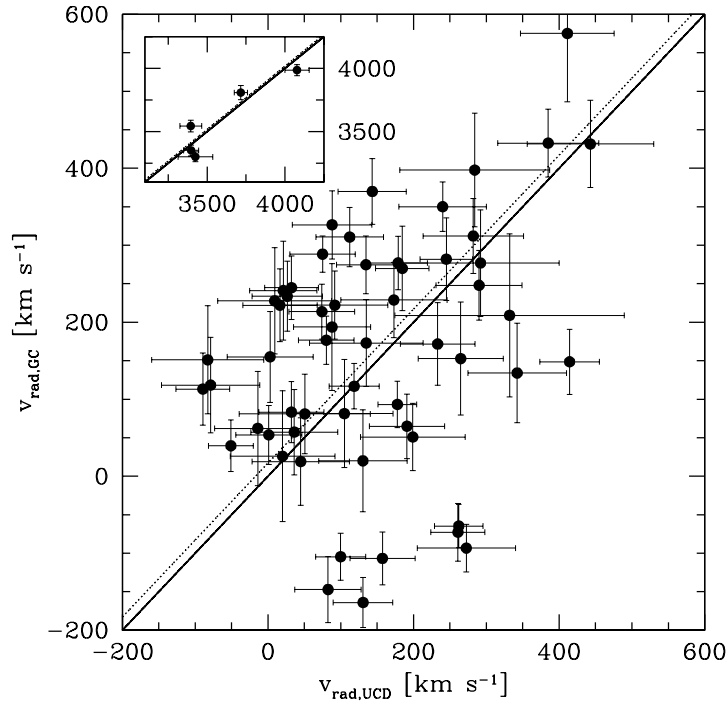
Fig. 3.4. Comparison of the radial velocities measured in the UCD survey to the radial velocities measured in the GC survey. The dotted line is the fitted relation with slope one. The solid line is the one-to-one relation. The inset in the upper left corner shows the comparison for cluster GCs/UCDs.

with the median wavelength offset $\delta\lambda$, the mean wavelength $\lambda_m = 5938.6$ Å, and c the speed of light. The error for $\Delta v_{\rm rad}$ was calculated from the rms of $\delta\lambda$. The obtained radial velocity shifts were of the order of 40–170 km s^{-1} (or 0.8–3.4 Å).

Since the observations span a period of several months up to more than one year (see Table 3.1), one has to check for systematic radial velocity offsets that are potentially caused by VIMOS instrument instabilities. In Fig. 3.3 the measured radial velocities of objects are compared, which were observed twice in one individual observing programme, i.e. within the UCD survey (pointing Nr. 1–4), or within the GC survey (pointing Nr. 5–6). For both surveys, a linear fit to the data points gives a relation with a slope consistent with one. Thus, the slope is fixed to $m = 1$, in order to determine the offset of the fitted relation from the one-to-one relation. For the GC sample, an offset of $\Delta_{\rm GC} = -17.0 \pm 14.4$ km s^{-1}, with a rms of 76.9 km s^{-1} is determined. Within the measurement uncertainties, this is consistent with the one-to-one relation. The clear outlier at $(v_{\rm rad,early}, v_{\rm rad,late}) \sim (4000, 3500)$ km s^{-1} was excluded from the fit, since the later measurement was with $R = 5.9$ at the border of what was regarded a reliable measurement (cf. Sect. 3.2), in contrast to $R = 10.3$ for the earlier measurement.

The UCD data points show a larger scatter, and the linear fit results in an offset of $\Delta_{\rm UCD} = 66.8 \pm 47.9$ km s^{-1}, with a rms of 144.8 km s^{-1}. However, there is no clear systematic velocity shift in one direction. For example, data points that compare the
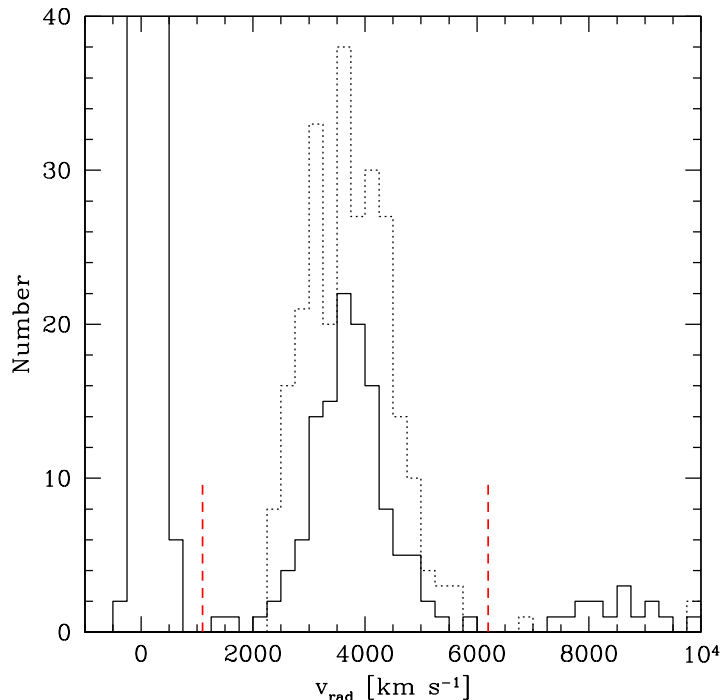
Fig. 3.5. Radial velocity histogram of objects with $v_{\rm rad} < 10\,000$ km s^{-1} (solid histogram). The dotted histogram shows the velocity distribution of Hydra I cluster galaxies (Christlein & Zabludoff 2003). The vertical dashed lines mark the velocity limits required for cluster membership in this study.

earliest with the latest observations lie above as well as below the one-to-one relation. For this reason and due to the rather large measurement uncertainties and the small sample size, no constant velocity shift was applied to the UCD data. The larger velocity scatter in the case of the UCD data set may be linked to the commonly known flexure problems of VIMOS, which can lead to misalignment of targets in their respective slits. In fact, many of the UCD targets were located at the very edge of their respective slits, making it in some cases impossible to extract a spectrum.

In Fig. 3.4, the radial velocities measured in the UCD survey are compared to the ones measured in the GC survey. To determine a possible systematic offset, a linear relation with slope $m = 1$ is fitted to the data. This results in a offset $\Delta_{\rm UCD/GC} = 17.1 \pm 18.1$ km s^{-1} with a rms of 162.0 km s^{-1} (dotted line in Fig. 3.4), which is consistent with the one-to-one relation. Again, the relatively large scatter can be attributed to the instrument instabilities of VIMOS.

3.3   Results

In total, 1236 individual compact objects were observed (including the objects from the previous programme 076.B-0293), compared to 1948 photometrically selected sources (cf.
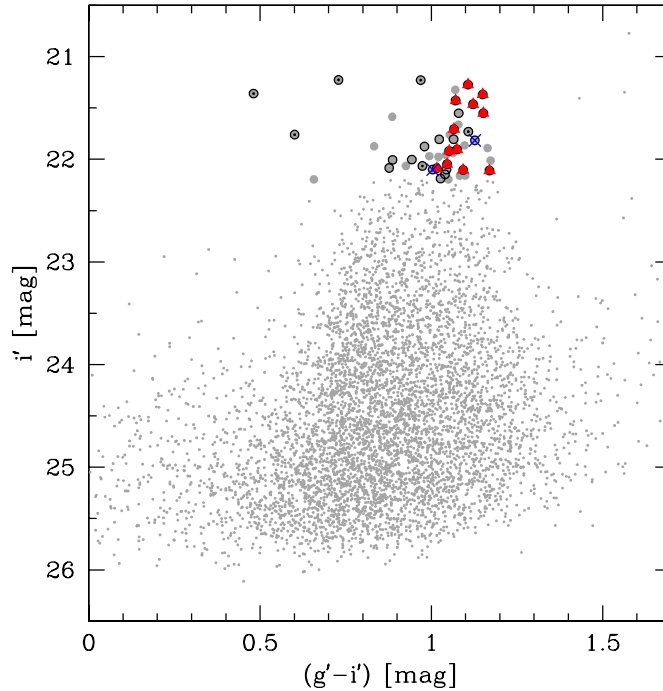
Fig. 3.6. Colour-magnitude diagram of the globular clusters around NGC 3311 (after W7W8). Note that the magnitudes and colours are not de-reddened. Objects selected for the spectroscopic survey are represented by large grey dots. Open circles mark those objects for which a slit could be allocated. The 12 cluster members are marked by red triangles, the 2 background objects by blue crosses, and the 6 foreground stars by small black dots.

Sect. 3.1). Within the surveyed area, the completeness in terms of slit allocation is thus about 63%. A radial velocity could be measured for 1018 objects (82% of the observed objects). 776 foreground stars, 124 background objects and 118 cluster GCs/UCDs were identified. The cluster membership criterion was $1100 < v_{\rm rad} < 6200$ km s^{-1} (see Fig. 3.5). Two objects with relatively low radial velocities ($v_{\rm rad} \sim 1500$ km s^{-1}) are considered cluster members, since also planetary nebulae with similar radial velocities have been identified in the Hydra I cluster (Ventimiglia et al. 2008, 2011). Towards higher radial velocities, there is a clear gap between cluster and background objects, the latter having radial velocities larger than $v_{\rm rad} \sim 7500$ km s^{-1}. A catalogue with the coordinates, magnitudes and colours (obtained from the VIMOS pre-images) and the radial velocities of the 118 cluster objects is given in Table A.5 in the appendix.

35 objects were selected for the sub-sample of slightly resolved UCD candidates (see Sect. 3.1.1). 27 of them were observed, yielding 20 background objects and 4 foreground stars. No radial velocity could be measured for the remaining 3 objects.

30 of the 48 selected UCD candidates from W7W8 could be observed. Figure 3.6 shows a colour-magnitude diagram (CMD) of the globular clusters around NGC 3311, as obtained from their Gemini South GMOS imaging in g' and i'. The spectroscopically observed
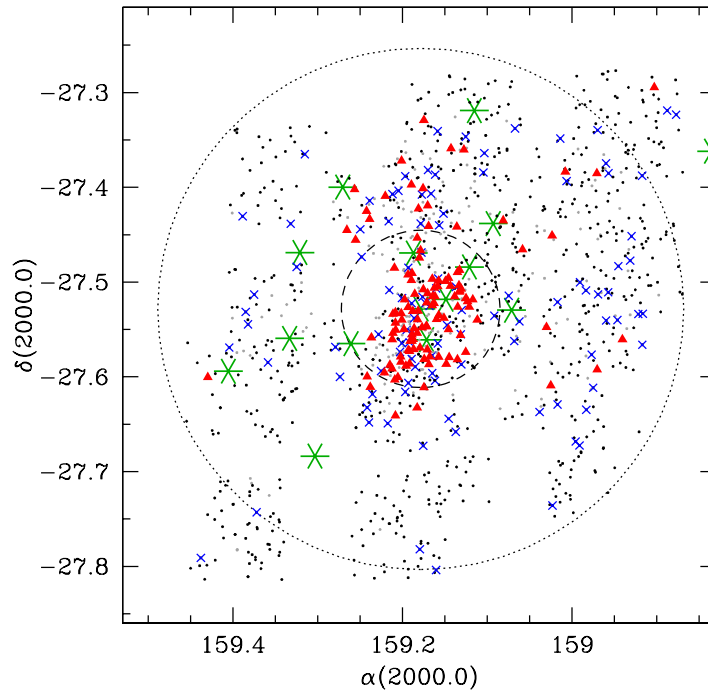
Fig. 3.7. Spatial distribution of all observed objects. Red triangles are cluster GCs/UCDs, blue crosses mark background objects. Small black dots are foreground stars, and small grey dots are objects for which no radial velocity could be determined. The large green asterisks are major cluster galaxies with apparent magnitudes $R < 14$ mag from the spectroscopic study of Christlein & Zabludoff (2003). The large dotted circle indicates the projected cluster core-radius of $r_c \sim 170~h^{-1}$ kpc (Girardi et al. 1995), adopting $h = 0.75$. The dashed circle marks a radius of $5'$ around NGC 3311.

objects are highlighted. For 20 of them a radial velocity could be measured, resulting in 12 cluster members, 6 foreground stars and 2 background objects.

Figure 3.7 presents a map of the entire sample of observed objects.

3.3.1 Photometric and structural properties

VLT/VIMOS imaging

The objects' instrumental magnitudes, as measured in the pre-images, were calibrated using the photometric zeropoints given by the ESO Quality Control and Data Processing Group[2]. Colours and magnitudes were then corrected for interstellar absorption and reddening, $A_V = 0.26$ mag and $E(V - R) = 0.05$ mag (Schlegel et al. 1998).

A CMD of all observed objects is plotted in Fig. 3.8. Adopting a Hydra I distance modulus of $(m - M) = 33.37$ mag (Mieske et al. 2005a), 52 of the identified cluster objects are brighter than $M_V = -11.0$ mag (see also Table A.5). This luminosity corresponds to a mass of $\gtrsim 6.5 \times 10^6$ solar masses, applying a mean UCD M/L ratio of 3 (e.g. Mieske et al.

---

[2]QCG, http://www.eso.org/observing/dfo/quality/
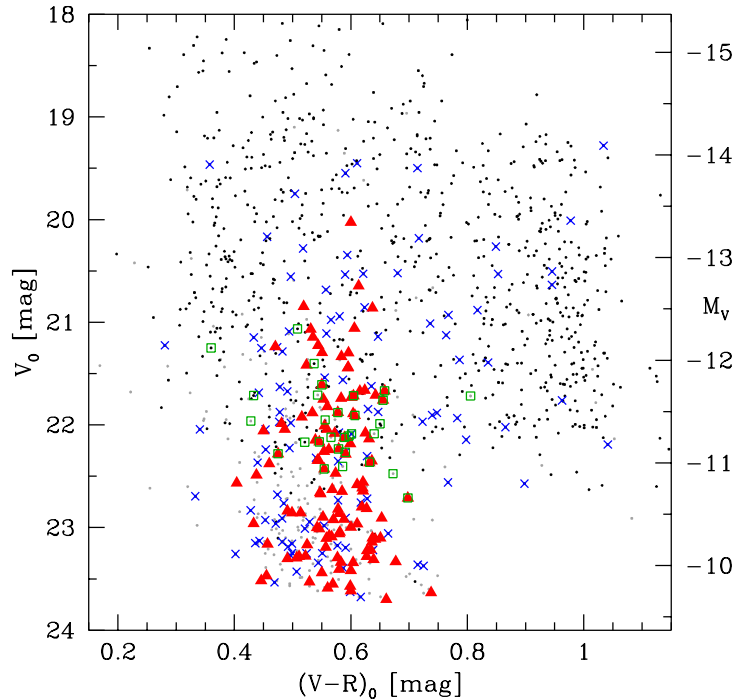
Fig. 3.8. Colour-magnitude diagram of the objects from Fig. 3.7, except for the major cluster galaxies. Green open squares mark the observed UCD candidates from W7W8. The right axis indicates the absolute V-band magnitude M_V.

2008). Such objects are generally called UCDs, although the distinction between UCDs and GCs is not clear at low luminosities. Even if assuming $M/L = 1$, these objects are still more luminous and more massive than ω Centauri, which is with $M_V = -10.29$ mag and a mass of 2.5×10^6 M$_\odot$ the most luminous and most massive globular cluster in our Galaxy (Harris 1996; van de Ven et al. 2006). Adopting this mass limit for the separation of GCs and UCDs, as suggested by Haşegan et al. (2005) and Mieske et al. (2008), there are even more than 80 UCDs in the sample. In comparison to the photometric studies of W7W8, there are 15 UCDs brighter than $M_V = -11.8$ mag, which is the magnitude of the brightest confirmed cluster object from their list of UCD candidates (see Fig. 3.8). The three brighter candidate objects turned out to be foreground stars.

The identified cluster GCs/UCDs have de-reddened colours of $0.40 < (V - R)_0 < 0.75$ mag, but they are not uniformly distributed in colour-space, as Fig. 3.9 shows. A bimodal GC colour distribution is expected for NGC 3311 (Wehner et al. 2008), and for the present data, a double Gaussian distribution is preferred to a single Gaussian distribution ($\chi_\nu^2 = 1.141$ and $\chi_\nu^2 = 2.784$, respectively). Fitting a double Gaussian function to the data results in a blue peak at $(V - R)_0 = 0.46$ mag and a red peak at $(V - R)_0 = 0.58$ mag. For a 13-Gyr population, these peaks correspond to metallicities of [Fe/H] ≈ -2.2 dex and [Fe/H] ≈ -0.4 dex, respectively (Bruzual & Charlot 2003). These estimates are consistent with the values derived for metal-poor and metal-rich GCs in a number of giant elliptical
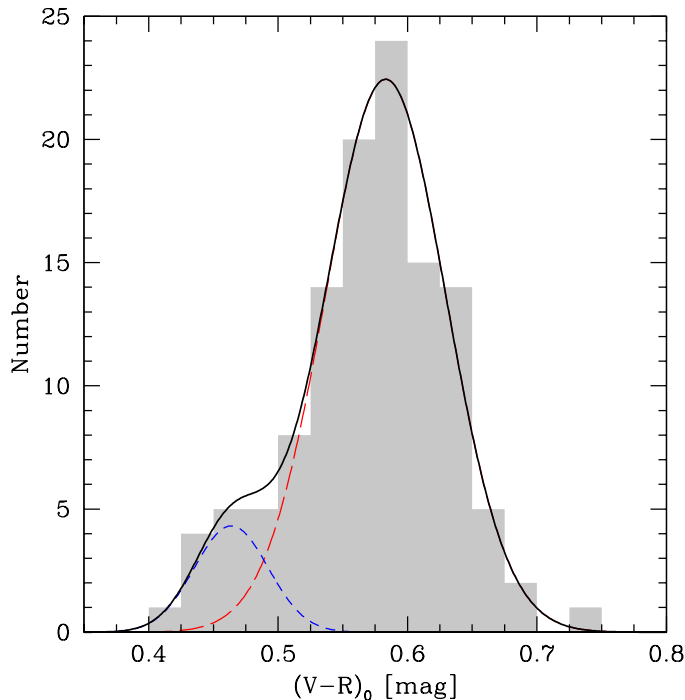
Fig. 3.9. Colour distribution of confirmed Hydra I GCs/UCDs (shaded histogram). The black curve is a double peak Gaussian function fitted to the data, the dashed curves are the single components.

galaxies (Brodie & Strader 2006, and references therein). Given this, a blue (metal-poor) and a red (metal-rich) sub-population with $(V - R)_0 < 0.5$ mag and $(V - R)_0 \geq 0.5$ mag, respectively, is defined for the following analyses (Sect. 3.3.2). The separating colour corresponds to a metallicity of $[\text{Fe/H}] \approx -1.4$ dex.

With $(V - R)_0 = 0.60$ mag, the brightest UCD in the sample (HUCD1) clearly belongs to the metal-rich sub-population and is located at the tip of the red GC sequence in the CMD. This confirms results of photometric studies, where the red GC sequence is found to extend to higher luminosities than the blue sequence (e.g. Wehner et al. 2008; Mieske et al. 2010).

HST/WFPC2 imaging

For 26 of the identified cluster GCs/UCDs, imaging is available in the HST archive. Two WFPC2 fields were observed in Cycle 6 with the PC1 chip centred on NGC 3311 and NGC 3309, respectively. The exposure times were 3700 s in $F555W$ and 3800 s in $F814W$ for the field centred on NGC 3311, and 4400 s in both filters for the NGC 3309 field (HST programme GO.06554.01-95A, PI: J.P. Brodie, see also Brodie et al. 2000).

The F555W and F814W images were bias, flat-field and bad pixel corrected. The sub-pixel dithered imaging allowed to eliminate cosmic-rays, hot pixels and improve the spatial resolution. To perform a PSF photometry on each individual WFPC2 detector,
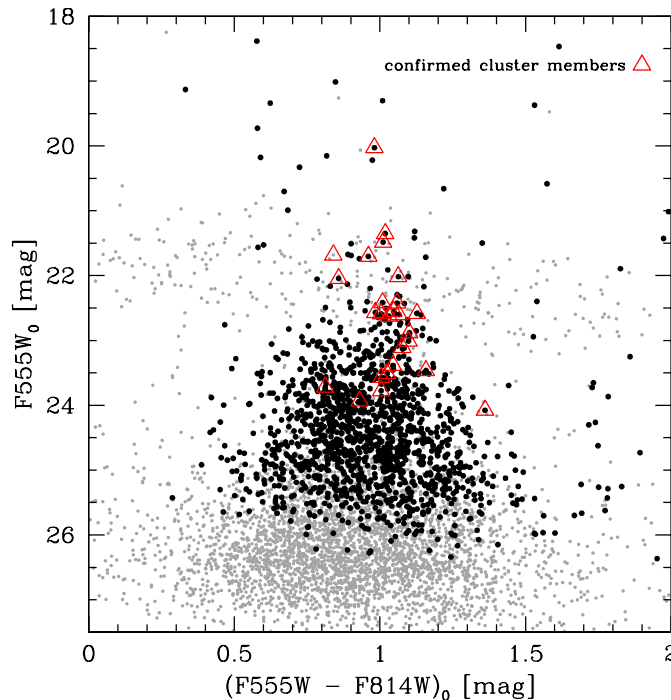
Fig. 3.10. Colour-magnitude diagram of all WFPC2 sources around NGC 3311 and NGC 3309. Black dots are objects with colour errors $(F555W - F814W)_0 < 0.1$ mag, grey dots are those with larger colour errors. Red open triangles mark the spectroscopically confirmed cluster GCs/UCDs.

a grid of 100×100 PSFs was created with the TinyTim[3] software package (Krist 1995). This library was used to create a spatially variable PSF model and perform PSF-fitting photometry with the `allstar` task in IRAF. Isolated stars were used to determine an aperture correction to $1.0''$ aperture diameter, which is the aperture used by Dolphin (2009) to derive the most up to date CTE corrections and photometric zero points for each of the WFPC2 chips. Finally, the VEGAMAG WFPC2 photometry was corrected for foreground extinction using Schlegel et al. (1998) dust maps towards the direction of both galaxies, and Cardelli et al. (1989) relations for $R_V = 3.1$ to calculate the absorption at the effective wavelengths for the WFPC2 filters. The following dereddening values were applied: $A_{F555W} = 0.261$ mag and $A_{F814W} = 0.156$ mag. To transform the VEGAMAG WFPC2 magnitudes to the standard Johnson/Cousins magnitudes, the Dolphin (2009) transformations were used, with the coefficients in their table 4 for the $(V - I)$ colour.

At a the adopted distance of 47.2 Mpc ($m - M = 33.37$ mag), one PC1 and WF2,3,4 pixel corresponds to 11 and 22 pc, respectively. For high signal-to-noise objects (typically $S/N \gtrsim 30$), one can reliably measure r_h down to 0.1 pix, i.e. ~ 2 pc. Therefore, it is

---

[3]TinyTim accounts for significant variation of the PSF as a function of wavelength (filter) due to diffraction, large angle scattering, field-dependence, aberrations, focus offsets between cameras and wavelength dependent charge diffusion (see http://www.stsci.edu/software/tinytim/)
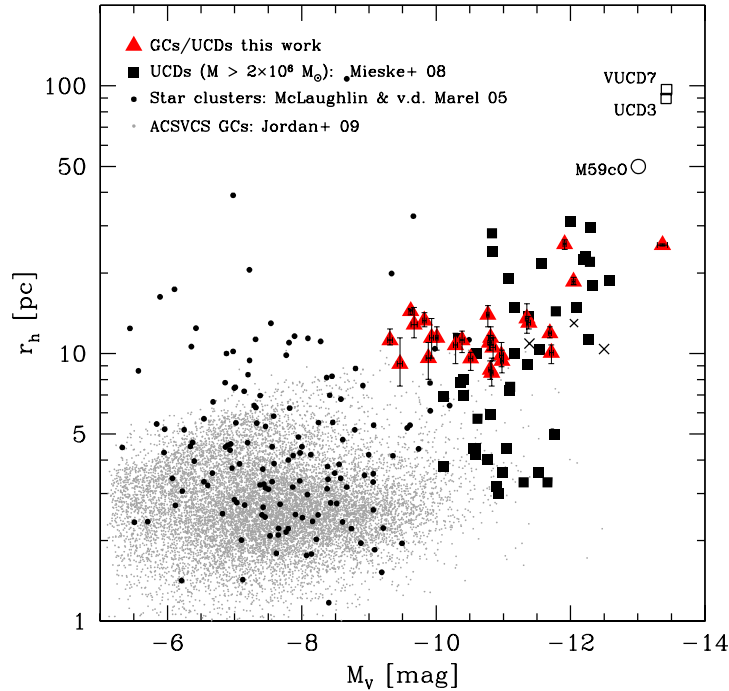
Fig. 3.11. Half-light radii and luminosities of the 26 cluster GCs/UCDs with HST imaging (see Table 3.2), in comparison to other star clusters and UCDs. Small crosses indicate the *core* components of VUCD7, UCD3 (both from Evstigneeva et al. 2007b), and M59cO (Chilingarian & Mamon 2008).

feasible to measure sizes for extended objects (such as UCDs and bright GCs) from the WFPC2 frames.

To measure the half-light radii r_h of the 26 spectroscopically confirmed objects, ten times sub-sampled PSFs were generated with TinyTim for $F555W$. Each PSF was tailored to the position of the object on the chip. Utilizing the `ishape` task of the `baolab` software package[4] (Larsen 1999), this PSF was used to model the object profile as an analytical function convolved with the (model) PSF. When sub-sampling is enabled, TinyTim does not include a convolution with the charge diffusion kernel (CDK), which additionally smears the stellar PSF. Thus, during fitting with `ishape`, the TinyTim PSF was convolved with a $F555W$ CDK, that simulates blurring caused by charge diffusion which is well understood for the $F555W$ filter.

All objects were modelled with King (1962) profiles with concentrations of the tidal-to-core radius of $r_\mathrm{t}/r_\mathrm{c} = 5, 15, 30$ and 100. The structural parameter measurements were adopted from the best χ^2 fit model. The output r_h is the r_h along the semi-major axis which needs to be corrected for ellipticity and brought to the geometrical mean value ('effective' r_h) by multiplying the square root of the major/minor axis ratio (for details see e.g. Eq. 1 in Georgiev et al. 2008).

---

[4]http://www.astro.uu.nl/~larsen/baolab/

Table 3.2. Photometric and structural properties of cluster GCs/UCDs with available HST imaging.

ID	$F555W_0$	$F814W_0$	V_0	$(V-I)_0$	r_h	r_h	$r_\mathrm{t}/r_\mathrm{c}$	S/N
	[mag]	[mag]	[mag]	[mag]	[pix]	[pc]		
HUCD1	20.027 ± 0.076	19.046 ± 0.085	20.00 ± 0.08	0.99 ± 0.11	$1.11^{+0.01}_{-0.01}$	$25.4^{+0.2}_{-0.2}$	5	134.4
HUCD8	21.350 ± 0.053	20.332 ± 0.072	21.32 ± 0.02	1.03 ± 0.03	$0.81^{+0.03}_{-0.02}$	$18.5^{+0.7}_{-0.5}$	15	62.6
HUCD14	21.483 ± 0.024	20.472 ± 0.032	21.46 ± 0.02	1.02 ± 0.04	$0.63^{+0.01}_{-0.02}$	$25.6^{+0.9}_{-1.1}$	5	64.0
HUCD18	22.044 ± 0.026	21.186 ± 0.011	22.02 ± 0.03	0.87 ± 0.03	$0.91^{+0.05}_{-0.09}$	$13.5^{+1.8}_{-1.6}$	30	55.1
HUCD21	21.703 ± 0.022	20.743 ± 0.030	21.68 ± 0.02	0.97 ± 0.04	$0.52^{+0.03}_{-0.02}$	$11.9^{+0.7}_{-0.5}$	5	50.1
HUCD30	22.016 ± 0.024	20.953 ± 0.039	21.99 ± 0.02	1.08 ± 0.05	$0.57^{+0.03}_{-0.03}$	$13.1^{+0.7}_{-0.7}$	15	47.8
HUCD35	21.681 ± 0.088	20.841 ± 0.084	21.66 ± 0.03	0.85 ± 0.04	$1.12^{+0.04}_{-0.05}$	$10.1^{+0.7}_{-0.9}$	5	43.9
HUCD39	22.569 ± 0.019	21.585 ± 0.033	22.54 ± 0.02	1.00 ± 0.04	$0.37^{+0.05}_{-0.04}$	$8.5^{+1.1}_{-0.9}$	30	29.4
HUCD42	22.424 ± 0.029	21.365 ± 0.032	22.40 ± 0.03	1.07 ± 0.04	$0.49^{+0.05}_{-0.02}$	$9.8^{+1.1}_{-0.9}$	5	37.2
HUCD44	22.416 ± 0.024	21.407 ± 0.023	22.39 ± 0.02	1.02 ± 0.03	$0.41^{+0.04}_{-0.04}$	$9.4^{+0.9}_{-0.9}$	30	37.3
HUCD46	22.625 ± 0.018	21.594 ± 0.029	22.60 ± 0.02	1.04 ± 0.03	$0.44^{+0.03}_{-0.04}$	$14.0^{+1.1}_{-1.4}$	15	28.2
HUCD47	22.590 ± 0.024	21.586 ± 0.045	22.56 ± 0.02	1.02 ± 0.05	$0.38^{+0.03}_{-0.03}$	$8.7^{+0.7}_{-0.7}$	30	34.0
54	22.550 ± 0.040	21.503 ± 0.049	22.52 ± 0.04	1.06 ± 0.06	$0.46^{+0.04}_{-0.05}$	$10.5^{+0.9}_{-1.1}$	30	27.9
59	22.601 ± 0.027	21.536 ± 0.032	22.58 ± 0.03	1.08 ± 0.04	$0.58^{+0.04}_{-0.03}$	$11.0^{+0.7}_{-0.7}$	5	27.0
61	23.108 ± 0.029	22.031 ± 0.046	23.08 ± 0.03	1.09 ± 0.05	$0.47^{+0.05}_{-0.07}$	$10.8^{+1.1}_{-1.6}$	30	22.6
66	22.582 ± 0.035	21.455 ± 0.035	22.56 ± 0.03	1.14 ± 0.05	$0.50^{+0.05}_{-0.03}$	$11.5^{+1.1}_{-0.7}$	5	27.4
68	22.880 ± 0.029	21.779 ± 0.037	22.86 ± 0.03	1.12 ± 0.05	$0.50^{+0.05}_{-0.03}$	$9.6^{+0.5}_{-0.9}$	5	21.4
69	23.009 ± 0.031	21.911 ± 0.024	22.98 ± 0.03	1.11 ± 0.04	$0.49^{+0.04}_{-0.05}$	$11.2^{+0.9}_{-1.1}$	5	20.8
90	23.511 ± 0.033	22.486 ± 0.045	23.49 ± 0.03	1.04 ± 0.06	$0.61^{+0.05}_{-0.06}$	$9.6^{+1.4}_{-1.6}$	5	14.8
94	23.463 ± 0.029	22.305 ± 0.016	23.44 ± 0.03	1.17 ± 0.03	$0.42^{+0.06}_{-0.07}$	$11.5^{+2.1}_{-1.8}$	15	17.2
99	23.385 ± 0.020	22.340 ± 0.036	23.36 ± 0.02	1.06 ± 0.04	$0.50^{+0.05}_{-0.05}$	$11.5^{+1.1}_{-1.1}$	5	17.4
101	23.570 ± 0.026	22.565 ± 0.038	23.54 ± 0.03	1.02 ± 0.05	$0.43^{+0.05}_{-0.04}$	$13.3^{+0.9}_{-0.7}$	5	13.1
110	23.722 ± 0.045	22.910 ± 0.035	23.70 ± 0.04	0.82 ± 0.06	$0.56^{+0.09}_{-0.06}$	$12.8^{+2.1}_{-1.4}$	5	12.1
112	23.935 ± 0.039	23.005 ± 0.053	23.91 ± 0.04	0.94 ± 0.07	$0.40^{+0.10}_{-0.07}$	$9.2^{+2.3}_{-1.6}$	15	10.6
114	23.775 ± 0.027	22.771 ± 0.033	23.75 ± 0.03	1.02 ± 0.04	$0.59^{+0.08}_{-0.07}$	$14.4^{+0.2}_{-0.5}$	5	11.7
115	24.077 ± 0.036	22.716 ± 0.035	24.06 ± 0.04	1.38 ± 0.05	$0.50^{+0.09}_{-0.08}$	$11.2^{+1.1}_{-0.5}$	5	10.5

Table 3.2 lists the photometric and structural properties of the 26 cluster GCs/UCDs, with the extinction corrected apparent $F555W_0$, $F814W_0$, and V_0 magnitudes in columns 2–4 and the $(V-I)_0$ colour in the fifth column. Columns 6 and 7 give the half-light radius r_h in pixels and in pc, respectively. Column 8 lists the tidal-to-core radius $r_\mathrm{t}/r_\mathrm{c}$ of the best fit model, and the last column gives the signal-to-noise ratio of the source detection.

The V_0 magnitudes derived from the HST images are, on average, 0.2–0.4 mag fainter than those measured in the VIMOS pre-images. Reasons for this discrepancy likely include the uncertainty in the VIMOS photometric zeropoints (no photometric standard was taken at the night of the pre-imaging), the different magnitude measurement techniques, and the uncertainty in the magnitude transformation of the HST data.

Figure 3.10 shows a colour-magnitude diagram of all WFPC2 sources around NGC 3309/3311, with the confirmed cluster GCs/UCDs highlighted. In Fig. 3.11, the half-light radii and luminosities of the Hydra I GCs/UCDs are compared to globular clusters from the ACS Virgo Cluster Survey (ACSVCS, Jordán et al. 2009), Milky Way, LMC/SMC and Fornax star clusters from McLaughlin & van der Marel (2005), UCDs from Mieske et al. (2008), and the compact object M59cO (Chilingarian & Mamon 2008).
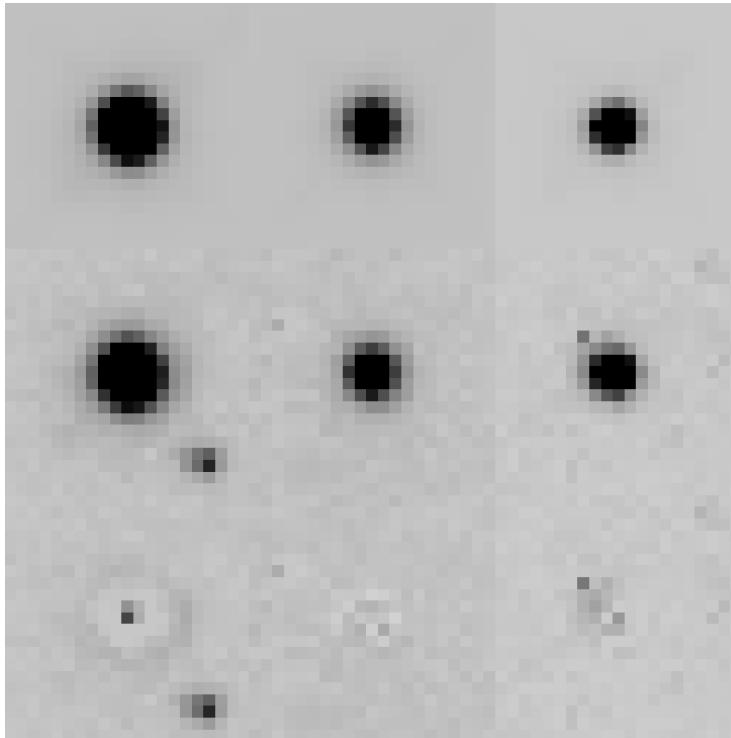
Fig. 3.12. Residual images for the three brightest UCDs with HST imaging. From left to right are sorted by luminosity: HUCD1, HUCD8 and HUCD14. From top to bottom are shown the PSF model, the object and the residual image. Each panel is 20×20 pixels in size.

The apparent g_{AB}-band magnitudes of the ACSVCS GCs were transformed into absolute V-band magnitudes using the relation $V = g_{AB} + 0.026 - 0.307 \cdot (g - z)_{AB}$ given in Peng et al. (2006), and a Virgo distance modulus of 31.09 mag (Mei et al. 2007). r_h is the average of the half-light radii measured in the g- and in the z-band. M_V and r_h of the star clusters from McLaughlin & van der Marel (2005) are the King models values. The tabulated masses of the UCDs from Mieske et al. (2008) were converted into M_V with the given M/L_V ratios and a solar absolute magnitude of $M_{V,\odot} = 4.83$ mag (Binney & Merrifield 1998). For M59cO, M_V was calculated from M_B using $B - V = 0.96$ mag (Fukugita et al. 1995).

The sizes, luminosities and colours of the Hydra I GC/UCDs are fully consistent with the ones of Virgo and Fornax UCDs (e.g. Evstigneeva et al. 2008; Mieske et al. 2008). A size-luminosity relation is visible for objects brighter than $M_V \sim -10$ mag, following the trend observed in other galaxy clusters. Below this magnitude, the size measurements with `ishape` are not regarded reliable, since the S/N is smaller than 20 for those objects (cf. Table 3.2).

With $M_V = -13.37$ mag, HUCD1 is the brightest object in the sample. Its luminosity corresponds to a mass of about 5×10^7 M$_\odot$ (assuming $M/L = 3$), or even $\sim 10^8$ M$_\odot$, if assuming a mass-to-light ratio larger than 5, which has been measured for several of the brightest UCDs in Virgo and Fornax (Mieske et al. 2008). Hence, HUCD1 has a

luminosity/mass comparable to the most massive UCDs in Virgo and Fornax (VUCD7 and UCD3), but with its half-light radius of $r_\mathrm{h} = 25.4$ pc, it is the most compact object among the highest luminosity UCDs. VUCD7 and UCD3 are known to feature a two-component light profile with an extended faint envelope and a smaller core component (Evstigneeva et al. 2007b), which is also indicated in Fig. 3.11. A weak indication for a faint halo is observed for HUCD1, but not for the other two luminous UCDs. This can be seen in Fig. 3.12, where from from left to right are shown the three brightest UCDs in the sample, and from top to bottom the according PSF model, the object and the residual (object minus PSF model) image. The residuals for HUCD1 are of the order of a few percent of the value of the corresponding science image pixel. However, King profiles are known not to represent well the outer regions of GCs (e.g. McLaughlin & van der Marel 2005), therefore one cannot affirmatively conclude that the observed residual halo of HUCD1 is due to a presence of a second component as for VUCD7 and UCD3.

3.3.2 Kinematics

The majority of the confirmed cluster GCs/UCDs is located in the immediate vicinity of NGC 3311, i.e. within a projected distance of $R = 5'$, or ~ 70 kpc (see Fig. 3.7). In Fig. 3.13, the objects apparent magnitudes and radial velocities are plotted versus the projected distance from NGC 3311. There appears to be a trend that brighter objects are in projection located further away from the central galaxy. This is, however, caused by selection effects, in the sense that the fields in which brighter objects have been selected reach further out in radius (cf. Fig. 3.1 and Sect. 3.1.1).

In order to clean the sample, an outlier rejection method was applied to the data as described in Schuberth et al. (2010). This method is based on the tracer mass estimator by Evans et al. (2003). In a first step, the quantity

$$m_N = \frac{1}{N} \sum_{i=1}^{N} v_i^2 \cdot R_i \tag{3.2}$$

is calculated, where v_i are the velocities of the considered objects, relative to the mean velocity $v_\mathrm{sys} = 3717$ km s^{-1} of the entire sample. R_i are the projected distances from NGC 3311, and N is the number of objects. Then, in an iterative process, the object with the largest contribution to m_N, i.e. $\max(v^2 \cdot R)$, is removed and m_N is again calculated for the remaining $N - 1$ objects. In this way, 5 outliers were identified (open symbols in Fig. 3.13).

The mean radial velocity $\bar{v}_\mathrm{rad}$ and the dispersion σ of the full and the cleaned sample were determined with the maximum likelihood estimator function `fitdistr`, which is implemented in the R-statistics software[5]. The values for $\bar{v}_\mathrm{rad}$ and σ before and after applying the outlier rejection method are listed in Table 3.3. The table also gives the dispersion σ_PM, as returned by the Pryor & Meylan (1993) estimator. This estimator additionally

---

[5]Venables & Ripley (2002), http://www.r-project.org.
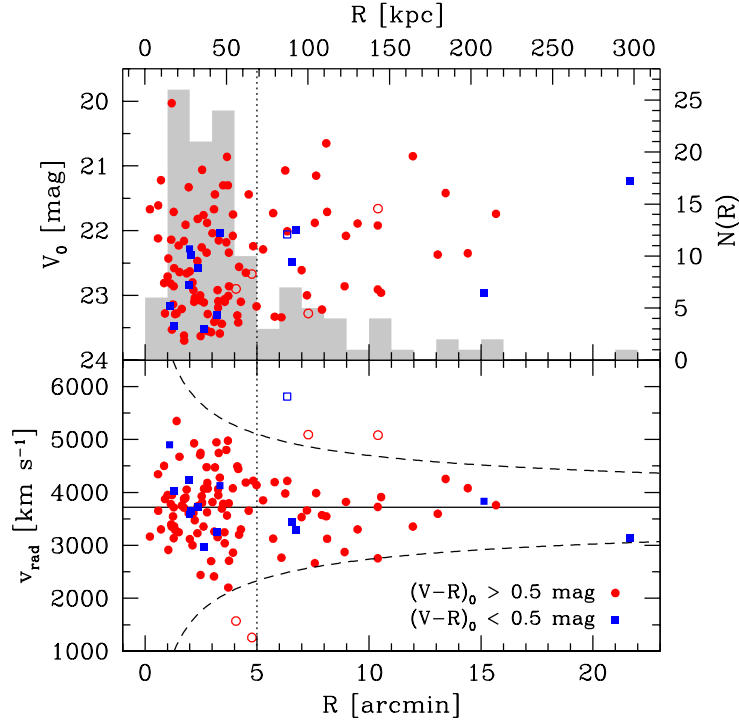
Fig. 3.13. Apparent magnitude V_0 and radial velocity v_{rad} of confirmed cluster GCs/UCDs as a function of R, the projected distance from NGC 3311. The histogram in the *upper panel* shows the number counts in radial bins of $1'$ width. The dashed curves in the *lower panel* envelope the objects that remain after applying the rejection algorithm (see text for details). They are of the form $v_{\mathrm{env}}(R) = v_{\mathrm{sys}} \pm \sqrt{C_{\mathrm{max}}/R}$, where C_{max} is the product $v^2 \cdot R$ for the first object that is not rejected, and v_{sys} is the mean radial velocity of all objects (solid line). Open symbols denote the rejected objects. The vertical dotted line divides the inner from the outer sample.

takes into account the individual measurement errors, i.e. the velocities are weighted by their respective uncertainties.

Mean radial velocities

The radial velocity distributions of the entire GC/UCD population, the red and the blue sub-population (see Sect. 3.3.1 and Fig. 3.9) are shown in Fig. 3.14. Each population is also sub-divided into a central population ($0' < R < 5'$) and an outer population ($R > 5'$). The mean radial velocities of the different GC/UCD samples are consistent with the range of radial velocities reported for NGC 3311 in the literature, i.e. $3700 \lesssim v_{\mathrm{rad}} \lesssim 3850$ km s^{-1} (e.g. Postman & Lauer 1995; Christlein & Zabludoff 2003; Wegner et al. 2003; Misgeld et al. 2008). This suggests that the GC/UCD system is dynamically rather associated to the cD galaxy NGC 3311, instead of belonging to the close-by giant elliptical galaxy NGC 3309, which has a significantly higher radial velocity of $\sim$4100 km s^{-1} (e.g. Christlein & Zabludoff 2003; Wegner et al. 2003; Misgeld et al. 2008). This result is supported by a detailed photometric study of the globular cluster system around NGC 3311 and NGC 3309 (Wehner et al.

Table 3.3. Mean radial velocities $\bar{v}_{\mathrm{rad}}$ and dispersions σ of the different (outlier cleaned) GC/UCD populations (cf. Fig. 3.14 and Fig. 3.15). σ_{PM} is the dispersion from the Pryor & Meylan (1993) estimator. The dividing magnitude for the faint and the bright sample is $M_V = -10.75$ mag. [*] Sample after applying the outlier rejection method (Sect. 3.3.2).

Population	N	$\bar{v}_{\mathrm{rad}}$ [km s^{-1}]	σ [km s^{-1}]	σ_{PM} [km s^{-1}]
All	118	3717 ± 65	710 ± 46	706 ± 46
All*	113	3715 ± 56	600 ± 40	596 ± 40
All, $R < 5'$	87	3715 ± 77	718 ± 54	714 ± 55
All*, $R < 5'$	85	3770 ± 69	632 ± 49	629 ± 49
All, $R \geq 5'$	31	3720 ± 123	686 ± 87	682 ± 88
All*, $R \geq 5'$	28	3548 ± 85	450 ± 60	444 ± 61
Red	104	3698 ± 69	705 ± 49	701 ± 49
Red*	100	3716 ± 61	611 ± 43	608 ± 44
Red, $R < 5'$	78	3702 ± 83	735 ± 59	731 ± 59
Red*, $R < 5'$	76	3762 ± 74	642 ± 52	639 ± 52
Red, $R \geq 5'$	26	3685 ± 119	607 ± 84	603 ± 85
Red*, $R \geq 5'$	24	3569 ± 96	471 ± 68	465 ± 69
Blue	14	3856 ± 195	729 ± 138	726 ± 138
Blue*	13	3706 ± 141	507 ± 99	502 ± 100
Blue, $R < 5'$	9	3830 ± 180	539 ± 127	535 ± 128
Blue, $R \geq 5'$	5	3902 ± 439	981 ± 310	920 ± 268
Blue*, $R \geq 5'$	4	3425 ± 129	257 ± 91	247 ± 94
Faint	58	3697 ± 107	817 ± 76	...
Bright	60	3735 ± 76	588 ± 54	...
Faint*	55	3755 ± 93	689 ± 66	...
Bright*	58	3676 ± 65	499 ± 46	...
Faint, $R < 5'$	49	3710 ± 119	833 ± 84	...
Bright, $R < 5'$	38	3722 ± 87	535 ± 61	...
Faint*, $R < 5'$	47	3808 ± 102	699 ± 72	...
Bright*, $R < 5'$	38	3722 ± 87	535 ± 61	...

2008). The authors show that the GC system of NGC 3311 is completely dominant in terms of specific frequency S_N.

Figures 3.7 and 3.13 show that the outer GCs/UCDs are spaciously distributed between 70 and 200 kpc away from the cluster centre. Only three of these objects are in projection located close to a major cluster galaxy. The full sample of 31 objects has a mean radial velocity which is consistent with the systemic velocity of NGC 3311, while the outlier-cleaned sample (28 objects) has a ~ 170 km s^{-1} lower mean radial velocity. However, both values agree within their uncertainties. These results suggest that most of the outer objects also belong to the NGC 3311 GC system. This is consistent with a study of the
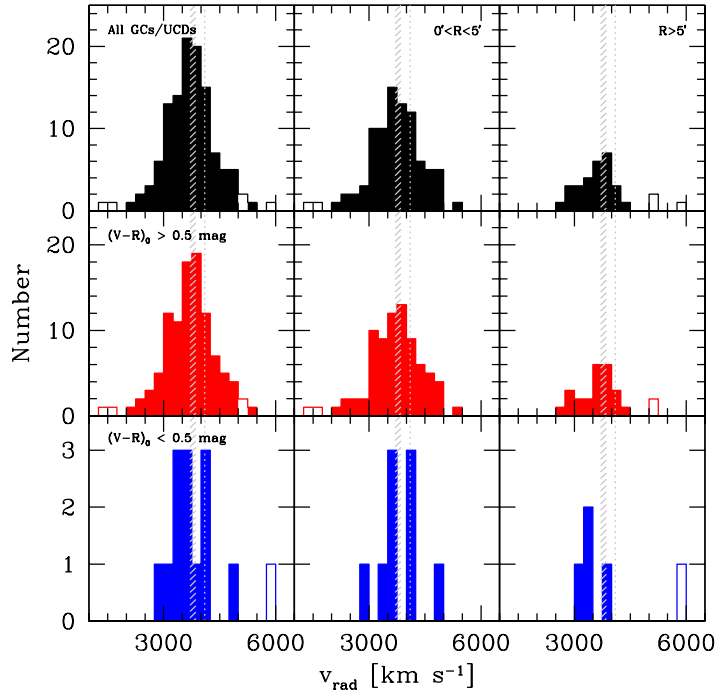
Fig. 3.14. Radial velocity distribution of all identified GCs/UCDs (*top left panel*), the red sub-population (*middle left panel*), and the blue sub-population (*bottom left panel*). Each population is radially binned in the panels of the *middle column* ($0' < R < 5'$) and the *right column* ($R > 5'$). In all panels, the open histogram represents the rejected objects, according to Fig. 3.13. The grey dashed area marks the range of radial velocities reported for NGC 3311 in the literature. The dotted vertical line indicates the systemic velocity of NGC 3309 at $\sim$4100 km s^{-1}.

GC system of NGC 1399, the central galaxy of the Fornax cluster, where its GC system could be traced out to a distance of $\sim$ 250 kpc (Bassino et al. 2006).

Velocity dispersions

In most of the cases, the two velocity dispersions (σ and σ_{PM}) given in Table 3.3 do not differ from each other by more than 6 km s^{-1}. The velocity dispersions of both the inner and the outer populations (without outlier rejection) are with $\sim$ 700 km s^{-1} comparable to what Christlein & Zabludoff (2003) found for the Hydra I cluster velocity dispersion, i.e. $\sigma = 724 \pm 31$ km s^{-1}. Naturally, the velocity dispersions of the outlier-cleaned samples are always lower than those of the full samples. However, removing the three objects above 5000 km s^{-1} and with distances $80 < R < 150$ kpc (see Fig. 3.13) would lead to a considerable drop in the velocity dispersion from $\sim$ 700 km s^{-1} to $\sim$ 450 km s^{-1} (cf. Table 3.3). It is, however, not possible to unambiguously determine which objects at distances larger than 70 kpc dynamically belong to a certain cluster galaxy, or rather react to the overall cluster potential. In the first case, a smaller velocity dispersion compared to the cluster galaxy velocity dispersion would be expected. This has for example been

observed for a sample of UCDs in the Coma cluster core (Chiboucas et al. 2010). If, on the other hand, the majority of the outer GCs/UCDs belongs to an intra-cluster population, one would expect the velocity dispersion to be of similar order to the velocity dispersion of the cluster galaxies, which is about 800 km s^{-1} at 100 kpc (Lokas et al. 2006). Since the GC/UCD velocity dispersion at distances larger than 70 kpc is statistically less well defined than for smaller distances, one cannot favour one of these scenarios. This holds for the full sample as well as for the red sub-sample. Due to the low number of objects, the values for the blue sub-populations are highly uncertain and do not allow a deeper analysis.

In Fig. 3.15, the velocity dispersion σ of bright and faint objects is compared by splitting the GC/UCD sample at six different magnitudes around $M_V = -11$ mag. This is done for both the full sample and the outlier-cleaned sample. Additionally, the same analysis is done only for objects within 5′ around NGC 3311 (see the lower two panels of Fig. 3.15).

In both the full and the outlier-cleaned sample, bright GCs/UCDs have a lower velocity dispersion than fainter objects. This is true for dividing magnitudes $M_V \lesssim -10.5$ mag, and it is most pronounced at $M_V = -10.75$ mag, at which also the sample sizes are almost identical. At this magnitude, the σ-values differ by more than 200 km s^{-1} ($\sim 3\sigma$ significance), and up to 300 km s^{-1} ($\sim 4\sigma$ significance) for objects with $R < 5'$ (see also Table 3.3). The differences for the outlier-cleaned samples (full and inner sample) are smaller, but still more than 160 km s^{-1}. At fainter dividing magnitudes the differences are not any longer significant.

At first view, the lower velocity dispersion of the bright sample might be explained by the selection effects described above (Sect. 3.3.2): due to the configuration of the VIMOS pointings (Fig. 3.1), bright objects are preferentially probed at larger projected distances to NGC 3311. At the same time, these objects exhibit a lower velocity dispersion, as can be seen in Fig. 3.13 and Table 3.3. However, when only regarding objects within 5′ around NGC 3311, the difference in σ is even larger and cannot only be explained by selection effects. The implications of this finding are discussed in more detail in Sect. 3.4.

Rotation

In order to further investigate the dynamical properties of the NGC 3311 GC system, the sample is restricted to objects within a projected distance of 5′ and with radial velocities $\pm 2\sigma$ around the mean of this sample. Then, their radial velocity is plotted as a function of their azimuthal position in the projected sky (Fig. 3.16). If the GC system was rotating as a whole, a sine pattern of the form

$$v_{\rm rad}(\Theta) = v_{\rm sys} + A_{\rm rot} \cdot \sin(\Theta - \Theta_0), \tag{3.3}$$

is expected in such a diagram, with $v_{\rm sys}$ being the mean radial velocity of the sample, $A_{\rm rot}$ the rotation amplitude and Θ_0 the projected rotation axis. It turns out that a meaningful fit to the data is not possible, neither to the individual data points nor to the binned data. The small sample size (only 83 objects) and a significant incompleteness of the sample at $\Theta \sim 65°$ and $\Theta \sim 200°$ prevents a deeper analysis.
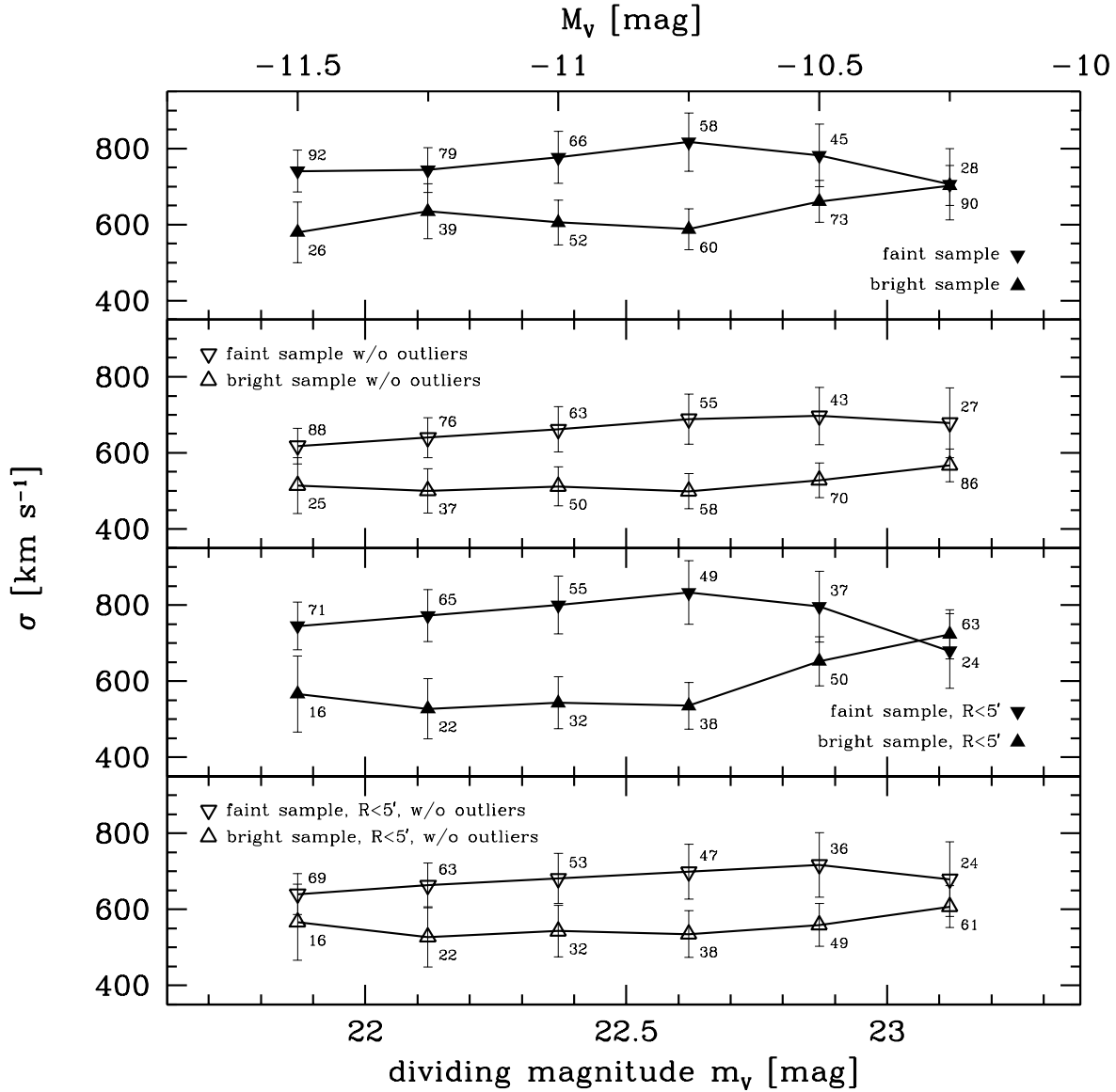
Fig. 3.15. Velocity dispersion σ of a bright and a faint sample as a function of the dividing magnitude m_V. The upper two panels show objects in the full radial range, the lower two panels only show objects with $R < 5'$ (cf. Fig. 3.13). The number of objects contained in the bright/faint sample is indicated next to each data point. The comparison is done for both the full sample (filled symbols) and the outlier-cleaned sample (open symbols).

3.4 Discussion and conclusions

With two extensive spectroscopic surveys it was confirmed that the core of the Hydra I galaxy cluster contains a large population of at least 50 UCDs, as it has been presumed on the basis of earlier photometric studies (Wehner & Harris 2007; Wehner et al. 2008).
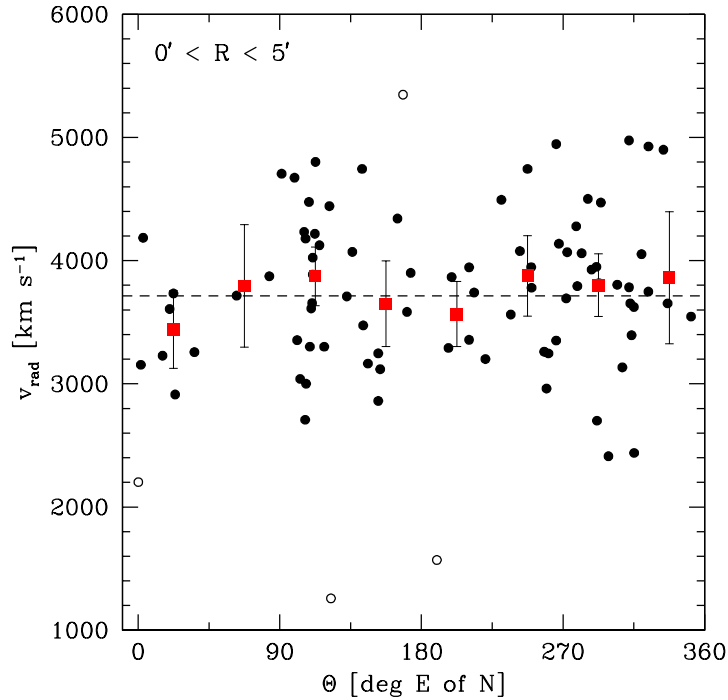
Fig. 3.16. Radial velocity $v_{\rm rad}$ as a function of azimuthal position Θ measured in degrees East of North on the projected sky. Filled circles are all objects within a projected radial distance of $R = 5'$ to NGC 3311. Open circles are objects that deviate more than 2σ from the mean radial velocity of the sample (dashed line) The red filled squares give the mean radial velocity of the objects in bins of 45 degrees. The error bars represent the 90% confidence interval of the mean.

The presence of the very pronounced diffuse light component of NGC 3311 implies that environmental effects have been very important in shaping the central region of the Hydra I cluster, probably more than in the case of the Fornax, Virgo and Centaurus clusters. The dust structure in the center of NGC 3311 is a clear evidence for a recent interaction with a gas-rich galaxy (see e.g. Fig. 3.17 and Grillmair et al. 1994). Together with the large number of UCDs, this strengthens the idea of an interaction driven UCD formation process in Hydra I, in which several UCDs are the remnant nuclei of dwarf galaxies whose stellar envelopes were stripped off during interaction with their host galaxy or galaxy cluster (Bekki et al. 2003).

This hypothesis is supported by the similar luminosities, colours and sizes of UCDs and nuclei of dwarf galaxies (e.g. Côté et al. 2006). Many of the confirmed Hydra I UCDs have much brighter magnitudes than UCD candidates previously identified in photometric studies (see Sect. 3.3.1). While the latter might rather represent the bright end of the globular cluster luminosity function (cf. Fig. 3.6), some of the brighter objects might be nuclei of stripped dwarf galaxies. At magnitudes brighter than $M_V \sim -12$ mag (see Figs. 3.8 and 3.10), objects are found that extend the red GC population towards higher

Fig. 3.17. Colour composite image of the dust lane in the core of NGC 3311 with HST/WFPC2 $F555W$ and $F814W$ filters. The field of view is $\sim 35 \times 35$ arcsec.

luminosities, as well as objects with rather blue colours, which coincide with nuclei of dwarf galaxies in the colour-magnitude diagram.

Norris & Kannappan (2011) suggested a general scheme of GC/UCD formation and the connection to galaxy nuclei (see also Da Rocha et al. 2011; Chilingarian et al. 2011). In this picture, objects below $M_V \sim -10$ mag are 'normal' GCs (red and blue) with a common mean size, plus a fraction of low-mass nuclei, indistinguishable from GCs. For magnitudes $-10 \gtrsim M_V \gtrsim -13$ mag , a mass-size and a mass-metallicity relation (the 'blue tilt') is observed (e.g. Haşegan et al. 2005; Mieske et al. 2010). UCDs (or giant globular clusters), extending the globular cluster luminosity function, as well as giant and dwarf nuclei populate this luminosity regime, the latter having on average bluer colours. In Hydra I, HUCD9, HUCD18 and HUCD35, all having rather blue colours, might be examples of such stripped dwarf galaxy nuclei. Even brighter (more massive) objects are expected to be exclusively stripped nuclei. Here, HUCD1 is the only object that meets this criterion. For the case of Hydra I, wide-field photometry, deeper and more accurate than the VIMOS photometry, would be required to perform a robust investigation of the practicability of this classification scheme.

An explanation for the difference in velocity dispersion of bright and faint GCs/UCDs (see Fig. 3.15) may be that the population of bright GCs/UCDs exhibits a steeper number density profile than the fainter population. This would be plausible in a scenario, where the brightest clusters formed in violent starbursts, which naturally occurred with higher

probability near the center of the galaxy cluster than at large radii. The different velocity dispersions would then be a simple consequence of the Jeans-equation, like the different dispersions of blue and red GCs in NGC 1399 (Richtler et al. 2004; Schuberth et al. 2010). A change in the number density profile would not be visible in the distribution of the slits in the spectroscopic surveys, which do not represent the true spatial distribution of the objects. A complete photometric sample over a larger radial range would be required for this kind of analysis. The study of Wehner et al. (2008) reaches out to only $3'$, and the authors do not comment on possible differences in the number density profiles of bright and faint objects.

Another, related view is that the dispersion of the fainter population may be boosted by objects on highly elongated orbits with large clustercentric distances. In the NGC 1399 system, objects with very high individual velocities are found, suggesting apogalactic distances as high as 400 kpc. Those objects may dynamically be assigned to the entire cluster rather than to the central galaxy (Richtler et al. 2004; Schuberth et al. 2010). Also the Hydra I data show that the objects with the highest individual velocities ($v_{\rm rad} \gtrsim 4900$ km s^{-1}) tend to be faint. However, more radial velocities would be necessary for a more detailed interpretation.

Chapter 4

The early-type dwarf galaxy population of the Centaurus cluster

Except for Sect. 4.3, this chapter is based on the publication
Misgeld, I., Hilker, M., & Mieske, S. 2009, A&A, 496, 683

In the following, the early-type dwarf galaxy population of the Centaurus cluster is studied. As for the Hydra I cluster (Chapter 2), the study is based on deep VLT/FORS1 images of the core region of the cluster. In Sect. 4.1 the observations, the sample selection and the photometric analysis of early-type dwarf galaxy candidates are discussed. The results of the photometric survey are presented in Sect. 4.2, while first results of a large spectroscopic follow-up survey are given in Sect. 4.3. The findings are summarized and discussed in Sect. 4.4.

The Centaurus cluster (Abell 3526), which is categorised as a cluster of richness class zero and Bautz-Morgen type I/II (Abell 1958; Bautz & Morgan 1970), is the dominant part of the Centaurus-Hydra supercluster (da Costa et al. 1986, 1987). It is characterised by an ongoing merger with an in-falling sub-group and irregular X-ray isophotes (Churazov et al. 1999; Furusho et al. 2001). The main cluster component is Cen30 with NGC 4696 at its dynamical centre, whereas Cen45 is the in-falling sub-group with NGC 4709 at its centre (Lucey et al. 1986; Stein et al. 1997). Figure 4.1 shows a DSS image of the central region of the Centaurus cluster with the 7 VLT/FORS1 fields indicated (see also Fig. 4.2).

Mieske et al. (2005a) derived the distance to Centaurus by means of surface brightness fluctuation (SBF) measurements. They found the SBF-distance to be 45.3 ± 2.0 Mpc ($(m - M) = 33.28 \pm 0.09$ mag). Tonry et al. (2001), however, measured a significantly shorter distance of 33.8 Mpc, which may partially be attributed to selection effects (see discussion in Mieske & Hilker 2003). For 78 cluster galaxies, a mean redshift of $v_{\rm rad} = 3656$ km s^{-1} was determined in Chiboucas & Mateo (2006). This corresponds to a distance of 50.8 ± 5.6 Mpc, assuming $H_0 = 72 \pm 8$ km s^{-1} Mpc^{-1} (Freedman et al. 2001), and agrees with the SBF-distance within the errors. Throughout this chapter, a Centaurus distance
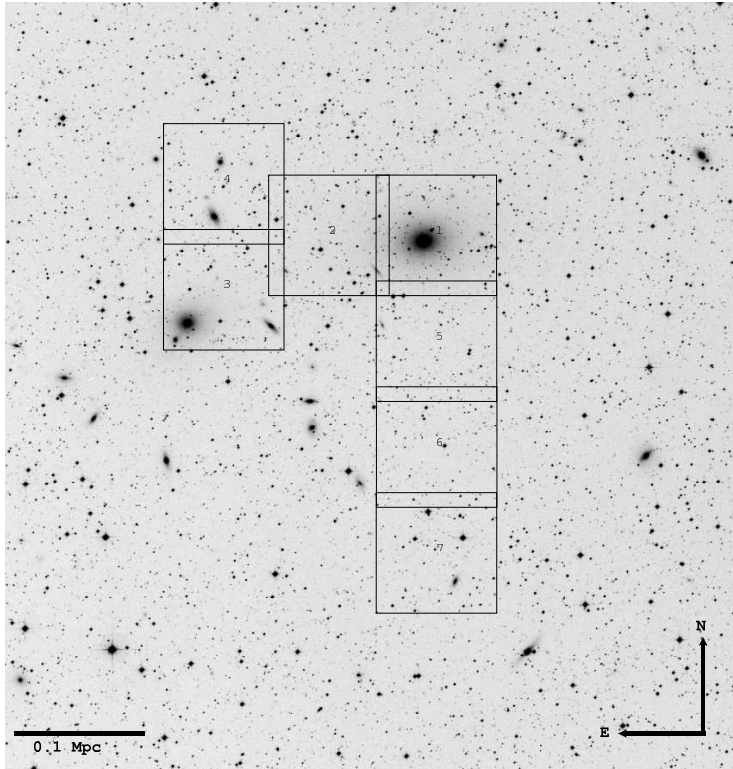
Fig. 4.1. $45' \times 45'$ (594×594 kpc at the cluster distance) image of the Centaurus cluster, extracted from the Digital Sky Survey (DSS). The squares represent the fields observed with VLT/FORS1 (cf. Fig. 4.2).

modulus of $(m - M) = 33.28$ mag is adopted (Mieske et al. 2005a), corresponding to a scale of 220 pc/arcsec.

4.1   Observations and sample selection

The observations were executed in a service mode run at the Very Large Telescope (VLT) of the European Southern Observatory (ESO observing programme 67.A-0358, PI: M. Hilker). Seven fields in the central part of the Centaurus cluster of size $7' \times 7'$ were observed in Johnson V and I filters, using the instrument FORS1 in imaging mode. The fields cover the central part of the Centaurus cluster with its sub-components Cen30 and Cen45, which are centred on NGC 4696 and NGC 4709, respectively (see Figs. 4.1 and 4.2). The exposure time was 4×373 s in V and 9×325 s in I. The seeing was excellent, ranging between $0.4''$ and $0.6''$. Additional short images (30 s in both filters) were taken to be able to analyse the brightest cluster galaxies, which are saturated on the long exposures. Furthermore, an eighth (background) field located about $2.5°$ west of NGC 4696 was observed.

The early-type galaxies for this study were selected based on morphology and spectroscopic redshifts. The FORS1 images contain 21 spectroscopically confirmed early-type cluster galaxies and one late-type (Sc) cluster galaxy (Jerjen & Dressler 1997; Stein et al.
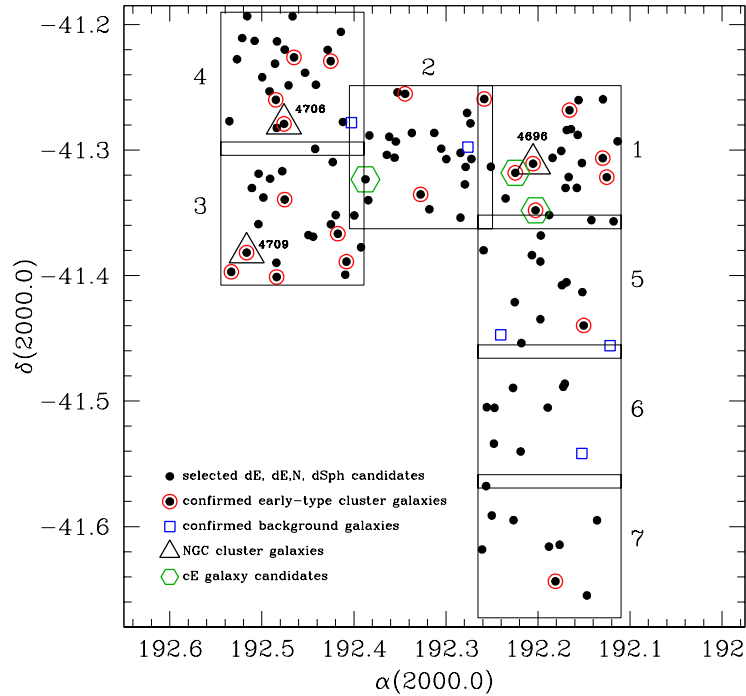
Fig. 4.2. Map of the seven VLT/FORS1 cluster fields (large open squares) with the selected dwarf galaxy candidates, the spectroscopically confirmed cluster members and background galaxies. The major cluster galaxies NGC 4696, NGC 4709 and NGC 4706 are marked by open triangles. Green open hexagons are compact elliptical galaxy (cE) candidates (see Sect. 4.2.5).

1997; Chiboucas & Mateo 2006, 2007; Mieske et al. 2007b). The cluster membership criterion was adopted to be $1700 < v_{\rm rad} < 5500$ km s^{-1}.

In order to identify new early-type dwarf galaxy candidates on the images, the same strategy was pursued as in the investigations of the dwarf galaxy populations in Fornax and Hydra I (Hilker et al. 2003; Mieske et al. 2007a; Misgeld et al. 2008). It is a combination of visual inspection and the use of SExtractor (Bertin & Arnouts 1996) detection routines (see also Sect. 2.2.1). First, several simulated Local Group (LG) dEs and dSphs (projected to the Centaurus cluster distance) were added to the images. Their magnitudes and central surface brightnesses were adopted according to the relations found by Grebel et al. (2003) and McConnachie & Irwin (2006). Afterwards, the images were inspected by eye, and candidate cluster dwarf galaxies were selected by means of their morphological resemblance to the simulated galaxies. The main selection criterion was a smooth surface brightness distribution and the lack of substructure or spiral arms. This first search resulted in the identification of 89 previously uncatalogued dE/dSph candidates, from which four are shown in Fig. 4.3.

In a second step, the SExtractor detection routines were used to quantify the detection completeness in the data (see Sect. 4.2.2), and to find more dwarf galaxy candidates, in particular at the faint magnitude and surface brightness limits. The detection sensitive SExtractor parameters were optimised such that a maximum number of objects from the by-
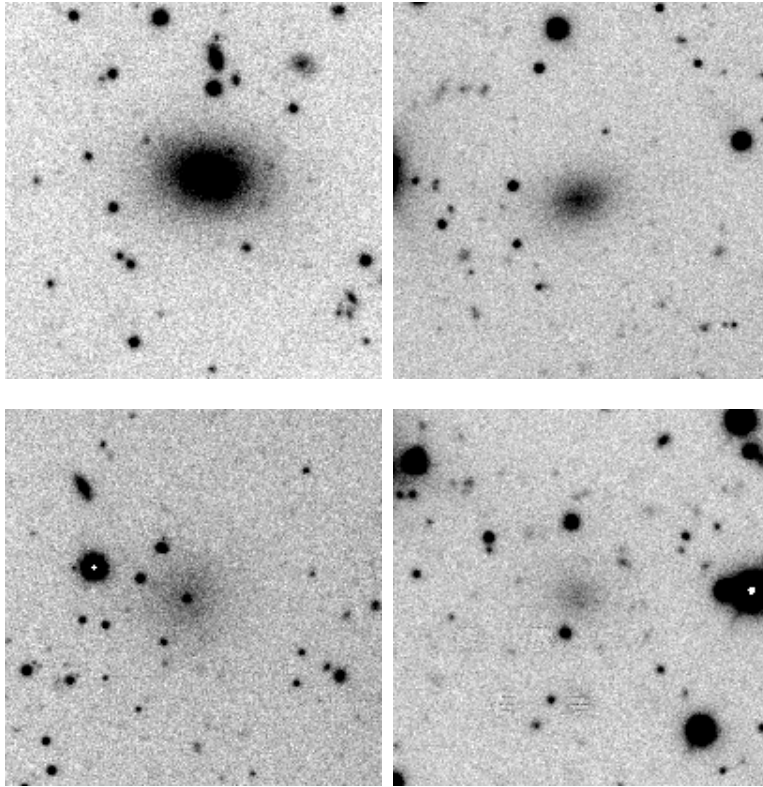
Fig. 4.3. Thumbnail images of four cluster dwarf galaxy candidates that fulfil the selection criteria (two dEs, one dE,N and one dSph). The objects' absolute magnitudes from the left to the right and from the top to the bottom are: $M_V = -14.4, -13.3, -13.2, -12.0$ mag, assuming a distance modulus of $(m - M) = 33.28$ mag (Mieske et al. 2005a). The thumbnail sizes are $40'' \times 40''$ (8.8×8.8 kpc at the cluster distance).

eye catalogue was recovered by the programme. Only 12 of the 89 obvious by-eye detections were not recovered, mostly due to their position close to another bright object or close to the image border. The search for new dwarf galaxy candidates was focused on those sources in the SExtractor output catalogue whose photometric parameters matched the parameter range of the simulated dwarf galaxies. For this, different cuts in the SExtractor output-parameters `mupeak`, `area` and `fwhm` were applied to constrain the output parameter space to the one found for the simulated LG dwarf galaxies (see also Sect. 2.3.4). Thus, barely resolved and apparently small objects with high central surface brightnesses were rejected, both being likely background galaxies. The applied cuts are described in detail in Sect. 4.2.2. In this way, 8 additional objects in the magnitude range $-11.0 < M_V < -9.4$ mag were found and added to the by-eye catalogue. On the background field, neither the visual inspection nor the SExtractor analysis resulted in the selection of an object.

In addition, five spectroscopically confirmed background early-type galaxies that are located in the observed fields were added to the photometric sample, in order to be able to compare their photometric properties with the ones of the objects in the by-eye catalogue. In total, the sample contains 123 objects, for which Fig. 4.2 shows a coordinate map.

4.1.1 Photometric analysis

For each selected object, thumbnail images were created with sizes extending well into the sky region (see Fig. 4.3). On these thumbnails the sky subtraction was performed, and elliptical isophotes were fitted to the galaxy images, using the IRAF-task `ellipse` in the `stsdas` package. During the fitting procedure the centre coordinates, the position angle and the ellipticity were fixed, except for some of the brightest cluster galaxies ($V_0 \lesssim 15.5$ mag) where the ellipticity or both the ellipticity and the position angle considerably changed from the inner to the outer isophotes. In those cases one or both parameters were allowed to vary.

The total apparent magnitude of each object was derived from a curve of growth analysis. The central surface brightness was determined by fitting an exponential as well as a Sérsic (1968) law to the surface brightness profile. The inner $1''$ (about 1.5 seeing disks) and the outermost part of the profile, where the measured surface brightness was below the estimated error of the sky background, were excluded from the fit. Corrections for interstellar absorption and reddening were taken from Schlegel et al. (1998), who give $A_V = 0.378$ mag and $E(V - I) = 0.157$ mag for the coordinates of NGC 4696. These values were adopted for all of the observed fields. Zero points, extinction coefficients and colour terms for the individual fields and filters are listed in Table A.3 in the appendix.

4.2 Global photometric and structural parameters

In this section the results of the photometric analysis are presented. In Sect. 4.2.1 the colour–magnitude and the magnitude-surface brightness relation of the Centaurus early-type dwarf galaxies are address and utilised to facilitate the distinction of cluster and background galaxies. The galaxy luminosity function of probable cluster members is studied in Sect. 4.2.2. The structural parameters of the cluster galaxies, as obtained from Sérsic fits to the surface brightness profiles, are presented in Sect. 4.2.3. Table A.4 in the appendix summarises the obtained photometric parameters of the 92 probable Centaurus cluster early-type galaxies.

4.2.1 Fundamental scaling relations

Figure 4.4 shows a colour–magnitude diagram of the sample of early-type galaxies, as defined in Sect. 4.1. Spectroscopically confirmed cluster galaxies ($V_0 \lesssim 18$ mag) form a colour–magnitude relation (CMR) in the sense that brighter galaxies are on average redder. This sequence continues down to the faint magnitude limit of the survey ($M_V \sim -10$ mag), which is comparable to the absolute magnitudes of the LG dwarf galaxies Sculptor and Andromeda III (Grebel et al. 2003; McConnachie & Irwin 2006). The larger scatter at faint magnitudes is consistent with the larger errors in $(V - I)_0$. The mean measured error in $(V - I)_0$ is 0.03, 0.08 and 0.13 mag for the three magnitude intervals indicated in Fig. 4.4. The intrinsic scatter of the datapoints in the same intervals is 0.06, 0.09 and 0.14 mag, respectively, only marginally larger than the measurement errors. The data do
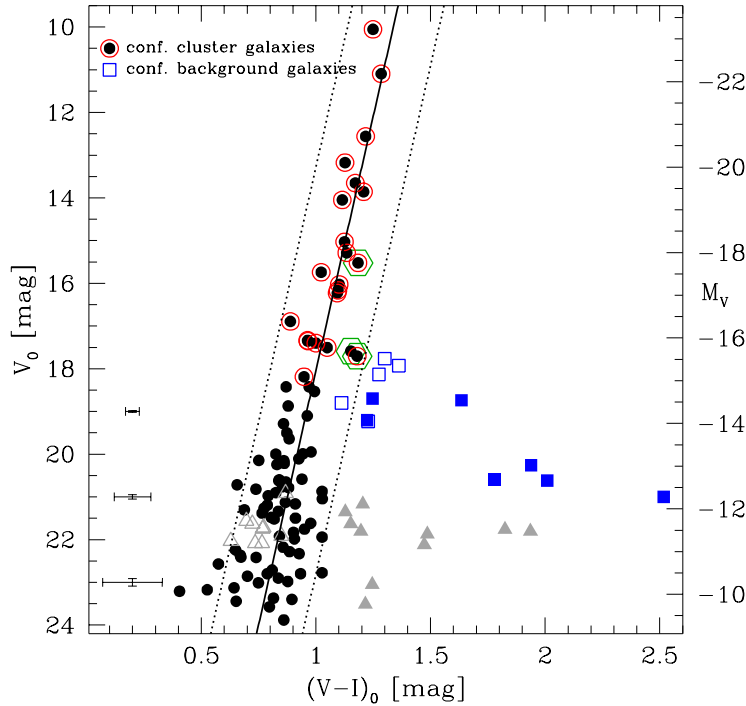
Fig. 4.4. Colour–magnitude diagram of early-type galaxies in the Centaurus cluster. Black dots are probable cluster galaxies, selected by their morphology. Red open circles (blue open squares) mark spectroscopically confirmed cluster members (background galaxies). Blue filled squares and grey filled triangles are probable background objects (see text for details). Grey open triangles are objects which do not follow the magnitude-surface brightness relation (cf. Fig. 4.5). Green open hexagons mark the candidates for compact elliptical galaxies (see Sect. 4.2.5). Typical errorbars are indicated on the left. The solid line is a linear fit to the cluster member candidates (Eq. (4.1)) with its 2σ deviations (dotted lines).

therefore not require an increase of metallicity or age spread among individual galaxies at faint luminosities, compared to brighter luminosities. For the linear fit, each data point was weighted by its colour error, resulting in:

$$(V - I)_0 = -0.042(\pm 0.001) \cdot M_V + 0.36(\pm 0.02) \qquad (4.1)$$

with a rms of 0.10. This is in good agreement with the CMRs observed in Hydra I, Fornax, Perseus and the LG (Grebel et al. 2003; Mieske et al. 2007a; Misgeld et al. 2008; Penny et al. 2011). Table 4.1 lists the CMR coefficients for each of those clusters. For consistency, the Hydra I data was re-fitted using the error weighted values, which slightly changes the coefficients given in Sect. 2.3.2.

The CMR can be used as a tool to distinguish cluster from background galaxies. This is important, since the selection of cluster galaxy candidates solely based on morphological criteria can lead to the contamination of the sample with background objects that only resemble cluster dwarf ellipticals. In the bright magnitude range the cluster galaxies are identified by their redshift. In the intermediate magnitude range ($17.8 < V_0 < 21.0$ mag), however, seven objects turn out to be likely background galaxies, although they passed the morphological selection criteria (filled squares in Fig. 4.4). All seven arguable objects have

Table 4.1. Fitting coefficients of the CMR, the magnitude-surface brightness relation, and the power-law slope α of the GLF, with errors given in parentheses.

| | $(V - I)_0 = A \cdot M_V + B$ | | $\mu_{V,0} = C \cdot M_V + D$ | | |
	A	B	C	D	α
Centaurus	-0.042	0.36	0.57	30.85	-1.14
	(0.001)	(0.02)	(0.07)	(0.87)	(0.12)
Hydra I	-0.044	0.36	0.67	31.57	-1.40
	(0.001)	(0.01)	(0.07)	(0.99)	(0.18)
Fornax	-0.033	0.52	0.68	32.32	-1.33
	(0.004)	(0.07)	(0.04)	(1.12)	(0.08)
Perseus	-0.028	0.62	...	...	...
	(0.013)	(0.18)	...	...	...
LG	-0.038	0.48	...	...	...
	(0.008)	(0.10)	...	...	...

de Vaucouleurs (1948) surface brightness profiles (also known as $R^{1/4}$ profiles), typical of giant elliptical galaxies. Five of those objects are too red to be a galaxy at $z \sim 0$, the other two share their position in the CMD with spectroscopically confirmed background galaxies (open squares in Fig. 4.4). Moreover, Fig. 4.9 shows that the confirmed background galaxies as well as the seven likely background objects clearly differ from the cluster galaxies, because of their high central surface brightness and their large Sérsic index. 10 more morphologically selected objects with $V_0 > 21$ mag are considered likely background objects, as their colours are significantly redder than those of other objects in the same magnitude range (see the filled triangles in Fig. 4.4).

For two objects in the sample (C-3-30 and C-1-47, see Table A.4), a colour could not be measured, since they were located close to the image borders, only fully visible on the V-band images. However, they have a typical dE morphology and they fall onto the magnitude-surface brightness relation (Fig. 4.5). They are thus treated as probable cluster dwarf galaxies in the following analyses[1].

In Fig. 4.5, the central surface brightness $\mu_{V,0}$ is plotted against the apparent magnitude V_0 for all objects in the sample, whose surface brightness profiles are well represented by an exponential law. These are all objects with $V_0 > 16.1$ mag (see Table A.4), except for two compact elliptical galaxy candidates, whose properties will be discussed in Sect. 4.2.5. A linear fit to the probable cluster galaxies (black dots) leads to:

$$\mu_{V,0} = 0.57(\pm 0.07) \cdot M_V + 30.85(\pm 0.87) \tag{4.2}$$

with a rms of 0.48. Given that the scatter in the data is much larger than the measured errors in both M_V and $\mu_{V,0}$, the data points are not error weighted. The fit errors were

---

[1]Follow-up spectroscopy confirmed the cluster member status (see Sect. 4.3).
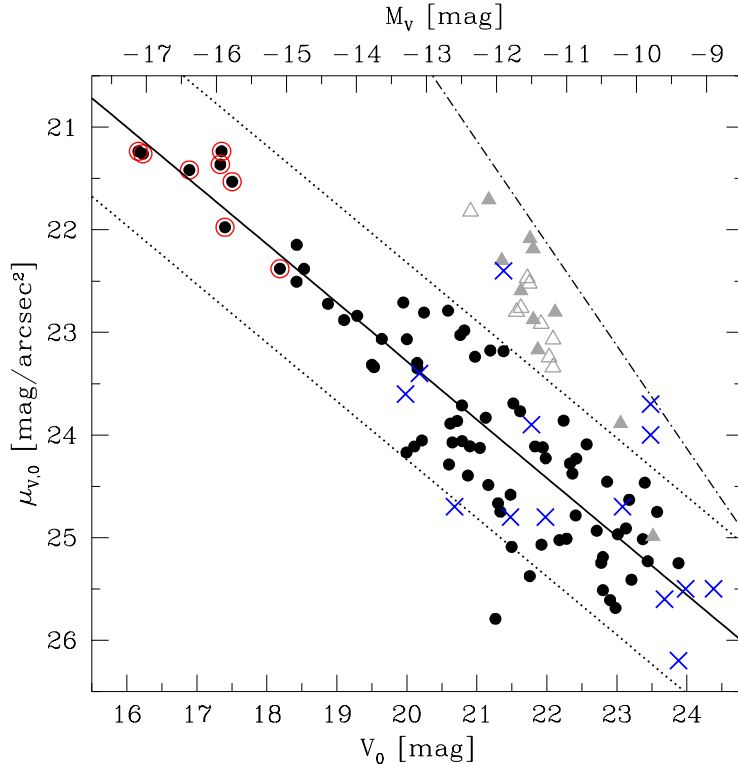
Fig. 4.5. Plot of the central surface brightness $\mu_{V,0}$, as derived from fitting an exponential law to the surface brightness profile, vs. the apparent magnitude V_0 for identified cluster dwarf galaxy candidates. Symbols are as in Fig. 4.4. Errors are comparable to the symbol sizes. The solid line is a linear fit to the black dots (Eq. (4.2)). Dotted lines are the 2σ deviations from the fit. Local Group dEs and dSphs, projected to the Centaurus distance, are given by the blue crosses (data from Grebel et al. (2003) and McConnachie & Irwin (2006)). A scale length of $0.6''$ for an exponential profile, representing the resolution limit of the images, is indicated by the dash-dotted line.

instead derived from random re-sampling of the data points within their measured scatter. The same method was used in Mieske et al. (2007a) for the Fornax dwarfs, and the Hydra I data (Chapter 2) is re-analysed in the same way. The magnitude-surface brightness relations of the three clusters agree within the errors (see Table 4.1).

When projected to the Centaurus distance, LG dwarf galaxies are mostly consistent with the same relation, with a few slightly more compact objects (Grebel et al. 2003; McConnachie & Irwin 2006). The likely background objects from Fig. 4.4 (grey filled triangles) do not follow the relation, but they have central surface brightnesses about 1 mag/arcsec^2 higher than other objects of the same magnitude.

An interesting sub-group of morphologically selected objects is marked by the open triangles. These nine objects are rather compact, having exponential scale lengths of $\lesssim 1''$, close to the resolution limit of the images. Although they lie on the cluster CMR (see Fig. 4.4), they are located more than 2σ away from the magnitude-surface brightness relation – just as the likely background galaxies that were identified by their position aside the CMR. This suggests that these nine questionable objects are in fact background
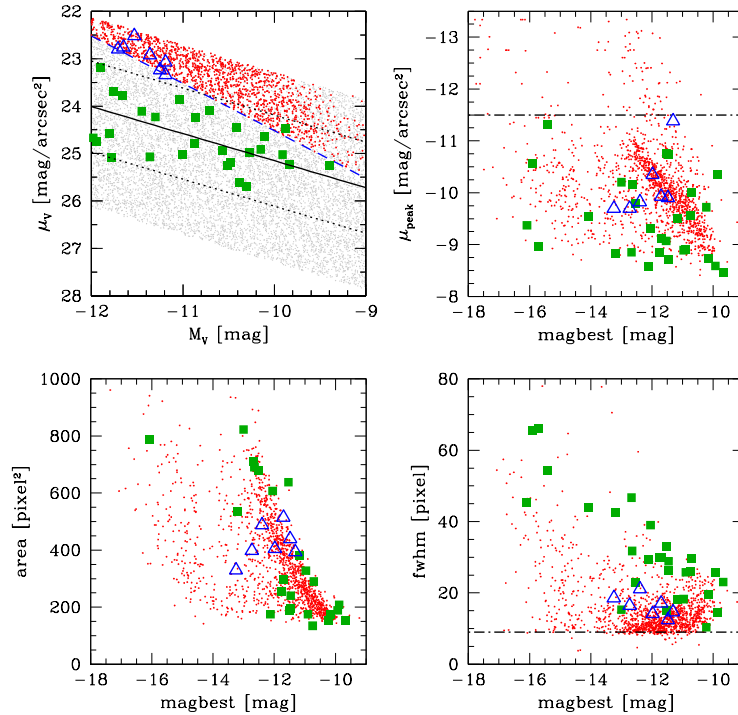
Fig. 4.6. SExtractor output-parameters of recovered simulated galaxies with an exponential scale length $< 1''$ (red dots). *The upper left panel* shows the input parameters absolute magnitude M_V and central surface brightness μ_V of the artificial galaxies (grey dots), together with the probable cluster dwarf galaxies (green solid squares) that were recovered by SExtractor. Equation (4.2) with its 2σ deviations is plotted as in Fig. 4.5. The blue dashed line indicates a scale length of $1''$ for an exponential profile. Blue open triangles are the questionable objects discussed in Sect. 4.2.1. The SExtractor output-parameter `magbest` is plotted against `mupeak` (*upper right*), `area` (*lower left*) and `fwhm` (*lower right*). Dash-dotted lines indicate the global cuts on `mupeak` and `fwhm` (see text for details).

galaxies with colours similar to the cluster galaxies. However, the LG dwarf galaxy Leo I (Grebel et al. 2003) falls into the same parameter range (Fig. 4.5). If these objects were actual cluster galaxies, they would account for about 10% of the whole dwarf galaxies population in the present sample. Given their uncertain nature, it will be analysed in Sect. 4.2.2 how they affect the shape of the galaxy luminosity function. Ultimately, it remains to be clarified by spectroscopic measurements, whether they represent a family of rather compact early-type cluster members or background galaxies.

4.2.2   The dwarf galaxy luminosity function

In order to study the faint-end of the galaxy luminosity function, the detection completeness in the data has to be quantified, and the galaxy number counts have to be corrected to that effect. For this, 10 000 simulated dwarf galaxies were randomly distributed in 500 runs in each of the seven cluster fields, using a C++ code. The background field was left out from this analysis, since no potential dwarf galaxy was identified in this field. The upper left panel of Fig. 4.6 illustrates the input-parameter range of the simulated galaxies,
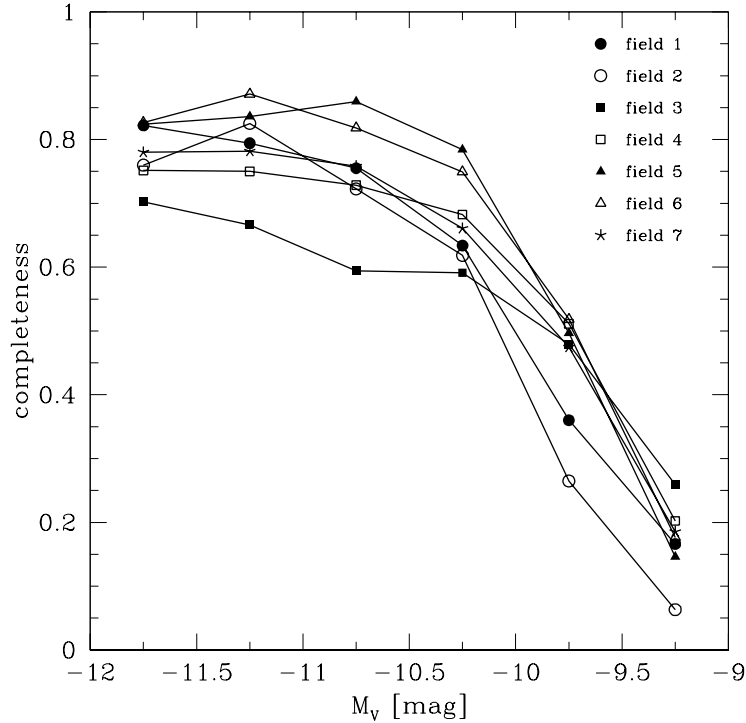
Fig. 4.7. Completeness as a function of magnitude (in 0.5 mag bins) for each of the seven cluster fields (cf. Fig. 4.2).

which extends well beyond the observed parameter space. The artificial galaxies were then recovered by SExtractor, and the SExtractor output-parameters `magbest`, `mupeak`, `area` and `fwhm` were compared with the parameters of the sample of probable cluster dwarf galaxies, as defined in Sect. 4.2.1.

In a first step, the SExtractor (Bertin & Arnouts 1996) star/galaxy separator was used to sort out wrongly recovered foreground stars, requiring `class_star` < 0.05. Aiming at the rejection of high surface brightness and barely resolved background objects, several cuts to other SExtractor output-parameters were applied afterwards. The objects to be rejected were required to have an exponential scale length shorter than $1''$. This is close to the seeing limit of the images, and it is the maximum scale length of the questionable objects from Sect. 4.2.1. The artificial galaxies with scale lengths $< 1''$ define well localised areas in plots of `magbest` versus `mupeak`, `area` and `fwhm` (see Fig. 4.6). Since also some of the previously selected dwarf galaxy candidates scatter into the same areas, only those objects were finally rejected that *simultaneously* occupied the locus of barely resolved galaxies in all three parameters `mupeak`, `area` and `fwhm`. In this way, only one of the previously selected probable cluster dwarf galaxies was missed, but more than 50% of objects with a scale length shorter than $1''$ were rejected. In order to further optimise the rejection of obvious background objects, additional global cuts at the upper limit of `mupeak` and the lower limit of `fwhm` were applied (Fig. 4.6).
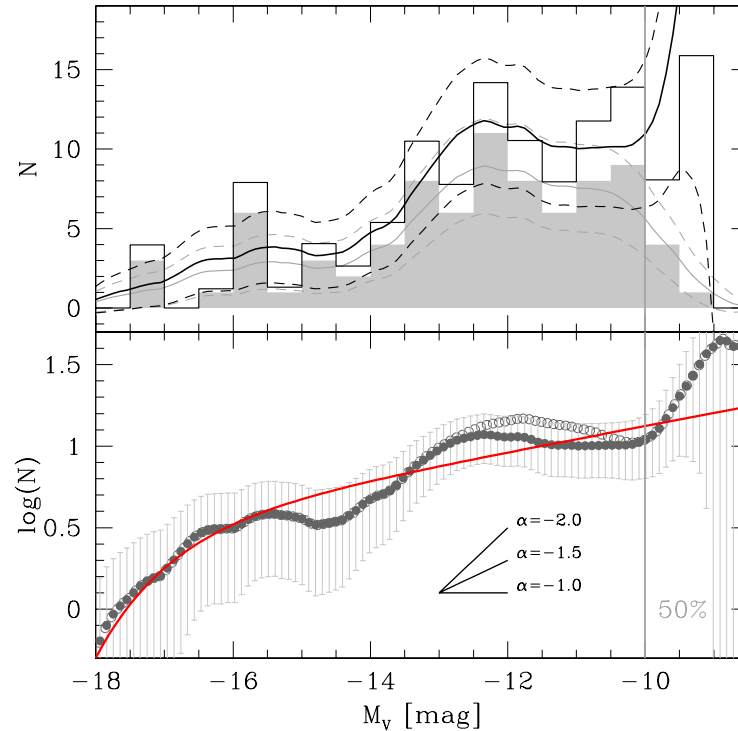
Fig. 4.8. Luminosity function of the Centaurus dwarf galaxies. The shaded histogram in the *upper panel* shows the uncorrected galaxy number counts. The open histogram gives the completeness corrected number counts. The thin grey and thick black curves are binning independent representations of the counts (Epanechnikov kernel with 0.5 mag width). Dashed curves are the 1σ uncertainties. *The lower panel* shows the completeness corrected galaxy number counts in logarithmic representation (filled circles). The best fitting Schechter function (red solid line) is overlaid. Open circles give the galaxy number counts including the questionable objects discussed in Sect. 4.2.1. Three different slopes α are indicated. The 50% completeness limit (averaged over all fields) is given by the vertical line.

Without the application of the cuts, SExtractor recovers 75-85% of the simulated galaxies at $M_V \leq -12$ mag, which reflects the geometrical incompleteness caused by blending. Applying the cuts in `mupeak`, `area` and `fwhm` rejects $\sim 25\%$ more artificial galaxies at $M_V \leq -12$ mag. This fraction is consistent with the fraction of visually classified actual galaxies with $M_V > -12$ mag that are excluded by applying the same cuts (9 out of 36). Given that all visually classified galaxies are included into the GLF, the completeness values for $M_V > -12$ mag are scaled up by 25%, so that they are consistent with the geometrical completeness at $M_V = -12$ mag (see Fig. 4.7).

The completeness corrected galaxy luminosity function for $-17.5 < M_V < -9.0$ mag is shown in Fig. 4.8. Due to the relatively low galaxy number counts (81 in this magnitude range), the GLF is only moderately well represented by a Schechter (1976) function. From the best fitting Schechter function a faint-end slope of $\alpha = -1.08 \pm 0.03$ is derived (excluding galaxies fainter than $M_V = -10$ mag). As the slope α dominates the shape of the GLF for magnitudes $M_V > -14$ mag, also a power-law is fitted to this interval, resulting in $\alpha = -1.14 \pm 0.12$. This characterises best the faint-end slope of the GLF. This result is
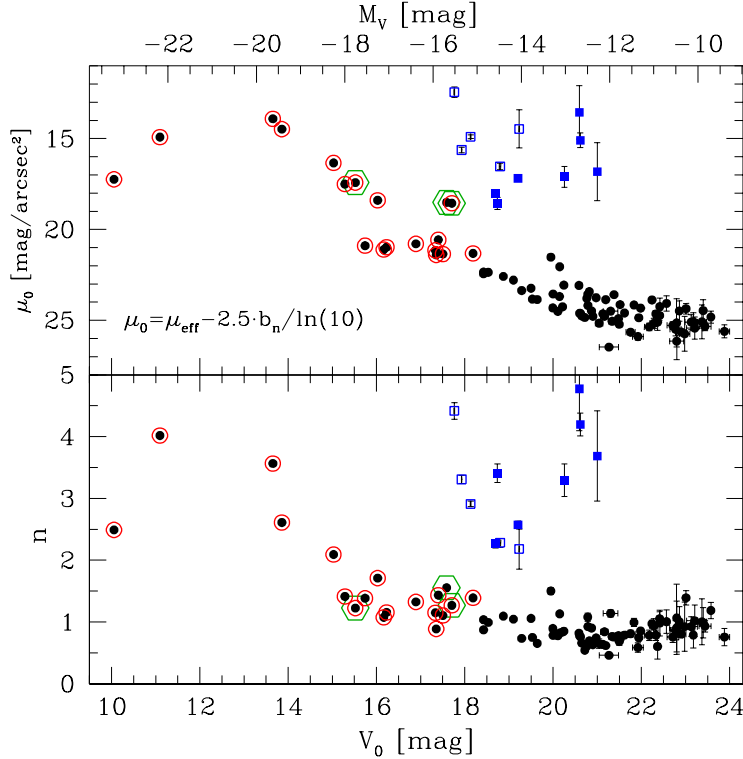
Fig. 4.9. Parameters of the Sérsic fits to the galaxy surface brightness profiles. The top (bottom) panel shows the central surface brightness μ_0 (profile shape index n) plotted vs. the galaxy magnitude. Black dots are all galaxies that were considered cluster members. Spectroscopically confirmed cluster galaxies are marked by red open circles. Blue open (filled) squares are confirmed (likely) background galaxies (cf. Fig. 4.4). The green open hexagons mark the three compact elliptical galaxy candidates (see Sect. 4.2.5).

consistent with the results of Chiboucas & Mateo (2006), who found $\alpha \sim -1.4 \pm 0.2$ for the Centaurus cluster. They used statistical corrections as well as spectroscopic redshifts and surface brightness–magnitude criteria for the construction of the GLF.

The nine questionable objects discussed in Sect. 4.2.1 have absolute magnitudes of $-12.4 < M_V < -11.2$ mag. Including them into the GLF does not significantly change the slope α in the interval $-14 < M_V < -10$ mag (see bottom panel of Fig. 4.8). Fitting a power-law leads to $\alpha = -1.17 \pm 0.12$.

In Table 4.1 the slope α is compared to the ones derived for the Fornax and Hydra I clusters (Mieske et al. 2007a; Misgeld et al. 2008). Also for those clusters α is obtained by fitting a power-law to the faint end of the GLF ($M_V > -14$ mag). With $-1.1 \gtrsim \alpha \gtrsim -1.4$ all slopes are significantly shallower than the predicted slope of ~ -2 for the mass spectrum of cosmological dark-matter haloes (e.g. Press & Schechter 1974; Moore et al. 1999; Jenkins et al. 2001).

4.2.3 Structural parameters from Sérsic fits

In addition to the exponential models, also Sérsic models were fitted to the galaxy surface brightness profiles. The fit parameters central surface brightness μ_0 and profile shape index n are plotted versus the galaxy magnitude in Fig. 4.9. μ_0 is given by $\mu_0 = \mu_{\mathrm{eff}} - 2.5 b_n / \ln(10)$, where μ_{eff} is the effective surface brightness and b_n is approximated by $b_n = 1.9992 n - 0.3271$ for $0.5 < n < 10$ (Graham & Driver 2005, and references therein). Three bright cluster galaxies (C-4-03/NGC 4706, C-3-04 and C-7-07, see Table A.4), morphologically classified as SAB(s)0, SB(s)0 and S0, showed two component surface brightness profiles (bulge + disk), which could not be fitted by a single Sérsic profile. They were excluded from the analysis.

The vast majority of cluster galaxies defines a continuous relation in the μ_0 vs. M_V diagram (top panel of Fig. 4.9). This relation runs from the faintest dwarf galaxies to bright cluster elliptical galaxies ($M_V \sim -20$ mag). This result is consistent with other studies that report on a continuous relation for both dwarf galaxies and massive E/S0 galaxies (e.g. Graham & Guzmán 2003; Gavazzi et al. 2005; Ferrarese et al. 2006; Côté et al. 2008; Misgeld et al. 2008). Only the two brightest galaxies in the sample (NGC 4696 and NGC 4709) deviate from this relation.

The bottom panel of Fig. 4.9 shows that also the profile shape index n continuously rises with the galaxy magnitude for $M_V \lesssim -14$ mag. Only the brightest cluster galaxy, NGC 4696, has an exceptionally low Sérsic index ($n = 2.5$). For $M_V \gtrsim -14$ mag, n basically stays constant with a mean value of 0.85. The spectroscopically confirmed background galaxies as well as the likely background objects in the sample can clearly be identified by their large Sérsic index and their high central surface brightness in comparison to the cluster galaxies. This motivates again the rejection of those object from the cluster galaxy sample. These results agree with former observations of a correlation of the Sérsic index with the galaxy luminosity (e.g. Young & Currie 1994; Infante et al. 2003; Ferrarese et al. 2006; Misgeld et al. 2008).

4.2.4 Galaxy sizes

In Fig. 4.10 the effective radii and absolute magnitudes of the Centaurus early-type galaxies are shown, together with the Hydra I early-type galaxies from Misgeld et al. (2008), galaxies from the ACS Virgo Cluster Survey (ACSVCS, Ferrarese et al. 2006), Local Group dwarf galaxies and known compact elliptical galaxies. References for the LG dwarfs and the cEs are given in the caption. The sizes of the Centaurus galaxies agree very well with the sizes of the Hydra I galaxies and the sizes of bright galaxies ($-20 < M_V < -16$ mag) in both samples are fully consistent with the ones obtained in Ferrarese et al. (2006) for the ACSVCS galaxies. The apparent g-band magnitudes of the ACSVCS galaxies were transformed into absolute V-band magnitudes, using the transformation $V = g + 0.026 - 0.307(g - z)$ mag given in Peng et al. (2006). The transformation is derived from a study of diffuse star clusters around the ACS Virgo galaxies. Since the cluster colours are very similar to those of the host galaxies ($1.1 < (g - z) < 1.6$ mag),
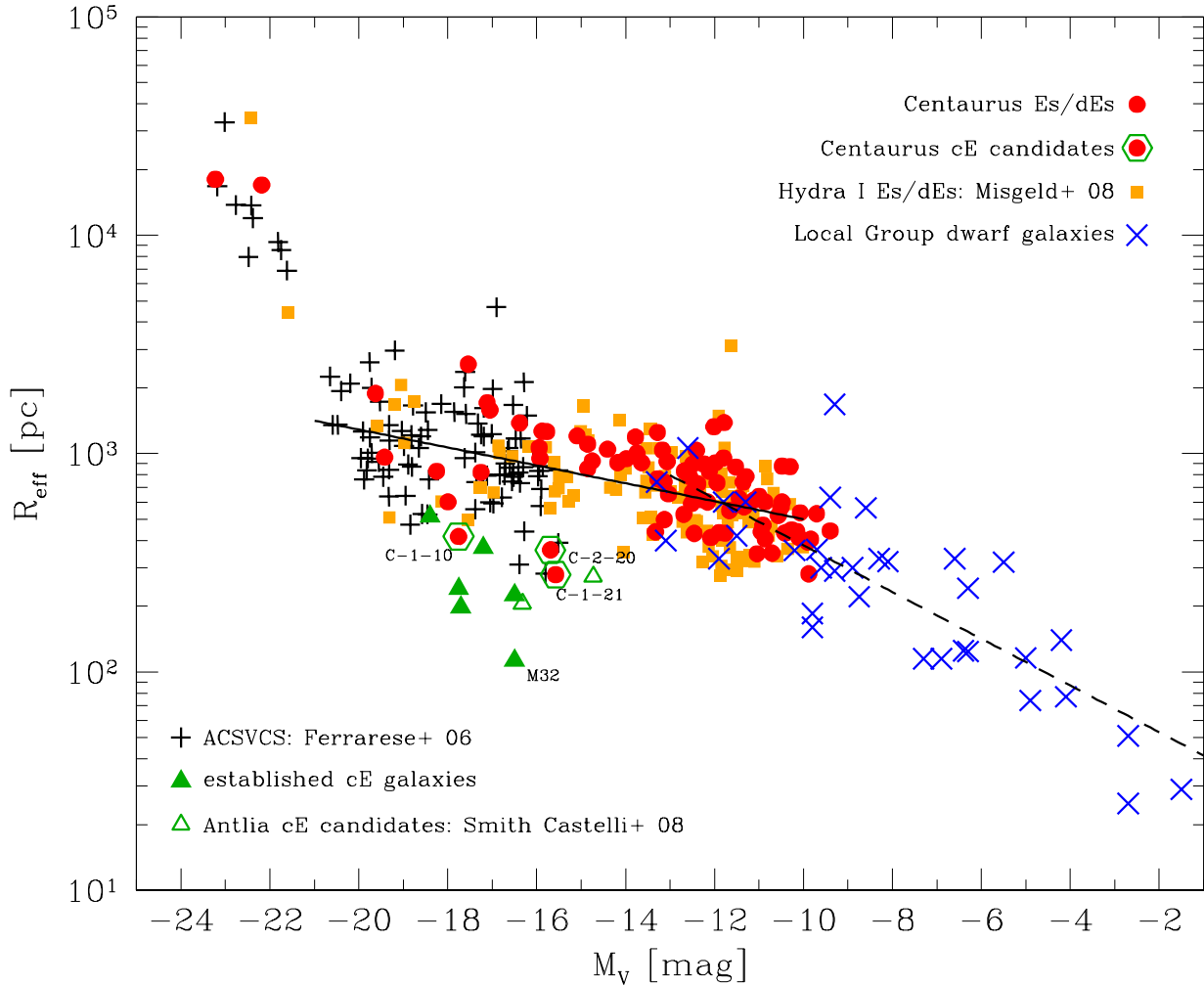
Fig. 4.10. Plot of the effective radius $R_{\rm eff}$ against the absolute magnitude M_V of the Centaurus early-type galaxies in comparison to Hydra I early-type galaxies from Misgeld et al. (2008), galaxies from the ACS Virgo Cluster Survey (Ferrarese et al. 2006), Local Group dwarf galaxies and compact elliptical galaxies. The established cEs are M32 (Bender et al. 1992, 1993; Grebel et al. 2003), A496cE (Chilingarian et al. 2007), NGC 4486B (Kormendy et al. 2009), NGC 5846A (Mahdavi et al. 2005; Smith Castelli et al. 2008b) and the two cEs from Mieske et al. (2005b). The two Antlia cE candidates are taken from Smith Castelli et al. (2008b). Sources for the LG dwarf galaxies are: Grebel et al. (2003) and Gilmore et al. (2007, and references therein) for Fornax, Leo I/II, Sculptor, Sextans, Carina and Ursa Minor; Martin et al. (2008) for Draco, Canes Venatici I/II, Hercules, Leo IV, Coma Berenices, Segue I, Bootes I/II, Ursa Major I/II and Willman I; McConnachie & Irwin (2006) for And I/II/III/V/VI/VII and Cetus; Zucker et al. (2007) for And IX/X; Martin et al. (2006) for And XI/XII/XIII and McConnachie et al. (2008) for And XVIII/XIX/XX. The solid line indicates the size–luminosity relation given by Eq. (4.3), the dashed line traces Eq.(4.4).

the transformation is considered a good approximation for the purposes of this study. A Virgo distance modulus of $(m - M) = 31.09$ mag is adopted, corresponding to a scale of 80.1 pc/arcsec (Mei et al. 2007). For the calculation of the V-band magnitude of the cE galaxy NGC 5846A, $V - R = 0.61$ mag (Fukugita et al. 1995) and the distance

Table 4.2. Photometric and structural parameters of the cE galaxy candidates. References for radial velocities: [a](Stein et al. 1997), [b](Chiboucas & Mateo 2007).

ID	R.A. (J2000.0)	Decl. (J2000.0)	P.A. [deg]	ε	M_V [mag]	$(V-I)_0$ [mag]	μ_0 [mag/arcsec^2]	$R_{\rm eff}$ [pc]	n	$v_{\rm rad}$ [km s^{-1}]	$D_{\rm NGC4696}$ [kpc]
C-1-10	12:48:53.9	-41:19:05.3	69	0.1	-17.76	1.18	17.42	418	1.23	2317^a	13
C-1-21	12:48:48.6	-41:20:52.8	39	0.0…0.2	-15.57	1.18	18.56	279	1.27	3053^b	30
C-2-20	12:49:33.0	-41:19:24.0	-68	0.1	-15.69	1.15	18.51	363	1.55	–	109

modulus $(m - M) = 32.08$ mag were applied, corresponding to a scale of 126 pc/arcsec (Smith Castelli et al. 2008b, and references therein).

The most striking feature in Fig. 4.10 is the continuous size–luminosity relation over a wide magnitude range. The effective radius slowly increases as a function of galaxy magnitude for $-21 < M_V < -10$ mag. The relation between $\log(R_{\rm eff})$ and M_V is indicated by the solid line in Fig. 4.10 and can be quantified as

$$\log(R_{\rm eff}) = -0.041(\pm 0.004) \cdot M_V + 2.29(\pm 0.06) \tag{4.3}$$

with an rms of 0.17. At magnitudes fainter than $M_V \gtrsim -13$ mag, the slope of the relation becomes slightly steeper. A fit to the data yields

$$\log(R_{\rm eff}) = -0.107(\pm 0.007) \cdot M_V + 1.51(\pm 0.07) \tag{4.4}$$

with an rms of 0.17 (dashed line in Fig. 4.10). In their study of photometric scaling relations of early-type galaxies in Fornax, Coma, Antlia, Perseus and the LG, de Rijcke et al. (2009) reported on a very similar behaviour. However, comparatively few data points are available for $M_V > -10$ mag, i.e. the regime of faint LG dwarf spheroidals, and there might be a bias towards the selection of more compact objects at fainter magnitudes, in the sense that at a given magnitude very extended low surface brightness galaxies are more likely to be missed than more compact ones. These selection effects are discussed in more detail in Sect. 5.2.1. Moreover, the two smallest LG dwarf galaxies Segue I and Willman I (Martin et al. 2008) are suspected to be globular star clusters or dSphs out of dynamical equilibrium, close to disruption, rather than ordinary dwarf galaxies (Gilmore et al. 2007).

Two groups of objects clearly deviate from the size–luminosity relations defined by the other objects. These are the brightest core galaxies ($M_V \lesssim -21$ mag) which show a very strong dependence of effective radius on absolute magnitude, and a few rather compact galaxies which fall below the main body of normal elliptical galaxies. The latter are discussed in more detail in the following subsection.

4.2.5 Compact elliptical galaxy candidates

Three unusual objects, having rather small effective radii compared to other cluster galaxies with similar magnitudes, stand out in Fig. 4.10. Do they belong to the class of the so-called compact elliptical galaxies (cEs)? For the three candidates, Table 4.2 lists the coordinates,
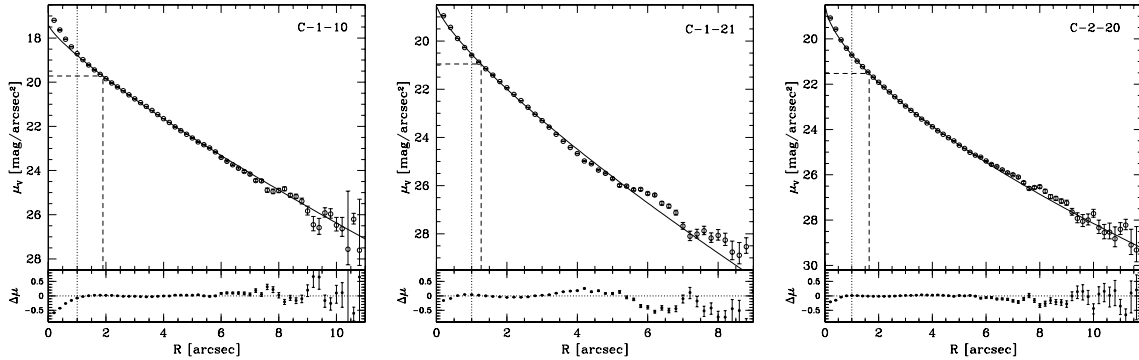
Fig. 4.11. Surface brightness profiles of the cE galaxy candidates. The extinction corrected surface brightness μ_V is plotted as a function of semi major axis radius R. The solid curve is the best fitting Sérsic law. The residuals $\Delta\mu = \mu_{V,\text{obs}} - \mu_{V,\text{fit}}$ are shown in the lower panels. Vertical dotted lines mark the seeing affected region $R < 1''$, which was excluded from the fit. The dashed lines indicate the effective surface brightness μ_{eff} and the effective radius R_{eff}.

the absolute magnitude M_V, the extinction corrected colour $(V - I)_0$, the central surface brightness μ_0, the effective radius R_{eff}, the Sérsic index n, the available radial velocity v_{rad} and the projected distance D_{NGC4696} to the central cluster galaxy NGC 4696. Also given are the position angle (P.A.) and the ellipticity ε used for the fit of elliptical isophotes to the galaxy image. Figure 4.11 shows for each of the cE galaxy candidates the Sérsic fits and the according residuals to their surface brightness profiles. The following three paragraphs describe in detail how the photometric parameters were obtained and try to judge whether the objects belong to the class of cE galaxies.

C-1-10 is a spectroscopically confirmed member of the Centaurus cluster. It is listed as CCC 70 in the Centaurus Cluster Catalogue and it is morphologically classified as an E0(M32) galaxy (Jerjen & Dressler 1997). The isophote fitting was performed on the 30 s exposure, since the long-exposure image was saturated at the object centre. Due to the projected proximity of C-1-10 to the giant galaxy NGC 4696, a model of the latter was created and subtracted before modelling the dwarf galaxy.

With an effective radius of $1.90''$ (418 pc) C-1-10 is the most compact object among the galaxies with similar magnitude in the Centaurus sample. However, it is larger than most of the cE galaxies mentioned in the literature (see Fig. 4.10). Only for NGC 5846A an even larger effective radius of ~ 500 pc is reported (Mahdavi et al. 2005). Moreover, C-1-10 does not have a particular high central surface brightness, but it falls exactly on the sequence of regular cluster dwarf galaxies (see upper panel of Fig. 4.9). Also its colour is consistent with the cluster CMR (Fig. 4.4). Given these properties, C-1-10 is rather a small elliptical galaxy than an exemplar of a cE galaxy.

C-1-21 is a confirmed Centaurus member (Chiboucas & Mateo 2007). The best model for C-1-21 was obtained with fixed centre coordinates and position angle, while the ellip-

ticity ε was allowed to vary $(0.0 < \varepsilon < 0.2)$. Its effective radius of $1.27''$, or 279 pc, is at least three times smaller than the ones of other cluster galaxies of the same luminosity (Fig. 4.10). This is comparable to the size of the two M32 twins in Abell 1689 (Mieske et al. 2005b), the cE galaxy A496cE (Chilingarian et al. 2007) and the cE candidate FS90 192 in the Antlia cluster (Smith Castelli et al. 2008b). The central surface brightness of C-1-21 is about 2 mag/arcsec^2 higher than the ones of equally bright cluster galaxies (see Fig. 4.9) and its colour is about 0.15 mag redder than expected from the cluster CMR (Eq. (4.1)). Interestingly, both colour and central surface brightness would be consistent with other cluster galaxies, if the object was about 2 mag brighter. This suggests that C-1-21 might originate from a higher mass elliptical or spiral galaxy, which was stripped by the strong tidal field of NGC 4696 (e.g. Faber 1973; Bekki et al. 2001b).

Since three common characteristics of cE galaxies, namely the small effective radius, the high central surface brightness and the projected location close to a brighter galaxy, are given, C-1-21 is considered a true cE galaxy.

C-2-20 is confirmed as a Centaurus cluster galaxy by the follow-up spectroscopy as detailed in Sect. 4.3. Its absolute magnitude, colour, central surface brightness and effective radius are very similar to those of C-1-21 (see Table 4.2). However, its relatively isolated position (see Fig. 4.2), far away from the giant galaxies, is unusual for a cE galaxy.

4.3 Follow-up spectroscopy

In this section, the results of the follow-up spectroscopy of the dwarf galaxy candidates found in the FORS1 images (Sect. 4.1) are presented. Other dwarf galaxy candidates, located in the surveyed areas but not in the FORS1 images, are not considered here. Figure 4.12 shows a map of the observed region in the core of the Centaurus cluster. Details on the observations and the data reduction can be found in Sect. 2.4.1.

A spectrum was obtained for 28 of the morphologically identified cluster dwarf galaxy candidates, including the two cE candidates C-2-20 and C-1-21 (see Sect. 4.2.5), and the two objects C-3-30 and C-1-47, for which no colour could be measured (see Sect. 4.2.1). Table 4.3 gives the photometric parameters and the radial velocities of the objects.

21 of the 28 dwarf galaxy candidates have a radial velocity that confirms their cluster membership. Only one object (C-6-55) turns out to be a background galaxy. No radial velocity could be determined for 6 objects, mostly due to their very low surface brightness (see Table 4.3). Therefore, the success rate of the morphological membership assignment (Sect. 4.1) is about 95%.

In Fig. 4.13, the radial velocity distribution all known Centaurus galaxies from Jerjen & Dressler (1997), Chiboucas & Mateo (2006), Mieske et al. (2007b) and this study is shown, with the 20 newly confirmed dwarf galaxies highlighted. Two of the new dwarf galaxies (C-2-51 and C-2-63) have rather high radial velocities. However, due to the large measurement errors (~ 250 km s^{-1}), they can still be regarded as Centaurus cluster members. The radial velocity distribution clearly shows the two well-known velocity
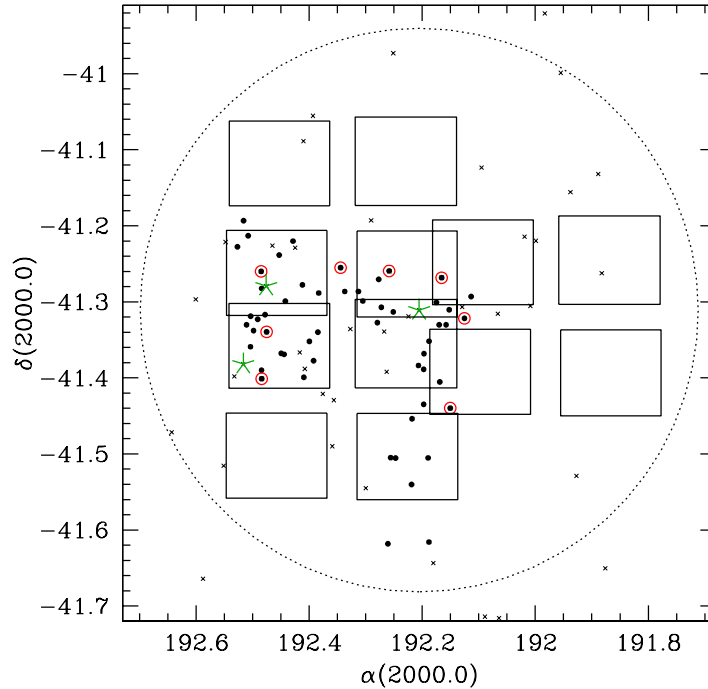
Fig. 4.12. Arrangement of the VIMOS pointings for the spectroscopic follow-up survey in Centaurus, with the dwarf galaxy candidates ($16.5 < V < 22.5$ mag and $\mu_V < 25$ mag/arcsec^2) from Fig. 4.5. Black filled circles are probable cluster galaxies, selected by their morphology. Red open circles mark cluster members, confirmed by radial velocity measurements. The pointings are arranged such that they cover a maximum number of those objects and a large fraction of the inner cluster region at the same time. The large dotted circle indicates the cluster core-radius of $r_c \sim 220\,h^{-1}$ kpc (Girardi et al. 1995), adopting $h = 0.75$. Green asterisks mark the location of the major NGC cluster galaxies. Small crosses are known Centaurus members from Stein et al. (1997), with luminosities at least 3–4 mag brighter than those of the targets.

sub-components Cen30 at $v_{\mathrm{rad}} \sim 3000$ km s^{-1}, dominated by NGC 4696, and Cen45 at $v_{\mathrm{rad}} \sim 4500$ km s^{-1}, dominated by NGC 4709. However, many more radial velocities are required, in order to investigate whether also the dwarf galaxy sample shows dynamical sub-components. The histogram in Fig. 4.13 also shows an indication for a third velocity component at ~ 2000 km s^{-1}. Although visible in their figure 3, Stein et al. (1997) did not comment on the origin of this peak. Whether or not it represents a true sub-component of the Centaurus cluster remains to be investigated.

Figure 4.14 shows updated versions of Fig. 4.4 and Fig. 4.5, with the newly confirmed cluster/background galaxies highlighted. The magnitude range of spectroscopically confirmed cluster dwarf galaxies is extended by about 4 magnitudes from $M_V \sim -16$ mag to $M_V \sim -12$ mag. Radial velocities could be successfully measured for objects with a surface brightness as low as ~ 24.5 mag/arcsec^2.
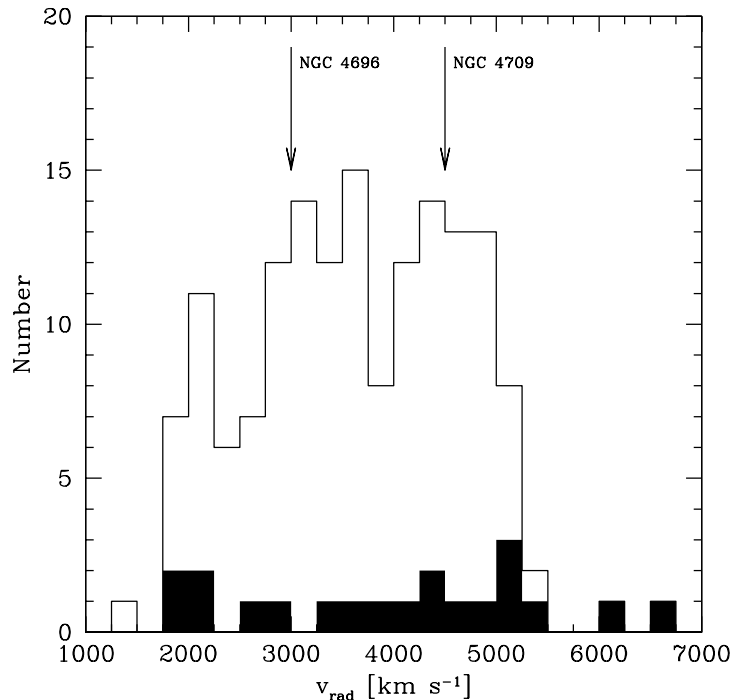
Fig. 4.13. Radial velocity distribution of all identified Centaurus cluster galaxies from Jerjen & Dressler (1997), Chiboucas & Mateo (2006), Mieske et al. (2007b) and this study. The filled histogram represents the 20 newly discovered faint dwarf galaxies. Arrows mark the individual radial velocities of NGC 4696 and NGC 4709.

4.4 Summary and discussion

In this chapter the early-type dwarf galaxy population of the Centaurus cluster was studied, based on deep VLT/FORS1 imaging data in Johnson V and I. Visual classification was combined with SExtractor based detection routines in order to select candidate objects on the images (Sect. 4.1). Fundamental scaling relations, such as the colour–magnitude relation and the magnitude-surface brightness relation were investigated (Sect. 4.2). Both relations were found to be consistent with the ones in the Fornax and Hydra I galaxy clusters (see Table 4.1). Moreover, LG dwarf galaxies projected to the Centaurus distance follow the same magnitude-surface brightness relation. Both scaling relations were used to define a sample of probable cluster galaxies, from which the galaxy luminosity function was constructed down to a limiting magnitude of $M_V = -10$ mag (Sect. 4.2.2).

4.4.1 The faint end of the galaxy luminosity function

From the completeness corrected galaxy number counts a very flat faint-end slope of the Centaurus GLF is derived. A power law describes best the shape of the faint end of the GLF. A slope of $\alpha = -1.14 \pm 0.12$ is measured (see Fig. 4.8 and Table 4.1). A similar value is obtained when fitting a Schechter function to the data ($\alpha \sim -1.1$). A flat GLF for the
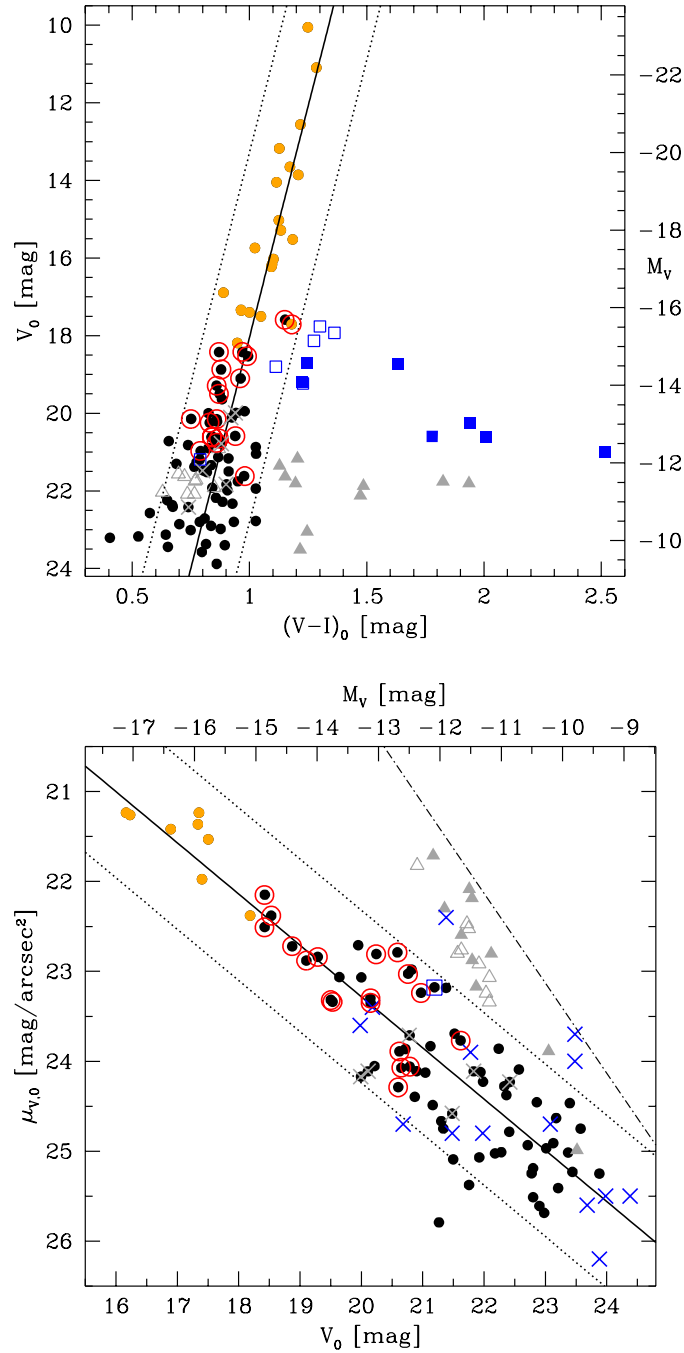
Fig. 4.14. Photometric properties of the newly confirmed Centaurus dwarf galaxies. The *top panel* shows an updated version of Fig. 4.4. The previously known cluster galaxies are represented by orange dots. The newly identified dwarf galaxies are marked by red open circles. Blue open squares are confirmed background galaxies, and grey crosses mark objects for which no redshift could be determined (cf. Table 4.3). The other symbols are as in Fig. 4.4. The *bottom panel* shows an updated version of Fig. 4.5, with the same symbols as in the upper panel.

Centaurus cluster was also derived by Chiboucas & Mateo (2006). The present result is consistent with the flat GLFs observed in other nearby galaxy clusters, for which the GLF was similarly constructed using morphological selection criteria (e.g. Trentham & Tully 2002; Hilker et al. 2003; Mieske et al. 2007a; Misgeld et al. 2008).

The cluster membership assignment by means of morphology and surface brightness is, of course, the key step for the entire analysis. Misclassifications have to be prevented as far as possible, but they can hardly be avoided entirely. In particular, it is often difficult to distinguish cluster dwarf galaxies with rather high surface brightnesses from background galaxies which only resemble the cluster galaxies. Indeed, nine questionable objects in were identified in the sample, having colours similar to the cluster dwarfs but with significantly higher surface brightnesses along with a rather compact morphology (cf. Sect. 4.2.1). Due to the fact that they deviate more than 2σ from the magnitude-surface brightness relation (Eq. (4.2)), which is defined by the probable cluster dwarf galaxies (see Fig. 4.5), it is likely that most of those objects do not belong to the cluster. In any case, they do not significantly influence the GLF, raising the faint-end slope marginally from $\alpha = -1.14$ to $\alpha = -1.17$ (cf. Sect. 4.2.2). As shown in Sect. 4.3 by means of follow-up spectroscopy, the morphological classification of the cluster dwarf galaxy candidates is highly reliable. This is due to the fact that the images were of excellent quality, allowing to detect very low surface brightnesses, and the use of photometric scaling relations to substantiate the morphological classifications.

Another caveat of a morphological selection is that one could potentially misclassify compact, M32-like cluster members as background objects, or vice versa (Trentham & Tully 2002). Three cE galaxy candidates were found in the photometric Centaurus sample, and all of them were confirmed as cluster members (see Sects. 4.2.5 and 4.3). However, cE galaxies are rare and have rather bright magnitudes (Fig. 4.10), so that they do not affect the shape of the faint end of the GLF.

Besides Virgo, Coma, Fornax and Hydra I, Centaurus is now the fifth galaxy cluster in the local Universe, whose GLF has been investigated down to the regime of dwarf spheroidal galaxies ($M_V \sim -10$ mag). Flat luminosity functions, which are contradictory to the predicted mass spectrum of cosmological dark-matter haloes (e.g. Press & Schechter 1974; Moore et al. 1999; Jenkins et al. 2001), have been derived for all of these environments. It seems to become apparent that this discrepancy to hierarchical cold dark matter models of galaxy formation is a common feature of various galaxy clusters/groups. However, one has to note that here primarily early-type galaxies in a rather limited region in the central part of the cluster were investigated. The slope of the GLF might considerably change if including the outer parts of the cluster into the analysis. Moreover, although not found in this study, late-type dwarf irregular galaxies might affect the shape of the GLF as well.

One of the simplest explanations for the discrepancy between the observed luminosity functions and the predicted mass spectrum is that there might be a large number of luminous satellites which has not yet been discovered. The discovery of the ultra-faint LG dwarf spheroidals in the SDSS might support this scenario. On the other hand, star formation might have been suppressed in a major fraction of low-mass dark matter halos with shallow potential wells (e.g. White & Rees 1978; Kauffmann et al. 1993; Verde et al.

2002). The third possible solution is the modification of the standard ΛCDM model of cosmological structure formation itself, for instance by allowing for self-interacting dark matter, or warm dark matter (e.g. Spergel & Steinhardt 2000; Bode et al. 2001).

4.4.2   The dependency of effective radius on luminosity

Structural parameters, such as central surface brightness μ_0, effective radius R_{eff} and profile shape index n, were derived for all probable cluster galaxies by fitting Sérsic (1968) models to the galaxy surface brightness profiles (Sect. 4.2.3). In plots of μ_0 and n versus the galaxy magnitude continuous relations were observed, ranging 10 orders of magnitude from $M_V = -20$ mag to the magnitude limit of the survey (Fig. 4.9). This confirms observations of continuous relations in the LG and other galaxy clusters, such as Fornax, Virgo and Hydra I (e.g. Young & Currie 1994; Graham & Guzmán 2003; Ferrarese et al. 2006; Côté et al. 2008; Misgeld et al. 2008, see also Sect. 2.3). Only the brightest cluster galaxies have central surface brightnesses which are lower than expected from the extrapolation of the relation defined by galaxies of lower luminosity. The deviation of these core galaxies from the M_V–μ_0 relation can be explained by mass depleted central regions due to the dynamical interaction of a supermassive black hole binary (Ferrarese et al. 2006, and references therein). A different point of view is, however, that these galaxies belong to a different sequence, almost perpendicular to the dE sequence, populated with bright early-type galaxies ($M_V \lesssim -20$ mag), for which the surface brightness decreases with increasing magnitude (e.g. Kormendy 1985; Bender et al. 1992; Kormendy et al. 2009).

The size–luminosity diagram is another tool to visualise a dis-/continuity between dwarf and giant elliptical galaxies. Combining the Centaurus data with studies of early-type galaxies in Hydra I (Chapter 2), Virgo (Ferrarese et al. 2006) and the LG, a well defined sequence is observed in such a diagram (see Fig. 4.10). For a wide magnitude range ($-21 \lesssim M_V \lesssim -13$ mag) the effective radius changes little with luminosity. For fainter magnitudes the slope of the size–luminosity relation steepens and the sequence continues all the way down to the ultra-faint LG dwarf galaxies ($M_V \sim -4$ mag), which have been identified in the SDSS (e.g. Martin et al. 2006, 2008; McConnachie & Irwin 2006; Gilmore et al. 2007; Zucker et al. 2007; McConnachie et al. 2008). Only the brightest core galaxies and compact elliptical galaxies deviate from the relation of ordinary elliptical galaxies (but see Graham & Worley 2008). The continuous surface brightness vs. absolute magnitude relation and the continuous sequence in the size–luminosity diagram were claimed to be caused by the gradual change of the Sérsic index n with the galaxy magnitude (e.g. Jerjen & Binggeli 1997; Graham & Guzmán 2003; Gavazzi et al. 2005), giving rise to the picture of a smooth transition from dwarf galaxies to more massive elliptical galaxies.

In contrast to this interpretation, Kormendy et al. (2009) and Janz & Lisker (2008) reported on a pronounced dichotomy of elliptical and spheroidal galaxies in the size–luminosity diagram, which is *not* caused by the gradual change of the galaxy light profile with luminosity. Kormendy et al. (2009) reaffirm results of older studies (e.g. Kormendy 1985; Binggeli & Cameron 1991; Bender et al. 1992, 1993) and claim that the dwarf galaxy

sequence intersects at $M_V \sim -18$ mag a second (much steeper) sequence, which consists of giant elliptical and S0 galaxies, and extends to the regime of cE galaxies (see also Dabringhausen et al. 2008). They conclude that massive elliptical and spheroidal galaxies are physically different and have undergone different formation processes. The latter were created by the transformation of late-type galaxies into spheroidals, whereas the giant ellipticals formed by mergers. By comparing the observations to models of ram-pressure stripping and galaxy harassment, Boselli et al. (2008) indeed found evidence for different formation mechanisms. Although the bulk of galaxies investigated in Ferrarese et al. (2006) falls into the magnitude range where the dichotomy should become apparent, these authors did not report on two distinct sequences (but see appendix B in Kormendy et al. 2009).

A greater picture of scaling relations of early-type stellar systems, covering many orders of magnitude in luminosity and size, is presented in Chapter 5.

Table 4.3. Photometry and redshifts of the newly confirmed cluster/background objects. The TDR value gives the significance of the cross-correlation result. The first two objects are compact elliptical galaxies (see Sect. 4.2.5). [a] Radial velocity determined from emission lines.

ID	V_0 [mag]	$(V-I)_0$ [mag]	$\mu_{V,0}$ [mag/arcsec^2]	TDR	$v_{\rm rad}$ [km s^{-1}]	$\Delta v_{\rm rad}$ [km s^{-1}]
C-2-20	17.59	1.15	...	11.15	2615	131
C-1-21	17.71	1.18	...	10.52	2955	132
C-3-23	18.42	0.97	22.51	4.67	5037	232
C-2-24	18.42	0.87	22.15	6.71	4986	198
C-2-25	18.53	0.99	22.38	6.65	2141	262
C-4-26	18.87	0.88	22.72	7.62	5052	200
C-2-27	19.10	0.96	22.88	3.77	3698	291
C-3-28	19.29	0.86	22.84	4.55	2778	314
C-4-29	19.50	0.87	23.32	6.09	4321	175
C-3-30	19.53	...	23.34	4.74	5350	172
C-4-33	19.99	0.94	24.17	...	...	...
C-2-35	20.11	0.92	24.11	...	...	...
C-1-36	20.15	0.75	23.30	3.59	4491	525
C-2-37	20.15	0.86	23.35	7.86	3894	162
C-4-39	20.24	0.83	22.81	6.40	4005	239
C-3-40	20.59	0.94	22.79	3.70	3413	258
C-5-41	20.60	0.84	24.29	5.65	2145	185
C-1-42	20.62	0.84	23.89	3.10	4516	260
C-3-43	20.65	0.87	24.07	2.96	1994	378
C-5-45	20.76	0.86	23.03	4.43	5072	162
C-1-46	20.78	0.88	23.71	...	...	...
C-1-47	20.79	...	24.06	4.59	1899	232
C-2-51	20.97	0.79	23.24	3.31	6084	268
C-6-55	21.19	0.79	23.18	...	63469^a	134
C-1-60	21.48	0.80	24.58	...	...	...
C-2-63	21.62	0.98	23.77	6.11	6568	249
C-4-65	21.83	0.90	24.11	...	...	...
C-4-75	22.42	0.74	24.23	...	...	...

Chapter 5

Families of dynamically hot stellar systems

This chapter is based on the publication
Misgeld, I., & Hilker, M. 2011, arXiv:1103.1628

Beginning with a pioneering paper by Brosche (1973), the well known Fundamental Plane (FP) relations have been used throughout the years by many authors to investigate global relationships among physical properties of stellar systems (mainly galaxies), such as surface brightness, absolute magnitude and physical size (e.g. Kormendy 1977, 1985; Djorgovski & Davis 1987; Bender et al. 1992, 1993; Burstein et al. 1997; Bernardi et al. 2003b; Belokurov et al. 2007; Kormendy et al. 2009, and many more).

However, some of these studies only focus on stellar systems of rather high luminosities/masses, excluding dwarf elliptical galaxies and globular clusters (e.g. Bender et al. 1992, 1993; Bernardi et al. 2003b). Belokurov et al. (2007) and Gilmore et al. (2007), on the other hand, examine globular clusters and faint dwarf galaxies, which are again not considered in Kormendy et al. (2009). In particular in early studies, there are considerable gaps in certain luminosity/mass ranges (e.g. Kormendy 1985; Burstein et al. 1997). New, unusual stellar systems have been discovered in nearby galaxy clusters and the Local Group (LG) during the last decade, such as ultra-compact dwarf galaxies (UCDs), compact elliptical galaxies (cEs), and ultra-faint LG dwarf spheroidal galaxies (for references see Sect. 5.1 and Table 5.1). They have to be included in FP studies, in order to investigate possible relations to the conventional stellar systems.

It is thus of great interest to study FP relations with a sample of stellar systems covering the parameter space in luminosity, mass and physical size as complete as possible. With that in mind, the structural properties of various early-type, mostly gas-poor stellar systems are investigated in this chapter. These dynamically hot stellar systems (i.e. stellar systems whose stars are on randomized orbits) span almost 25 orders of magnitude in luminosity, corresponding to 10 orders of magnitude in stellar mass, and 5 orders of magnitude in size. With up-to-date data on local galaxy cluster dwarf galaxies, ultra-faint LG dwarf

spheroidals, cEs, UCDs and nuclear star clusters, this has not been shown before with such a complete coverage. Note that it is not the aim of this chapter to present the correct sampling of the luminosity function of individual types of objects. This is the task of large imaging surveys (e.g. SDSS), or dedicated cluster surveys [e.g. ACS Virgo Cluster Survey (ACSVCS)].

5.1 Sample description

This section describes, how the basic FP parameters effective radius R_{eff}, absolute V-band magnitude M_V, and stellar mass $M_\star$ were compiled. The the original source papers give a description of how R_{eff} was derived for the individual objects. The following objects are included in this study:

- Giant elliptical galaxies, dwarf elliptical galaxies and bulges (including M32) from Bender et al. (1993). For these objects, M_V was calculated from the given absolute B-band magnitudes and the $B - V$ colours.

- Early-type galaxies from the ACSVCS Virgo Cluster Survey (Ferrarese et al. 2006). The apparent g_{AB}-band magnitudes were transformed into absolute V-band magnitudes using the relation $V = g_{\text{AB}} + 0.026 - 0.307 \cdot (g - z)_{\text{AB}}$ given in Peng et al. (2006), and a Virgo distance modulus of 31.09 mag (Mei et al. 2007). The same transformations were applied to a sample of nuclei of nucleated dwarf galaxies (dE,Ns) from the ACSVCS (Côté et al. 2006).

- Bona fide extragalactic globular clusters (GCs) from the ACSVCS (Jordán et al. 2009). M_V was calculated in the same manner as for the ACSVCS galaxies. Note that here, R_{eff} of all objects from the ACSVCS is the average of the half-light radii measured in the g- and in the z-band.

- Early-type galaxies (giant ellipticals and dwarf ellipticals) from the photometric studies of the galaxy clusters Hydra I and Centaurus (Misgeld et al. 2008, 2009). A Hydra I distance modulus of 33.37 mag, and a Centaurus distance modulus of 33.28 mag was adopted (Mieske et al. 2005a).

- Compact elliptical galaxies identified in the HST/ACS Coma Cluster Treasury Survey (Price et al. 2009). M_V was estimated from the tabulated absolute B-band magnitudes, using $B - V = 0.96$ mag (Fukugita et al. 1995).

- Milky Way, LMC, SMC and Fornax star clusters from McLaughlin & van der Marel (2005). The values for M_V and R_{eff} were taken from the King models.

- Hydra I UCDs from Chapter 3, with $S/N > 20$ (see Table 3.2).

- UCDs with masses larger than 10^6 M$_\odot$ from Mieske et al. (2008), including the most massive UCDs in Fornax (UCD3) and Virgo (VUCD7). The tabulated masses were converted into M_V with the given M/L_V ratios and a solar absolute magnitude of $M_{V,\odot} = 4.83$ mag (Binney & Merrifield 1998).

- A sample of 22 nuclear star clusters (NCs) of spiral galaxies for which both the effective radii and the magnitudes in V and I are reported in Böker et al. (2004) and Rossa et al. (2006).

The photometric and structural parameters for the remaining objects, i.e. for the compact elliptical galaxies A496cE, NGC 4486B, NGC 5846A, NGC 5846cE, and for the two cEs in the galaxy cluster Abell 1689, for the compact object M59cO, and for the LG dwarf galaxies are listed in Table 5.1. M_V and R_{eff} of NGC 5846A were calculated by adopting $V - R = 0.61$ mag (Fukugita et al. 1995), and a distance modulus of $(m - M) = 32.08$ mag (Smith Castelli et al. 2008b, and references therein). The absolute magnitude of the LG dwarf galaxies, for which only the V-band luminosity L_V is given in the source-paper, was calculated by $M_V = M_{V,\odot} - 2.5 \log(L_V/L_\odot)$.

5.1.1 Stellar mass estimates

In order to estimate the stellar mass $M_\star$ of a particular object, relations between its broad band colour and the stellar mass-to-light ratio M/L_V were derived, using Maraston (2005) simple stellar population (SSP) models.

For the objects from Bender et al. (1993), a 13-Gyr SSP model was used, assuming a Kroupa (2001) initial mass function (IMF) and a red horizontal branch. The M/L_V–colour relation was parametrized as

$$\frac{M}{L_V} = 4.500 + 1.934 \cdot \arctan\left[8.464 \cdot ((B - V) - 0.998)\right], \tag{5.1}$$

and is valid for $0.65 < (B - V) < 1.20$ mag. The stellar masses of the compact elliptical galaxies NGC 4486B and NGC 5846A were derived in the same manner (see Table 5.1).

The same SSP model, i.e. 13-Gyr, Kroupa IMF, red horizontal branch, was used for deriving the M/L_V ratios of the early-type galaxies and GCs from the ACSVCS (Eq. (5.2)), and the Hydra I and Centaurus UCDs and early-type galaxies (Eq. (5.3)):

$$\frac{M}{L_V} = 4.466 + 1.869 \cdot \arctan\left[4.385 \cdot ((g - z)_{\text{AB}} - 1.478)\right], \tag{5.2}$$

$$\frac{M}{L_V} = 4.408 + 1.782 \cdot \arctan\left[11.367 \cdot ((V - I) - 1.162)\right]. \tag{5.3}$$

These relations are valid for $0.80 < (g - z)_{\text{AB}} < 1.90$ mag and $0.80 < (V - I) < 1.40$ mag, respectively.

Table 5.1. Absolute magnitudes M_V, effective radii $R_{\rm eff}$, and stellar masses $M_\star$ of compact elliptical galaxies, the compact object M59cO, and Local Group dwarf galaxies. The references are: (HL) HyperLeda, http://leda.univ-lyon1.fr/; (1) Chilingarian et al. (2008); (2) Kormendy et al. (2009); (3) Bender et al. (1993); (4) Smith Castelli et al. (2008b); (5) Mieske et al. (2005b); (6) Chilingarian & Mamon (2008); (7) Grebel et al. (2003); (8) Gilmore et al. (2007, and references therein); (9) Irwin et al. (2007); (10) Martin et al. (2008); (11) Łokas et al. (2005); (12) Belokurov et al. (2009); (13) de Jong et al. (2010); (14) Belokurov et al. (2010); (15) McConnachie & Irwin (2006); (16) Kalirai et al. (2010, and references therein); (17) Collins et al. (2010); (18) McConnachie et al. (2008); (19) Martin et al. (2009); (20) Chilingarian & Bergond (2010); (21) Mateo (1998). $^{(*)}$ M_V derived from M_B with $B - V = 0.96$ mag (Fukugita et al. 1995). $^{(\dagger)}$ $M_\star$ derived from $B - V$ (see Sect. 5.1.1). $^{(\dagger\dagger)}$ $M_\star$ derived from $g - i$ (see Sect. 5.1.1).

Name	M_V [mag]	$R_{\rm eff}$ [pc]	$M_\star$ [$M_\odot$]	Ref.
A496cE	-18.0^*	470	$5.8 \times 10^{9\,\dagger\dagger}$	1
NGC 4486B	-17.7	198	$4.3 \times 10^{9\,\dagger}$	2, 3
NGC 5846A	-18.4	517	$9.5 \times 10^{9\,\dagger}$	4, HL
NGC 5846cE	-16.9^*	291	2.2×10^{9}	20
CG$_{\rm A1689,1}$	-17.2	370	$4.3 \times 10^{9\,\dagger\dagger}$	5
CG$_{\rm A1689,2}$	-16.5	225	$2.3 \times 10^{9\,\dagger\dagger}$	5
M59cO	-13.0^*	50	9.1×10^{7}	6
Sagittarius	-15.0	500	...	7, 8
Sculptor	-9.8	160	$1.8 \times 10^{6\,\dagger}$	7, 8, HL
Fornax	-13.1	400	$2.8 \times 10^{7\,\dagger}$	8, 21
Leo I	-11.9	330	$1.1 \times 10^{7\,\dagger}$	8, 21
Leo II	-9.8	185	$1.4 \times 10^{6\,\dagger}$	8, 21
Sextans	-9.4	630	...	8
Carina	-9.3	290	$1.1 \times 10^{6\,\dagger}$	8, HL
Ursa Minor	-8.9	300	$1.9 \times 10^{6\,\dagger}$	8, 21
Leo T	-7.1	170	1.0×10^{5}	9
Canes Venatici I	-8.6	564	3.0×10^{5}	10
Canes Venatici II	-4.9	74	8.0×10^{3}	10
Hercules	-6.6	330	3.7×10^{4}	10
Coma Berenices	-4.1	77	4.8×10^{3}	10
Boötes I	-6.3	242	3.4×10^{4}	10
Boötes II	-2.7	51	1.4×10^{3}	10
Ursa Major I	-5.5	318	1.9×10^{4}	10
Ursa Major II	-4.2	140	5.4×10^{3}	10
Willman I	-2.7	25	1.5×10^{3}	10
Draco	-8.8	221	3.2×10^{5}	10, 11
Segue I	-1.5	29	6.0×10^{2}	10
Segue II	-2.5	34	...	12
Leo IV	-5.8	206	...	13
Leo V	-5.2	133	...	13

Table 5.1. continued

Name	M_V [mag]	R_{eff} [pc]	$M_\star$ $[M_\odot]$	Ref.
Pisces II	−5.0	60	...	14
Cetus	−11.3	600	...	15
Tucana	−9.5	274	$1.1 \times 10^{6\,\dagger}$	16, 21
And I	−11.8	682	$9.7 \times 10^{6\,\dagger}$	16, 21
And II	−12.6	1248	$2.3 \times 10^{7\,\dagger}$	16, HL
And III	−10.2	482	$2.5 \times 10^{6\,\dagger}$	16, HL
And V	−9.6	300	...	15
And VI/Pegasus	−11.5	420	$6.3 \times 10^{6\,\dagger}$	15, 21
And VII	−13.3	791	...	16
And IX	−8.1	552	...	17
And X	−8.1	339	...	16
And XI	−6.9	145	...	17
And XII	−6.4	289	...	17
And XIII	−6.7	203	...	17
And XIV	−8.3	413	...	16
And XVIII	−9.7	363	...	18
And XIX	−9.3	1683	...	18
And XX	−6.3	124	...	18
And XXI	−9.9	875	...	19
And XXII	−6.5	217	...	19

For the galaxy nuclei from Côté et al. (2006), an 11-Gyr SSP model (Kroupa IMF, red horizontal branch) was applied, in order to account for the younger ages of those objects (e.g. Côté et al. 2006; Paudel & Lisker 2009; Paudel et al. 2010, and references therein). The M/L_V ratios are then given by

$$\frac{M}{L_V} = 3.861 + 1.701 \cdot \arctan\left[3.795 \cdot \left((g - z)_{\text{AB}} - 1.448\right)\right], \qquad (5.4)$$

for the colour range $0.80 < (g - z)_{\text{AB}} < 1.90$ mag.

The stellar masses of 11 LG dwarf galaxies (see Table 5.1) were calculated from their $B - V$ colours, as given in Mateo (1998) and HyperLeda (Paturel et al. 2003). For these objects, a M/L_V–colour relation from an 11-Gyr SSP model (Kroupa IMF, blue horizontal branch) was derived, accounting for the, on average, younger ages and lower metallicities:

$$\frac{M}{L_V} = 4.002 + 1.729 \cdot \arctan\left[7.619 \cdot \left((B - V) - 0.990\right)\right], \qquad (5.5)$$

valid for $0.65 < (B - V) < 1.20$ mag.

The stellar masses of the two cEs from Mieske et al. (2005b) were derived from the tabulated SDSS $(g - i)$ colours. First, these colours were transformed to $(V - I)$, using the

Table 5.2. Photometric and structural parameters of the objects used in this study. The references are: (1) Bender et al. (1993); (2) Ferrarese et al. (2006); (3) Misgeld et al. (2008); (4) Misgeld et al. (2009); (5) Mieske et al. (2008); (6) Côté et al. (2006); (7) McLaughlin & van der Marel (2005); (8) Jordán et al. (2009); (9) Price et al. (2009); (10) Böker et al. (2004) and Rossa et al. (2006); (11) see Table 5.1 for detailed references. This table is available in its entirety in a machine-readable form at the CDS. A portion is shown here for guidance regarding its form and content.

ID	Ref.	M_V [mag]	$\log(R_{\rm eff})$ [pc]	$\log(M_\star)$ $[M_\odot]$	$\log(\Sigma_{\rm eff})$ $[M_\odot\ {\rm pc}^{-2}]$
N0315	1	-24.6	4.486	12.432	2.662
N0584	1	-22.6	3.724	11.535	3.289
N0636	1	-21.6	3.562	11.088	3.166
N0720	1	-22.6	3.840	11.608	3.130
⋮	⋮	⋮	⋮	⋮	⋮

relation $(V - I) = 0.671 \cdot (g - i) + 0.359$ from Jordi et al. (2006). Then, the stellar mass-to-light ratio was calculated with Eq. (5.3). The same method was applied to the compact elliptical A496cE from Chilingarian et al. (2008), although here the $(g' - i')$ colours from the CFHT MegaCam filter system were used, which is however very similar to the SDSS filter system.

Accounting for the, on average, younger ages of nuclear star clusters (Rossa et al. 2006, and references therein), an 8-Gyr SSP model (Kroupa IMF, red horizontal branch) was used to derive their M/L_V ratios from the $V - I$ colours:

$$\frac{M}{L_V} = 2.913 + 1.269 \cdot \arctan\left[6.847 \cdot ((V - I) - 1.120)\right]. \tag{5.6}$$

This relation is valid for $0.80 < (V - I) < 1.40$ mag.

For comparison, stellar mass-to-light ratios for the above mentioned objects were also computed, using M/L_V–colour relations derived from Bruzual & Charlot (2003) SSP models (8-/11-/13-Gyr, Chabrier IMF). These models return smaller M/L_V ratios, depending on the actual colour of the object. The percent differences[1] between the M/L_V ratios of the two models are 1–10% for Eq. (5.1) and Eq. (5.5), 11–25% for Eq. (5.2) and Eq. (5.4), and 11–37% for Eq. (5.3) and Eq. (5.6). The resulting differences in stellar mass, however, appear small in a logarithmic representation, and therefore do not change the conclusions.

For the Coma cEs from Price et al. (2009), $M_\star$ was computed with the given B-band luminosities and stellar M/L_B ratios, assuming a solar absolute B-band luminosity of $M_{B,\odot} = 5.48$ mag (Binney & Merrifield 1998).

The stellar masses of the Milky Way, LMC, SMC and Fornax star clusters (King model values) were directly taken from McLaughlin & van der Marel (2005).

---

[1]The percent difference of two values x_1 and x_2 is defined as Diff $= \left|\frac{x_1 - x_2}{(x_1 + x_2)/2}\right| \times 100$.

Since only for a few of the UCDs from Mieske et al. (2008) stellar masses can be derived, the tabulated dynamical masses were used here. The differences between dynamical masses and stellar masses are smaller than 6% of the UCD mass, and therefore do not change the results.

In Table 5.2, available at the CDS, the full catalogue of photometric and structural parameters of the objects used in this study is presented (except for the Hydra I UCDs from Table 3.2). The first column is the object ID as given in the original source paper. A reference to the source paper is given in column 2. The third column lists the absolute V-band magnitude M_V. Columns 4, 5 and 6 give the logarithm of the effective radius R_{eff}, the stellar mass $M_\star$, and the effective mass surface density Σ_{eff}, respectively.

5.2   Scaling relations

Figure 5.1 shows the R_{eff}–M_V plane for the objects discussed in Sect. 5.1. In this plane, two distinct families or branches of objects can be identified. The first, 'galaxian', family comprises elliptical galaxies (giants and dwarfs), cEs and ultra-faint LG dwarf spheroidals, covering the full magnitude range of $-25 < M_V < -2$ mag (coloured symbols, except for the red triangles). The second family consists of 'star cluster-like' objects, i.e. GCs, UCDs, nuclei of dE,Ns and NCs (black/grey symbols and red triangles). Note, that this separation is only based on the morphological appearance of the objects, and does not imply that objects of one family have all formed by the same physical processes.

At this point it is worth mentioning two different ways of dividing galaxies/star clusters into separate families. Based on luminosity, size and surface brightness, Kormendy et al. (2009) distinguished between a sequence of elliptical galaxies (ranging from typical giant elliptical galaxies to cEs like M32) and a sequence of spheroidal galaxies (see their fig. 38). Similarly, Forbes et al. (2008) reported on a common sequence of giant elliptical galaxies, cEs and UCDs/GCs in a plot of virial mass ($\propto \sigma^2 R_h$) vs. stellar mass (their fig. 13), again with dwarf spheroidal galaxies deviating from this sequence (see also Dabringhausen et al. 2008).

The second point of view is that (giant) elliptical galaxies and dwarf elliptical galaxies form a continuous sequence, extending from galaxies with a central light deficit to galaxies with a central light excess, based on the evaluation of the outer light profile by a Sérsic law (e.g. Graham & Guzmán 2003; Ferrarese et al. 2006; Côté et al. 2007). In this picture, cEs and UCDs would be outliers of the galaxy sequence. In a similar manner, Tollerud et al. (2011) defined a one-dimensional fundamental curve through the mass-radius-luminosity space, connecting all spheroidal galaxies. Again, GCs and UCDs do not follow this fundamental curve relation. It is, however, not the scope of this chapter to enter the discussion on which of those viewpoints is more appropriate.
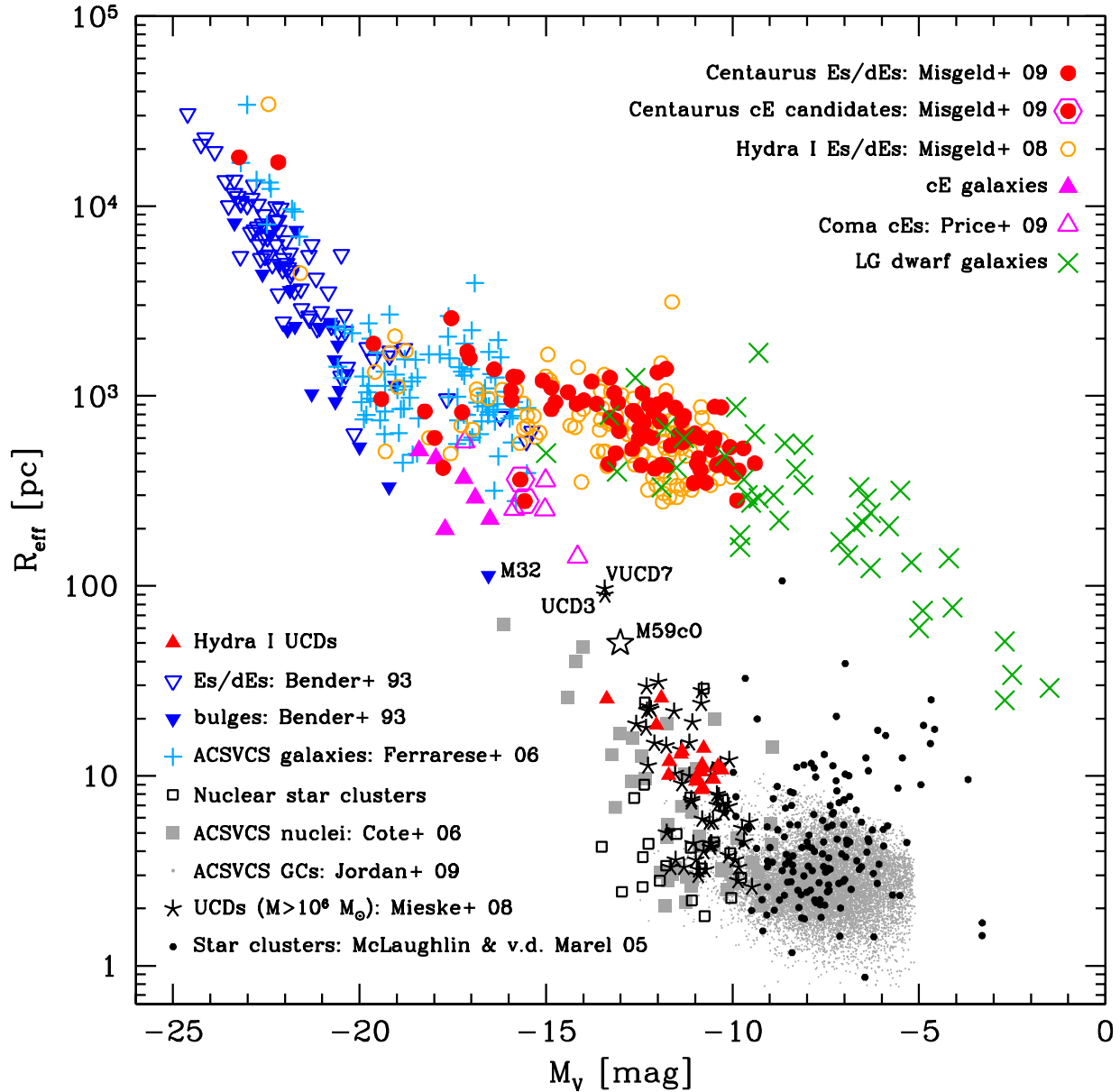
Fig. 5.1. Effective radius $R_{\rm eff}$ plotted versus absolute V-band magnitude M_V for the stellar systems described in Sect. 5.1. Note the observational limit for the ACSVCS GCs at $M_V = -5$ mag.

5.2.1 Galaxies as distance indicators

An interesting feature in Fig. 5.1 is is the nearly constant mean effective radius of $R_{\rm eff} \sim$ 1 kpc for galaxies with $-21 \lesssim M_V \lesssim -10$ mag, which is equivalent to about 5 orders of magnitude in stellar mass (cf. Fig. 5.4). Equation 4.3 quantifies the relation between $\log(R_{\rm eff})$ and M_V for this particular magnitude range. In order to determine to what extend the constancy of $R_{\rm eff}$ and its downturn at fainter magnitudes is affected by selection effects, Fig. 5.2 shows an enlargement of Fig. 5.1, with various detection limits indicated.
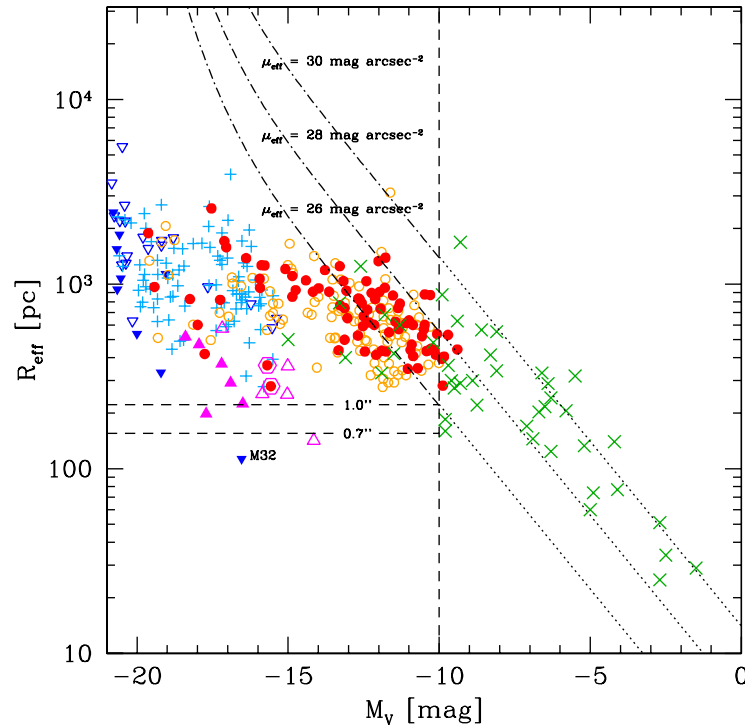
Fig. 5.2. Enlargement of Fig. 5.1 with various detection limits indicated. Only 'galaxy-like' objects are plotted, with the same symbols as in Fig. 5.1. The three (dash-)dotted lines indicate surface brightness limits of $\mu_{\mathrm{eff}} = 26, 28, 30$ mag arcsec^{-2} (see text for more details). The horizontal dashed lines represent resolution limits of $0.7''$ and $1.0''$, respectively, at the distance of Hydra I and Centaurus (Mieske et al. 2005a). The vertical dashed line marks the 50% completeness limit for the Hydra I and Centaurus dwarf galaxies at $M_V \sim -10$ mag (Misgeld et al. 2008, 2009).

The (dash-)dotted lines mark surface brightness limits of $\mu_{\mathrm{eff}} = 26, 28, 30$ mag arcsec^{-2}. For calculating these limits, equations (9) and (12) from Graham & Driver (2005) were used, approximating $\langle\mu\rangle_{\mathrm{e,abs}} \approx \langle\mu\rangle_{\mathrm{e}}$. As $\langle\mu\rangle_{\mathrm{e}}$ is a function of the Sérsic index n (equations (8) and (9) in Graham & Driver 2005), the profile shape index was set to $n = 1$ for $M_V > -10$ mag. For brighter magnitudes, a 3rd order polynomial was fitted to the Hydra I and Centaurus data, to describe n as a function of M_V. The SDSS detection limit is ~ 30 mag arcsec^{-2} (Koposov et al. 2008). The surface brightness limit in the Hydra I/Centaurus data is 27–28 mag arcsec^{-2}. Also indicated in Fig. 5.2 are typical seeing limits of $0.7''$ and $1.0''$ at the distance of Hydra I and Centaurus, as well as the 50% completeness limit for the Hydra I and Centaurus dwarf galaxies at $M_V \sim -10$ mag (see also Sects. 2.3.4 and 4.2.2).

At low luminosities ($M_V > -10$ mag) the trend of R_{eff} with M_V is clearly affected by the SDSS detection limit for LG dwarf spheroidals, causing a steeper slope of the $\log(R_{\mathrm{eff}})$–M_V relation. Very extended, low surface brightness objects cannot be detected at these magnitudes. For the Hydra I/Centaurus dwarf galaxies this is only true close to the 50% completeness limit, as indicated in Fig. 5.2. However, the inclusion of objects with large effective radii and low surface brightnesses, which could have potentially been missed at

Table 5.3. Results of the distance measurements. a is the slope of the size–luminosity relation. References for the literature distance moduli $(m - M)_{\text{lit}}$ are: [a] Mieske et al. (2005a); [b] Mei et al. (2007); [c] Dirsch et al. (2003); [d] Blakeslee et al. (2009).

Sample	a	$\langle r_{\text{e}} \rangle$	$\langle r_{\text{e}} \rangle_{\text{cor}}$	D	D_{cor}	$(m - M)$	$(m - M)_{\text{cor}}$	$(m - M)_{\text{lit}}$
	[arcsec mag^{-1}]	[arcsec]	[arcsec]	[Mpc]	[Mpc]	[mag]	[mag]	[mag]
Hydra I	-0.35 ± 0.07	3.58 ± 0.19	4.06 ± 0.56	57.6 ± 6.5	50.8 ± 8.7	33.80 ± 0.57	33.53 ± 0.85	33.37^a
Centaurus	-0.32 ± 0.06	4.25 ± 0.25	4.76 ± 0.49	48.5 ± 5.7	43.3 ± 6.2	33.43 ± 0.58	33.18 ± 0.72	33.28^a
Virgo	-1.05 ± 0.14	11.08 ± 0.42	11.46 ± 1.63	18.6 ± 2.0	18.0 ± 3.1	31.35 ± 0.53	31.28 ± 0.87	31.09^b
Antlia	-0.46 ± 0.11	5.49 ± 0.24	5.57 ± 0.58	37.6 ± 4.1	37.0 ± 5.3	32.88 ± 0.55	32.84 ± 0.72	32.73^c
Fornax	-0.84 ± 0.23	7.47 ± 0.45	8.27 ± 1.03	27.6 ± 3.2	24.9 ± 4.0	32.20 ± 0.58	31.98 ± 0.80	31.51^d

these luminosities, would rather lead to a flatter $\log(R_{\text{eff}})$–M_V relation. Further objects that could have been missed due to limited image resolution, are very compact, M32-like galaxies. These objects, however, fall below the main body of normal elliptical galaxies and do not bias the $\log(R_{\text{eff}})$–M_V relation.

Hence, the nearly constant mean effective radius, which is observed over a wide range of magnitudes is not caused by selection biases, but is rather a genuine phenomenon. If confirmed in more galaxy clusters, this feature could serve as a distance indicator, provided that one can accurately determine the structural parameters of galaxies over a wide range of magnitudes. First efforts in this direction have already been made (e.g. Smith Castelli et al. 2008a, and references therein).

The potential of this distance indicator is further investigated in Fig. 5.3. Plotted is the apparent effective radius vs. the apparent magnitude of early-type galaxies in Hydra I, Centaurus, Virgo (Ferrarese et al. 2006; Lieder et al. 2011, in prep.), Antlia (Smith Castelli et al. 2008a), and Fornax (Hilker et al. 2003; Mieske et al. 2007a). For each sample, the slope of the size–luminosity relation a, and the mean effective radius $\langle r_{\text{e}} \rangle$ was measured. In order not to be affected by the selection effects discussed before, each sample was restricted to a magnitude range of $-20 \lesssim M_V \lesssim -12$ mag, according to the distance moduli given in the literature. Additionally, obvious outliers and the two cEs in Centaurus were excluded (grey symbols in Fig. 5.3). The V-band magnitude of the Antlia galaxies was calculated, using eq. (2) from Smith Castelli et al. (2008a). The slope a was determined by fitting a linear relation to the data, applying a 3σ rejection algorithm. The mean effective radius $\langle r_{\text{e}} \rangle$ was used to calculate the cluster distance D, employing

$$D = \frac{d}{\delta}, \tag{5.7}$$

in which δ is the apparent mean effective radius $\langle r_{\text{e}} \rangle$ in angular units, and d is the true mean effective radius in pc, for which a value of $d = 1.0 \pm 0.1$ kpc was assumed (the exact mean value measured in Fig. 5.1 in the magnitude range $-20 < M_V < -12$ mag is $d = 982$ pc).

Due to the negative slope of the size–luminosity relation, and due to the shape of the galaxy luminosity function, the mean effective radius $\langle r_{\text{e}} \rangle$ is biased towards smaller values,
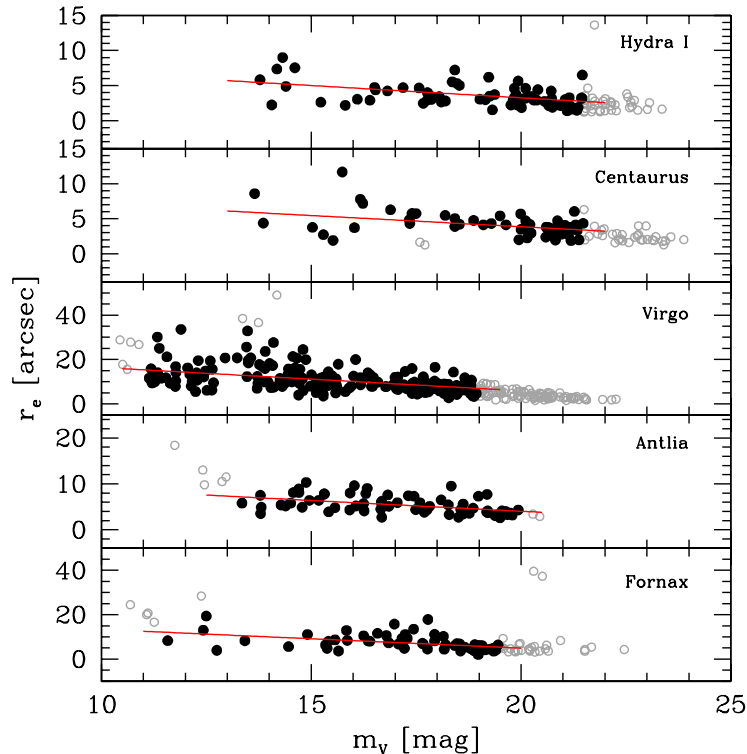
Fig. 5.3. Size–luminosity relations in nearby galaxy clusters. The effective radius r_e is plotted against the apparent magnitude m_V. Filled black circles are the galaxies used for the measurements of the slope of the size–luminosity relation (as indicated by the red solid lines), and the mean effective radius (see also Table 5.3). Grey open circles denote the rejected objects.

caused by more data points with lower values of r_e at faint magnitudes. In order to correct for this bias, each sample was subdivided into bins of 2 mag width. Then, the mean effective radius of each bin was determined, and the average of those values was defined as the final, corrected $\langle r_e \rangle_{cor}$.

Table 5.3 summarizes the results of the measurements. Column 2 gives the slope a of the size–luminosity relation, columns 3–8 list both the uncorrected and corrected values of the mean effective radius in arcsec, the resulting distance in Mpc, and the according distance modulus. For comparison, the literature distance moduli are given in the last column.

In all clusters considered, the slope of the size–luminosity relation is shallow. For Hydra I, Centaurus and Antlia the measured values agree within the errors, only in Virgo and Fornax the slope is slightly steeper. This justifies the assumption of an almost constant effective radius over a wide range of galaxy luminosities and different cluster environments. The derived distance moduli are well in agreement with the reported literature values (within about 0.2 mag), although the values have rather large errors, caused by the scatter in the observed effective radii and the slope of the size–luminosity relation. Only for Fornax a distance modulus was measured which deviates $\sim +0.5$ mag from the literature value. This might be caused by having only a few data points available at magnitudes brighter

than $m_V = 15$ mag (see Fig. 5.3), leading to an overall smaller mean effective radius an thus to a larger distance modulus. Note that at intermediate and low luminosities, the scatter of the size–luminosity relation might artificially be reduced by the non-detection of both very extended low-surface brightness objects and very compact objects. The latter (e.g. cEs) are, however, rare compared to the number of regular dwarf elliptical galaxies, and have thus been excluded from the analyses. At the lowest luminosities considered ($M_V \sim -12$ mag), very extended objects might have been missed, but the comparison with LG dwarf galaxies shows that the number of such non-detections should be small (cf. Fig. 5.2).

In summary, the use of galaxy mean effective radii seems to offer a reasonable alternative to estimate the cluster distance, given that it is possible to identify the suitable magnitude range to perform the measurements. On the one hand, one has to avoid the magnitude regime where the steep size–luminosity relation of giant elliptical galaxies sets in, and on the other hand, one has to take care of not being affected by surface brightness limitations at faint luminosities.

5.2.2   The sizes of hot stellar systems

Although having a large range of luminosities in common ($-15 \lesssim M_V \lesssim -5$ mag), dwarf galaxies and star clusters/UCDs are well separated in size, the latter being approximately two orders of magnitude smaller. This has previously been noted by Gilmore et al. (2007), stating that there are no stable objects in a size gap between ~ 30 pc and ~ 120 pc. However, Fig. 5.1 shows that with several UCDs, compact elliptical galaxies, very extended star clusters and ultra-faint LG dwarf galaxies, this size gap is not as well-defined as it appeared in Gilmore et al. (2007), in particular at bright ($M_V \sim -15$ mag) and very faint ($M_V \gtrsim -5$ mag) magnitudes. Some of the faint star clusters and dwarf spheroidal galaxies are certainly in an unstable stage of disruption or evaporation, and will therefore not reside at their position in the diagram for a very long time. Whether this is also true for very bright and massive objects in this size range, like M32, UCD3, VUCD7 or M59cO, remains an open question. These objects might originate from larger and more luminous galaxies, now being transformed by tidal interactions with a major host galaxy (e.g. Bekki et al. 2001b, 2003; Drinkwater et al. 2003). Yet, there remains a prominent, 'hole-like' region in between the galaxy- and the star cluster-branch, with only very few objects therein.

Another interesting feature in Fig. 5.1 is the steep size–luminosity relation for giant elliptical galaxies and bulges above a magnitude of $M_V \sim -20$ mag. Surprisingly, a similar relation is visible for cEs, the nuclei of dE,Ns, UCDs and NCs. Thus, there is a boundary, in the sense that the effective radius of a stellar system of a given luminosity is larger than $\log(R_{\mathrm{eff}}) = -0.33 \cdot M_V - 3.90$. The relation for the compact systems, however, sets in at much lower magnitudes of $M_V \sim -10$ mag. Below this limit the star cluster sizes are largely independent of magnitude, just like the sizes of (dwarf) elliptical galaxies below $M_V \sim -20$ mag.

The boundary remains visible when looking at the size–mass plane in Fig. 5.4. Even more, giant elliptical galaxies and nuclei of dE,Ns define the same sharp edge in the diagram,
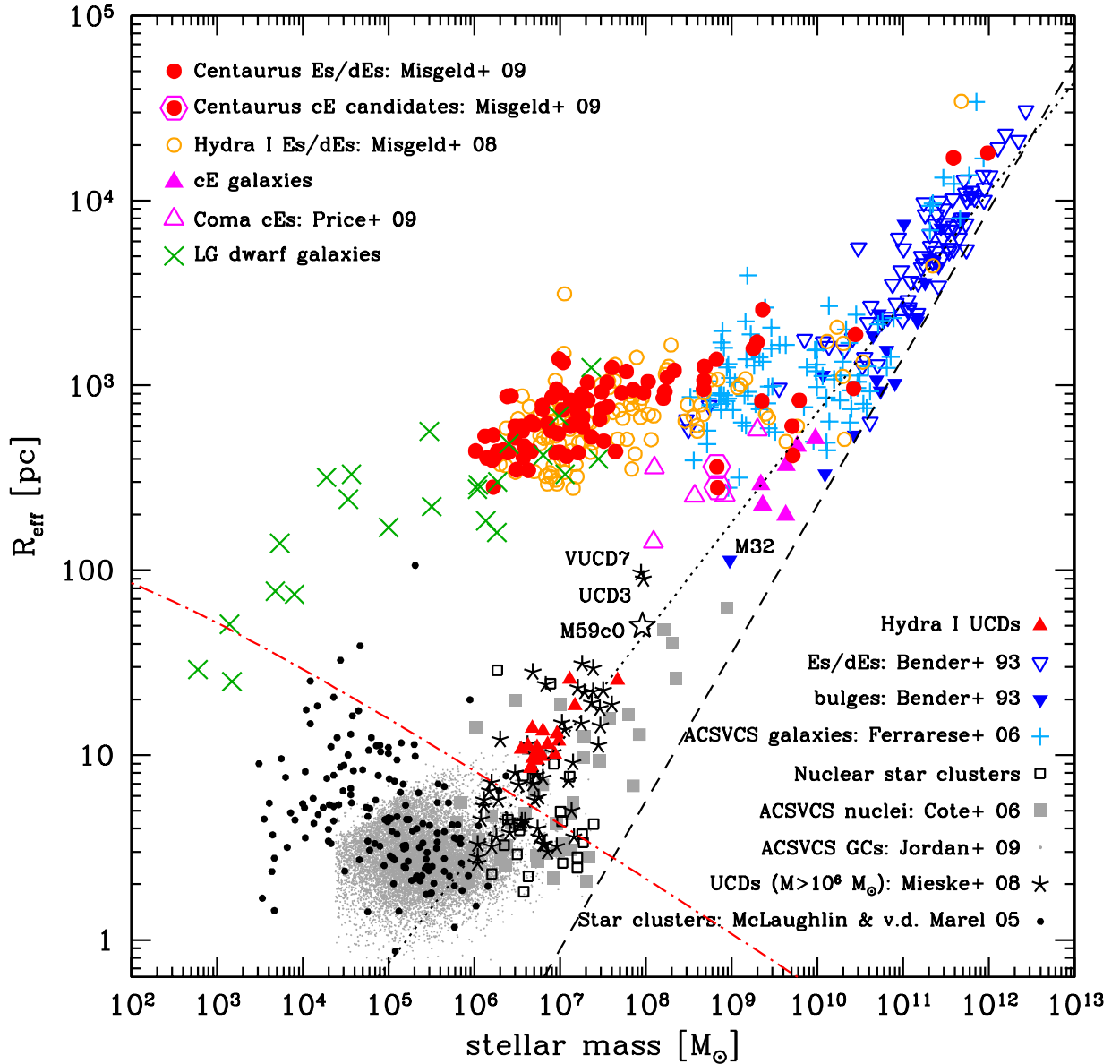
Fig. 5.4. Effective radius R_{eff} plotted versus stellar mass $M_\star$ for all objects, for which $M_\star$ was computed as outlined in Sect. 5.1.1. Symbols are as in Fig. 5.1. The dashed line represents Eq. (5.8), the dotted line is the size–mass relation from Dabringhausen et al. (2008). The (red) dash-dotted line shows Eq. (5.9) for t_{rel} equal to a Hubble time.

i.e. there is a maximum stellar mass for a given effective radius. No object, whether star cluster or galaxy, is located beyond this limit, i.e. there is a 'zone of avoidance' in the parameter space. In κ-space, this has already been noted in Burstein et al. (1997) as the 'zone of exclusion'. The boundary is illustrated by the dashed line in Fig. 5.4, which was

adapted by eye to the data. In other words, the effective radius of an object of a given mass is always larger than:

$$R_{\text{eff}}(M) \geq c_1 \cdot M_\star^{4/5}, \tag{5.8}$$

with $c_1 = 2.24 \cdot 10^{-6}$ pc $M_\odot^{-4/5}$. In between the giant elliptical galaxies and the nuclei of dE,Ns, i.e. in the mass interval $10^9 \lesssim M_\star \lesssim 10^{10}$ $M_\odot$, several compact elliptical galaxies, including M32, can be found close to this edge. Dabringhausen et al. (2008) already mentioned a common size–mass relation for UCDs and giant elliptical galaxies (see also fig. 6 in Pflamm-Altenburg & Kroupa 2009). The slope these authors found for their fitted relation is proportional to $M^{3/5}$ (see dotted line in Fig. 5.4).

Murray (2009) predicted a mass–radius relation $r_{cl} \propto M_{cl}^{3/5}$ for star clusters with an initial mass $M_{cl} \gtrsim 3 \times 10^6$ $M_\odot$, which were supported by radiation pressure during their formation process. The difference between the size–mass relation $\propto M^{3/5}$ and Eq. (5.8) can be explained by including NCs and the nuclei of dE,Ns, which are at the same mass up to ten times smaller than UCDs (see also Evstigneeva et al. 2008). These objects might have already formed more compact than isolated star clusters via recurrent gas inflow, which causes repeated star formation events (e.g. Walcher et al. 2005; Rossa et al. 2006).

It is interesting to mention the study of Gieles et al. (2010), stating that low-mass GCs might have formed with the same size–mass relation as their more massive counterparts, and have until the present day moved away from this relation because of dynamical evolution. Dabringhausen et al. (2008) give a formula for the median two-body relaxation time t_{rel} in stellar systems, which depends on the mass M and the half-light radius r_{e} of the system (their eq. (6)). Rearranging this equation gives

$$r_{\text{e}} = \left[\frac{G \left(\log \left(M/M_\odot \right) \cdot t_{\text{rel}} \right)^2}{0.0548\, M} \right]^{1/3}, \tag{5.9}$$

with $G = 0.0045$ pc^3 $M_\odot^{-1}$ Myr^{-2}. In Fig. 5.4 this relation is plotted for t_{rel} equal to a Hubble time (red dash-dotted line). Objects below this line can thus have undergone considerable dynamical evolution since their formation, provided that they are old objects. It turns out that almost all low-mass GCs ($M_\star \lesssim 10^6$ $M_\odot$) fall below this line, and that in the mass interval $10^6 \lesssim M_\star \lesssim 10^7$ $M_\odot$ the line divides very well objects which show a size-mass relation from objects which do not show such a relation (see also Fig. 5.5). This supports the picture of low-mass GCs being considerably affected by dynamical evolution, as outlined in Gieles et al. (2010). Interestingly, also the ultra-faint dwarf spheroidals Segue I and Willman I fall below this line. They are suspected to be objects out of dynamical equilibrium and close to disruption, rather than ordinary dwarf spheroidal galaxies (Gilmore et al. 2007; Niederste-Ostholt et al. 2009).

5.2.3   Galaxies and their star cluster mates

Although galaxies and star clusters occupy different locations in the R_{eff}–M_V plane, they still show intriguing parallels, like the size–mass relation which sets in above a certain mass

limit (see Sect. 5.2.2). The similarities become even more obvious when plotting the mass surface density averaged over the projected effective radius,

$$\Sigma_{\text{eff}} = M_\star / 2\pi R_{\text{eff}}^2, \tag{5.10}$$

versus the stellar mass $M_\star$, as shown in Fig. 5.5. For both star clusters and galaxies, a sequence of increasing mass surface density with increasing stellar mass becomes visible. The stellar systems with the highest mass surface densities (up to 7.5×10^5 $M_\odot$ pc^{-2}) are NCs and nuclei of dE,Ns. However, they are embedded in spiral galaxies and dwarf galaxies, respectively. The densest *isolated* systems are the most massive GCs and UCDs.

Both sequences are close to identical, except for an offset of $\sim 10^3$ in mass and $\sim 10^2$ in surface density. Above a certain stellar mass, a kink towards lower mass surface densities appears. Galaxies with $M_\star \gtrsim 5 \times 10^{10}$ $M_\odot$ as well as star clusters above $M_\star \sim 2 \times 10^6$ $M_\odot$ are arranged almost orthogonally to the main sequences. This results in a mass dependent maximum mass surface density, which is a consequence of the size–mass relation found in Fig. 5.4. Combining Eq. (5.8) and Eq. (5.10) yields

$$\Sigma_{\text{eff}}(M) \leq c_2 \cdot M_\star^{-3/5}, \tag{5.11}$$

with $c_2 = 3.17 \cdot 10^{10}$ pc^{-2} $M_\odot^{8/5}$. For comparison, Walcher et al. (2005) find the empty top right region of Fig. 5.5 to be confined by $\Sigma_{\text{eff}} \propto M^{-1/2}$, very similar to what is found here. Note, however, that they plot Σ_{eff} against the dynamical mass rather than the stellar mass.

Again, in the Σ_{eff}–$M_\star$ plane most cE galaxies reside offset to the main body of elliptical galaxies towards higher mass surface densities at a given stellar mass. This is caused by a mean size difference of ~ 730 pc between cEs (including M32) and regular elliptical galaxies in the mass range of the cEs ($10^8 \lesssim M_\star \lesssim 2 \times 10^{10}$ $M_\odot$). However, the largest cEs share the locus of normal elliptical galaxies (see also Fig. 5.1 and Fig. 5.4). Since cEs like M32 are suspected to be the result of galaxy stripping processes (e.g. Faber 1973; Bekki et al. 2001b), one would have to investigate the true formation history of each questionable object in order to decide whether it is a compact elliptical galaxy having experienced intense tidal stripping, or simply a rather small genuine elliptical galaxy. Based on their observed broad-band colours, many cEs are found redwards of the colour-magnitude relation of regular cluster early-type galaxies (e.g. Misgeld et al. 2009; Price et al. 2009, see also Fig. 4.4). This can be interpreted as support for the stripping scenario, if the progenitor galaxy was a more luminous/massive galaxy, obeying the colour-magnitude relation.

The red dash-dotted line in Fig. 5.5 shows Eq. (5.10) with R_{eff} as given by Eq. (5.9) and a median two-body relaxation time t_{rel} equal to a Hubble time. Thus, it divides the Σ_{eff}–$M_\star$ plane into an area to the left of the line, in which objects have a two-body relaxation time shorter than a Hubble time (and thus their shape parameters might be changed within a Hubble time), and into an area in which t_{rel} is longer than a Hubble time (to the right of the line). Kroupa (1998) postulated that star cluster-like objects with masses $\lesssim 10^9$ $M_\odot$ and t_{rel} longer than a Hubble time, evolved from massive stellar superclusters, which were created during gas-rich galaxy mergers (see also Fellhauer & Kroupa 2002). Figure 5.5 now suggests that UCDs with masses $\gtrsim 2 \times 10^6$ $M_\odot$ could indeed be the descendants of
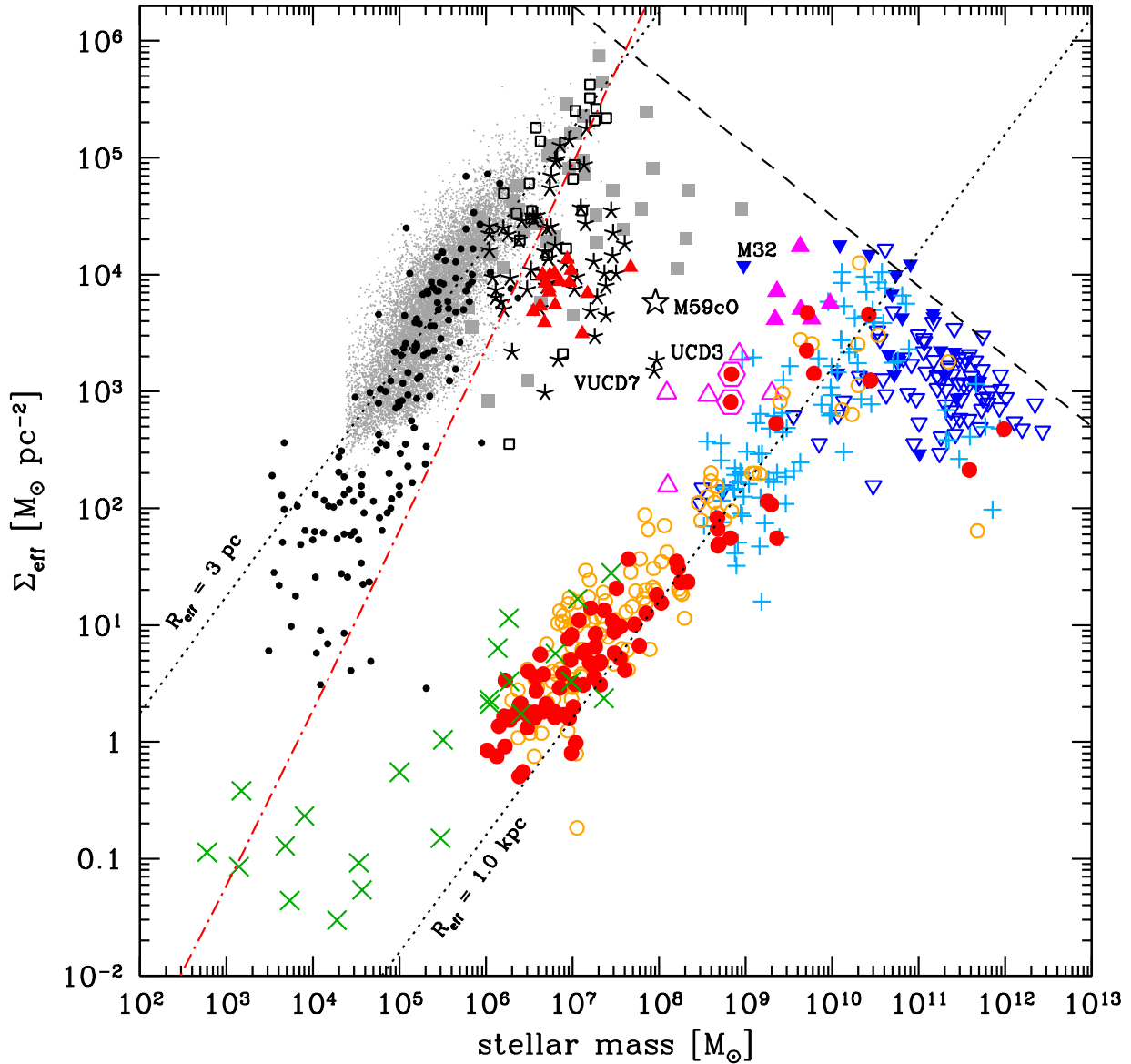
Fig. 5.5. Mass surface density averaged over the projected effective radius, $\Sigma_{\mathrm{eff}} = M_\star/2\pi R_{\mathrm{eff}}^2$, plotted versus stellar mass $M_\star$ for all objects from Fig. 5.4. The dashed line represents Eq. (5.11), the dotted lines mark the loci of objects with a constant radius of $R_{\mathrm{eff}} = 1.0$ kpc and $R_{\mathrm{eff}} = 3$ pc. The (red) dash-dotted line shows Eq. (5.10) with R_{eff} as given by Eq. (5.9) and t_{rel} equal to a Hubble time.

such stellar superclusters. The most massive UCDs are in fact observed in high density regions, i.e. galaxy clusters, where the central giant elliptical galaxies most probably formed via violent dissipative processes, like intense starbursts or early, gas-rich galaxy mergers. Interestingly, massive young clusters (with $M_\star > 10^7 \, \mathrm{M_\odot}$) in starburst and merging galaxies already show a size–mass relation similar to those of UCDs (Kissler-Patig et al. 2006).
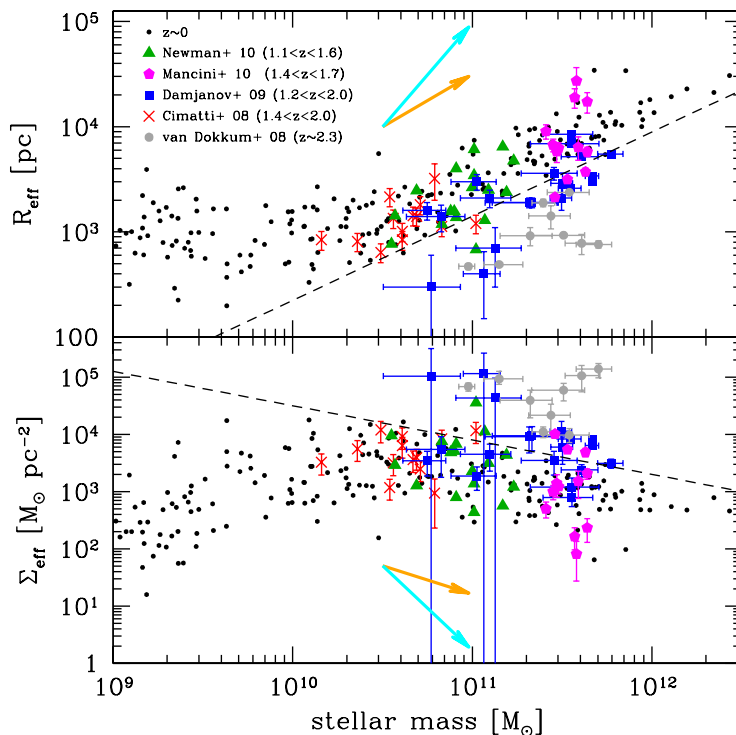
Fig. 5.6. Enlargement of Fig. 5.4 (*upper panel*) and Fig. 5.5 (*lower panel*). Only 'galaxy-like' objects with $M_\star > 10^9$ M$_\odot$ are plotted (black dots). The coloured symbols denote high redshift early-type galaxies. The orange (cyan) vectors indicate the size/surface density evolution according to the virial theorem for major (minor) galaxy mergers. The length of the vectors indicates a mass increase by a factor of 3.

5.2.4   Zone of avoidance

The sharply defined maximum stellar mass for a given half-light radius (Eq. (5.8)), which translates into a maximum mass surface density (Eq. (5.11)), is evident for giant elliptical galaxies as well as for cEs, UCDs, nuclei of dE,Ns and NCs. No galaxy in the local Universe is found in the 'zone of avoidance' beyond this boundary. This raises the question of whether it is coincidence or a physical law that causes this phenomenon.

In Fig. 5.6, the distribution of local early-type galaxies (ETGs) and high-redshift ($1.1 \lesssim z \lesssim 2.3$) ETGs is compared in the $R_{\rm eff}$–$M_\star$ and the $\Sigma_{\rm eff}$–$M_\star$ planes. The high-z ETGs are taken from Cimatti et al. (2008), van Dokkum et al. (2008), Damjanov et al. (2009), Mancini et al. (2010) and Newman et al. (2010), and have stellar masses of $2 \times 10^{10} \lesssim M_\star \lesssim 5 \times 10^{11}$ M$_\odot$. The position of most of the high-z ETGs is fully consistent with their $z \sim 0$ counterparts, i.e. also the high-redshift galaxies are not located beyond the critical boundaries given by Eqs. (5.8) and (5.11).

An exception is the sample from van Dokkum et al. (2008). At a given stellar mass these ETGs have significantly smaller effective radii, corresponding to effective surface densities being several times higher than those of local ETGs. However, Mancini et al. (2010) showed that the sizes of high-z ETGs can be underestimated by up to a factor of 3 at low S/N, preventing the detection of extended low surface brightness profiles, which

are typical for massive elliptical galaxies. The underestimation of the profile shape index n can also lead to a wrong determination of the effective radius R_{eff} (see Hopkins et al. 2009). Moreover, the stellar mass estimates decisively depend on the choice of the stellar population model. The ETG masses in the van Dokkum et al. (2008) sample are derived from Bruzual & Charlot (2003) models, thus, they are $\approx$ 40–50% higher than masses derived from Maraston (2005) models (Maraston et al. 2006; Cimatti et al. 2008; Mancini et al. 2010). Given these possible sources of size underestimation and mass overestimation, respectively, the van Dokkum et al. (2008) ETGs might still be consistent with the $z \sim 0$ objects.

Based on the virial theorem it can be shown that the radius r of an evolving ETG increases linearly with stellar mass in the case of major mergers, and as the square of the mass in the case of minor mergers (e.g. Naab et al. 2009). Indeed, there is observational evidence that the most massive ellipticals follow a linear one-to-one relation between r and $M_\star$ (Tiret et al. 2010). Regardless of which process, major or minor mergers, is mainly responsible for their subsequent mass assembly, the high-z ETGs will move approximately along the boundary ($r \propto M_\star$), or away from it ($r \propto M_\star^2$), but they will not move across the limit (see Fig. 5.6).

The slope of the size–mass relation of the local ETGs is consistent with major merger evolution. The scatter might be caused by the effects of minor mergers. Even very compact high-z ETGs (e.g. van Dokkum et al. 2008) can end up on the size–mass relation of $z \sim$ 0 galaxies via successive major and minor mergers (cf. Fig. 5.6). This reinforces the interpretation of the 'zone of avoidance' for $z \sim 0$ ETGs as the result of galaxy evolution.

5.2.5   Internal accelerations

The acceleration a star experiences at the effective radius inside a pressure-supported system is

$$a_{\mathrm{eff}} = \frac{GM}{R_{\mathrm{eff}}^2}, \tag{5.12}$$

where $M = 0.5 \cdot M_\star$ is the stellar mass within R_{eff}. Combining this with Eq. (5.10) yields the mass surface density as a function of a_{eff}:

$$\Sigma(a_{\mathrm{eff}}) = \frac{a_{\mathrm{eff}}}{\pi G}. \tag{5.13}$$

Setting $a_{\mathrm{eff}} = a_0 = 3.9$ pc Myr^{-2}, which is the critical acceleration parameter in the theory of modified Newtonian dynamics (MOND, Milgrom 1983), the mass surface density dividing the Newtonian from the MONDian regime is $\Sigma_{a_0} = 275.9$ M$_\odot$ pc^{-2}. This is indicated in Fig. 5.7 by the shaded area (see also fig. 7 in Kroupa et al. 2010).

Except for several very low mass GCs, dwarf galaxies with stellar masses below $\sim$ 10^8 M$_\odot$ are the only objects residing deep in the MONDian regime ($a_{\mathrm{eff}} < a_0$). Apparently, the limit Σ_{a_0} is not connected to a change in the structural properties of the galaxies, as the sequence of increasing mass surface density continues up to $M_\star \sim 10^{10}$ M$_\odot$. It is, however, interesting to note that these low mass dwarf galaxies are the only objects
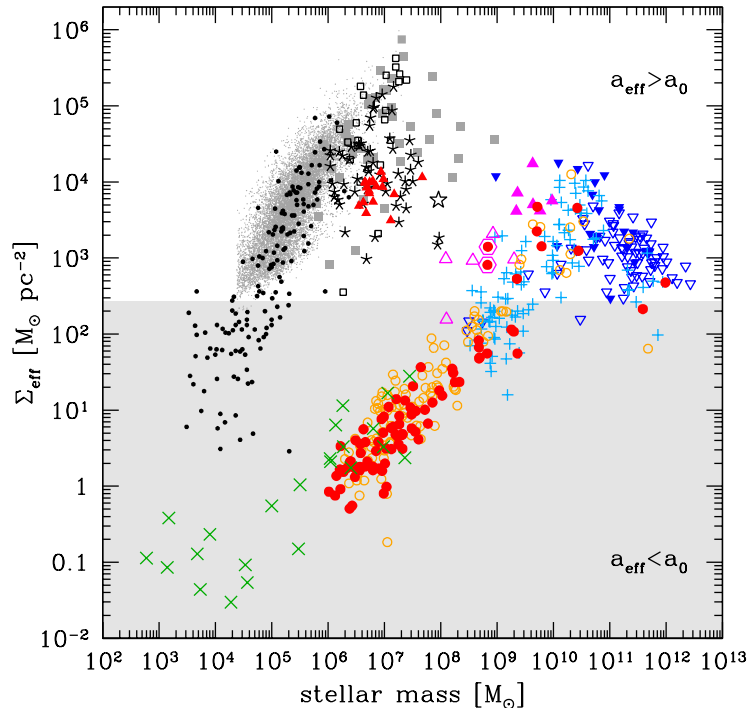
Fig. 5.7. Same as Fig. 5.5, but with the region shaded, in which a star in the stellar system experiences at the effective radius an acceleration smaller than $a_0 = 3.9$ pc Myr^{-2}.

which exhibit very high dynamical mass-to-light ratios (e.g. Dabringhausen et al. 2008; Forbes et al. 2008). Kroupa et al. (2010) discuss this phenomenon in a cosmological context, and conclude that the combination of high dynamical mass-to-light ratios with $a < a_0$ is natural in a MONDian universe.

5.3 Summary and conclusions

In this chapter it was shown that scaling relations of dynamically hot stellar systems can be studied over a remarkable range in parameter space. Besides giant elliptical galaxies and GCs, large samples of cEs, UCDs, dwarf elliptical galaxies of nearby galaxy clusters, and Local Group ultra-faint dwarf spheroidals were included for the first time. In this way, a smooth sampling of the $R_{\rm eff}$–M_V plane, the $R_{\rm eff}$–$M_\star$ plane, and the $\Sigma_{\rm eff}$–$M_\star$ plane was achieved over ten orders of magnitude in stellar mass and five orders of magnitude in effective radius.

One of the main features in the $R_{\rm eff}$–M_V plane is the almost constant effective radius of galaxies in a certain magnitude range ($-20 \lesssim M_V \lesssim -12$ mag). Under the assumption that this is true for galaxies in all local galaxy clusters, this feature was used to determine the distances to Hydra I, Centaurus, Virgo, Antlia and Fornax, for which the structural parameters of a sufficiently large number of galaxies in the right magnitude range are available (Sect. 5.2.1). It turns out that the distance estimations are in good agreement

with the distances obtained with other methods, although the values derived here have rather large errors.

Star clusters and galaxies form two different families, well distinguishable in terms of their structural properties size and mass surface density. However, a closer look at the $R_{\rm eff}$–$M_\star$ and the $\Sigma_{\rm eff}$–$M_\star$ planes reveals some intriguing common features (see Fig. 5.4 and Fig. 5.5). For example, the similar size–mass relation of giant elliptical galaxies, cEs, UCDs, nuclei of dE,Ns and NCs, which sharply defines a maximum stellar mass for a given half-light radius (Eq. (5.8)), translating into a maximum mass surface density, as given by Eq. (5.11), creating a 'zone of avoidance' beyond these limits. Not only local early-type galaxies do not appear beyond these limits, but also most of the high-redshift galaxies ($1 \lesssim z \lesssim 2$) presented here coincide with their local counterparts in the size/surface density–mass plane (see Fig. 5.6). Given the uncertain estimates of stellar masses and effective radii of some of the high-z galaxies (e.g. van Dokkum et al. 2008), they might already at this time be consistent with the $z \sim 0$ objects, or they might evolve onto the relations observed for the local galaxies via subsequent merging events (Sect. 5.2.4). However, present data on the structural parameters and stellar masses of high-z ETGs are still rather limited. High quality data for a larger number of ETGs are required to be able to reach a definite conclusion on whether or not these objects are structurally different from their local counterparts.

The slope of the size–mass relation for giant elliptical galaxies is consistent with $r \propto M_\star$. This slope is predicted by the virial theorem for major galaxy mergers (see Sect. 5.2.4). UCDs, NCs and nuclei of dE,Ns, on the other hand, can also be created by merger events (e.g. Kroupa 1998; Walcher et al. 2005; Capuzzo-Dolcetta & Miocchi 2008). Depending on the actual cluster orbital energy, the size–mass relation for merged stellar clusters is $R \propto M^\beta$, with $0.5 < \beta < 1$ (Merritt, unpublished[2]), well in agreement with the observed slopes of $R_{\rm eff} \propto M^{3/5}$ or $R_{\rm eff} \propto M^{4/5}$. If regarding the size–mass relation as the consequence of a maximum possible stellar mass density, this might tell us something about how stars can be distributed in unrelaxed stellar systems (the median two-body relaxation time is longer than a Hubble time for these objects).

In this chapter, the mean mass surface density within the half-light radius was examined. This radius is for giant elliptical galaxies at least 20 times larger than for star clusters. Hence, regions of very different size are probed. A better measure would be the surface density in the very central part of the particular object. Hopkins et al. (2010) determined this quantity for a variety of stellar systems and indeed found a maximum central stellar surface density of $\Sigma_{\rm max} \sim 10^{11}$ M$_\odot$ kpc^{-2}. They concluded that feedback from massive stars likely accounts for the observed $\Sigma_{\rm max}$. Unfortunately, the central density is not available with a sufficient completeness for all the stellar systems presented in this chapter.

The scaling relations presented here also allow to study possible formation and evolutionary scenarios, in particular those of compact stellar systems like UCDs. In contrast to usual globular clusters, these enigmatic objects exhibit a size–mass relation and enhanced

---

[2]see also presentation at ESO workshop 'Central Massive Objects: The Stellar Nuclei - Black Hole Connection', http://www.eso.org/sci/meetings/cmo2010/Presentations/Day2/Merritt-rev.pdf

mass-to-light ratios (e.g. Mieske et al. 2008). Their location in the Σ_{eff}–$M_\star$ plane (Fig. 5.5) indicates that they are also dynamically distinct from globular clusters. With a two-body relaxation time longer than a Hubble time, they are more closely related to galaxy-like stellar systems than to regular star clusters, which have undergone considerable dynamical evolution.

In order to better understand the similarities and differences between galaxies and star clusters, and also within each family of objects, one would have to measure homogeneously the line of sight velocity dispersion along with the structural and photometric parameters (size, luminosity or surface brightness) for all of those objects. Such data would allow to explore different FP relations (e.g. the Faber-Jackson relation, Faber & Jackson 1976), or the phase-space density (e.g. Walcher et al. 2005; Gilmore et al. 2007) of the entire spectrum of dynamically hot stellar systems. First studies aiming in this direction revealed interesting possible connections between galaxies and star clusters (e.g. Zaritsky et al. 2006a,b, 2011; Forbes et al. 2008, 2011). However, all of these studies are lacking in large samples of low mass dwarf elliptical/spheroidal galaxies ($M_\star \lesssim 10^9\ \mathrm{M}_\odot$), since it is still challenging (or even impossible) to obtain accurate velocity dispersions for such low surface brightness objects. This will be a promising science case for future ground- and space-based telescopes like the E-ELT or the JWST.

Chapter 6

Summary and outlook

In this thesis, the properties of early-type stellar systems in the nearby galaxy clusters Hydra I and Centaurus have been investigated, in particular focusing on the characterization of early-type dwarf galaxies (dEs and dSphs) and the so-called ultra-compact dwarf galaxies (UCDs).

In Chapter 2 and 4, dwarf galaxies have been identified in Hydra I and Centaurus, using morphological selection criteria and scaling relations between luminosity, colour and surface brightness. The galaxy luminosity function (GLF) has been constructed from the completeness corrected number counts. It turned out that the faint-end slope of the GLF is much shallower than the slope of the mass spectrum of cosmological dark-matter haloes predicted by hierarchical cold dark matter models of galaxy formation. This result is consistent with the observations made in other nearby galaxy clusters like Fornax, Virgo and Coma. Potential sources of errors in the construction of the GLF and possible reasons for the discrepancy between observations and theory have been discussed.

In Chapter 3, the discovery of a large number of UCDs in the Hydra I galaxy cluster has been presented. The UCDs have been identified by means of spectroscopic redshift measurements, and their basic parameters luminosity, colour and size have been compared to UCDs from other galaxy clusters. The brightest UCD in Hydra I is one of the most massive UCDs ever discovered. Moreover, the dynamics of the GC/UCD system have been investigated. It turned out that the brightest UCDs have a significantly lower velocity dispersion than a sample of fainter objects. This result has been interpreted in the context of different UCD formation channels.

In Chapter 5, luminosity, size, stellar mass and projected mass surface density of the Hydra I and Centaurus dwarf galaxies have been compared to other early-type stellar systems, such as massive elliptical galaxies, ultra-faint Local Group dwarf spheroidals, UCDs and GCs, resulting in a parameter space coverage of 25 orders of magnitude in luminosity, 10 orders of magnitude in mass and 5 orders of magnitude in size.

In summary, it has been shown that the detailed morphological examination of faint dwarf galaxies, which has until recently been limited to the Local Group and the rather nearby clusters Fornax and Virgo, can also be performed in the more distant clusters Hydra I and Centaurus, using deep imaging from 8 m-class telescopes like the VLT. Moreover,

extensive spectroscopic surveys with multi-object spectrographs like VIMOS allowed to identify dwarf galaxies and UCDs in in large numbers in those clusters, broadening the environmental baseline of dwarf galaxy/UCD studies.

6.1   Future prospects

In order to further advance the research in the areas addressed in this thesis, spectroscopic as well as photometric follow-up observations have to be performed. First results from a spectroscopic survey of faint dwarf galaxies in the Hydra I and Centaurus cluster have been presented in Sects. 2.4 and 4.3. The obtained data will allow to thoroughly determine the faint end of the GLF, using direct cluster membership assignment, in order to (dis-)prove the predictions of CDM models of galaxy formation. With this extended data set, now adding Hydra I and Centaurus to the well studied clusters Fornax and Virgo and the Local Group, it will be possible to investigate in an unbiased way how the faint-end slope of the GLF varies with cluster properties: how does the shape of the GLF and the overall frequency of dwarfs scale with host cluster mass/density, evolutionary state?

By analysing the photometric and structural parameters of confirmed cluster galaxies, the investigation of photometric scaling relations of cluster early-type galaxies on the basis of a large, redshift-selected samples can be continued. This includes the colour-magnitude relation (CMR), the magnitude-surface brightness relation and the distribution of the cluster galaxies in the size–luminosity plane. With a large sample of cluster galaxies one can probe the scatter of the CMR and the magnitude-surface brightness relation. A true scatter in these relations that is not caused by observational errors would point to different evolutionary paths of dwarf galaxies (e.g. Janz & Lisker 2009). Together with age/metallicity estimates, this will provide further insight into the diversity of dwarf galaxies.

However, probing dwarf galaxies only in the core regions of galaxy clusters will not result in a complete picture. Therefore, multi-band wide field imaging is required to characterize the dwarf galaxy population across the entire cluster. What is the abundance of dwarf galaxies as a function of cluster-centric distance? How do the luminosity function and the basic scaling relations (e.g. the CMR) depend on the probed region? What is the ratio of early-type to late-type dwarf galaxies? What is the evolutionary state of dwarf galaxies in the outer region of a cluster in comparison to the core region? New survey telescopes like VISTA and VST are the ideal tools to perform these kinds of observations.

Important information is also contained in the kinematics of dwarf galaxies in clusters, which allow a deeper insight into the connection of the dwarf galaxy population to the cluster as a whole. Because of their large number, dwarf galaxies are ideal tracers for the velocity structure and mass distribution in clusters. Drinkwater et al. (2001) performed a dynamical analysis of a sample of 108 Fornax cluster galaxies. For 55 dwarf galaxies with $-16 < M_B < -13.5$ mag they found a larger velocity dispersion ($\sigma_v = 429 \pm 41$ km s^{-1}) than for 53 giant galaxies ($\sigma_v = 308 \pm 30$ km s^{-1}). They concluded that the dwarf galaxies form a distinct population, being dominated by in-falling objects, whereas the giants are virialized. Whether this also holds for other clusters has to be tested.

During the past decade, UCDs have been discovered in large numbers in the galaxy clusters Fornax, Virgo, Coma, Centaurus and Hydra I (see Chapter 3). However, up to now, only a few UCDs have been found in low-density environments. Therefore, a systematic study of UCDs in low-density environments has to be performed, as Norris & Kannappan (2011) started to do in three field/group environments. Using the recently available VISTA science verification data, which includes deep imaging of the nearby edge-on spiral galaxy NGC 253, it will be possible to investigate how frequent massive UCDs are in yet another low-density environment. This can be compared to the central regions of massive galaxy clusters and to the Local Group. What is the luminosity range and the spatial distribution of UCDs in comparison to the overall globular cluster system? Do UCDs represent the high-mass end of the GC luminosity function, or are they a separate class of objects?

Following the photometric identification and characterization of GCs/UCDs, spectroscopic follow-up observations are eligible, in order to verify their nature and to investigate their kinematics and stellar population content. Measuring line indices of confirmed UCDs will allow to compare their α abundances to those published for UCDs in Fornax, Virgo and Centaurus (e.g. Mieske et al. 2006, 2007b; Evstigneeva et al. 2007b), as well as to (nucleated) dwarf elliptical galaxies (e.g. Geha et al. 2003; Michielsen et al. 2007). This will tackle the question of whether or not the dE/dE,N population is the parent population of UCDs.

A further goal must be to study the *internal* dynamics of UCDs, in order to derive dynamical masses and mass-to-light ratios. For this, high-resolution spectra have to be obtained, using e.g. VLT/FLAMES, which allows the observation of up to 130 targets at the same time over a 25 arcmin diameter field of view (e.g. Mieske et al. 2008; Chilingarian et al. 2011). These data will allow to analyse how the M/L ratios relate to predictions from stellar population models, and how they fit into the trend of increasing M/L with mass among compact stellar systems. Are high M/L ratios a fundamental trend equally common to all UCDs, or do environmental variations of this trend exist? The latter may be expected if competing formation channels dominate in different environments.

Finally, the ultimate test to discriminate between possible UCD formation scenarios is to study their stellar population content over the full spectral range, from the UV to the NIR. With the new VLT/XSHOOTER instrument this is possible for bright UCDs out to the distance of the Virgo cluster. By comparing the full spectral energy distribution (SED) with available empirical and theoretical population synthesis models, it will be possible to tackle the key scientific questions of whether UCDs contain *single* or *multiple* stellar populations and whether the chemical compositions of UCDs resemble those of their possible progenitors (dwarf galaxy nuclei). Multiple stellar populations in UCDs would suggest that they formed via the successive merging of star clusters (not necessarily having the same age and chemical composition) into a nuclear star cluster, or via the episodic star formation triggered by the infall of gas over several Gyr. On the other hand, if UCDs originate either from the merging of young massive star clusters, which formed under similar conditions during gas-rich galaxy mergers, or from the collapse of a single massive molecular cloud, one would expect a narrow range of ages and a moderate spread in metallicity, well described by a single stellar population.

Appendix A

Tables

Table A.1 gives the photometric calibration coefficients for the 7 observed Hydra I fields, as indicated in Fig. 2.4. Zero points (ZP), extinction coefficients k and colour terms (CT) are given for the two filters V and I.

Table A.1. Photometric calibration coefficients of the VLT/FORS1 fields in Hydra I.

Field	ZP_V	ZP_I	k_V	k_I	CT_V	CT_I
1	27.477	26.629	-0.160	-0.090	0.04	-0.04
2	27.529	26.643	-0.160	-0.090	0.04	-0.04
3	27.529	26.643	-0.160	-0.090	0.04	-0.04
4	27.529	26.643	-0.160	-0.090	0.04	-0.04
5	27.532	26.665	-0.160	-0.090	0.04	-0.04
6	27.532	26.665	-0.160	-0.090	0.04	-0.04
7	27.532	26.679	-0.160	-0.090	0.04	-0.04

Table A.2 lists the photometric parameters of the sample of 111 early-type galaxies in the Hydra I cluster. The table is ordered by increasing apparent magnitude. The first column gives the object ID, in which HCC stands for Hydra I Cluster Catalogue. Right ascension and declination (J2000.0) are given in columns two and three. The fourth and fifth column list the extinction corrected magnitude V_0 and the colour $(V - I)_0$. In columns six and seven, the central surface brightness $\mu_{V,0}$ and the scale length h_R of an exponential fit to the surface brightness profile are listed. For objects with $V_0 \leq 16.1$ mag, $\mu_{V,0}$ and h_R are not given, since the surface brightness profile is not well described by an exponential law. Columns eight, nine and ten give the effective surface brightness μ_{e}, the effective radius R_{e} and the profile shape index n, as obtained from a Sérsic fit. The physical scale is 0.2 kpc/arcsec at the assumed distance modulus of $(m - M) = 33.07$ mag (Mieske et al. 2005a). The last column gives the radial velocities derived in this study as well as those from CZ03. Table A.2 is available in a machine readable form at the CDS (J/A+A/486/697).

Table A.2. The Hydra I Cluster Catalogue (HCC).

ID	$\alpha(2000.0)$ [h:m:s]	$\delta(2000.0)$ [°:′:″]	V_0 [mag]	$(V-I)_0$ [mag]	$\mu_{V,0}$ [mag arcsec^{-2}]	h_R [arcsec]	μ_e [mag arcsec^{-2}]	R_e [arcsec]	n	$v_{\rm rad}$ [km s^{-1}]
HCC-001[c]	10:36:42.8	-27:31:42.0	10.93 ± 0.01	1.26 ± 0.02			24.30 ± 0.01	150.25 ± 0.34	4.00	3818 ± 45
HCC-002[d]	10:36:35.7	-27:31:06.4	11.78 ± 0.02	1.27 ± 0.04			21.15 ± 0.01	19.35 ± 0.03	3.43	4099 ± 27
HCC-003[b,e]	10:36:22.4	-27:26:17.3	12.36 ± 0.01	1.25 ± 0.01						3614 ± 29
HCC-004[b,f]	10:37:37.3	-27:35:39.4	13.03 ± 0.01	1.26 ± 0.01						3976 ± 14
HCC-005	10:36:27.7	-27:19:10.8	13.78 ± 0.01	1.25 ± 0.01			19.90 ± 0.01	5.84 ± 0.01	2.24	3376 ± 20
HCC-006	10:36:44.9	-27:28:10.1	14.06 ± 0.01	1.17 ± 0.01			18.67 ± 0.02	2.23 ± 0.01	2.66	2735 ± 80^a
HCC-007	10:36:41.2	-27:33:39.6	14.18 ± 0.01	1.19 ± 0.01			20.70 ± 0.01	7.36 ± 0.01	2.09	4830 ± 13
HCC-008[b]	10:37:20.1	-27:33:35.6	14.21 ± 0.01	1.20 ± 0.01						4069 ± 14
HCC-009	10:36:29.0	-27:29:02.2	14.32 ± 0.01	1.18 ± 0.01			21.49 ± 0.01	9.00 ± 0.02	1.96	4774 ± 80^a
HCC-010	10:36:23.0	-27:21:16.8	14.40 ± 0.01	1.27 ± 0.01			20.35 ± 0.01	4.88 ± 0.01	1.75	3059 ± 18
HCC-011	10:36:24.8	-27:34:54.8	14.61 ± 0.01	1.18 ± 0.01			21.57 ± 0.00	7.54 ± 0.02	2.12	2895 ± 20
HCC-012[b]	10:36:35.0	-27:28:45.4	14.85 ± 0.01	1.16 ± 0.01						4708 ± 17
HCC-013	10:36:35.5	-27:28:13.6	15.23 ± 0.01	1.13 ± 0.01			20.01 ± 0.01	2.63 ± 0.01	1.91	3199 ± 13
HCC-014	10:36:49.1	-27:23:20.0	15.81 ± 0.01	1.18 ± 0.01			20.32 ± 0.01	2.17 ± 0.01	2.44	4474 ± 80^a
HCC-015	10:37:38.1	-27:35:58.8	16.10 ± 0.01	1.12 ± 0.01			21.17 ± 0.00	3.05 ± 0.01	1.35	3995 ± 14
HCC-016	10:36:56.9	-27:34:03.5	16.40 ± 0.01	1.20 ± 0.02	20.01 ± 0.03	2.10 ± 0.02	21.36 ± 0.01	2.91 ± 0.01	1.64	4468 ± 24
HCC-017	10:36:42.7	-27:35:08.7	16.51 ± 0.01	1.08 ± 0.01	20.64 ± 0.01	3.23 ± 0.02	22.15 ± 0.01	4.74 ± 0.02	1.50	3572 ± 29
HCC-018	10:37:47.0	-27:34:21.8	16.53 ± 0.01	1.04 ± 0.01	20.01 ± 0.01	2.62 ± 0.02	21.84 ± 0.01	4.39 ± 0.01	0.98	4861 ± 53
HCC-019	10:36:52.6	-27:32:14.7	16.82 ± 0.02	1.10 ± 0.03	20.79 ± 0.02	2.53 ± 0.02	22.63 ± 0.02	4.24 ± 0.04	1.66	5735 ± 55
HCC-020	10:36:26.9	-27:23:25.6	17.19 ± 0.01	1.04 ± 0.02	20.80 ± 0.01	2.82 ± 0.01	22.60 ± 0.01	4.71 ± 0.02	0.95	4223 ± 49
HCC-021	10:37:17.3	-27:35:33.7	17.57 ± 0.03	1.09 ± 0.04	21.45 ± 0.02	2.66 ± 0.03	23.41 ± 0.02	4.67 ± 0.06	1.38	3700 ± 41
HCC-022	10:36:40.4	-27:32:56.5	17.67 ± 0.03	0.99 ± 0.04	20.46 ± 0.02	1.56 ± 0.02	22.17 ± 0.01	2.46 ± 0.01	1.38	4605 ± 37
HCC-023	10:36:48.9	-27:30:01.9	17.77 ± 0.04	1.09 ± 0.07	21.54 ± 0.07	2.52 ± 0.07	23.23 ± 0.02	3.99 ± 0.04	1.16	4479 ± 44
HCC-024	10:36:50.2	-27:30:47.7	17.77 ± 0.02	0.98 ± 0.03	20.81 ± 0.02	1.71 ± 0.02	22.71 ± 0.02	2.94 ± 0.03	1.35	5270 ± 32
HCC-025	10:37:13.7	-27:30:25.2	17.87 ± 0.05	1.11 ± 0.07	21.10 ± 0.03	1.79 ± 0.02	22.99 ± 0.03	3.04 ± 0.05	1.61	2879 ± 37
HCC-026	10:36:46.0	-27:31:25.1	17.87 ± 0.08	0.93 ± 0.05	21.13 ± 0.03	2.02 ± 0.03	23.00 ± 0.04	3.43 ± 0.06	1.30	4225 ± 159^a
HCC-027	10:36:45.7	-27:30:32.1	18.05 ± 0.06	1.13 ± 0.09	21.49 ± 0.04	2.03 ± 0.04	23.36 ± 0.02	3.42 ± 0.04	1.36	5251 ± 89^a
HCC-028	10:36:43.1	-27:25:30.1	18.10 ± 0.01	1.12 ± 0.01	20.92 ± 0.01	1.59 ± 0.01	22.73 ± 0.01	2.65 ± 0.01	1.10	3937 ± 38
HCC-029	10:37:00.2	-27:29:53.4	18.20 ± 0.01	1.06 ± 0.01	20.90 ± 0.02	1.72 ± 0.01	22.66 ± 0.01	2.80 ± 0.01	1.13	3275 ± 47
HCC-030	10:36:50.8	-27:23:02.3	18.36 ± 0.01	0.88 ± 0.01	22.01 ± 0.02	3.00 ± 0.04	24.05 ± 0.01	5.53 ± 0.02	1.40	4306 ± 134^a
HCC-031	10:38:04.6	-27:32:44.9	18.42 ± 0.01	0.98 ± 0.02	23.06 ± 0.01	4.66 ± 0.03	24.73 ± 0.01	7.22 ± 0.05	1.18	2418 ± 256^a
HCC-032	10:36:26.0	-27:35:51.6	18.47 ± 0.01	0.93 ± 0.01	22.52 ± 0.01	3.15 ± 0.01	24.35 ± 0.01	5.30 ± 0.02	1.01	
HCC-033	10:37:48.9	-27:33:03.0	18.53 ± 0.02	0.94 ± 0.02	22.68 ± 0.01	3.04 ± 0.01	24.47 ± 0.01	5.01 ± 0.02	0.94	
HCC-034	10:36:58.6	-27:34:26.3	19.02 ± 0.09	0.94 ± 0.11	22.20 ± 0.07	1.93 ± 0.07	23.96 ± 0.10	3.05 ± 0.18	1.06	4962 ± 79
HCC-035	10:36:32.5	-27:32:23.3	19.15 ± 0.02	1.07 ± 0.03	22.27 ± 0.02	1.78 ± 0.02	24.10 ± 0.01	2.98 ± 0.01	1.11	
HCC-036	10:36:41.3	-27:23:36.7	19.23 ± 0.02	0.79 ± 0.02	23.32 ± 0.02	3.43 ± 0.04	25.31 ± 0.01	6.19 ± 0.04	1.26	
HCC-037	10:36:43.1	-27:35:43.5	19.25 ± 0.01	0.92 ± 0.02	22.58 ± 0.02	2.09 ± 0.02	24.37 ± 0.01	3.49 ± 0.01	0.90	
HCC-038	10:36:28.7	-27:14:36.4	19.32 ± 0.01	0.67 ± 0.01	20.86 ± 0.01	0.91 ± 0.01	22.70 ± 0.01	1.54 ± 0.01	0.96	3989 ± 80^a
HCC-039	10:36:38.8	-27:25:07.9	19.37 ± 0.02	1.03 ± 0.04	22.81 ± 0.02	2.28 ± 0.02	24.57 ± 0.01	3.72 ± 0.01	0.80	
HCC-040	10:37:39.6	-27:35:32.7	19.76 ± 0.02	1.01 ± 0.04	22.14 ± 0.03	1.37 ± 0.02	23.90 ± 0.01	2.23 ± 0.01	1.10	2758 ± 75
HCC-041	10:36:43.7	-27:17:29.9	19.81 ± 0.01	0.97 ± 0.02	22.38 ± 0.02	1.75 ± 0.02	24.19 ± 0.01	2.89 ± 0.02	1.42	
HCC-042	10:36:35.9	-27:19:36.2	19.84 ± 0.01	0.71 ± 0.01	23.27 ± 0.03	2.71 ± 0.04	25.10 ± 0.01	4.62 ± 0.02	0.59	
HCC-043	10:36:40.6	-27:25:19.1	19.84 ± 0.03	1.09 ± 0.05	22.93 ± 0.02	1.94 ± 0.02	24.76 ± 0.01	3.27 ± 0.02	0.91	
HCC-044	10:36:45.1	-27:14:29.4	19.88 ± 0.03	1.10 ± 0.04	23.47 ± 0.03	2.27 ± 0.03	25.24 ± 0.02	3.77 ± 0.03	0.76	
HCC-045	10:36:44.4	-27:31:22.8	19.91 ± 0.12	1.23 ± 0.16	24.66 ± 0.17	2.67 ± 0.24	24.10 ± 0.02	2.22 ± 0.03	1.72	4252 ± 60
HCC-046	10:37:23.1	-27:35:56.7	19.93 ± 0.02	0.89 ± 0.03	23.91 ± 0.02	3.51 ± 0.06	25.62 ± 0.03	5.66 ± 0.10	0.81	
HCC-047	10:36:33.8	-27:27:41.1	19.94 ± 0.03	0.96 ± 0.04	22.60 ± 0.04	1.46 ± 0.02	24.23 ± 0.01	2.24 ± 0.01	1.11	
HCC-048	10:37:11.3	-27:31:30.3	20.01 ± 0.02	1.14 ± 0.03	21.72 ± 0.03	1.09 ± 0.01	23.57 ± 0.01	1.86 ± 0.01	0.78	2876 ± 38
HCC-049	10:37:56.0	-27:32:41.9	20.05 ± 0.02	0.94 ± 0.03	23.04 ± 0.02	1.84 ± 0.02	24.86 ± 0.02	3.12 ± 0.02	0.84	
HCC-050	10:37:39.1	-27:33:42.3	20.11 ± 0.06	0.87 ± 0.07	23.88 ± 0.02	2.65 ± 0.03	25.77 ± 0.05	4.62 ± 0.14	1.11	
HCC-051	10:38:04.7	-27:32:22.5	20.12 ± 0.01	1.06 ± 0.02	22.56 ± 0.03	1.97 ± 0.03	24.29 ± 0.01	3.21 ± 0.02	0.68	
HCC-052	10:36:55.4	-27:35:55.1	20.25 ± 0.01	1.16 ± 0.01	23.36 ± 0.03	2.22 ± 0.05	25.02 ± 0.03	3.45 ± 0.05	0.72	
HCC-053	10:37:03.7	-27:35:47.7	20.30 ± 0.02	1.27 ± 0.03	22.96 ± 0.04	1.76 ± 0.04	24.76 ± 0.02	2.93 ± 0.03	0.82	
HCC-054	10:36:44.9	-27:23:01.4	20.37 ± 0.01	0.95 ± 0.02	22.82 ± 0.02	1.76 ± 0.02	24.59 ± 0.01	2.92 ± 0.01	0.77	
HCC-055	10:36:37.2	-27:22:54.7	20.40 ± 0.07	0.94 ± 0.10	24.40 ± 0.03	2.88 ± 0.06	26.03 ± 0.04	4.42 ± 0.10	0.73	
HCC-056	10:37:51.2	-27:32:39.4	20.56 ± 0.05	0.77 ± 0.05	23.63 ± 0.09	1.78 ± 0.08	25.29 ± 0.03	2.74 ± 0.05	1.56	
HCC-057	10:36:48.2	-27:28:52.2	20.66 ± 0.01	0.95 ± 0.04	22.70 ± 0.06	1.33 ± 0.04	24.36 ± 0.02	2.13 ± 0.02	0.64	
HCC-058	10:36:41.5	-27:16:37.3	20.72 ± 0.08	1.13 ± 0.13	24.38 ± 0.03	2.86 ± 0.06	25.96 ± 0.04	4.24 ± 0.10	0.70	
HCC-059	10:37:12.5	-27:29:52.3	20.73 ± 0.05	1.03 ± 0.07	23.91 ± 0.04	1.93 ± 0.04	25.65 ± 0.04	3.14 ± 0.06	0.71	
HCC-060	10:38:03.0	-27:35:46.9	20.73 ± 0.03	0.87 ± 0.03	23.21 ± 0.03	1.62 ± 0.03	25.04 ± 0.02	2.75 ± 0.03	0.71	
HCC-061	10:36:29.3	-27:27:23.7	20.75 ± 0.04	0.94 ± 0.07	23.16 ± 0.03	1.42 ± 0.02	24.94 ± 0.02	2.35 ± 0.02	0.69	
HCC-062	10:36:31.0	-27:17:58.5	20.75 ± 0.01	0.97 ± 0.01	22.37 ± 0.03	1.11 ± 0.02	24.23 ± 0.02	1.90 ± 0.01	1.06	
HCC-063	10:38:06.3	-27:35:25.5	20.92 ± 0.04	0.92 ± 0.05	23.23 ± 0.05	1.42 ± 0.03	24.85 ± 0.02	2.17 ± 0.26	1.10	
HCC-064	10:36:29.8	-27:33:27.0	20.97 ± 0.05	0.86 ± 0.06	23.10 ± 0.05	1.20 ± 0.03	25.06 ± 0.03	2.14 ± 0.02	0.69	
HCC-065	10:36:43.7	-27:32:57.7	21.05 ± 0.03	0.94 ± 0.05	23.66 ± 0.04	1.79 ± 0.04	25.47 ± 0.05	2.99 ± 0.09	1.04	
HCC-066	10:37:41.6	-27:32:21.6	21.10 ± 0.02	0.94 ± 0.02	22.50 ± 0.02	0.84 ± 0.01	24.31 ± 0.03	1.40 ± 0.02	1.14	
HCC-067	10:36:35.8	-27:15:51.5	21.15 ± 0.08	0.68 ± 0.09	24.29 ± 0.04	1.97 ± 0.04	26.08 ± 0.07	3.26 ± 0.14	0.80	
HCC-068	10:36:25.9	-27:17:23.6	21.20 ± 0.01	0.87 ± 0.01	22.93 ± 0.06	1.12 ± 0.04	24.77 ± 0.04	1.93 ± 0.04	0.95	
HCC-069	10:36:23.8	-27:13:19.2	21.23 ± 0.03	1.00 ± 0.05	22.95 ± 0.01	0.99 ± 0.01	24.74 ± 0.02	1.63 ± 0.01	0.93	
HCC-070	10:36:47.3	-27:24:13.2	21.33 ± 0.02	0.80 ± 0.03	22.41 ± 0.09	0.86 ± 0.03	24.24 ± 0.02	1.48 ± 0.01	0.56	
HCC-071	10:36:45.6	-27:34:57.4	21.36 ± 0.05	0.83 ± 0.07	22.84 ± 0.12	1.00 ± 0.05	24.92 ± 0.02	1.86 ± 0.01	0.48	
HCC-072	10:36:48.3	-27:26:46.7	21.44 ± 0.07	1.00 ± 0.12	24.42 ± 0.04	2.05 ± 0.06	26.06 ± 0.13	3.24 ± 0.28	0.77	
HCC-073	10:36:31.0	-27:15:15.0	21.45 ± 0.06	1.01 ± 0.10	24.52 ± 0.05	1.95 ± 0.06	26.24 ± 0.07	3.18 ± 0.14	0.62	
HCC-074	10:36:24.0	-27:27:46.9	21.46 ± 0.08	0.92 ± 0.12	25.22 ± 0.05	3.79 ± 0.13	26.98 ± 0.20	6.51 ± 0.98	0.88	
HCC-075	10:36:22.9	-27:35:41.5	21.50 ± 0.04	1.07 ± 0.06	22.71 ± 0.05	0.77 ± 0.02	24.42 ± 0.05	1.21 ± 0.03	1.30	
HCC-076	10:36:26.5	-27:32:16.0	21.52 ± 0.05	0.64 ± 0.06	23.05 ± 0.06	0.89 ± 0.03	24.70 ± 0.04	1.34 ± 0.03	1.11	
HCC-077	10:36:21.3	-27:31:22.0	21.52 ± 0.10	0.83 ± 0.13	24.53 ± 0.06	1.82 ± 0.08	26.53 ± 0.37	3.55 ± 1.10	1.08	
HCC-078	10:36:40.8	-27:19:39.0	21.53 ± 0.08	1.05 ± 0.07	24.34 ± 0.08	1.75 ± 0.08	25.88 ± 0.10	2.52 ± 0.14	0.84	
HCC-079	10:36:26.6	-27:27:12.6	21.53 ± 0.06	0.83 ± 0.09	24.31 ± 0.06	1.79 ± 0.08	26.04 ± 0.07	2.91 ± 0.12	0.86	
HCC-080	10:36:24.6	-27:11:43.9	21.54 ± 0.04	0.92 ± 0.05	23.36 ± 0.04	1.11 ± 0.02	25.03 ± 0.04	1.75 ± 0.02	0.69	
HCC-081	10:36:26.5	-27:32:41.6	21.57 ± 0.06	0.78 ± 0.06	23.96 ± 0.08	1.32 ± 0.05	25.90 ± 0.07	2.33 ± 0.08	0.80	
HCC-082	10:36:33.5	-27:26:59.5	21.59 ± 0.04	0.77 ± 0.04	25.09 ± 0.04	3.41 ± 0.09	26.55 ± 0.10	4.64 ± 0.28	0.61	

Table A.2. continued

ID	$\alpha(2000.0)$	$\delta(2000.0)$	V_0	$(V-I)_0$	$\mu_{V,0}$	h_R	μ_e	R_e	n	v_{rad}
	[h:m:s]	[°:′:″]	[mag]	[mag]	[mag arcsec^{-2}]	[arcsec]	[mag arcsec^{-2}]	[arcsec]		[km s^{-1}]
HCC-083	10:36:27.4	-27:31:27.8	21.66 ± 0.04	0.97 ± 0.06	23.62 ± 0.06	1.34 ± 0.04	25.29 ± 0.05	2.12 ± 0.05	0.98	
HCC-084	10:36:28.0	-27:30:55.1	21.68 ± 0.04	0.94 ± 0.05	22.88 ± 0.04	0.75 ± 0.02	24.71 ± 0.05	1.28 ± 0.03	0.88	
HCC-085	10:38:11.9	-27:35:46.9	21.70 ± 0.05	1.01 ± 0.07	24.31 ± 0.06	1.89 ± 0.07	26.15 ± 0.11	3.23 ± 0.23	0.79	
HCC-086	10:36:37.9	-27:11:40.7	21.71 ± 0.02	0.87 ± 0.03	23.21 ± 0.03	0.97 ± 0.01	25.01 ± 0.02	1.62 ± 0.01	0.91	
HCC-087	10:36:39.0	-27:21:25.5	21.75 ± 0.05	1.07 ± 0.08	26.28 ± 0.05	7.75 ± 0.51	28.09 ± 0.36	13.65 ± 4.62	0.95	
HCC-088	10:36:36.6	-27:12:41.2	21.76 ± 0.10	0.84 ± 0.12	24.36 ± 0.04	1.70 ± 0.05	26.20 ± 0.19	2.79 ± 0.31	1.13	
HCC-089	10:36:57.3	-27:35:13.2	21.76 ± 0.07	0.68 ± 0.08	24.15 ± 0.09	1.34 ± 0.07	25.94 ± 0.11	2.28 ± 0.12	0.86	
HCC-090	10:36:36.4	-27:35:41.1	21.88 ± 0.02	0.86 ± 0.03	22.91 ± 0.05	0.76 ± 0.02	24.72 ± 0.03	1.28 ± 0.02	0.75	
HCC-091	10:36:52.1	-27:31:46.7	21.88 ± 0.01	0.93 ± 0.01	22.70 ± 0.12	0.79 ± 0.01	24.73 ± 0.02	1.47 ± 0.01	0.50	
HCC-092	10:36:28.0	-27:29:36.7	21.96 ± 0.03	0.68 ± 0.04	24.91 ± 0.04	2.00 ± 0.06	26.39 ± 0.16	2.80 ± 0.28	0.69	
HCC-093	10:36:56.5	-27:30:24.8	22.00 ± 0.03	0.93 ± 0.06	23.17 ± 0.06	0.86 ± 0.03	24.93 ± 0.04	1.41 ± 0.03	0.65	
HCC-094	10:36:22.2	-27:33:08.5	22.01 ± 0.06	0.75 ± 0.04	24.71 ± 0.04	1.93 ± 0.05	26.46 ± 0.09	3.11 ± 0.12	0.91	
HCC-095	10:36:32.8	-27:15:15.2	22.01 ± 0.12	0.72 ± 0.15	24.59 ± 0.09	1.59 ± 0.07	26.16 ± 0.11	2.33 ± 0.13	0.73	
HCC-096	10:36:35.4	-27:15:20.7	22.13 ± 0.04	0.91 ± 0.07	24.14 ± 0.05	1.37 ± 0.04	25.77 ± 0.08	2.11 ± 0.07	0.72	
HCC-097	10:36:53.8	-27:31:36.3	22.14 ± 0.06	0.68 ± 0.06	24.45 ± 0.05	1.42 ± 0.05	26.49 ± 0.49	2.68 ± 0.97	1.10	
HCC-098	10:36:49.9	-27:19:46.7	22.15 ± 0.09	0.65 ± 0.11	24.07 ± 0.10	1.14 ± 0.06	25.42 ± 0.05	1.49 ± 0.04	0.75	
HCC-099	10:36:24.6	-27:22:09.3	22.16 ± 0.10	1.08 ± 0.14	25.05 ± 0.11	1.82 ± 0.11	26.54 ± 0.13	2.53 ± 0.19	0.70	
HCC-100	10:36:25.0	-27:21:58.1	22.24 ± 0.18	1.03 ± 0.25	25.07 ± 0.11	2.00 ± 0.12	26.28 ± 0.22	2.26 ± 0.35	0.53	
HCC-101	10:37:39.5	-27:34:05.8	22.27 ± 0.04	1.10 ± 0.08	23.33 ± 0.06	0.84 ± 0.03	25.15 ± 0.06	1.40 ± 0.04	1.08	
HCC-102	10:36:24.5	-27:14:06.6	22.52 ± 0.19	0.69 ± 0.24	25.39 ± 0.09	2.12 ± 0.11	27.36 ± 0.23	3.82 ± 0.47	1.14	
HCC-103	10:36:38.0	-27:35:39.8	22.55 ± 0.04	0.98 ± 0.04	24.60 ± 0.05	1.99 ± 0.07	26.39 ± 0.18	3.35 ± 0.42	0.83	
HCC-104	10:38:07.0	-27:32:03.5	22.59 ± 0.08	0.87 ± 0.09	24.40 ± 0.05	1.24 ± 0.04	25.99 ± 0.14	1.84 ± 0.14	0.71	
HCC-105	10:37:58.5	-27:31:16.7	22.62 ± 0.12	0.78 ± 0.14	25.08 ± 0.05	1.65 ± 0.06	26.80 ± 0.32	2.63 ± 0.57	0.87	
HCC-106	10:36:39.7	-27:32:41.2	22.64 ± 0.06	0.96 ± 0.12	24.52 ± 0.09	1.17 ± 0.07	26.38 ± 0.74	2.01 ± 1.52	1.02	
HCC-107	10:37:52.4	-27:32:19.5	22.70 ± 0.06	0.81 ± 0.13	24.81 ± 0.05	1.63 ± 0.06	26.74 ± 0.17	2.88 ± 0.30	1.11	
HCC-108	10:36:35.5	-27:13:35.9	22.78 ± 0.14	0.82 ± 0.22	24.58 ± 0.08	1.07 ± 0.05	26.02 ± 0.08	1.48 ± 0.06	0.47	
HCC-109	10:36:24.4	-27:35:30.7	23.01 ± 0.12	0.73 ± 0.16	24.62 ± 0.13	1.01 ± 0.08	26.31 ± 0.26	1.60 ± 0.24	0.73	
HCC-110	10:36:27.5	-27:32:12.3	23.06 ± 0.09	0.83 ± 0.11	25.17 ± 0.07	1.84 ± 0.09	26.63 ± 0.93	2.56 ± 4.82	0.63	
HCC-111	10:36:47.3	-27:13:30.3	23.36 ± 0.16	0.95 ± 0.22	24.48 ± 0.17	0.87 ± 0.61	26.57 ± 0.52	1.63 ± 0.29	0.74	

[a] radial velocity taken from Christlein & Zabludoff (2003); [b] galaxies showing a two component surface brightness profile, not well fitted by a single Sérsic law; [c] NGC 3311; [d] NGC 3309; [e] NGC 3308; [f] NGC 3316

Table A.3 gives the photometric calibration coefficients for the seven observed Centaurus cluster fields, as indicated in Fig. 4.2, and the background field (field 8). Zero points (ZP), extinction coefficients k and colour terms (CT) are given for the two filters V and I.

Table A.3. Photometric calibration coefficients of the VLT/FORS1 fields in Centaurus.

Field	ZP_V	ZP_I	k_V	k_I	CT_V	CT_I
1	27.531	26.672	-0.135	-0.061	0.026	-0.061
2	27.523	26.675	-0.135	-0.061	0.026	-0.061
3	27.518	26.668	-0.135	-0.061	0.026	-0.061
4	27.505	26.659	-0.135	-0.061	0.026	-0.061
5	27.516	26.678	-0.135	-0.061	0.026	-0.061
6	27.516	26.678	-0.135	-0.061	0.026	-0.061
7	27.531	26.672	-0.135	-0.061	0.026	-0.061
8	27.510	26.628	-0.135	-0.061	0.026	-0.061

Table A.4 lists the photometric parameters of the sample of 92 probable Centaurus cluster early-type galaxies. The table is ordered by increasing apparent magnitude. The first column gives the object ID, in which the first number refers to the field in which the object is located (cf. Fig. 4.2). Right ascension and declination (J2000.0) are given in columns two and three. The fourth and fifth column contain the extinction corrected magnitude V_0 and colour $(V-I)_0$. In columns six and seven, the central surface brightness $\mu_{V,0}$ and the scale length h_R of an exponential fit to the surface brightness profile are listed. $\mu_{V,0}$ and h_R are not given for objects, whose surface brightness profiles are not well described by an exponential law, i.e. objects brighter than $V_0 = 16.1$ mag and the three cE galaxy candidates (see Sect. 4.2.5). Columns eight, nine and ten give the effective surface brightness μ_{eff}, the effective radius R_{eff} and the profile shape index n, as obtained from a Sérsic fit. The physical scale is 0.22 kpc/arcsec at the assumed distance modulus of $(m-M) = 33.28$ mag (Mieske et al. 2005a). Table A.4 is available in a machine readable form at the CDS (J/A+A/496/683).

Table A.4. Catalogue of the probable Centaurus cluster early-type galaxies.

ID	$\alpha(2000.0)$ [h:m:s]	$\delta(2000.0)$ [°:′:″]	V_0 [mag]	$(V-I)_0$ [mag]	$\mu_{V,0}$ [mag arcsec^{-2}]	h_R [arcsec]	μ_{eff} [mag arcsec^{-2}]	R_{eff} [arcsec]	n
C-1-01[c]	12:48:49.3	-41:18:39.1	10.05 ± 0.01	1.25 ± 0.03			22.29 ± 0.01	82.07 ± 0.03	2.49 ± 0.01
C-3-02[d]	12:50:04.0	-41:22:54.1	11.10 ± 0.02	1.28 ± 0.02			23.28 ± 0.01	77.25 ± 0.14	4.02 ± 0.01
C-4-03[b,e]	12:49:54.2	-41:16:44.9	12.56 ± 0.01	1.22 ± 0.01					
C-3-04[b]	12:49:38.0	-41:23:20.2	13.17 ± 0.01	1.13 ± 0.01					
C-4-05	12:49:51.6	-41:13:34.2	13.65 ± 0.01	1.17 ± 0.02			21.29 ± 0.01	8.57 ± 0.01	3.57 ± 0.01
C-3-06	12:50:08.0	-41:23:49.3	13.86 ± 0.01	1.21 ± 0.01			19.79 ± 0.01	4.38 ± 0.01	2.61 ± 0.01
C-7-07[b]	12:48:43.5	-41:38:36.8	14.05 ± 0.01	1.11 ± 0.01					
C-1-08	12:48:31.1	-41:18:23.3	15.03 ± 0.03	1.12 ± 0.04			20.52 ± 0.01	3.77 ± 0.01	2.09 ± 0.01
C-2-09	12:49:18.6	-41:20:07.3	15.29 ± 0.01	1.13 ± 0.01			20.22 ± 0.01	2.73 ± 0.01	1.41 ± 0.01
C-1-10	12:48:53.9	-41:19:05.3	15.52 ± 0.01	1.18 ± 0.01			19.72 ± 0.01	1.90 ± 0.01	1.23 ± 0.01
C-3-11	12:49:40.2	-41:21:60.0	15.74 ± 0.02	1.02 ± 0.03			23.54 ± 0.01	11.67 ± 0.01	1.38 ± 0.01
C-4-12	12:49:42.0	-41:13:44.9	16.03 ± 0.01	1.10 ± 0.01			21.75 ± 0.01	3.73 ± 0.01	1.71 ± 0.01
C-4-13	12:49:56.4	-41:15:35.8	16.17 ± 0.01	1.10 ± 0.01	21.24 ± 0.01	4.62 ± 0.01	23.08 ± 0.01	7.77 ± 0.01	1.08 ± 0.01
C-1-14	12:48:39.8	-41:16:05.7	16.23 ± 0.01	1.09 ± 0.01	21.26 ± 0.01	4.24 ± 0.01	23.12 ± 0.01	7.19 ± 0.01	1.15 ± 0.01

Table A.4. continued

ID	$\alpha(2000.0)$	$\delta(2000.0)$	V_0	$(V-I)_0$	$\mu_{V,0}$	h_R	μ_{eff}	R_{eff}	n
	[h:m:s]	[°:′:″]	[mag]	[mag]	[mag arcsec^{-2}]	[arcsec]	[mag arcsec^{-2}]	[arcsec]	
C-5-15	12:48:36.1	-41:26:23.2	16.89 ± 0.01	0.89 ± 0.02	21.42 ± 0.01	3.72 ± 0.01	23.31 ± 0.01	6.28 ± 0.01	1.32 ± 0.01
C-1-16	12:48:30.1	-41:19:17.8	17.34 ± 0.01	0.96 ± 0.01	21.36 ± 0.01	2.80 ± 0.01	23.29 ± 0.01	4.85 ± 0.01	1.15 ± 0.01
C-2-17	12:49:02.0	-41:15:33.7	17.35 ± 0.01	0.96 ± 0.01	21.24 ± 0.01	2.67 ± 0.01	22.97 ± 0.01	4.33 ± 0.01	0.89 ± 0.01
C-3-18	12:49:56.2	-41:24:04.0	17.40 ± 0.01	1.00 ± 0.01	21.97 ± 0.01	4.18 ± 0.01	23.33 ± 0.01	5.75 ± 0.01	1.43 ± 0.01
C-3-19	12:49:54.1	-41:20:21.9	17.50 ± 0.01	1.05 ± 0.01	21.53 ± 0.01	3.39 ± 0.01	23.40 ± 0.01	5.73 ± 0.01	1.11 ± 0.01
C-2-20	12:49:33.0	-41:19:24.0	17.59 ± 0.01	1.15 ± 0.01			21.53 ± 0.01	1.65 ± 0.01	1.55 ± 0.01
C-1-21	12:48:48.6	-41:20:52.8	17.71 ± 0.01	1.18 ± 0.01			20.95 ± 0.01	1.27 ± 0.01	1.27 ± 0.01
C-2-22	12:49:22.7	-41:15:18.7	18.19 ± 0.02	0.95 ± 0.04	22.38 ± 0.01	3.63 ± 0.01	23.98 ± 0.01	5.48 ± 0.01	1.39 ± 0.01
C-3-23	12:49:46.6	-41:22:08.7	18.42 ± 0.01	0.97 ± 0.01	22.51 ± 0.01	3.00 ± 0.01	24.33 ± 0.01	5.02 ± 0.01	1.04 ± 0.01
C-2-24	12:49:05.4	-41:18:25.6	18.42 ± 0.01	0.87 ± 0.02	22.15 ± 0.01	2.40 ± 0.01	23.88 ± 0.01	3.88 ± 0.01	0.87 ± 0.01
C-2-25	12:49:32.3	-41:20:23.8	18.53 ± 0.01	0.99 ± 0.02	22.38 ± 0.01	2.58 ± 0.02	24.16 ± 0.01	4.21 ± 0.03	0.99 ± 0.01
C-4-26	12:49:48.7	-41:14:18.3	18.87 ± 0.01	0.88 ± 0.02	22.72 ± 0.01	2.78 ± 0.01	24.60 ± 0.01	4.76 ± 0.02	1.09 ± 0.01
C-2-27	12:49:06.5	-41:16:13.4	19.10 ± 0.01	0.96 ± 0.02	22.88 ± 0.01	2.47 ± 0.01	24.70 ± 0.01	4.13 ± 0.03	1.05 ± 0.01
C-3-28	12:49:56.2	-41:23:23.4	19.29 ± 0.02	0.86 ± 0.03	22.84 ± 0.01	2.59 ± 0.01	24.60 ± 0.01	4.31 ± 0.01	0.73 ± 0.01
C-4-29	12:49:56.1	-41:16:56.4	19.50 ± 0.04	0.87 ± 0.05	23.32 ± 0.01	3.18 ± 0.01	25.18 ± 0.02	5.41 ± 0.05	1.06 ± 0.02
C-3-30^a	12:49:34.1	-41:22:38.8	19.53 ± 0.01		23.34 ± 0.01	2.75 ± 0.02	25.11 ± 0.01	4.56 ± 0.03	0.75 ± 0.02
C-6-31	12:48:52.5	-41:32:24.5	19.64 ± 0.03	0.88 ± 0.05	23.06 ± 0.02	2.40 ± 0.02	24.92 ± 0.09	4.13 ± 0.02	0.65 ± 0.01
C-3-32	12:49:38.3	-41:23:57.5	19.95 ± 0.01	0.98 ± 0.02	22.71 ± 0.02	1.27 ± 0.01	24.43 ± 0.01	1.99 ± 0.02	1.50 ± 0.05
C-4-33	12:49:46.1	-41:17:56.7	19.99 ± 0.05	0.94 ± 0.07	24.17 ± 0.02	3.53 ± 0.03	25.91 ± 0.02	5.68 ± 0.07	0.89 ± 0.01
C-2-34	12:49:20.9	-41:17:11.0	20.00 ± 0.03	0.82 ± 0.06	23.07 ± 0.02	2.05 ± 0.02	24.90 ± 0.01	3.49 ± 0.02	0.78 ± 0.01
C-2-35	12:49:13.2	-41:17:56.0	20.11 ± 0.04	0.92 ± 0.05	24.11 ± 0.03	2.92 ± 0.06	25.84 ± 0.02	4.72 ± 0.06	0.78 ± 0.02
C-1-36	12:48:37.9	-41:19:48.7	20.15 ± 0.03	0.75 ± 0.06	23.30 ± 0.02	2.00 ± 0.02	25.11 ± 0.02	3.37 ± 0.03	0.82 ± 0.02
C-2-37	12:49:15.1	-41:17:10.9	20.15 ± 0.01	0.86 ± 0.02	23.35 ± 0.04	2.09 ± 0.04	24.15 ± 0.01	2.27 ± 0.01	1.13 ± 0.01
C-1-38	12:48:40.8	-41:19:48.7	20.21 ± 0.04	0.86 ± 0.05	24.05 ± 0.01	2.70 ± 0.03	25.72 ± 0.03	4.18 ± 0.06	0.84 ± 0.03
C-4-39	12:49:38.9	-41:16:39.5	20.24 ± 0.03	0.83 ± 0.05	22.81 ± 0.01	1.82 ± 0.01	24.55 ± 0.01	2.97 ± 0.03	0.85 ± 0.01
C-3-40	12:50:02.6	-41:19:48.9	20.59 ± 0.01	0.94 ± 0.02	22.79 ± 0.01	1.48 ± 0.01	24.50 ± 0.01	2.39 ± 0.01	0.82 ± 0.01
C-5-41	12:48:47.4	-41:23:19.8	20.60 ± 0.03	0.84 ± 0.04	24.29 ± 0.03	2.44 ± 0.05	25.95 ± 0.04	3.78 ± 0.07	0.78 ± 0.03
C-1-42	12:48:45.1	-41:21:06.5	20.62 ± 0.04	0.84 ± 0.05	23.89 ± 0.05	2.03 ± 0.05	25.92 ± 0.02	3.79 ± 0.05	0.76 ± 0.02
C-3-43	12:50:00.9	-41:19:07.9	20.65 ± 0.05	0.87 ± 0.09	24.07 ± 0.03	2.27 ± 0.04	25.83 ± 0.02	3.75 ± 0.04	0.66 ± 0.02
C-7-44	12:49:02.6	-41:37:05.7	20.72 ± 0.05	0.66 ± 0.07	23.86 ± 0.05	2.12 ± 0.05	25.67 ± 0.02	3.57 ± 0.04	0.54 ± 0.01
C-5-45	12:48:40.6	-41:24:19.3	20.76 ± 0.02	0.86 ± 0.03	23.03 ± 0.02	1.64 ± 0.02	24.75 ± 0.01	2.69 ± 0.01	0.61 ± 0.01
C-1-46	12:49:00.3	-41:18:48.0	20.78 ± 0.04	0.88 ± 0.06	23.71 ± 0.01	1.80 ± 0.02	25.56 ± 0.05	3.04 ± 0.07	1.08 ± 0.07
C-1-47^a	12:48:27.2	-41:17:35.1	20.79 ± 0.05		24.06 ± 0.03	2.46 ± 0.04	25.84 ± 0.03	4.07 ± 0.06	0.93 ± 0.03
C-4-48	12:50:03.8	-41:11:36.0	20.82 ± 0.03	0.74 ± 0.04	22.98 ± 0.01	1.27 ± 0.01	24.57 ± 0.01	1.96 ± 0.01	0.69 ± 0.02
C-3-49	12:49:35.9	-41:21:07.5	20.87 ± 0.06	1.03 ± 0.07	24.40 ± 0.02	3.01 ± 0.04	26.09 ± 0.04	4.71 ± 0.10	0.90 ± 0.03
C-3-50	12:49:47.9	-41:22:04.0	20.90 ± 0.05	0.82 ± 0.07	24.11 ± 0.02	2.07 ± 0.03	25.80 ± 0.02	3.30 ± 0.02	0.63 ± 0.01
C-2-51	12:49:32.0	-41:17:18.2	20.97 ± 0.03	0.79 ± 0.04	23.24 ± 0.03	1.69 ± 0.03	25.01 ± 0.02	2.81 ± 0.03	0.74 ± 0.02
C-5-52	12:48:52.3	-41:27:13.7	21.04 ± 0.09	1.03 ± 0.13	24.13 ± 0.07	2.17 ± 0.06	26.21 ± 0.05	4.07 ± 0.09	0.65 ± 0.08
C-5-53	12:48:47.4	-41:26:05.1	21.13 ± 0.04	0.87 ± 0.06	23.83 ± 0.06	1.59 ± 0.04	25.67 ± 0.02	2.73 ± 0.03	0.64 ± 0.03
C-4-54	12:50:01.9	-41:12:46.9	21.16 ± 0.08	0.91 ± 0.12	24.49 ± 0.04	2.30 ± 0.05	26.25 ± 0.04	3.77 ± 0.07	0.84 ± 0.03
C-6-55	12:49:01.4	-41:30:17.6	21.19 ± 0.01	0.79 ± 0.02	23.18 ± 0.03	1.18 ± 0.02	24.85 ± 0.02	1.88 ± 0.02	0.62 ± 0.03
C-7-56	12:48:32.6	-41:35:41.9	21.27 ± 0.22	0.77 ± 0.31	25.79 ± 0.03	4.64 ± 0.14	27.12 ± 0.03	6.04 ± 0.10	0.46 ± 0.02
C-4-57	12:50:05.1	-41:12:38.8	21.30 ± 0.17	0.69 ± 0.21	24.67 ± 0.01	2.32 ± 0.03	26.61 ± 0.06	4.12 ± 0.13	1.14 ± 0.06
C-3-58	12:49:40.8	-41:21:06.5	21.34 ± 0.08	0.84 ± 0.10	24.75 ± 0.03	2.21 ± 0.06	26.35 ± 0.04	3.34 ± 0.08	0.76 ± 0.04
C-3-59	12:49:57.9	-41:19:22.2	21.38 ± 0.03	0.76 ± 0.04	23.18 ± 0.01	1.24 ± 0.01	24.87 ± 0.01	1.98 ± 0.01	0.75 ± 0.02
C-1-60	12:48:36.5	-41:18:37.1	21.48 ± 0.04	0.80 ± 0.10	24.58 ± 0.04	2.78 ± 0.08	26.25 ± 0.05	4.34 ± 0.10	0.78 ± 0.05
C-2-61	12:49:08.2	-41:21:13.8	21.50 ± 0.04	0.91 ± 0.07	25.09 ± 0.03	5.93 ± 0.33	26.35 ± 0.10	6.31 ± 0.40	0.69 ± 0.06
C-6-62	12:48:59.3	-41:30:19.3	21.52 ± 0.02	0.82 ± 0.04	23.69 ± 0.04	1.25 ± 0.03	25.35 ± 0.04	1.96 ± 0.04	0.72 ± 0.04
C-2-63	12:49:07.1	-41:19:38.4	21.62 ± 0.04	0.98 ± 0.06	23.77 ± 0.15	1.25 ± 0.07	25.95 ± 0.05	2.49 ± 0.07	0.79 ± 0.04
C-4-64	12:49:58.0	-41:15:11.6	21.75 ± 0.10	0.95 ± 0.15	25.38 ± 0.03	2.50 ± 0.06	27.06 ± 0.08	3.94 ± 0.16	0.81 ± 0.06
C-4-65	12:50:06.5	-41:13:39.7	21.83 ± 0.04	0.90 ± 0.09	24.11 ± 0.02	1.68 ± 0.02	25.95 ± 0.05	2.84 ± 0.07	0.99 ± 0.07
C-1-66	12:48:34.1	-41:21:20.8	21.92 ± 0.12	0.84 ± 0.16	25.07 ± 0.15	2.07 ± 0.16	26.81 ± 0.10	3.37 ± 0.18	0.59 ± 0.08
C-3-67	12:49:54.7	-41:19:00.7	21.94 ± 0.05	1.03 ± 0.07	24.12 ± 0.10	1.42 ± 0.07	26.12 ± 0.05	2.59 ± 0.06	0.75 ± 0.05
C-5-68	12:48:47.3	-41:22:05.1	21.98 ± 0.03	0.91 ± 0.05	24.23 ± 0.02	2.41 ± 0.05	25.83 ± 0.05	3.56 ± 0.10	0.85 ± 0.04
C-3-69	12:49:42.0	-41:21:33.0	22.18 ± 0.11	0.86 ± 0.15	25.02 ± 0.07	1.77 ± 0.08	26.70 ± 0.09	2.79 ± 0.15	0.78 ± 0.09
C-6-70	12:48:45.5	-41:30:18.8	22.24 ± 0.04	0.65 ± 0.04	23.86 ± 0.02	0.97 ± 0.02	25.64 ± 0.09	1.58 ± 0.09	0.97 ± 0.06
C-4-71	12:49:39.4	-41:12:21.1	22.28 ± 0.09	0.88 ± 0.13	25.01 ± 0.05	1.71 ± 0.06	26.85 ± 0.11	2.89 ± 0.15	0.94 ± 0.12
C-3-72	12:50:00.9	-41:21:32.5	22.33 ± 0.05	0.93 ± 0.08	24.28 ± 0.05	1.24 ± 0.02	25.99 ± 0.06	2.00 ± 0.07	0.79 ± 0.08
C-3-73	12:49:59.6	-41:20:16.1	22.37 ± 0.07	0.67 ± 0.15	24.38 ± 0.09	1.35 ± 0.01	26.05 ± 0.08	2.14 ± 0.08	0.60 ± 0.20
C-1-74	12:48:39.4	-41:17:00.0	22.41 ± 0.06	0.67 ± 0.11	24.78 ± 0.06	1.58 ± 0.06	26.66 ± 0.11	2.73 ± 0.16	1.05 ± 0.11
C-4-75	12:49:42.8	-41:13:12.6	22.42 ± 0.06	0.74 ± 0.07	24.23 ± 0.05	1.12 ± 0.03	26.02 ± 0.09	1.85 ± 0.07	0.98 ± 0.21
C-1-76	12:48:42.0	-41:18:02.6	22.57 ± 0.06	0.58 ± 0.08	24.09 ± 0.08	0.96 ± 0.04	25.90 ± 0.08	1.59 ± 0.07	1.00 ± 0.19
C-3-77	12:49:41.5	-41:18:34.6	22.71 ± 0.13	0.81 ± 0.13	24.93 ± 0.16	1.48 ± 0.12	26.57 ± 0.07	2.37 ± 0.07	0.76 ± 0.09
C-1-78	12:48:37.6	-41:17:16.7	22.77 ± 0.12	1.03 ± 0.18	25.25 ± 0.09	1.56 ± 0.10	27.02 ± 0.13	2.58 ± 0.18	0.87 ± 0.16
C-2-79	12:49:05.6	-41:16:43.4	22.80 ± 0.06	0.93 ± 0.07	25.19 ± 0.14	1.55 ± 0.27	27.10 ± 0.59	2.73 ± 1.68	1.06 ± 0.55
C-4-80	12:49:45.9	-41:14:52.7	22.80 ± 0.16	0.79 ± 0.26	25.51 ± 0.14	1.80 ± 0.14	27.76 ± 0.42	3.99 ± 1.23	0.91 ± 0.43
C-5-81	12:48:49.6	-41:23:01.5	22.86 ± 0.05	0.70 ± 0.08	24.46 ± 0.07	1.16 ± 0.05	26.31 ± 0.16	1.97 ± 0.17	1.00 ± 0.25
C-2-82	12:49:06.9	-41:18:48.5	22.90 ± 0.10	0.84 ± 0.14	25.61 ± 0.14	1.54 ± 0.22	27.03 ± 0.12	1.98 ± 0.20	0.80 ± 0.02
C-2-83	12:49:25.4	-41:18:21.9	22.98 ± 0.12	0.88 ± 0.15	25.69 ± 0.08	2.53 ± 0.18	27.39 ± 0.43	3.96 ± 1.30	0.92 ± 0.40
C-1-84	12:48:31.1	-41:15:34.4	23.01 ± 0.07	0.75 ± 0.08	24.97 ± 0.11	1.09 ± 0.07	27.02 ± 0.15	2.03 ± 0.20	1.39 ± 0.11
C-2-85	12:49:24.6	-41:15:14.5	23.13 ± 0.14	0.64 ± 0.19	24.91 ± 0.18	1.16 ± 0.15	26.75 ± 0.22	2.00 ± 0.35	0.93 ± 0.16
C-1-86	12:48:40.0	-41:19:17.4	23.17 ± 0.06	0.53 ± 0.09	24.63 ± 0.12	1.12 ± 0.10	26.44 ± 0.17	1.88 ± 0.20	0.79 ± 0.21
C-7-87	12:48:42.4	-41:36:52.1	23.21 ± 0.19	0.41 ± 0.27	25.41 ± 0.09	1.38 ± 0.14	27.29 ± 0.26	2.44 ± 0.47	1.02 ± 0.25
C-5-88	12:48:28.3	-41:21:24.5	23.37 ± 0.10	0.82 ± 0.11	25.01 ± 0.16	1.03 ± 0.11	26.90 ± 0.45	1.79 ± 0.70	1.00 ± 0.37
C-7-89	12:48:45.2	-41:36:57.3	23.40 ± 0.14	0.90 ± 0.04	24.47 ± 0.16	0.78 ± 0.08	26.25 ± 0.25	1.28 ± 0.22	0.99 ± 0.25
C-6-90	12:48:59.5	-41:32:02.1	23.44 ± 0.14	0.65 ± 0.19	25.23 ± 0.05	1.12 ± 0.05	27.00 ± 0.12	1.84 ± 0.13	0.93 ± 0.09
C-5-91	12:49:02.2	-41:22:47.5	23.57 ± 0.04	0.80 ± 0.05	24.75 ± 0.11	1.01 ± 0.10	27.04 ± 0.17	2.41 ± 0.27	1.19 ± 0.13
C-2-92	12:49:08.2	-41:18:08.3	23.88 ± 0.12	0.86 ± 0.15	25.25 ± 0.15	1.30 ± 0.17	26.89 ± 0.20	2.01 ± 0.30	0.76 ± 0.14

$^{(a)}$ galaxies for which no colour could be measured; $^{(b)}$ galaxies showing a two component surface brightness profile, not well fitted by a single Sérsic law; $^{(c)}$ NGC 4696; $^{(d)}$ NGC 4709; $^{(e)}$ NGC 4706

Table A.5 lists the 118 identified cluster GCs/UCDs. The first column gives the object ID, right ascension and declination (J2000.0) are given in columns two and three. The fourth column lists R, the projected distance in arcmin to NGC 3311. Columns 5 and 6 list the extinction corrected apparent magnitude V_0 and the colour $(V-R)_0$. The last column gives the radial velocity $v_{\rm rad}$ with the according error. The table is ordered by increasing apparent magnitude.

Table A.5. Catalogue of the 118 identified cluster GCs/UCDs.

ID	$\alpha(2000.0)$ [h:m:s]	$\delta(2000.0)$ [°:′:″]	R [arcmin]	V_0 [mag]	$(V-R)_0$ [mag]	$v_{\rm rad}$ [km s^{-1}]
HUCD1	10:36:42.5	-27:32:52.9	1.19	20.03	0.60	3352 ± 42
HUCD2	10:36:19.4	-27:26:05.9	8.09	20.65	0.61	3547 ± 52
HUCD3	10:36:41.9	-27:19:44.8	11.96	20.85	0.52	3354 ± 56
HUCD4	10:36:34.8	-27:34:45.8	3.66	20.86	0.64	3563 ± 43
HUCD5	10:36:34.4	-27:30:15.3	2.55	21.06	0.61	3804 ± 61
HUCD6	10:36:43.9	-27:37:57.3	6.26	21.07	0.53	3980 ± 50
HUCD7	10:36:42.1	-27:24:03.5	7.64	21.15	0.53	3986 ± 43
HUCD8	10:36:43.8	-27:32:22.2	0.71	21.22	0.54	3301 ± 53
HUCD9	10:35:36.7	-27:17:40.2	21.67	21.24	0.47	3137 ± 72
HUCD10	10:36:31.8	-27:29:13.8	3.70	21.30	0.55	4976 ± 46
HUCD11	10:36:32.4	-27:29:22.1	3.49	21.30	0.60	3784 ± 49
HUCD12	10:36:45.5	-27:29:52.2	1.95	21.33	0.58	3608 ± 99
HUCD13	10:36:01.9	-27:23:01.3	13.42	21.42	0.52	4254 ± 86
HUCD14	10:36:31.4	-27:30:25.7	3.12	21.44	0.60	4472 ± 57
HUCD15	10:36:49.3	-27:36:01.9	4.63	21.44	0.59	3655 ± 60
HUCD16	10:36:41.1	-27:31:18.0	0.59	21.61	0.55	3653 ± 48
HUCD17	10:36:06.0	-27:36:33.3	10.40	21.66	0.62	5082 ± 43
HUCD18	10:36:43.5	-27:31:49.4	0.22	21.67	0.66	3165 ± 63
HUCD19	10:36:32.0	-27:30:12.7	3.08	21.67	0.62	2412 ± 71
HUCD20	10:36:14.0	-27:27:56.4	8.13	21.71	0.64	3124 ± 74
HUCD21	10:36:47.4	-27:31:06.6	1.28	21.71	0.60	3716 ± 43
HUCD22	10:36:58.0	-27:35:58.9	5.72	21.73	0.60	3127 ± 77
HUCD23	10:37:43.1	-27:36:00.9	15.67	21.74	0.58	3760 ± 40
HUCD24	10:36:56.8	-27:33:30.7	3.93	21.75	0.55	2861 ± 72
HUCD25	10:36:44.8	-27:34:15.6	2.61	21.76	0.66	3354 ± 37
HUCD26	10:36:35.0	-27:32:59.9	2.35	21.82	0.56	3742 ± 96
HUCD27	10:36:35.0	-27:29:44.4	2.77	21.88	0.58	3624 ± 61
HUCD28	10:36:52.9	-27:24:33.1	7.58	21.88	0.53	2664 ± 91
HUCD29	10:36:48.2	-27:22:18.5	9.49	21.89	0.60	3301 ± 39
HUCD30	10:36:50.0	-27:31:54.9	1.81	21.91	0.61	3901 ± 48
HUCD31	10:36:05.6	-27:27:04.0	10.39	21.92	0.52	3725 ± 62
HUCD32	10:36:57.3	-27:26:01.1	6.74	21.99	0.48	3294 ± 60

Table A.5. continued

ID	$\alpha(2000.0)$ [h:m:s]	$\delta(2000.0)$ [°:′:″]	R [arcmin]	V_0 [mag]	$(V-R)_0$ [mag]	$v_{\rm rad}$ [km s^{-1}]
HUCD33	10:36:43.4	-27:25:20.9	6.35	22.01	0.56	4217 ± 61
HUCD34	10:36:48.5	-27:34:43.4	3.34	22.04	0.49	4125 ± 52
HUCD35	10:36:31.7	-27:30:32.0	3.01	22.04	0.56	3818 ± 59
HUCD36	10:37:01.2	-27:27:19.5	6.35	22.06	0.45	5810 ± 70
HUCD37	10:36:35.6	-27:35:11.0	3.92	22.08	0.63	4078 ± 35
HUCD38	10:36:07.2	-27:32:51.4	8.97	22.08	0.57	3821 ± 89
HUCD39	10:36:45.1	-27:31:51.1	0.58	22.12	0.59	4342 ± 60
HUCD40	10:36:39.4	-27:30:53.6	1.17	22.14	0.63	3395 ± 70
HUCD41	10:36:37.8	-27:34:44.2	3.29	22.15	0.54	4745 ± 65
HUCD42	10:36:36.3	-27:32:16.3	1.74	22.16	0.55	3867 ± 53
HUCD43	10:36:48.4	-27:35:03.1	3.63	22.18	0.60	4802 ± 46
HUCD44	10:36:48.1	-27:32:23.3	1.50	22.23	0.58	3248 ± 51
HUCD45	10:36:50.2	-27:36:10.3	4.83	22.24	0.56	4218 ± 87
HUCD46	10:36:33.2	-27:30:54.8	2.53	22.26	0.55	3927 ± 61
HUCD47	10:36:50.7	-27:32:01.0	1.99	22.28	0.48	3584 ± 68
HUCD48	10:36:40.6	-27:26:27.3	5.27	22.29	0.59	3850 ± 56
HUCD49	10:36:46.3	-27:34:18.6	2.75	22.34	0.54	4477 ± 68
HUCD50	10:36:28.1	-27:31:06.7	3.74	22.34	0.54	3794 ± 78
HUCD51	10:35:45.7	-27:33:38.4	14.41	22.35	0.64	4079 ± 66
HUCD52	10:35:52.9	-27:35:32.3	13.07	22.37	0.63	3596 ± 69
53	10:36:39.5	-27:29:48.3	2.07	22.38	0.46	3653 ± 59
54	10:36:44.5	-27:30:44.7	1.04	22.43	0.55	2914 ± 53
55	10:36:45.3	-27:29:26.5	2.34	22.47	0.57	3229 ± 80
56	10:36:40.9	-27:25:09.0	6.57	22.49	0.44	3439 ± 61
57	10:36:30.1	-27:34:26.3	4.20	22.56	0.62	3201 ± 81
58	10:36:46.4	-27:29:32.1	2.34	22.57	0.40	3734 ± 71
59	10:36:38.3	-27:32:21.4	1.30	22.58	0.61	3358 ± 69
60	10:36:50.0	-27:38:27.5	6.99	22.61	0.62	3532 ± 57
61	10:36:50.0	-27:32:35.0	2.00	22.63	0.57	3119 ± 78
62	10:36:43.8	-27:33:13.0	1.54	22.64	0.62	4674 ± 64
63	10:36:43.8	-27:27:12.3	4.50	22.65	0.59	4185 ± 51
64	10:36:38.0	-27:30:16.6	1.86	22.66	0.55	4053 ± 71
65	10:36:53.1	-27:35:43.6	4.77	22.67	0.55	1259 ± 91
66	10:36:39.1	-27:31:20.1	1.01	22.71	0.70	3950 ± 55
67	10:36:45.3	-27:33:43.9	2.12	22.80	0.62	3001 ± 83
68	10:36:39.5	-27:31:28.1	0.85	22.81	0.63	4502 ± 54
69	10:36:41.2	-27:32:46.7	1.15	22.82	0.58	3780 ± 47
70	10:36:44.9	-27:33:36.4	1.98	22.84	0.49	4234 ± 54
71	10:37:01.5	-27:24:07.4	8.91	22.86	0.50	2874 ± 51

Table A.5. continued

ID	$\alpha(2000.0)$	$\delta(2000.0)$	R	V_0	$(V-R)_0$	$v_{\rm rad}$
	[h:m:s]	[°:′:″]	[arcmin]	[mag]	[mag]	[km s^{-1}]
72	10:36:47.0	-27:35:18.1	3.75	22.86	0.51	2708 ± 79
73	10:36:38.8	-27:30:55.0	1.28	22.86	0.58	3134 ± 76
74	10:36:26.8	-27:32:23.5	4.06	22.90	0.55	1570 ± 86
75	10:36:34.2	-27:21:32.3	10.39	22.91	0.65	2755 ± 61
76	10:36:45.8	-27:33:43.9	2.16	22.92	0.59	3612 ± 47
77	10:36:43.2	-27:28:27.6	3.24	22.92	0.57	3154 ± 69
78	10:35:53.0	-27:23:06.7	15.14	22.96	0.43	3830 ± 68
79	10:36:30.6	-27:21:37.1	10.54	22.96	0.61	3912 ± 52
80	10:36:43.0	-27:34:09.3	2.46	23.00	0.60	4706 ± 58
81	10:37:03.7	-27:26:42.0	7.23	23.00	0.54	3659 ± 59
82	10:36:42.9	-27:27:59.1	3.72	23.01	0.55	2202 ± 51
83	10:36:49.9	-27:33:02.0	2.22	23.04	0.58	3474 ± 56
84	10:36:40.5	-27:35:12.2	3.55	23.06	0.58	3247 ± 48
85	10:36:50.7	-27:33:13.2	2.48	23.08	0.56	4745 ± 66
86	10:36:31.5	-27:33:21.0	3.27	23.09	0.57	3946 ± 56
87	10:36:50.9	-27:35:28.4	4.28	23.10	0.65	3301 ± 55
88	10:36:46.0	-27:35:10.0	3.56	23.10	0.64	3040 ± 93
89	10:36:37.7	-27:29:55.2	2.19	23.10	0.56	4927 ± 72
90	10:36:32.3	-27:31:34.7	2.63	23.11	0.64	4068 ± 59
91	10:36:42.1	-27:30:28.1	1.25	23.14	0.64	3546 ± 96
92	10:36:40.9	-27:30:42.7	1.10	23.16	0.46	4901 ± 70
93	10:36:41.9	-27:36:40.4	4.98	23.17	0.53	4137 ± 59
94	10:36:30.0	-27:31:01.9	3.26	23.19	0.56	4060 ± 56
95	10:36:39.0	-27:30:22.1	1.64	23.21	0.63	3748 ± 99
96	10:36:45.5	-27:23:49.7	7.90	23.22	0.63	3571 ± 46
97	10:36:46.4	-27:31:35.8	0.89	23.28	0.52	3874 ± 92
98	10:36:58.2	-27:25:30.2	7.29	23.28	0.51	5091 ± 85
99	10:36:48.3	-27:31:59.1	1.41	23.28	0.63	5347 ± 54
100	10:36:50.9	-27:33:38.4	2.80	23.29	0.58	4071 ± 68
101	10:36:37.7	-27:32:05.8	1.34	23.29	0.51	3291 ± 48
102	10:36:50.3	-27:29:06.7	3.19	23.30	0.49	3257 ± 62
103	10:36:32.4	-27:34:53.6	4.12	23.31	0.64	4494 ± 67
104	10:36:32.6	-27:26:30.0	5.79	23.33	0.68	4194 ± 54
105	10:36:57.1	-27:36:38.4	6.09	23.34	0.58	2767 ± 77
106	10:36:41.9	-27:34:52.6	3.19	23.34	0.60	4946 ± 73
107	10:36:40.3	-27:34:43.3	3.09	23.41	0.58	3261 ± 56
108	10:36:51.5	-27:35:14.6	4.16	23.42	0.60	4443 ± 60
109	10:36:29.1	-27:31:34.8	3.43	23.44	0.55	3693 ± 60
110	10:36:44.7	-27:32:55.5	1.31	23.47	0.46	4024 ± 53

Table A.5. continued

ID	α(2000.0)	δ(2000.0)	R	V_0	$(V - R)_0$	$v_{\rm rad}$
	[h:m:s]	[°:′:″]	[arcmin]	[mag]	[mag]	[km s^{-1}]
111	10:36:40.9	-27:34:15.9	2.61	23.52	0.45	2962 ± 64
112	10:36:41.2	-27:32:49.4	1.20	23.53	0.53	3948 ± 77
113	10:36:46.0	-27:34:22.2	2.78	23.55	0.57	4179 ± 46
114	10:36:31.9	-27:30:37.1	2.95	23.57	0.60	2701 ± 65
115	10:36:29.6	-27:31:12.8	3.34	23.59	0.56	4279 ± 63
116	10:36:47.5	-27:32:58.9	1.74	23.62	0.60	3710 ± 86
117	10:36:35.8	-27:29:56.6	2.48	23.63	0.74	2439 ± 77
118	10:36:45.3	-27:33:19.8	1.75	23.70	0.66	3887 ± 53

Bibliography

Abell, G. O. 1958, ApJS, 3, 211

Adami, C., Le Brun, V., Biviano, A., et al. 2009, A&A, 507, 1225

Adami, C., Scheidegger, R., Ulmer, M., et al. 2006, A&A, 459, 679

Bassino, L. P., Faifer, F. R., Forte, J. C., et al. 2006, A&A, 451, 789

Bassino, L. P., Muzzio, J. C., & Rabolli, M. 1994, ApJ, 431, 634

Baumgardt, H. & Mieske, S. 2008, MNRAS, 391, 942

Bautz, L. P. & Morgan, W. W. 1970, ApJ, 162, L149

Bekki, K., Couch, W. J., & Drinkwater, M. J. 2001a, ApJ, 552, L105

Bekki, K., Couch, W. J., Drinkwater, M. J., & Gregg, M. D. 2001b, ApJ, 557, L39

Bekki, K., Couch, W. J., Drinkwater, M. J., & Shioya, Y. 2003, MNRAS, 344, 399

Belokurov, V., Walker, M. G., Evans, N. W., et al. 2010, ApJ, 712, L103

Belokurov, V., Walker, M. G., Evans, N. W., et al. 2009, MNRAS, 397, 1748

Belokurov, V., Zucker, D. B., Evans, N. W., et al. 2007, ApJ, 654, 897

Bender, R., Burstein, D., & Faber, S. M. 1992, ApJ, 399, 462

Bender, R., Burstein, D., & Faber, S. M. 1993, ApJ, 411, 153

Bernardi, M., Sheth, R. K., Annis, J., et al. 2003a, AJ, 125, 1849

Bernardi, M., Sheth, R. K., Annis, J., et al. 2003b, AJ, 125, 1866

Bernardi, M., Sheth, R. K., Annis, J., et al. 2003c, AJ, 125, 1882

Bertin, E. & Arnouts, S. 1996, A&AS, 117, 393

Binggeli, B. & Cameron, L. M. 1991, A&A, 252, 27

Binggeli, B. & Jerjen, H. 1998, A&A, 333, 17

Binggeli, B., Sandage, A., & Tammann, G. A. 1985, AJ, 90, 1681

Binney, J. & Merrifield, M. 1998, Galactic astronomy, ed. Binney, J. & Merrifield, M.

Blakeslee, J. P. & Barber DeGraaff, R. 2008, AJ, 136, 2295

Blakeslee, J. P., Jordán, A., Mei, S., et al. 2009, ApJ, 694, 556

Bode, P., Ostriker, J. P., & Turok, N. 2001, ApJ, 556, 93

Böker, T., Sarzi, M., McLaughlin, D. E., et al. 2004, AJ, 127, 105

Boselli, A., Boissier, S., Cortese, L., & Gavazzi, G. 2008, A&A, 489, 1015

Brodie, J. P., Larsen, S. S., & Kissler-Patig, M. 2000, ApJ, 543, L19

Brodie, J. P. & Strader, J. 2006, ARA&A, 44, 193

Brosche, P. 1973, A&A, 23, 259

Bruzual, G. & Charlot, S. 2003, MNRAS, 344, 1000

Bullock, J. S. 2010, ArXiv:1009.4505

Burstein, D., Bender, R., Faber, S., & Nolthenius, R. 1997, AJ, 114, 1365

Capuzzo-Dolcetta, R. & Miocchi, P. 2008, ApJ, 681, 1136

Cardelli, J. A., Clayton, G. C., & Mathis, J. S. 1989, ApJ, 345, 245

Chen, Y. Q., Zhao, G., Nissen, P. E., Bai, G. S., & Qiu, H. M. 2003, ApJ, 591, 925

Chiboucas, K. & Mateo, M. 2006, AJ, 132, 347

Chiboucas, K. & Mateo, M. 2007, ApJS, 170, 95

Chiboucas, K., Tully, R. B., Marzke, R. O., et al. 2010, ArXiv:1009.3950

Chilingarian, I., Cayatte, V., Chemin, L., et al. 2007, A&A, 466, L21

Chilingarian, I. V. & Bergond, G. 2010, MNRAS, 405, L11

Chilingarian, I. V., Cayatte, V., Durret, F., et al. 2008, A&A, 486, 85

Chilingarian, I. V. & Mamon, G. A. 2008, MNRAS, 385, L83

Chilingarian, I. V., Mieske, S., Hilker, M., & Infante, L. 2011, MNRAS, 66

Christlein, D. & Zabludoff, A. I. 2003, ApJ, 591, 764

Churazov, E., Gilfanov, M., Forman, W., & Jones, C. 1999, ApJ, 520, 105

Cimatti, A., Cassata, P., Pozzetti, L., et al. 2008, A&A, 482, 21

Collins, M. L. M., Chapman, S. C., Irwin, M. J., et al. 2010, MNRAS, 407, 2411

Conselice, C. J., Gallagher, III, J. S., & Wyse, R. F. G. 2003, AJ, 125, 66

Côté, P., Ferrarese, L., Jordán, A., et al. 2008, in IAU Symposium, Vol. 246, IAU Symposium, 377–386

Côté, P., Ferrarese, L., Jordán, A., et al. 2007, ApJ, 671, 1456

Côté, P., Piatek, S., Ferrarese, L., et al. 2006, ApJS, 165, 57

da Costa, L. N., Numes, M. A., Pellegrini, P. S., et al. 1986, AJ, 91, 6

da Costa, L. N., Willmer, C., Pellegrini, P. S., & Chincarini, G. 1987, AJ, 93, 1338

Da Rocha, C., Mieske, S., Georgiev, I. Y., et al. 2011, A&A, 525, A86

Dabringhausen, J., Hilker, M., & Kroupa, P. 2008, MNRAS, 386, 864

Dabringhausen, J., Kroupa, P., & Baumgardt, H. 2009, MNRAS, 394, 1529

Damjanov, I., McCarthy, P. J., Abraham, R. G., et al. 2009, ApJ, 695, 101

De Filippis, E., Paolillo, M., Longo, G., et al. 2011, ArXiv:1102.5310

de Jong, J. T. A., Martin, N. F., Rix, H., et al. 2010, ApJ, 710, 1664

de Rijcke, S., Penny, S. J., Conselice, C. J., Valcke, S., & Held, E. V. 2009, MNRAS, 393, 798

de Vaucouleurs, G. 1948, Annales d'Astrophysique, 11, 247

Diemand, J., Kuhlen, M., Madau, P., et al. 2008, Nat, 454, 735

Dirsch, B., Richtler, T., & Bassino, L. P. 2003, A&A, 408, 929

Dirsch, B., Richtler, T., Geisler, D., et al. 2004, AJ, 127, 2114

Djorgovski, S. & Davis, M. 1987, ApJ, 313, 59

Dolphin, A. E. 2009, PASP, 121, 655

Drinkwater, M. J., Gregg, M. D., & Colless, M. 2001, ApJ, 548, L139

Drinkwater, M. J., Gregg, M. D., Couch, W. J., et al. 2004, Publications of the Astronomical Society of Australia, 21, 375

Drinkwater, M. J., Gregg, M. D., Hilker, M., et al. 2003, Nat, 423, 519

Drinkwater, M. J., Jones, J. B., Gregg, M. D., &

Phillipps, S. 2000a, Publications of the Astronomical Society of Australia, 17, 227

Drinkwater, M. J., Phillipps, S., Jones, J. B., et al. 2000b, A&A, 355, 900

Evans, N. W., Wilkinson, M. I., Perrett, K. M., & Bridges, T. J. 2003, ApJ, 583, 752

Evstigneeva, E. A., Drinkwater, M. J., Jurek, R., et al. 2007a, MNRAS, 378, 1036

Evstigneeva, E. A., Drinkwater, M. J., Peng, C. Y., et al. 2008, AJ, 136, 461

Evstigneeva, E. A., Gregg, M. D., Drinkwater, M. J., & Hilker, M. 2007b, AJ, 133, 1722

Faber, S. M. 1973, ApJ, 179, 423

Faber, S. M. & Jackson, R. E. 1976, ApJ, 204, 668

Fellhauer, M. & Kroupa, P. 2002, MNRAS, 330, 642

Fellhauer, M. & Kroupa, P. 2005, MNRAS, 359, 223

Ferguson, H. C. & Binggeli, B. 1994, A&ARv, 6, 67

Ferguson, H. C. & Sandage, A. 1988, AJ, 96, 1520

Ferguson, H. C. & Sandage, A. 1991, AJ, 101, 765

Ferrarese, L., Côté, P., Jordán, A., et al. 2006, ApJS, 164, 334

Ferreras, I., Charlot, S., & Silk, J. 1999, ApJ, 521, 81

Firth, P., Drinkwater, M. J., Evstigneeva, E. A., et al. 2007, MNRAS, 382, 1342

Forbes, D. & Kroupa, P. 2011, ArXiv:1101.3309

Forbes, D., Spitler, L., Graham, A., et al. 2011, ArXiv:1101.2460

Forbes, D. A., Lasky, P., Graham, A. W., & Spitler, L. 2008, MNRAS, 389, 1924

Freedman, W. L., Madore, B. F., Gibson, B. K., et al. 2001, ApJ, 553, 47

Fukugita, M., Shimasaku, K., & Ichikawa, T. 1995, PASP, 107, 945

Furusho, T., Yamasaki, N. Y., Ohashi, T. S. R., et al. 2001, PASJ, 53, 421

Gallazzi, A., Charlot, S., Brinchmann, J., & White, S. D. M. 2006, MNRAS, 370, 1106

Gavazzi, G., Donati, A., Cucciati, O., et al. 2005, A&A, 430, 411

Geha, M., Guhathakurta, P., & van der Marel, R. P. 2003, AJ, 126, 1794

Georgiev, I. Y., Goudfrooij, P., Puzia, T. H., & Hilker, M. 2008, AJ, 135, 1858

Gieles, M., Baumgardt, H., Heggie, D. C., & Lamers, H. J. G. L. M. 2010, MNRAS, 408, L16

Gilmore, G., Wilkinson, M. I., Wyse, R. F. G., et al. 2007, ApJ, 663, 948

Girardi, M., Biviano, A., Giuricin, G., Mardirossian, F., & Mezzetti, M. 1993, ApJ, 404, 38

Girardi, M., Biviano, A., Giuricin, G., Mardirossian,

F., & Mezzetti, M. 1995, ApJ, 438, 527

Girardi, M., Giuricin, G., Mardirossian, F., Mezzetti, M., & Boschin, W. 1998, ApJ, 505, 74

Goerdt, T., Moore, B., Kazantzidis, S., et al. 2008, MNRAS, 385, 2136

Graham, A. W. & Driver, S. P. 2005, Publications of the Astronomical Society of Australia, 22, 118

Graham, A. W. & Guzmán, R. 2003, AJ, 125, 2936

Graham, A. W. & Worley, C. C. 2008, MNRAS, 388, 1708

Grebel, E. K. 2001, Astrophysics and Space Science Supplement, 277, 231

Grebel, E. K., Gallagher, III, J. S., & Harbeck, D. 2003, AJ, 125, 1926

Gregg, M. D., Drinkwater, M. J., Evstigneeva, E., et al. 2009, AJ, 137, 498

Grillmair, C. J., Faber, S. M., Lauer, T. R., et al. 1994, AJ, 108, 102

Haşegan, M., Jordán, A., Côté, P., et al. 2005, ApJ, 627, 203

Harris, W. E. 1996, AJ, 112, 1487

Harris, W. E. 2009, ApJ, 699, 254

Hau, G. K. T., Spitler, L. R., Forbes, D. A., et al. 2009, MNRAS, 394, L97

Hilker, M. 2009, UCDs - A Mixed Bag of Objects, ed. Richtler, T. & Larsen, S., 51

Hilker, M., Baumgardt, H., Infante, L., et al. 2007, A&A, 463, 119

Hilker, M., Infante, L., Vieira, G., Kissler-Patig, M., & Richtler, T. 1999, A&AS, 134, 75

Hilker, M., Mieske, S., & Infante, L. 2003, A&A, 397, L9

Hopkins, P. F., Bundy, K., Murray, N., et al. 2009, MNRAS, 398, 898

Hopkins, P. F., Murray, N., Quataert, E., & Thompson, T. A. 2010, MNRAS, 401, L19

Horne, K. 1986, PASP, 98, 609

Infante, L., Mieske, S., & Hilker, M. 2003, Ap&SS, 285, 87

Irwin, M. J., Belokurov, V., Evans, N. W., et al. 2007, ApJ, 656, L13

Janz, J. & Lisker, T. 2008, ApJ, 689, L25

Janz, J. & Lisker, T. 2009, ApJ, 696, L102

Jenkins, A., Frenk, C. S., White, S. D. M., et al. 2001, MNRAS, 321, 372

Jerjen, H. & Binggeli, B. 1997, in Astronomical Society of the Pacific Conference Series, Vol. 116, The Nature of Elliptical Galaxies; 2nd Stromlo Symposium, ed. M. Arnaboldi, G. S. Da Costa, & P. Saha, 239

Jerjen, H., Binggeli, B., & Freeman, K. C. 2000, AJ, 119, 593

Jerjen, H. & Dressler, A. 1997, A&AS, 124, 1

Jerjen, H. & Murdin, P. 2000, Luminosity Function of Galaxies, ed. Murdin, P.

Jones, J. B., Drinkwater, M. J., Jurek, R., et al. 2006, AJ, 131, 312

Jordán, A., Peng, E. W., Blakeslee, J. P., et al. 2009, ApJS, 180, 54

Jordi, K., Grebel, E. K., & Ammon, K. 2006, A&A, 460, 339

Kalirai, J. S., Beaton, R. L., Geha, M. C., et al. 2010, ApJ, 711, 671

Kambas, A., Davies, J. I., Smith, R. M., Bianchi, S., & Haynes, J. A. 2000, AJ, 120, 1316

Karachentsev, I. D. & Kashibadze, O. G. 2006, Astrophysics, 49, 3

Kashikawa, N., Shimasaku, K., Yagi, M., et al. 1995, ApJ, 452, L99

Kauffmann, G., White, S. D. M., & Guiderdoni, B. 1993, MNRAS, 264, 201

King, I. 1962, AJ, 67, 471

Kissler-Patig, M. 2004, in Astronomical Society of the Pacific Conference Series, Vol. 322, The Formation and Evolution of Massive Young Star Clusters, ed. H. J. G. L. M. Lamers, L. J. Smith, & A. Nota, 535

Kissler-Patig, M., Brodie, J. P., Schroder, L. L., et al. 1998, AJ, 115, 105

Kissler-Patig, M., Jordán, A., & Bastian, N. 2006, A&A, 448, 1031

Klypin, A., Kravtsov, A. V., Valenzuela, O., & Prada, F. 1999, ApJ, 522, 82

Kodama, T. & Arimoto, N. 1997, A&A, 320, 41

Koposov, S., Belokurov, V., Evans, N. W., et al. 2008, ApJ, 686, 279

Köppen, J., Weidner, C., & Kroupa, P. 2007, MNRAS, 375, 673

Kormendy, J. 1977, ApJ, 218, 333

Kormendy, J. 1985, ApJ, 295, 73

Kormendy, J., Fisher, D. B., Cornell, M. E., & Bender, R. 2009, ApJS, 182, 216

Krist, J. 1995, in Astronomical Society of the Pacific Conference Series, Vol. 77, Astronomical Data Analysis Software and Systems IV, ed. R. A. Shaw, H. E. Payne, & J. J. E. Hayes, 349

Kroupa, P. 1998, MNRAS, 300, 200

Kroupa, P. 2001, MNRAS, 322, 231

Kroupa, P., Famaey, B., de Boer, K. S., et al. 2010, A&A, 523, A32

Kroupa, P. & Weidner, C. 2003, ApJ, 598, 1076

Larsen, S. S. 1999, A&AS, 139, 393

LeFevre, O., Saisse, M., Mancini, D., et al. 2003, in Society of Photo-Optical Instrumentation Engineers (SPIE) Conference Series, Vol. 4841, Society of Photo-Optical Instrumentation Engineers (SPIE) Conference Series, ed. M. Iye & A. F. M. Moorwood, 1670–1681

Lisker, T., Grebel, E. K., & Binggeli, B. 2008, AJ, 135, 380

Łokas, E. L., Mamon, G. A., & Prada, F. 2005, MNRAS, 363, 918

Łokas, E. L., Wojtak, R., Gottlöber, S., Mamon, G. A., & Prada, F. 2006, MNRAS, 367, 1463

López-Cruz, O., Barkhouse, W. A., & Yee, H. K. C. 2004, ApJ, 614, 679

Lucey, J. R., Currie, M. J., & Dickens, R. J. 1986, MNRAS, 221, 453

Madrid, J. P., Graham, A. W., Harris, W. E., et al. 2010, ApJ, 722, 1707

Mahdavi, A., Trentham, N., & Tully, R. B. 2005, AJ, 130, 1502

Mancini, C., Daddi, E., Renzini, A., et al. 2010, MNRAS, 401, 933

Maraston, C. 2005, MNRAS, 362, 799

Maraston, C., Bastian, N., Saglia, R. P., et al. 2004, A&A, 416, 467

Maraston, C., Daddi, E., Renzini, A., et al. 2006, ApJ, 652, 85

Martin, N. F., de Jong, J. T. A., & Rix, H.-W. 2008, ApJ, 684, 1075

Martin, N. F., Ibata, R. A., Irwin, M. J., et al. 2006, MNRAS, 371, 1983

Martin, N. F., McConnachie, A. W., Irwin, M., et al. 2009, ApJ, 705, 758

Mateo, M. L. 1998, ARA&A, 36, 435

McConnachie, A. W., Huxor, A., Martin, N. F., et al. 2008, ApJ, 688, 1009

McConnachie, A. W. & Irwin, M. J. 2006, MNRAS, 365, 1263

McLaughlin, D. E., Secker, J., Harris, W. E., & Geisler, D. 1995, AJ, 109, 1033

McLaughlin, D. E. & van der Marel, R. P. 2005, ApJS, 161, 304

Mei, S., Blakeslee, J. P., Côté, P., et al. 2007, ApJ, 655, 144

Michielsen, D., Koleva, M., Prugniel, P., et al. 2007, ApJ, 670, L101

Mieske, S. & Hilker, M. 2003, A&A, 410, 445

Mieske, S., Hilker, M., & Infante, L. 2002, A&A, 383, 823

Mieske, S., Hilker, M., & Infante, L. 2004, A&A, 418, 445

Mieske, S., Hilker, M., & Infante, L. 2005a, A&A, 438, 103

Mieske, S., Hilker, M., Infante, L., & Jordán, A. 2006, AJ, 131, 2442

Mieske, S., Hilker, M., Infante, L., & Mendes de Oliveira, C. 2007a, A&A, 463, 503

Mieske, S., Hilker, M., Jordán, A., Infante, L., & Kissler-Patig, M. 2007b, A&A, 472, 111

Mieske, S., Hilker, M., Jordán, A., et al. 2008, A&A, 487, 921

Mieske, S., Hilker, M., Misgeld, I., et al. 2009, A&A, 498, 705

Mieske, S., Infante, L., Hilker, M., et al. 2005b, A&A, 430, L25

Mieske, S., Jordán, A., Côté, P., et al. 2010, ApJ, 710, 1672

Mieske, S. & Kroupa, P. 2008, ApJ, 677, 276

Milgrom, M. 1983, ApJ, 270, 365

Milne, M. L., Pritchet, C. J., Poole, G. B., et al. 2007, AJ, 133, 177

Misgeld, I., Hilker, M., & Mieske, S. 2009, A&A, 496, 683

Misgeld, I., Mieske, S., & Hilker, M. 2008, A&A, 486, 697

Mobasher, B., Colless, M., Carter, D., et al. 2003, ApJ, 587, 605

Moore, B., Ghigna, S., Governato, F., et al. 1999, ApJ, 524, L19

Murray, N. 2009, ApJ, 691, 946

Naab, T., Johansson, P. H., & Ostriker, J. P. 2009, ApJ, 699, L178

Newman, A. B., Ellis, R. S., Treu, T., & Bundy, K. 2010, ApJ, 717, L103

Niederste-Ostholt, M., Belokurov, V., Evans, N. W., et al. 2009, MNRAS, 398, 1771

Norris, M. A. & Kannappan, S. J. 2011, ArXiv:1102.0001

Paturel, G., Petit, C., Prugniel, P., et al. 2003, A&A, 412, 45

Paudel, S. & Lisker, T. 2009, Astronomische Nachrichten, 330, 969

Paudel, S., Lisker, T., Kuntschner, H., Grebel, E. K., & Glatt, K. 2010, MNRAS, 405, 800

Peng, E. W., Côté, P., Jordán, A., et al. 2006, ApJ, 639, 838

Penny, S. J. & Conselice, C. J. 2008, MNRAS, 383, 247

Penny, S. J., Conselice, C. J., de Rijcke, S., et al. 2011, MNRAS, 410, 1076

Pflamm-Altenburg, J. & Kroupa, P. 2009, MNRAS, 397, 488

Phillipps, S., Drinkwater, M. J., Gregg, M. D., & Jones, J. B. 2001, ApJ, 560, 201

Poggianti, B. M., Bridges, T. J., Mobasher, B., et al. 2001, ApJ, 562, 689

Postman, M. & Lauer, T. R. 1995, ApJ, 440, 28

Press, W. H. & Schechter, P. 1974, ApJ, 187, 425

Price, J., Phillipps, S., Huxor, A., et al. 2009, MN-RAS, 397, 1816

Pritchet, C. J. & van den Bergh, S. 1999, AJ, 118, 883

Pryor, C. & Meylan, G. 1993, in Astronomical Society of the Pacific Conference Series, Vol. 50, Structure and Dynamics of Globular Clusters, ed. S. G. Djorgovski & G. Meylan, 357

Quintana, H., Ramirez, A., & Way, M. J. 1996, AJ, 111, 603

Rakos, K. & Schombert, J. 2004, AJ, 127, 1502

Rejkuba, M., Dubath, P., Minniti, D., & Meylan, G. 2007, A&A, 469, 147

Richter, O.-G. 1987, A&AS, 67, 237

Richter, O.-G., Huchtmeier, W. K., & Materne, J. 1982, A&A, 111, 193

Richtler, T., Dirsch, B., Gebhardt, K., et al. 2004, AJ, 127, 2094

Rines, K. & Geller, M. J. 2008, AJ, 135, 1837

Rossa, J., van der Marel, R. P., Böker, T., et al. 2006, AJ, 132, 1074

Sabatini, S., Davies, J., Scaramella, R., et al. 2003, MNRAS, 341, 981

Sandage, A. & Binggeli, B. 1984, AJ, 89, 919

Schechter, P. 1976, ApJ, 203, 297

Schlegel, D. J., Finkbeiner, D. P., & Davis, M. 1998, ApJ, 500, 525

Schuberth, Y., Richtler, T., Hilker, M., et al. 2010, A&A, 513, A52

Scodeggio, M., Franzetti, P., Garilli, B., et al. 2005, PASP, 117, 1284

Secker, J. & Harris, W. E. 1996, ApJ, 469, 623

Secker, J., Harris, W. E., & Plummer, J. D. 1997, PASP, 109, 1377

Sérsic, J. L. 1968, Atlas de galaxias australes (Cordoba, Argentina: Observatorio Astronomico, 1968)

Smith Castelli, A. V., Bassino, L. P., Richtler, T., et al. 2008a, MNRAS, 386, 2311

Smith Castelli, A. V., Faifer, F. R., Richtler, T., & Bassino, L. P. 2008b, MNRAS, 391, 685

Sparke, L. S. & Gallagher, III, J. S. 2000, Galaxies in the universe : an introduction, ed. Sparke, L. S. & Gallagher, J. S., III

Spergel, D. N. & Steinhardt, P. J. 2000, Physical Review Letters, 84, 3760

Springel, V., Wang, J., Vogelsberger, M., et al. 2008, MNRAS, 391, 1685

Stein, P., Jerjen, H., & Federspiel, M. 1997, A&A, 327, 952

Tamura, T., Makishima, K., Fukazawa, Y., Ikebe, Y., & Xu, H. 2000, ApJ, 535, 602

Taylor, M. A., Puzia, T. H., Harris, G. L., et al. 2010, ApJ, 712, 1191

Tiret, O., Salucci, P., Bernardi, M., Maraston, C., & Pforr, J. 2010, MNRAS, 1737

Tollerud, E. J., Bullock, J. S., Graves, G. J., & Wolf, J. 2011, ApJ, 726, 108

Tonry, J. & Davis, M. 1979, AJ, 84, 1511

Tonry, J. L., Dressler, A., Blakeslee, J. P., et al. 2001, ApJ, 546, 681

Trentham, N. & Hodgkin, S. 2002, MNRAS, 333, 423

Trentham, N., Sampson, L., & Banerji, M. 2005, MNRAS, 357, 783

Trentham, N. & Tully, R. B. 2002, MNRAS, 335, 712

Ulmer, M. P., Bernstein, G. M., Martin, D. R., et al. 1996, AJ, 112, 2517

van de Ven, G., van den Bosch, R. C. E., Verolme, E. K., & de Zeeuw, P. T. 2006, A&A, 445, 513

van den Bergh, S. 1977, ApJ, 212, 317

van den Bergh, S. 1992, A&A, 264, 75

van den Bergh, S. 1999, A&ARv, 9, 273

van den Bergh, S. 2000, The Galaxies of the Local Group (The galaxies of the Local Group, by Sidney Van den Bergh. Published by Cambridge, UK: Cambridge University Press, 2000 Cambridge Astrophysics Series Series, vol no: 35, ISBN: 0521651816.)

van Dokkum, P. G. 2001, PASP, 113, 1420

van Dokkum, P. G., Franx, M., Kriek, M., et al. 2008, ApJ, 677, L5

van Zee, L., Barton, E. J., & Skillman, E. D. 2004, AJ, 128, 2797

Venables, W. N. & Ripley, B. D. 2002, Modern Applied Statistics with S, 4th edn. (New York: Springer)

Ventimiglia, G., Arnaboldi, M., & Gerhard, O. 2008, Astronomische Nachrichten, 329, 1057

Ventimiglia, G., Arnaboldi, M., & Gerhard, O. 2011, A&A, 528, A24

Verde, L., Oh, S. P., & Jimenez, R. 2002, MNRAS, 336, 541

Visvanathan, N. & Sandage, A. 1977, ApJ, 216, 214

Walcher, C. J., van der Marel, R. P., McLaughlin, D., et al. 2005, ApJ, 618, 237

Wegner, G., Bernardi, M., Willmer, C. N. A., et al. 2003, AJ, 126, 2268

Wehner, E. M. H. & Harris, W. E. 2007, ApJ, 668, L35

Wehner, E. M. H., Harris, W. E., Whitmore, B. C., Rothberg, B., & Woodley, K. A. 2008, ApJ, 681, 1233

Weidner, C., Kroupa, P., & Larsen, S. S. 2004, MN-RAS, 350, 1503

White, S. D. M. & Rees, M. J. 1978, MNRAS, 183, 341

Whitmore, B. C., Zhang, Q., Leitherer, C., et al. 1999, AJ, 118, 1551

Worthey, G. 1994, ApJS, 95, 107

Yagi, M., Kashikawa, N., Sekiguchi, M., et al. 2002, AJ, 123, 87

Yamanoi, H., Tanaka, M., Hamabe, M., et al. 2007, AJ, 134, 56

Young, C. K. & Currie, M. J. 1994, MNRAS, 268, L11

Zaritsky, D., Gonzalez, A. H., & Zabludoff, A. I. 2006a, ApJ, 642, L37

Zaritsky, D., Gonzalez, A. H., & Zabludoff, A. I. 2006b, ApJ, 638, 725

Zaritsky, D., Zabludoff, A. I., & Gonzalez, A. H. 2011, ApJ, 727, 116

Zucker, D. B., Kniazev, A. Y., Martínez-Delgado, D., et al. 2007, ApJ, 659, L21

Danksagung

Gracias amigos!

Astronomy

Clock strikes twelve and moondrops burst
Out at you from their hiding place
Like acid and oil on a madman's face
His reasons tend to fly away
Like lesser birds on the four winds
Like silver scrapes in May
And now the sand's become a crust
Most of you have gone away

Come Susie dear, let's take a walk
Just out there upon the beach
I know you'll soon be married
And you want to know where winds come from
Well it's never said at all
On the map that Carrie reads
Behind the clock back there you know
At the Four Winds Bar

Four winds at the Four Winds Bar
Two doors locked and windows barred
One door to let to take you in
The other one just mirrors it

Hellish glare and inference
The other one's a duplicate
The Queenly flux, eternal light
Or the light that never warms
Yes the light that never, never warms
Yes the light that never
Never warms

The clock strikes twelve and moondrops burst
Out at you from their hiding place
Miss Carrie nurse and Susie dear
Would find themselves at Four Winds Bar

It's the nexus of the crisis
And the origin of storms
Just the place to hopelessly
Encounter time and then came me

Call me Desdinova
Eternal light
These gravely digs of mine
Will surely prove a sight
And don't forget my dog
Fixed and consequent

Astronomy...a star

Lebenslauf

Ingo Misgeld

Geburtsdatum: 20.01.1980
Geburtsort: Essen

08/1990 – 05/1999	Privates Gymnasium Vinzenz-Pallotti-Kolleg, Rheinbach
08/1999 – 06/2000	Zivildienst am Internat des Vinzenz-Pallotti-Kollegs, Rheinbach
09/2000 – 08/2006	Studium der Physik am Physikalischen Institut der Rheinischen Friedrich-Wilhelms-Universität Bonn
09/2006 – 09/2007	Diplomarbeit am Argelander-Institut für Astronomie (AIfA), Bonn Betreuer: Prof. Dr. Klaas S. de Boer (AIfA, Bonn), Dr. Michael Hilker (ESO, Garching)
11/2007 – 12/2009	Doktorarbeit am European Southern Observatory (ESO), Garching bei München Betreuer: Dr. Michael Hilker (ESO, Garching), Dr. Steffen Mieske (ESO, Chile), Prof. Dr. Pavel Kroupa (AIfA, Bonn)
01/2010 – 06/2011	Doktorarbeit an der Universtäts-Sternwarte München (USM) Betreuer: Prof. Dr. Ralf Bender (USM, München), Dr. Michael Hilker (ESO, Garching), Dr. Steffen Mieske (ESO, Chile)

München, den 19.04.2011